

A Large-Signal Multi-tone Time Domain Waveform Measurement System with Broadband Active Load Impedance Control

**A thesis submitted to Cardiff University
In candidature for the degree of**

Doctor of Philosophy

By

Tudor Vyvyan Williams M.Eng.

Division of Electrical and Electronic Engineering
School of Engineering
Cardiff University
United Kingdom

December 2007

UMI Number: U585070

All rights reserved

INFORMATION TO ALL USERS

The quality of this reproduction is dependent upon the quality of the copy submitted.

In the unlikely event that the author did not send a complete manuscript and there are missing pages, these will be noted. Also, if material had to be removed, a note will indicate the deletion.



UMI U585070

Published by ProQuest LLC 2013. Copyright in the Dissertation held by the Author.
Microform Edition © ProQuest LLC.

All rights reserved. This work is protected against
unauthorized copying under Title 17, United States Code.



ProQuest LLC
789 East Eisenhower Parkway
P.O. Box 1346
Ann Arbor, MI 48106-1346

DECLARATION

This work has not previously been accepted in substance for any degree and is not concurrently submitted in candidature for any degree.

Signed J. V. Williams (candidate)

Date 20/05/2008

STATEMENT 1

This thesis is being submitted in partial fulfillment of the requirements for the degree of PhD

Signed J. V. Williams (candidate)

Date 20/05/2008

STATEMENT 2

This thesis is the result of my own independent work/investigation, except where otherwise stated.

Other sources are acknowledged by explicit references.

Signed J. V. Williams (candidate)

Date 20/05/2008

STATEMENT 3

I hereby give consent for my thesis, if accepted, to be available for photocopying and for inter-library loan, and for the title and summary to be made available to outside organisations.

Signed J. V. Williams (candidate)

Date 20/05/2008

STATEMENT 4: PREVIOUSLY APPROVED BAR ON ACCESS

I hereby give consent for my thesis, if accepted, to be available for photocopying and for inter-library loans **after expiry of a bar on access previously approved by the Graduate Development Committee.**

Signed J. V. Williams (candidate)

Date 20/05/2008

Summary

This thesis presents a novel large-signal, multi-tone, time domain waveform measurement and engineering system, which builds upon existing large-signal measurement approaches. The presented system allows for a more considered, and scientific process to be adopted in the design of modern day communications systems. The ultimate aim of this work is to reduce the need for an iterative design approach by providing a measurement system that offers detailed information about a device or circuit without the need for prototyping, it is hoped that such an approach will one day lead to a 'right first time' design approach by allowing ultra-rapid data collection with measurements conducted in realistic environments while employing realistic stimuli.

The main contributions to the field of research come in two areas; firstly developments that allow for accurate time domain measurement of complex modulated signals using commercially available equipment; and secondly in the area of active impedance control, where novel developments were made allowing active control of impedance across a modulated bandwidth.

The first research area addressed is the fundamental difficulty in sampling multi-tone waveforms, where the main achievements have been the realisation of a novel frequency-folded and interleaved sampling approach. This approach, with appropriate time-alignment and averaging allows the efficient collection of high-quality vectorial information for all significant distortion terms, for all bands of interest. This means that for the first time off-the-shelf sampling oscilloscopes with limited memory depth can be used capture multi-tone signals in sufficient detail to observe all critical device performance.

The second area of research investigated suitable impedance control architectures. Measurement of large-signal multi-tone information is only useful if the broadband impedance environment can also be controlled, only then can we allow a full understanding of the device, and provide the fundamental ability to engineer waveforms for optimum device performance. The main achievement in this area was the development and realisation of a novel architecture that allows active impedance control over a modulated bandwidth.

Acknowledgements

Firstly I would like to thank my supervisor Prof. Paul Tasker, firstly for giving me the opportunity to study for this degree at all, in rather unique circumstances, but more importantly for the help and support throughout the course of the PhD. His knowledge across such a wide area of microwave engineering is second to none and our numerous technical conversations have been a pleasure. I would also like to thank my second supervisor Dr. Johannes Benedikt for his support and mentoring over the last few years.

I am also grateful to the financial support provided by Cardiff University School of Engineering.

My time so far at Cardiff University has been made so enjoyable by the excellent working atmosphere in the centre for high frequency engineering. In particular, I would like to thank Dr. Jonathan Lees, firstly for proof reading this thesis, but more importantly for his friendship and enthusiasm for the subject, which has kept me focused during my PhD. I would also like to thank another friend and colleague Peter McGovern, who even when times got tough made me laugh. Also, Ziad Aboush for his friendship throughout the duration of my studies. I should also mention Simon Woodington, who has taken over much of the work presented here, and in the process has taught me as much as I have him. I have made a number of other friends, who have been very supportive more recently but unfortunately they too numerous to mention here, but they know who they are.

I owe a debt of gratitude to my family, without their help, support and encouragement I would not have started this thesis, let alone finished it. My special thanks therefore go to my wife Natalie, who has been so supportive even when this work has seemingly taken over my life, and also to my parents who have always encouraged me to do my best in life.

List of Publications

First Author Publications

Williams, T.; Benedikt, J.; Tasker, P.J. "***Fully Functional 'Real Time' Non-Linear Device Characterization System Incorporating Active Load Control***" 36th European Microwave Conference, September 2006, Page(s): 1610-1613

Williams, T.; Benedikt, J.; Tasker, P.J. "***Application of a novel active envelope load pull architecture in large signal device characterization***" 35th European Microwave Conference, October 2005, Volume 1.

Williams, T.; Benedikt, J.; Tasker, P.J. "***Experimental evaluation of an active envelope load pull architecture for high speed device characterization***" IEEE MTT-S International Microwave Symposium Digest, June 2005.

Williams, T.; Benedikt, J.; Tasker, P.J. "***Novel base-band envelope load pull architecture [RF device testing]***" High Frequency Postgraduate Student Colloquium, 2004 6-7 Sept. 2004 Page(s):157 - 161

Joint Publications

Alghanim A.; Lees J.; Williams T.; Benedikt J., Tasker P.J. "***Using active IF load-pull to investigate electrical base-band memory effects in high-power LDMOS transistors***" IEEE Asia-Pacific Microwave Conference 2007

Alghanim A.; Lees J.; Williams T.; Benedikt J., Tasker P.J. "***Investigation of Electrical Base-Band Memory Effects in High Power 20W LDMOS Amplifiers***" 37th European Microwave Conference, 2007, Page(s):48-51

Gaddi, R.; Williams, T.; Benedikt, J.; Tasker, P. J.; Giacomozzi, F.; Margesin, B.; Gnudi, A.; "***Large-Signal Vectorial Load-Pull Characterization of MEMS RF-Actuation***" IEEE Microwave and Wireless Components Letters Volume 17, Issue 12, Dec. 2007 Page(s):903 - 905

Table of Contents

Chapter 1 – Introduction.....	Page 1
1.1 Industrial Perspective.....	Page 1
1.2 Project Aim – Enabling Technology for Right-First-Time Design.....	Page 2
1.3 Existing Large Signal Measurement Systems.....	Page 3
1.4 A New Multi-Tone Large Signal Measurement and Engineering System.....	Page 4
1.5 Multi-tone large signal Waveform Capture.....	Page 5
1.6 Impedance control for multi-tine signals.....	Page 8
1.7 Thesis Overview.....	Page 9
1.8 References.....	Page 12
Chapter 2 – Realisation of a Non-Linear Multi-Tone Waveform Measurement System.....	Page 14
2.1 Motivation.....	Page 14
2.2 RF Measurement Systems.....	Page 15
2.2.1 Linear (Small Signal) Measurement Architectures.....	Page 16
2.2.2 Non-Linear Measurement Systems.....	Page 17
2.2.3 Existing Multi-tone measurement Solutions.....	Page 28
2.3 Requirement for an all-encompassing Solution.....	Page 33
2.4 Realised CW Measurement Architecture.....	Page 34
2.4.1 Realised Multi-tone Measurement Architecture.....	Page 36
2.5 Multi-tone sampling Implementation.....	Page 38
2.5.1 Introduction to Sampling Oscilloscopes.....	Page 39
2.5.2 Standard Sampling Approach.....	Page 41
2.5.3 Compressed Frequency Sampling Approach.....	Page 43
2.5.4 Theory of Compressed Frequency Sampling Approach.....	Page 46
2.6 Compressed Frequency Sampling Application Issues.....	Page 51
2.6.1 Spectral Overflow and Folding.....	Page 51
2.6.2 Limited Tone-Spacing Grid.....	Page 51
2.6.3 Error on the Trigger re-arm time.....	Page 56
2.6.4 Issues Moving to Higher Clock Frequencies.....	Page 57
2.7 Multi-Tone Software Time Alignment.....	Page 58
2.8 System Calibration.....	Page 61
2.9 Chapter Summary.....	Page 62
2.10 References.....	Page 65
Chapter 3 – Validation of a Non-Linear Multi--tone Waveform Measurement System.....	Page 68
3.1 Introduction.....	Page 68
3.2 Small Signal and CW Waveform Verification.....	Page 69
3.2.1 Small Signal Validation.....	Page 70
3.2.2. Active Device – Power Performance Validation.....	Page 74
3.2.3 Active Device – Comparison of Measured Waveforms.....	Page 76
3.3 Verification of compressed Frequency, Time-Interleaved Sampling Approach and Time Alignment Algorithm.....	Page 85
3.3.1 Validation of the Time Interleaved Sampling.....	Page 86

3.3.2 Validation of the Software Waveform Alignment.....	Page 88
3.4 CW Verification using Multi-tone measurement Setup.....	Page 91
3.5 System Impedance Sensitivity Analysis.....	Page 93
3.6 Multi-Tone Verification Using Spectrum Analyser.....	Page 95
3.7 Chapter Summary.....	Page 105
3.8 References.....	Page 107
Chapter 4 – Realisation of Impedance Control Architectures for Multi-Tone Measurements.....	Page 108
4.1 Motivation.....	Page 108
4.2 Impedance Control and Waveform Engineering.....	Page 109
4.3 Existing Impedance Control Solutions.....	Page 110
4.4 Base-Band Impedance Control.....	Page 117
4.5 RF Impedance Control.....	Page 120
4.5.1 Theory of Operation.....	Page 121
4.5.2 Control Electronics.....	Page 122
4.5.2.1 Characterisation of Control Electronics.....	Page 126
4.5.3 Demodulator Selection and Characterisation.....	Page 128
4.5.3.1 Demodulator Characterisation.....	Page 131
4.5.4 Modulator Selection and Characterisation.....	Page 137
4.5.4.1 Modulator Characterisation.....	Page 140
4.6 Error Flow Model of the Envelope Load-Pull Loop.....	Page 143
4.7 Final Electronics Block with Conditioning Electronics.....	Page 147
4.7.1 Demodulator Conditioning Block.....	Page 148
4.7.2 Modulator Conditioning Block.....	Page 151
4.8 Chapter Summary.....	Page 153
4.9 References.....	Page 156
Chapter 5 – Validation of the Envelope Load-Pull Architecture...	Page 159
5.1 Introduction.....	Page 159
5.2 Optimised Configuration of the Envelope Load-Pull Architecture.....	Page 160
5.3 Verification of the X-Y Control.....	Page 161
5.3.1 Demonstration of Impedance control Using Device Measurements.....	Page 166
5.4 Verification of Architecture Under Varying Input Power.....	Page 172
5.4.1 Demonstration of Impedance Tracking Under Varying Power Using Device Measurements.....	Page 176
5.5 Verification of Architecture under Varying Input Phase.....	Page 178
5.6 Determining the Bandwidth of the Envelope Load-Pull Architecture.....	Page 181
5.7 Chapter Summary.....	Page 186
5.8 References.....	Page 188
Chapter 6 – Application of the Waveform Measurement and Engineering System.....	Page 189
6.1 Introduction.....	Page 189
6.1.1 Envelope Domain Extraction.....	Page 190
6.2 Introduction to Real-Time Measurements.....	Page 191
6.2.1 Real Time Power Sweeps.....	Page 192

6.2.1.1 Engineering the Stimulus.....	Page 193
6.2.1.2 'Real-Time' Power Sweep – Device Measurement.....	Page 197
6.2.2 Real Time Load-Pull Sweeps.....	Page 199
6.2.2.1 Real-Time Load Sweep – Device Measurement.....	Page 201
6.2.2.2 Real-Time Load-Pull for Analysis of DC-RF Dispersion.	Page 203
6.3 Memory Investigations.....	Page 205
6.4 Multi-Tone Time Domain Waveforms – Depth of Captured Information.....	Page 209
6.5 Chapter Summary.....	Page 214
6.6 References.....	Page 215
Chapter 7 – Conclusions and Future Work.....	Page 217
7.1 Conclusion.....	Page 217
7.2 Future Work.....	Page 220
7.2.1 Increase Operational Bandwidth of Modulated Load-Pull...	Page 221
7.2.2 Extending the Bandwidth of the Base-Band Measurements	Page 222
7.2.3 Integration of a Spectrum Analyser into the Multi-tone Measurement System.....	Page 222
7.2.4 Optimisation of Multi-Tone Alignment and Averaging Process.....	Page 224
7.2.5 Increase the Bandwidth of the new Multi-tone Waveform Measurement System.....	Page 226
7.3 References.....	Page 228
APPENDICES	
Appendix 1 – Compressed Frequency Sampling – Worked Example.....	A1
Appendix 2 – System Error Coefficients.....	A7
Appendix 3 – Research Publications.....	A15

List of acronyms

RF – Radio Frequency
PA – Power Amplifier
CW – Continuous Wave (Excitation containing only 1 frequency)
CAD – Computer Aided Design
DUT – Device Under Test
A/D – Analogue to Digital
DAC – Digital to Analogue Convertor
VNA – Vector Network Analyser
MTA – Microwave Transition Analyser
NLVNA – Non-Linear Vector Network Analyser
VSA – Vector Signal Analyser
SA – Spectrum Analyser
LSNA – Large Signal Network Analyser
AWG – Arbitrary Waveform Generator
ESG – Economy Signal Generator
CSA – Communication Signal Analyser
SRD – Step Recovery Diode
CDMA – Code Division Multiple Access
SNR – Signal to Noise Ratio
GPIB – General Purpose Instrument Bus
IF – Intermediate Frequency
DSP – Digital Signal Processing
FPGA – Field Programmable Gate Array
FFT – Fast Fourier Transform
HBT – Hetrojunction Bipolar Transistor
pHEMT - Pseudomorphic High Electron Mobility Transistors
LDMOS – Laterally Diffused Metal Oxide Semiconductor
HFET – Hetrojunction Field Effect Transistor
AlGaN – Aluminium Gallium Nitride
GaN – Gallium Nitride
GaAs – Gallium Arsenide

ET – Envelope Tracking
AM/PM – Amplitude Modulation to Phase Modulation
ADS – Advanced Design System
LO – Local Oscillator
SNR – Signal to Noise Ratio
ACPR – Adjacent Channel Power Ratio
BER – Bit Error Rate
EVM – Error Vector Magnitude

Other Terminology

a1 – Incident travelling wave at port one of a device
b1 – Reflected travelling wave at port one of a device
a2 – Incident travelling wave at port two of a device
b2 – Reflected travelling wave at port two of a device
V1 – Voltage at the input terminal of a device
V2 – Voltage at the output terminal of a device
I1 – Current at the input terminal of a device
I2 – Current at the output terminal of a device
IM3 – Third Order Intermodulation Distortion Products
IM5 – Fifth Order Intermodulation Distortion Products
IM7 – Seventh Order Intermodulation Distortion Products
IGOR – Programming Environment produced by Wavemetrics
I – In Phase
Q – Quadrature Phase
Device Memory – When past operating conditions affect the current device performance
Electrical Memory – Device memory caused by varying envelope, fundamental or harmonic impedances
Thermal Memory – Device memory caused by electro-thermal coupling typically at modulation rates up to a few MHz
Trapping effects – device memory caused by charge trapping related to impact ionisation

Chapter 1 - Introduction

1.1 Industrial Perspective

Modern mobile communication systems stem from an evolution that began in the early nineteenth century, when the first attempts of “mobile radio” were used to communicate with vehicles without the use of wire [1]. The first fully automated mobile phone system, called ‘mobile telephone system A’ was developed by Ericsson and released in 1956 in Sweden. The weight of the mobile handset was a significant 40 Kg, and the network had 150 subscribers when it was introduced, and only 600 when it was decommissioned in 1983 [2]. From these modest beginnings, the last 20 years have seen an explosion in the number of subscribers to mobile phone networks. Figure 1.1 is a plot taken from wireless intelligence, a global database of mobile market information showing the dramatic rise in subscriptions [3]. Recent estimates are predicting numbers of global mobile subscribers to grow to 3.3 billion by 2010. To place this into context, assuming a worldwide population of 6 billion, this means that within the next few years, every other person on the planet will own a mobile phone. Furthermore, recent years have seen the humble mobile

phone evolve into a personal communications device, providing multi-media wireless solutions including voice, video, graphics, audio and broad-band internet access. This 'bandwidth-hungry' evolution combined with the massive growth in subscribers has led directly to the creation of a number of complex, multi-carrier modulation schemes employing, amongst other things, a combination of phase and amplitude modulation, that strive to make the most efficient use of the spectrum in order to meet demand.

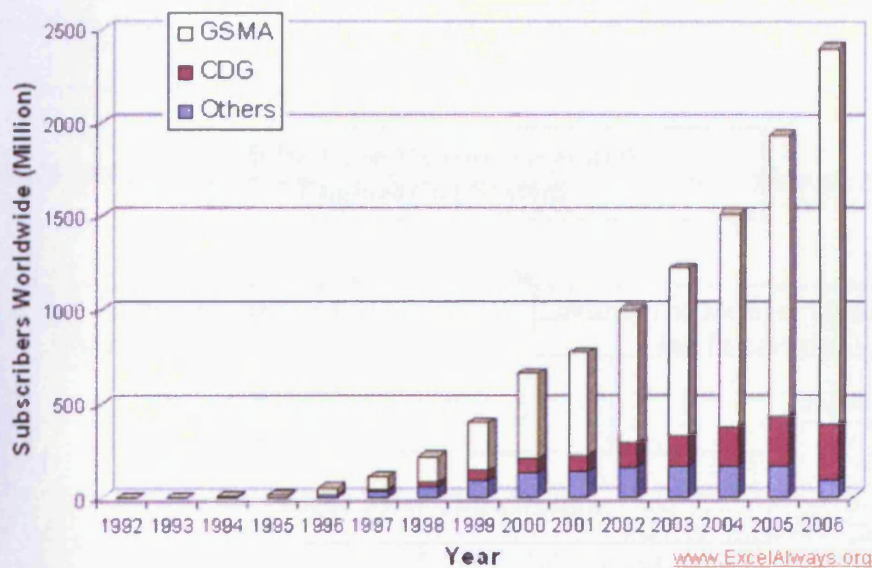
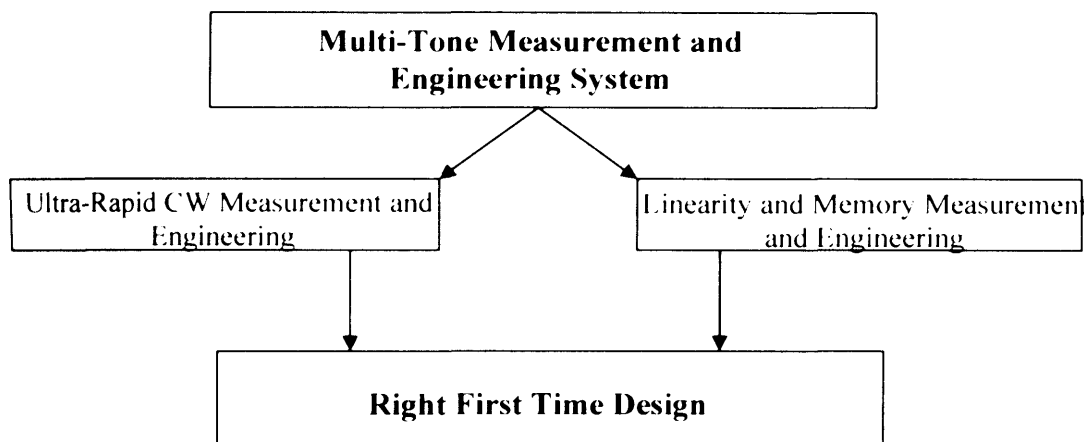


Figure 1.1 – Graph showing the dramatic increase in global mobile subscription from 1992 to 2006

1.2 Project Aim – Enabling Technology for Right-first-time design

Even today, the majority of RF design is conducted with only very limited non-linear information describing the devices being used. Hence, linear data or mathematical approximations are often used. This results in a design approach that requires a significant number of time consuming iterations to produce a product that meets all of the required specifications and conforming to tight spectral masks. This is clearly a highly undesirable and unsustainable situation in the mobile communications industry where rapid growth and competition has meant that time-to-market has become an absolutely critical

factor. Furthermore, the increasingly complex evolution of modulation schemes means that RF and specifically Power Amplifier (PA) design is becoming an ever more challenging problem. The work described in this thesis therefore looks to solve this issue by developing a large-signal measurement system that allows the ultra-rapid collection of Continuous Wave (CW) data sets in addition to linearity and memory measurement and engineering, allowing for a time efficient, 'right-first-time' design process that dramatically decreases time-to-market. The desired measurement flow is shown in figure 1.2.



*Figure 1.2 – The Fundamental Goal of a Right-First-Time Design process
Highlighting required measurements and enabling technology*

1.3 Existing Large Signal Measurement Systems

A number of relatively new, large signal waveform measurement concepts have been developed to allow for a considered, scientific and logical design approach. In fact, large signal measurements are rapidly gaining acceptance as very powerful tools in the characterisation and modelling of non-linear devices and circuits. They have been proven to be very effective, for instance, in the optimisation of efficiency and linearity of devices and circuits, a process that is vital for any successful, modern-day mobile communication system [4-6]. Measured RF waveforms are also ideal for use in model generation where

measurement data can be directly integrated into a Computer Aided Design (CAD) environment.

There remain however two significant issues that need to be addressed: firstly, existing solutions are slow to capture information, which in turn leads to extended measurement periods in order to collect the sufficient data required for accurate prediction of the performance of the device or system, or indeed to generate an accurate device model. This is one problem that has resulted in a reluctance on the part of industry to buy-in to the approach, instead choosing to continue to use the established, yet inferior, iterative design approach. Secondly, the majority of the developed large-signal measurement systems are based upon CW excitation. Although this approach is of great worth and has generally been accepted, modulation schemes are becoming more and more complex and the ability of a model based on a device's response to CW excitation to predict the device performance under such schemes must be questioned.

1.4 A New Multi-tone Large Signal Measurement and Engineering System

In this work, a large-signal measurement system has been developed with the ability to overcome the aforementioned issues. The developed system can measure modulated (multi-tone about a carrier) signals and the excitation used can now be much more representative of the final application, leading to greater confidence in measured results. The system incorporates active load-pull capabilities that allow direct engineering of the waveforms for optimisation of linearity, efficiency and removal of electrical memory.

Furthermore, using a simple, slowly-modulated excitation or a slowly-modulated impedance environment, it will be shown that the developed system is capable of exciting and measuring a device in a quasi-CW mode. This ultra-rapid CW measurement approach offers a significant advantage that is expected to lead to an increased take-up of large signal measurement concepts in both modelling and device characterisation applications.

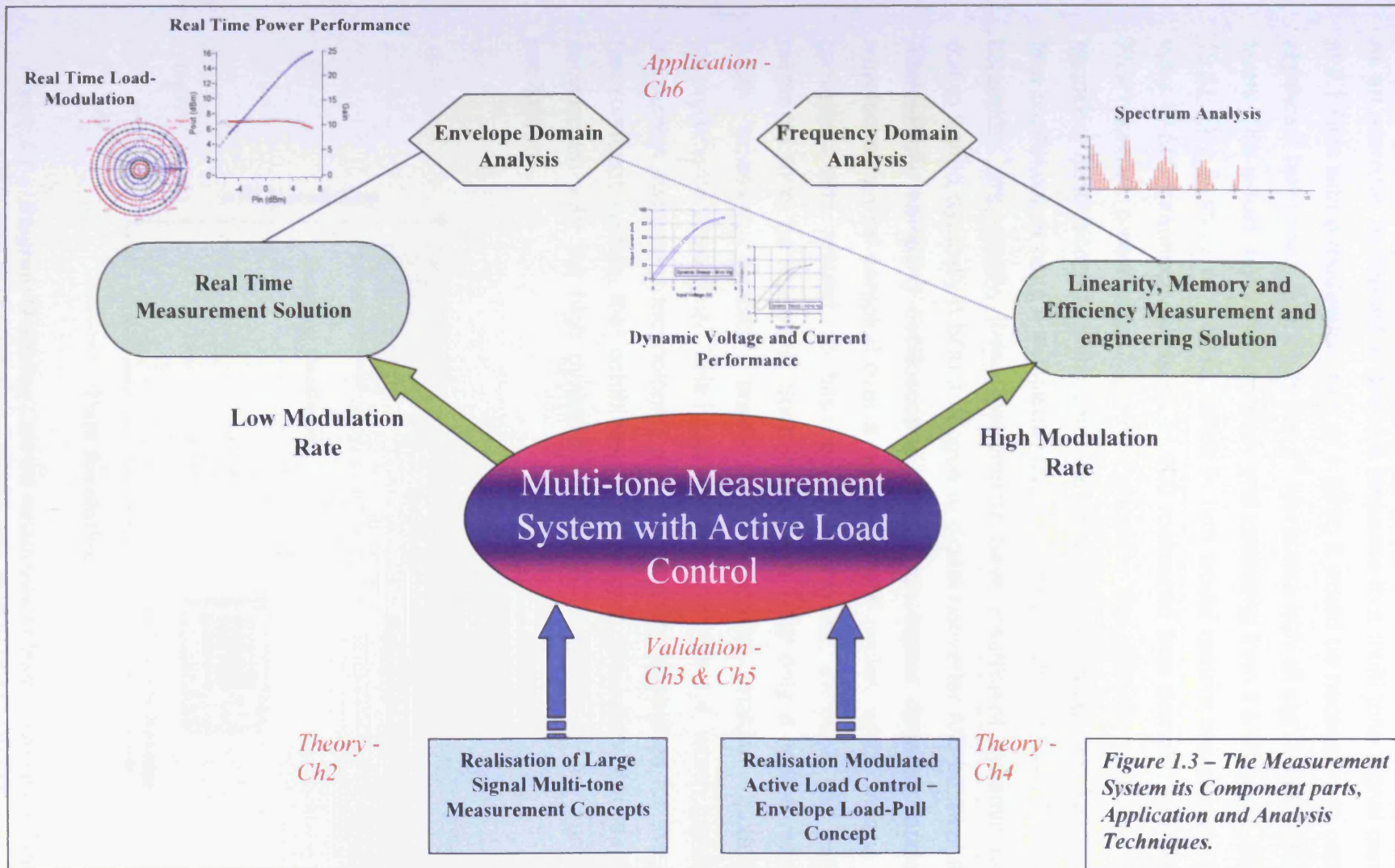
As the system is centred on the measurement of large-signal RF waveforms, it is vital to include the ability to engineer the impedance

environment around the Device Under Test (DUT). Unlike linear measurements, where the impedance can be mathematically transformed, the only way to determine the performance of a non-linear device operating within a particular impedance environment is to actually measure the device within that environment. The research is therefore made up of two parts: the first deals with the complexities of *capturing* modulated waveforms whilst the second deals with complexities of *engineering* the impedance environments, as the impedance must now be maintained over a modulation bandwidth. The developed measurement system and its sub-components, along with the application space, are highlighted in figure 1.3.

1.5 Multi-tone Large Signal Waveform Capture

Any multi-tone measurement system, in order to be effective, must capture the magnitude and phase of all components generated by the DUT. Such captured data allows a true 'envelope' representation of the modulated signals being generated that provides for meaningful device characterisation relative to the device boundary conditions. It is therefore clearly essential for the developed measurement system to capture information at the base-band, the fundamental-band and all significant harmonic bands.

As previously mentioned, the majority of large-signal measurement systems that currently exist are focused around the collection of CW data, with very few allowing the measurement of modulation. This is mainly due to the complexity that modulated measurement introduces: in order to capture all distortion terms in the device output it is necessary to capture a sufficiently fine frequency grid, from base-band frequencies right up to harmonic band-frequency.



As an example, to capture a device's response to a multi-tone signal centred at 2.1 GHz with a modulation rate of 1 MHz, it would be necessary to capture significant harmonics (e.g. up to the 5th harmonic) with all significant distortion terms. This would require a frequency grid stretching from 1 MHz up to around 10.51 GHz in steps of 1 MHz, which in turn would require the capture of at least 10,500 frequency points so 21,000 measured time domain data points. This becomes problematic if we now consider the currently available high-frequency oscilloscopes, which can be placed into two categories. Firstly, real time oscilloscopes have a sufficiently large memory depth but have limited RF bandwidth. Importantly, these instruments have insufficient dynamic range due to limited (typically 8 bits) analogue to digital converter A/D bit resolution. Alternatively, sampling oscilloscopes offer much higher dynamic range as waveforms can be sampled over a number of RF cycles, which means A/D converters with around 16 bits can be employed, although the signals measured must be repetitive. Such instruments offer only a limited memory depth however, typically around 4000 points, making modulated measurements impractical. This is summarised in figure 1.4, which highlights the current instrument technologies and the desired capabilities for the new measurement system, that combines the large data resolution of a real-time oscilloscope with the high dynamic range and bandwidth of the sampling oscilloscope.

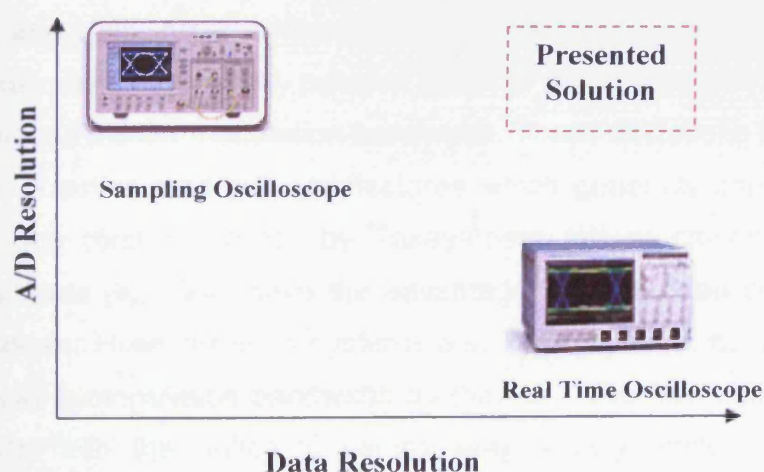


Figure 1.4 – Diagram Outlining Current measurement instrument capabilities, along with the requirements for the new measurement solution

This thesis presents a solution to the outlined issue by employing a sampling oscilloscope in addition to a novel compressed frequency sampling approach, along with time-interleaved waveform capture to accurately and efficiently capture multi-tone performance.

1.6 Impedance Control for Multi-tone Signals

As the measurement system is designed to capture multi-tone, large-signal information, it is clear that for the captured information to be useful, it must be possible to engineer the impedance environment around the device. As the signals used in the system are modulated, this means that any impedance control must be able to operate across a modulated bandwidth. Furthermore, control is required over the base-band, fundamental-band and significant harmonic bands.

Several impedance control architectures have been developed with the bulk of characterisation systems employing passive load-pull tuners such as those developed by Maury microwave [7]. However, such systems suffer from three fundamental disadvantages. Firstly, any losses between the device and the tuner prevent the emulation of loads that lie close to the perimeter of the Smith chart. Secondly, due to their passive architecture, passive systems are difficult to scale to lower frequencies, hindering their application to impedance control at base-band frequencies. Finally, such systems are essentially narrow-band and allow impedance control only at single, specific frequencies. Consequentially and importantly, passive systems fail to maintain a constant impedance across a wide modulation bandwidth. These limitations have led to the evolution of active load-pull architectures which generally consist of two types; open-loop (first presented by Takayamma [8]) or closed-loop (first presented by Bava [9]). Both have the advantage that they can compensate for system losses. However such systems also typically offer no solution for load-pull across a modulation bandwidth as they are also essentially narrow-band solutions with the ability to control only a very limited number of frequency components. This problem becomes apparent for example when we consider an open-loop architecture such as that presented in [10], where a

separate signal generator is required for each frequency to be controlled. Even in the case of simple modulation, such as two-tone, this leads to a requirement of two sources to control the two fundamental tones, another two sources to control the IM3 products, another two to control the IM5 products and so on, and this is even before the base-band and harmonic-band impedances are considered. It is clear that such an approach soon becomes impractical.

This thesis will present a solution to these issues, where two approaches are adopted; base-band and RF band solutions. At the base-band, an open loop, active load-pull architecture is applied while at RF frequencies, a novel 'envelope' load-pull architecture is employed to allow control of impedance across a modulated bandwidth.

1.7 Thesis Overview

The thesis is divided into two main parts; the first addresses the realisation and validation of the multi-tone measurement system, and the second addresses the realisation and validation of impedance control architectures that allow engineering of the multi-tone waveforms. Finally a demonstration of a number of possible applications for the new multi-tone measurement and waveform engineering system are presented.

Chapter 2 presents a thorough literature review of existing measurement solutions employed in the characterisation and modelling of devices for the mobile communications industry. The realised multi-tone measurement system is then discussed in two sections; the first detailing the required hardware, which integrates base-band and RF test-sets required to capture all of the significant distortion products at the device input and output. The second section discusses the novel sampling approach required to allow the capture of multi-tone information using a standard sampling oscilloscope with a limited memory depth. Finally, application issues with the final architecture are discussed and, where relevant, solutions are presented.

Chapter 3 outlines the steps taken to validate the non-linear, multi-tone waveform measurement system presented in chapter 2. Firstly a CW comparison is conducted using two well-established, large-signal

measurement systems, providing the fundamental evidence that the system is measuring magnitude and phase information accurately over a good dynamic range. The same CW comparison is then repeated, but with the system set up in its multi-tone measurement configuration, thus verifying the multi-tone sampling approach outlined in the previous chapter. Finally a spectrum analyser is used to validate the measurement system under multi-tone excitation, with measurements conducted over the entire dynamic range of the new measurement system. Further to the system comparisons, theory is used throughout the chapter to confirm that the system is operating correctly.

Chapter 4 begins with a literature review of existing impedance emulation strategies, paying particular regard to issues related to employing multi-tone stimuli. This chapter then focuses on two different impedance emulation strategies; one for base-band frequency components and one for RF frequency components. The IF impedance control strategy leads directly on from previous research so is not covered in great detail. For RF frequency control, a novel impedance control architecture is presented. The solution termed 'envelope load-pull' is capable of maintaining constant impedance across a modulation bandwidth. The theory behind the architecture and required hardware is discussed. Characterisation of the individual hardware components required to form the load-pull architecture is then conducted. In each case the non-ideal nature of the components and the effect on the final solution are discussed. Finally, conditioning circuitry is designed and realised that aims to minimise these errors.

Chapter 5 presents a full verification of the realised envelope load-pull architecture, highlighting the ability of the architecture to maintain constant impedance under varying drive conditions and across a modulated bandwidth. The useable bandwidth of the architecture is also characterised and discussed. This useable bandwidth is found to be limited by a group delay around the envelope load-pull loop system itself, thus limiting application of the impedance control architecture to the real time applications presented in chapter 6.

Chapter 6 provides a number of applications of the multi-tone, large-signal waveform measurement and engineering system. The first measurements will

consider novel applications of the system published in [11-13], which involve using slowly modulated excitation or impedance environment to conduct ultra-rapid CW measurements. The next investigation shows application of the system to memory investigations as presented in [14-15], using the system's ability to vary the tone spacing of a two-tone excitation while controlling the impedance of the base-band distortion terms. The final section of this chapter discusses the depth of information that is contained within the multi-tone waveforms, highlighting the importance of capturing all of the significant spectral components contained within the device output. The benefit of presenting data in the envelope domain is also discussed.

Chapter 7 makes final conclusions and discusses remaining limitations. Possible future work to expand and improve the developed measurement system is also suggested.

1.8 References

1. Husni Hammuda “*Cellular mobile radio systems : designing systems for capacity optimization*” Chichester ; New York : John Wiley & Sons, 1997. TK6570.M6.H2
2. Olof Billström, Lars Cederquist, Magnus Ewerbring, Gunnar Sandegren and Jan Uddenfeldt “*Fifty years with mobile phones From novelty to no. 1 consumer product*” Ericsson review, NO. 03, 2006.
3. <https://www.wirelessintelligence.com> (The global database of mobile market information), accessed October 2007.
4. Roff, Chris; Benedikt, Johannes; Tasker, Paul J. “*Design Approach for Realization of Very High Efficiency Power Amplifiers*” IEEE/MTT-S International Microwave Symposium 2007 Page(s):143 - 146
5. Benedikt, J.; Gaddi, R.; Tasker, P.J.; Goss, M. “*High-power time-domain measurement system with active harmonic load-pull for high-efficiency base-station amplifier design*” IEEE Transactions on Microwave Theory and Techniques, Volume 48, Issue 12, Dec. 2000 Page(s):2617 – 2624
6. Lees, J.; Benedikt, J.; Hilton, K.P.; Powell, J.; Balmer, R.S.; Uren, M.J.; Martin, T.; Tasker, P.J. “*Characterisation of an experimental gallium nitride microwave Doherty amplifier*” 2005 European Microwave Conference, Volume 2, 4-6 Oct. 2005.
7. Technical data sheet 4T-070 Maury Microwave. “*High-Gamma Automated Tuners (HGTTM)*”
8. Takayama, Y. “*A New Load-Pull Characterization Method for Microwave Power Transistors*” MTT-S International Microwave Symposium Digest 1976, Volume 76, Issue 1, Page(s):218 – 220.
9. Bava, G.P.; Pisani, U.; Pozzolo, V. “*Active load technique for load-pull characterisation at microwave frequencies*” Electronics Letters, Volume 18, Issue 4, February 18 1982 Page(s):178 – 180.
10. Benedikt, J.; Gaddi, R.; Tasker, P.J.; Goss, M. “*High-power time-domain measurement system with active harmonic load-pull for high-efficiency base-station amplifier design*” IEEE Transactions on Microwave Theory and Techniques, Volume 48, Issue 12, Dec. 2000 Page(s):2617 – 2624.
11. Williams, T.; Benedikt, J.; Tasker, P.J.; “*Experimental evaluation of an active envelope load pull architecture for high speed device characterization*” IEEE/MTT-S International Microwave Symposium 2005.
12. Williams, T.; Benedikt, J.; Tasker, P.J.; “*Application of a novel active envelope load pull architecture in large signal device characterization*” 2005 European Microwave Conference, Volume 1, 4-6 Oct. 2005.

13. Williams, T.; Benedikt, J.; Tasker, P.J.; ***“Fully Functional “Real Time” Non-Linear Device Characterization System Incorporating Active Load Control”*** 2006 European Microwave Conference, Page(s):1610-1613.

14. Alghanim A.; Lees J.; Williams T.; Benedikt J., Tasker P.J. ***“Using active IF load-pull to investigate electrical base-band memory effects in high-power LDMOS transistors”*** IEEE Asia-Pacific Microwave Conference 2007.

15. Alghanim A.; Lees J.; Williams T.; Benedikt J., Tasker P.J. ***“Investigation of Electrical Base-Band Memory Effects in High Power 20W LDMOS Amplifiers”*** 2007 European Microwave Conference, Page(s):48-51.

Chapter 2 - Realisation of a non-linear Multi-tone Waveform Measurement System

2.1 Motivation

Large-signal, CW waveform measurements are becoming recognised as playing an important role in supporting the design of non-linear devices and circuits. The presented system looks to build upon these measurement systems, pushing the boundaries by moving towards multi-tone excitation. This move comes from two driving factors; the first is a requirement for faster CW device characterisation, since ideally the non-linear measurements are converted into some form of data-set look-up model. The accuracy of these models is obviously dependent on the density of measured information. It will be demonstrated that using multi-tone stimulus or a modulated impedance environment, it is possible to perform ultra-rapid CW characterisation allowing faster data collection, faster model availability and thus faster time-to-market for products. The second driving factor comes from the dramatic increase in the complexity of modulation schemes, often operating over wide bandwidths.

As such schemes become more prevalent, the link between conventional CW measurements and the eventual stimulus the device or circuit encounters in the final application become tenuous. This results in a need to perform additional measurements under more realistic stimuli, allowing the performance of the device in the measurement system to be directly related to the final application. Such a system would also allow for a thorough investigation into the optimum stimuli to predict accurately device and circuit behaviour.

2.2 RF Measurement Systems

The recent growth of mobile communication systems has created multinational companies boasting multi-million pound turnovers; a growing global market combined with a demand for an end product that not only exceeds its predecessors in terms of functionality, but also in terms of performance, is continually pushing the industry to evolve and change. A prime example is the requirement for new modulation schemes to ensure the highest spectral efficiency and high data rates. It is clear that in order to meet the growing demand for performance, a faster, more flexible and accurate turnaround in the design and realisation of RF devices, circuits and systems is required to enable the continued success of the industry.

For this reason all measurement activity should ideally be used purely in the generation and validation of computer aided design (CAD) models, allowing the design and optimisation of devices and circuits to be conducted within simulation environments. This however is not the case as non-linear models of RF devices have largely proved inadequate as they lack the robustness and accuracy required for the power amplifier design process. The main reason for this unfortunate situation is a lack of relevant large signal measurement data available that can easily be imported into a CAD environment. This problem is compounded by the ever changing modulation schemes used to transmit the data, which has led to the capabilities of existing measurement architectures falling further behind the requirements demanded. The following literature review of existing measurement

technology will highlight this problem, showing a need for research into an all encompassing measurement solution for modern day communication system development. It is clear that such a system should allow for device characterisation under realistic operating conditions such as excitation of modulation dynamics under realistic load conditions, allowing for example investigations into linearity and memory when a device is in a realistic state of operation. The speed of non-linear measurements must also be addressed as the detailed data-sets required to make accurate large signal models, even in the CW case, often lead to unrealistic timescales for model generation.

2.2.1 Linear (Small Signal) Measurement Architectures

A large proportion of existing RF measurement architectures are based around the established and mature technology of the Vector Network Analyser (VNA). Such systems measure s-parameters, which describe the behaviour of electrical networks when undergoing various steady state stimuli by small signals. This is achieved by measuring the incident (forward) and reflected (reverse) travelling waves at the input and output of a device or circuit. The s-parameters are the ratio of incident to reflected or incident to transmitted travelling waves. For a two port device the reflection ratio S_{11} gives the input port reflection coefficient, whereas the transmission ratio S_{21} gives the forward voltage transfer coefficient. The definitions of the s-parameters for a two port device are shown in figure 2.1.

Such systems thus capture useful information; for example, s-parameters can be used to derive many commonly used design parameters such as the complex linear gain, stability, input/output return loss and voltage reflection coefficient. In fact s-parameters completely describe the behaviour of a device under test (DUT) under linear conditions. The VNA architecture is limited however to analysis under single-tone or continuous wave (CW) operation where only one frequency is used to stimulate the device at a time. Such analysis ignores the vital effects of distortion such as generated mixing components and memory effects. In other words, systems that capture and use s-parameter data can only be used while the superposition principle holds

true [1]. This means that such systems are limited to linear measurements where there is no energy transfer from the stimulus to other harmonic frequencies. By definition, these systems cannot therefore, at least in their standard mode of operation, uncover the detailed large signal performance of a device. This clearly leads to a rather tenuous extrapolation process when this data is used in large signal device models.

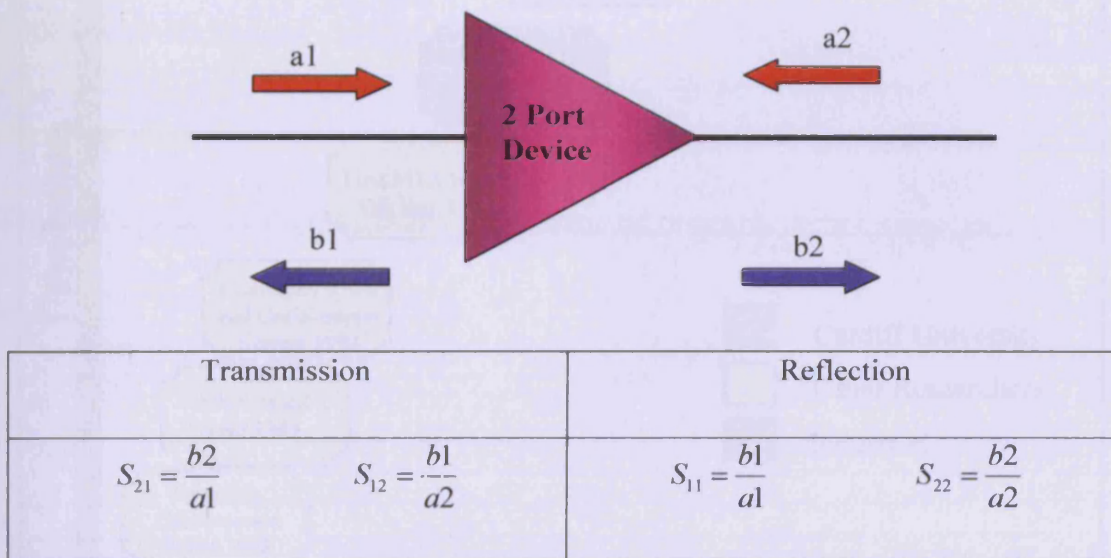


Figure 2.1 – S-parameters definition for a Two-Port Device

2.2.2 Non-Linear Measurement Systems

An increasing drive for enhanced performance means that devices are commonly operated far closer to compression, firmly in their non-linear regions. Clearly then there is a need for measurement solutions that analyse the large signal behaviour of the device, circuit or system. This has led to development in recent years of large-signal measurement systems with the ability to measure the non-linear time domain performance of devices and circuits, such as the absolute voltage and current waveforms that exist at the device plane. Some of the milestone achievements in the evolution of non-linear measurement systems are highlighted in figure 2.2.

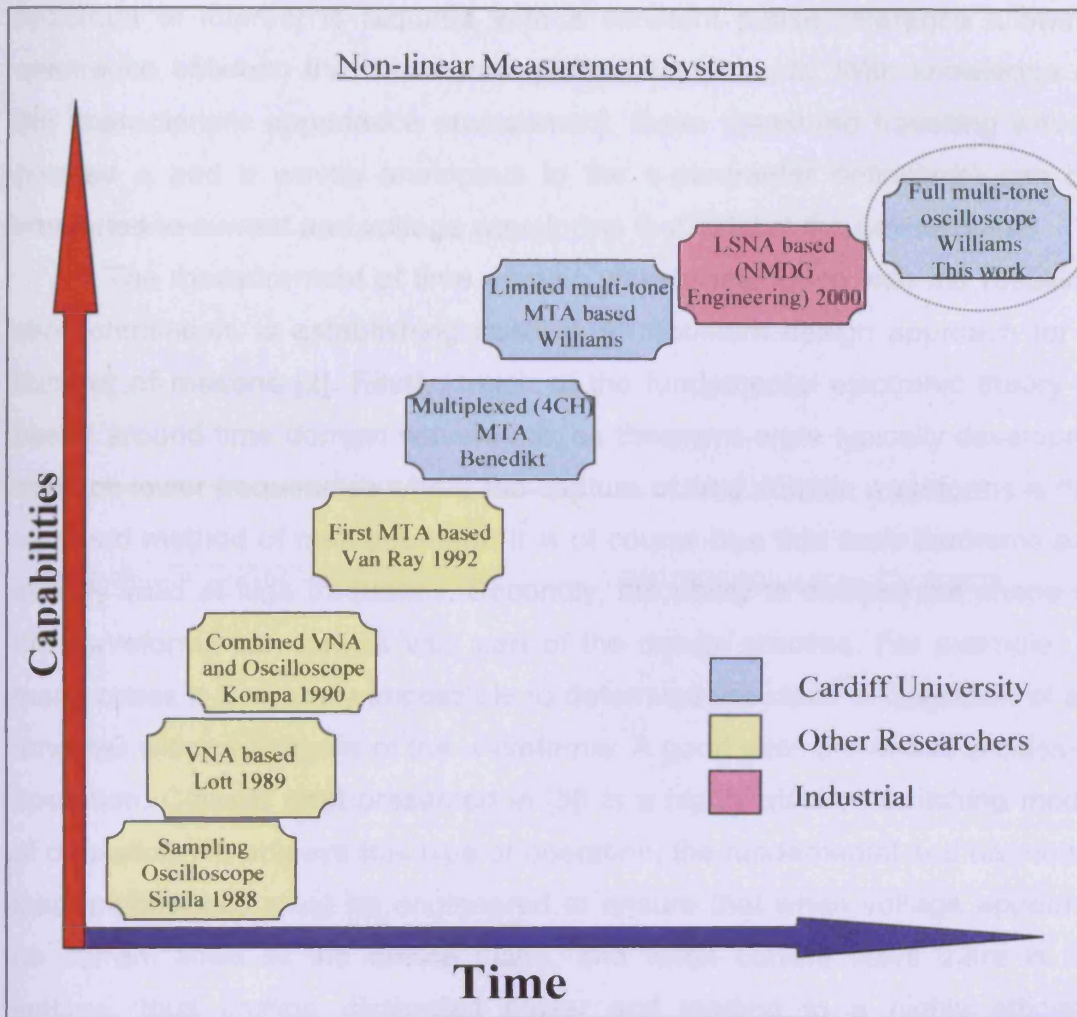


Figure 2.2 – Non-linear Measurement System Milestones

The measurement of RF signals poses an interesting challenge; at low frequencies, voltage and current can be directly measured utilising a high impedance probe to measure voltage and a low impedance probe to measure the current. This however is not possible at the very high frequencies used in modern day mobile communication systems. At these frequencies, it becomes impossible to maintain high or low impedances across the entire bandwidth, ruling out the use of voltage and current probes. Instead, an alternative, non-invasive approach is required. The common approach adopted is to use directional couplers to separate off a small fraction of the forward (incident) and reverse (reflected) travelling waves, which are then measured using a sampling instrument. It is important to note that measurement of the entire

spectrum of interest is required with a constant phase reference allowing coherence between the measured spectral components. With knowledge of the characteristic impedance environment, these measured travelling waves (termed a and b waves analogous to the s-parameter definitions) can be converted to current and voltage waveforms that exist at the device plane.

The measurement of time domain waveforms, along with the resulting characterisation, is establishing itself as an optimum design approach for a number of reasons [2]. Firstly, much of the fundamental electronic theory is based around time domain waveforms, as theorems were typically developed at much lower frequencies where the capture of time domain waveforms is the standard method of measurement. It is of course true that such theorems are equally valid at high frequency. Secondly, the ability to analyse the shape of the waveforms can form a vital part of the design process. For example, in many cases it is virtually impossible to determine the class of operation of an amplifier without analysis of the waveforms. A good example of this is class-E operation. Class-E (first presented in [3]) is a highly efficient switching mode of operation. To achieve this type of operation, the fundamental and harmonic load impedances must be engineered to ensure that when voltage appears, no current flows at the device plane, and when current flows there is no voltage, thus limiting dissipated power and leading to a highly efficient operation. However, the only way to truly convince oneself of this class of operation is to view the voltage and current waveforms that exist at the device plane. Whilst much literature exists explaining the required impedances for particular amplifier modes of operation, without viewing the actual waveforms there is often no guarantee that the device is actually operating in that state. Additionally, it has been shown that through waveform engineering, it is possible to systematically maximise device performance in terms of efficiency, linearity or gain by analysis and manipulation of the waveforms [4,5] thus removing the need for a blind, trial and error design approach. For this reason, the collection and use of waveforms in waveform engineering is beginning to be accepted as the optimum design solution, as only waveforms capture all of the relevant information i.e. magnitude and phase of the measured spectra. The shape of the time domain waveforms are completely described only by

both considering magnitude *and* phase of the individual spectra, thus signals possessing the same power spectra can produce an entirely different time domain waveform, which if applied as an input will naturally excite the DUT in different ways. Measured waveform data also naturally interfaces with the simulation environment as most non-linear CAD software utilise waveforms at the numerous nodes through various mathematical techniques.

Due to the aforementioned benefits of waveform measurement, various large signal waveform measurement systems have been developed over the last 20 years. One of the first attempts was based around sampling oscilloscope technology. A more detailed description of the way sampling oscilloscopes operate is included later in this chapter. The first large signal waveform measurement system based around a sampling oscilloscope was presented by Sipila et al, in 1988 [6]. The measurement system architecture is shown in figure 2.3 and uses a two-channel, high frequency sampling oscilloscope and collects only two of the 4 travelling waves; the reflected input wave b_1 and transmitted output waveform b_2 . Using knowledge of the s-parameters of the linear input and output coupling networks at fundamental and harmonic frequencies, the non-sinusoidal device waveforms are then determined.

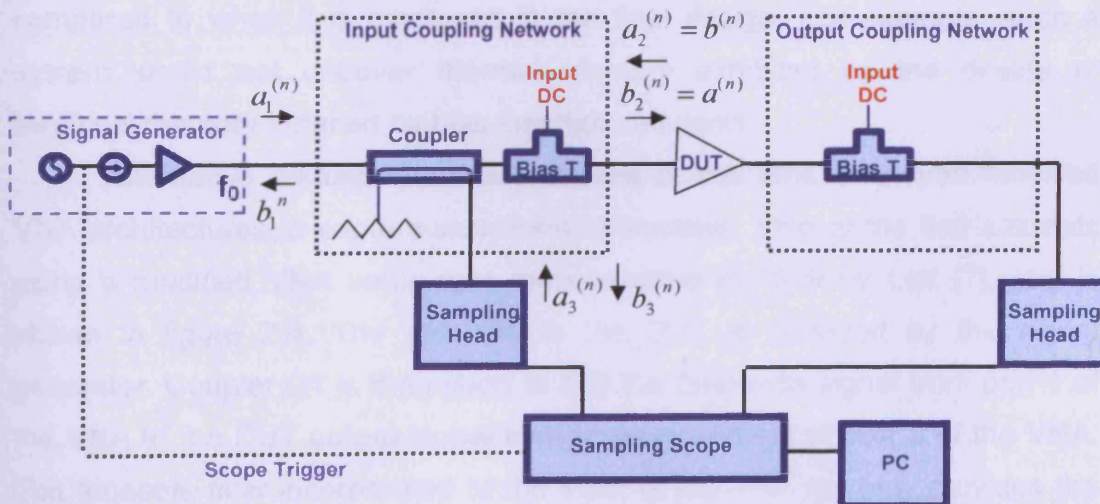


Figure 2.3 – Waveform measurement system based around a two channel sampling oscilloscope, presented by Sipila [6]

In this arrangement, the measurement system is calibrated by measuring the s-parameters of the measurement system allowing for correction of errors caused by losses, mismatches, and imperfect directivities in the measurement system. Measured time domain waveforms are converted into the frequency domain in order for vector error correction to be applied, before applying an inverse transform to retrieve the de-embedded time domain information. This approach is seen as important in the development of large-signal measurement systems as it allowed for adoption of calibration procedures akin to those developed for the more established VNA technology. Disadvantages of this architecture include only measuring 2 of the 4 travelling waves, which leads to a requirement to measure the s-parameters of the input and output coupling networks, leading to an increased likelihood of error in measurement. The architecture also suffers from noise introduced by the trigger jitter reducing the dynamic range when compared to the mixer-based approach adopted in VNA's. These errors become quite large at frequencies above about 5GHz, limiting the application of this systems to frequencies less than 2 GHz when accurate information at the harmonics is required. Once again the architecture is limited to purely single-tone device characterisation, meaning that the device is excited in a very different way when it is measured compared to when it is employed in the final design. For example, such a system would not uncover thermal memory exhibited by the device or electrical memory induced by bias insertion networks.

Alternative measurement approaches at this time employed modified VNA architectures to capture waveform information. One of the first attempts using a modified VNA setup was demonstrated in 1989 by Lott [7], and is shown in figure 2.4. The stimulus to the DUT is provided by the signal generator. Coupler C1 is then used to add the reference signal from port 1 of the VNA to the DUT output signal before measurement at port 2 of the VNA. The tuneable filter incorporated at the input of the VNA not only provides the instrument with a very high dynamic range but also allows separate measurement of the fundamental and harmonic components up to the fourth harmonic, without having to separate the frequency components.

A millimetre-wave Schottky diode was used as a 'golden diode' or absolute phase reference to calibrate for absolute phase, since it has a well defined phase relationship between fundamental and harmonic frequencies. This measurement approach is limited however by the fact that only the output of the device is measured. Furthermore there is no easy way to extend the capabilities of the system to allow the fundamental and harmonic impedances around the device to be engineered. It is unlikely, particularly in measurements of high power devices, that 50Ω would give optimum performance. The system is therefore only useful for devices and circuits that have, or have been, pre-matched to a 50Ω impedance.

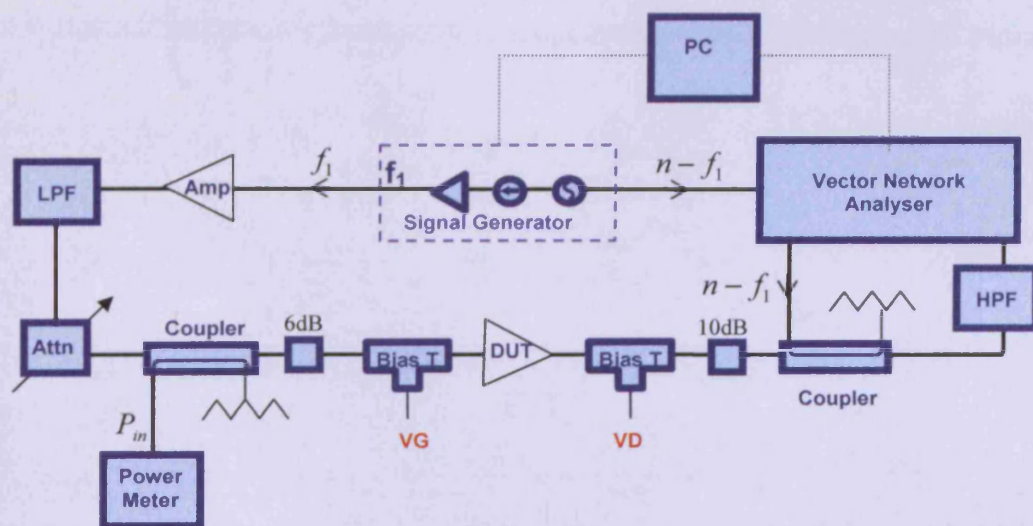


Figure 2.4 – VNA Based Waveform Measurement Architecture as presented by Lott et al [7]

Once again, the biggest limitation comes from the CW nature of system, which means multi-tone stimuli cannot be used during measurement.

An alternative system with extended capabilities, again based around the VNA, is presented by Barataud et al. [8]. In this approach, a commercially available VNA was modified in order to measure all four incident and reflected power waves. The schematic of the modified VNA test set is shown in figure 2.5. The R_B input is used for the reference signal and is generated by splitting the input RF signal and passing one-half through a step recovery diode (SRD), producing a fixed phase reference signal.

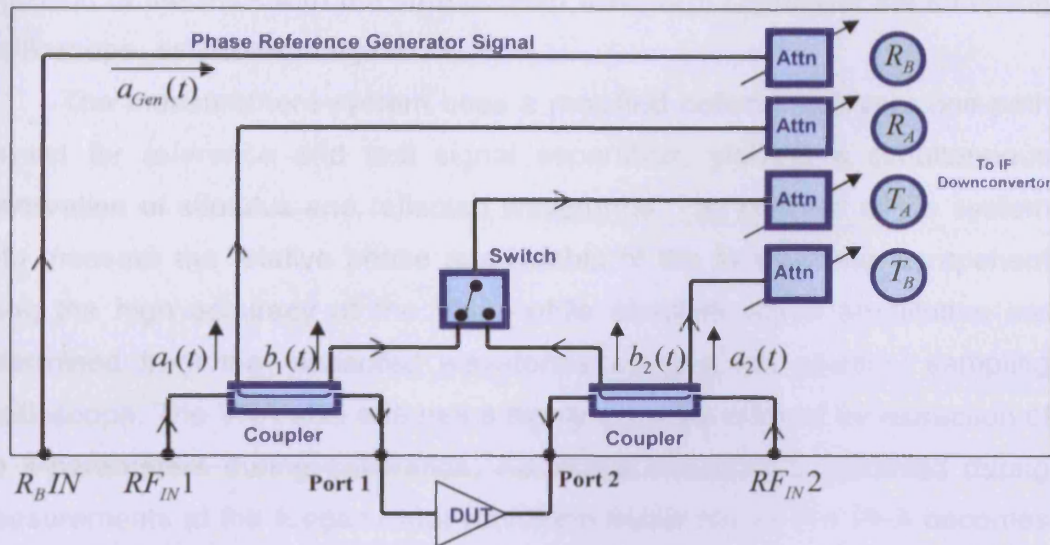


Figure 2.5 – Modified VNA test set presented by Barataud et al. [8]

This system allows for the display of calibrated time domain voltage and current waveforms at the device plane. Amplitude calibration is achieved by attaching known standards to the measurement ports. Phase calibration is achieved through the use of the SRD, which produces a signal with very well behaved and known phase relationship at all of the measured frequencies. This measurement architecture offers a more complete measurement solution than that presented by Lott et al. in [7] as it allows for calibrated measurement of both input and output voltage and current waveforms. In addition ports are made available for source and load impedance control allowing for waveform engineering at both the input and output of the device. However device characterisation is again limited only to CW performance, and there is no option for the addition of multi-tone capabilities. Due to the requirement of a frequency sweep for each measured harmonic, any architecture based around the VNA is also inherently slow, and accurate phase coherence is difficult to achieve. The concepts developed in [8] also form the basis of a further advanced VNA measurement solution that have recently emerged, specifically the PNA-X from Agilent [9].

An alternative architecture that combines both a VNA and a sampling oscilloscope was presented by Kompa in 1990 [10]. The architecture adopted a novel approach to combine the high dynamic range, frequency domain

approach of the VNA with the time domain waveform capture of the sampling oscilloscope, as shown in figure 2.6.

The measurement system uses a modified network analyser one-path test-set for reference and test signal separation, yielding a simultaneous observation of stimulus and reflected waveforms. The concept of the system is to measure the relative phase relationship of the fundamental component using the high accuracy of the VNA, while absolute signal amplitudes are determined from the measured waveforms using a two channel sampling oscilloscope. The VNA also ensures a highly accurate method for extraction of the s-parameters during calibration. Additional accuracy is achieved during measurements at the fundamental waveform frequency as the VNA becomes part of the measurement and is constantly used to measure fundamental magnitude and phase.

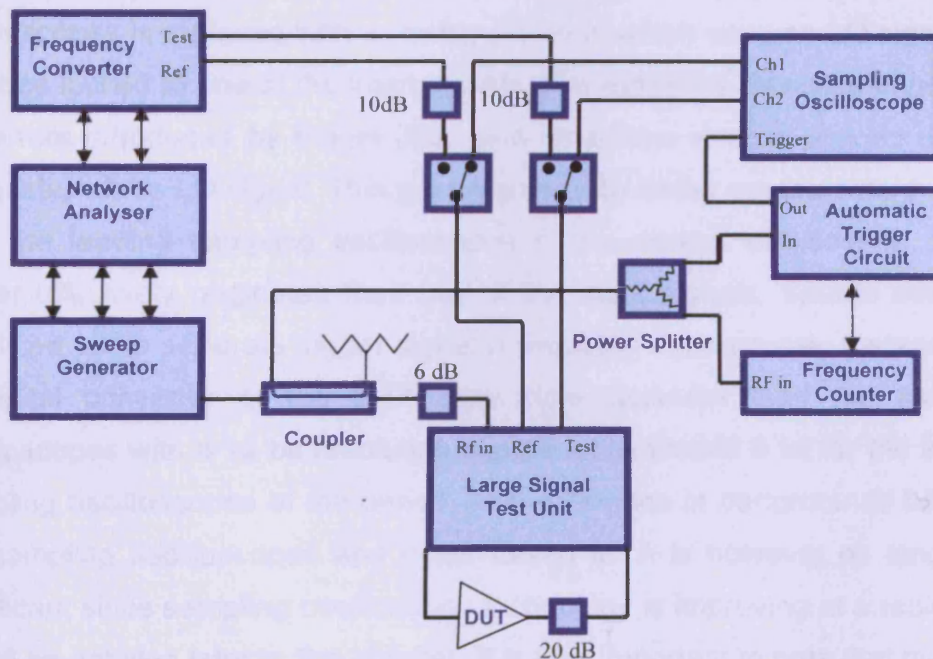


Figure 2.6 – Waveform measurement system combining VNA and sampling oscilloscope proposed by Kompa [10]

The information collected using the oscilloscope then allows measurement of the actual incident and reflected waveforms. Again the measurement system has only two measurement channels, which are used to measure input

stimulus and the transmission of the device. Reflected travelling waves are not measured. Instead, the integrated VNA is used during calibration to estimate the response of the input and output networks, thus introducing uncertainty into the measurements. Again the architecture is limited to purely single tone device characterisation.

The Microwave Transition Analyser (MTA) became the optimum instrument for waveform measurement soon after its release by Agilent in 1992. The instrument operates as a wideband, time domain sampling oscilloscope in its main mode of operation, but has the capability to conduct narrow band swept frequency measurements and act as a VNA to measure s-parameters with a very high dynamic range. The first system using the MTA was presented by Van Raay et al. in 1992 [11]. At this point in time, the MTA was superior when compared to other sampling oscilloscopes for two main reasons; firstly, the sample-and-hold trigger employed in sampling oscilloscopes is replaced with a mixing process, which uses an LO signal that is phase locked to one of the input signals. The system is therefore immune to the errors introduced by trigger jitter, and time-base error is defined only by the quality of the LO signal. This gave significantly better measurement results than the leading sampling oscilloscopes of the period. Additionally, as the trigger effectively originates from one of the input signals, system design is simplified as no separate trigger signal is required. Furthermore, the analogue to digital converter of the MTA was more accurate than the sampling oscilloscopes with a 12 bit resolution compared to around 8 bit for the leading sampling oscilloscopes of the period. This difference in performance between the sampling oscilloscopes and mixer based MTA is however no longer as significant since sampling oscilloscope technology is improving at a rapid rate, as will be detailed later in this chapter. It is also important to note that the MTA is now an unsupported instrument, although a 4-channel instrument based on the MTA, called a Non Linear Vector Network Analyser (NLVNA) is now available, and this instrument will be discussed in more detail later in this chapter. The measurement architecture employed by Van Raay [11] is shown in figure 2.7.

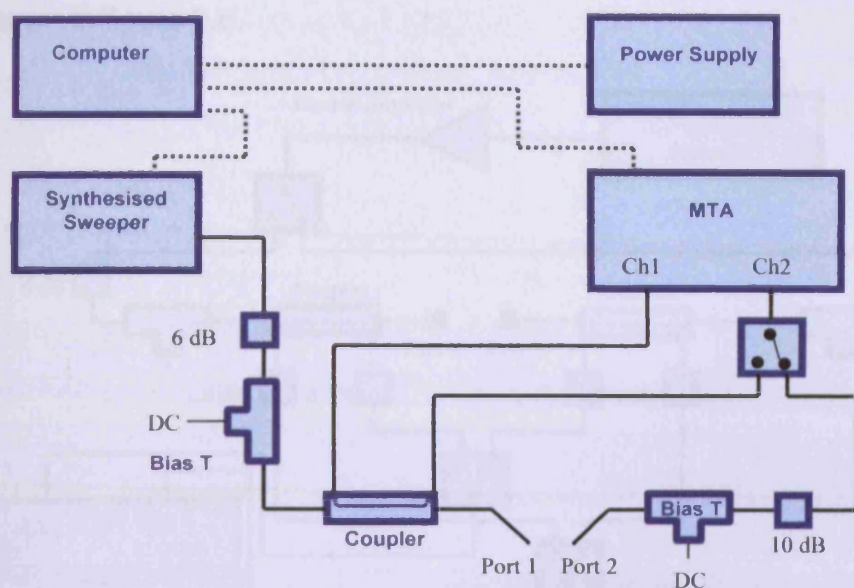


Figure 2.7 – Waveform measurement system Based around the MTA, proposed by Van Raay [11]

The system allows the collection of three out of the four of the travelling waves, so is still essentially a one-path measurement system. The system can however be employed at much higher frequencies than the previous systems with a bandwidth of 40 GHz. Calibration was completed in a similar way to other waveform measurement systems discussed earlier in this chapter utilising vector error correction. In this case however the MTA is used as a VNA to measure the s-parameters of the test set, and from these the error coefficients can then be extracted. Although more accurate than the sample and hold oscilloscope based architectures discussed earlier, this MTA based solution suffered from similar drawbacks; most importantly its confinement to the measurement of CW waveforms.

Demmler et al. present an extension employing an MTA in [12]. The measurement system architecture is similar to that presented in [11], however the power handling capacity has been extended to allow the characterisation of large power amplifiers in a 50 Ω environment. This system does however suffer from the same drawbacks as the previous system. A further extension to the systems capabilities is presented by Benedikt in [13], where a multiplexing network has been added to the architecture, effectively turning the 2 channel MTA into a 4 channel receiver. The modified architecture is

shown in figure 2.8.

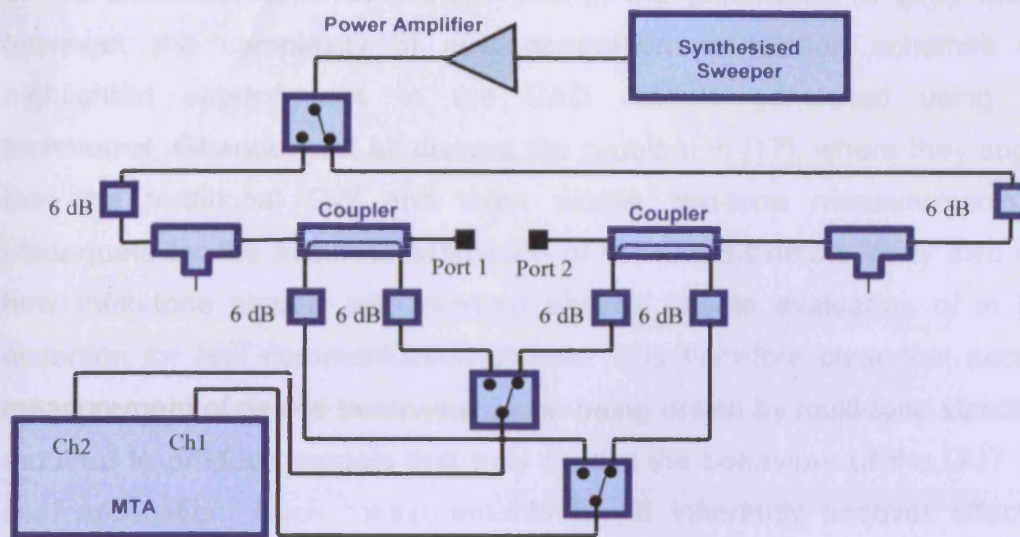


Figure 2.8 – Waveform measurement system based around the MTA with multiplexing for collection of all 4 travelling waves Benedikt [13]

This architecture allows all 4 travelling waves to be collected synchronously. To achieve this, 3 measurements are required to collect the waveforms; the first measures the input incident and reflected waveforms a_1 and b_1 , the second measurement is required to calculate the phase reference between input and output a_1 and b_2 , whilst the third measurement measures the output transmitted and reflected waveforms a_2 and b_2 . These travelling waves are calibrated to the device reference plane using vector error correction. The travelling waves can then be easily converted into the voltage and current waveforms. In this state the architecture readily lends itself to further extension where load variation can be applied at the input and output of the device as presented in [13]. A further step was taken in 1995 where the Agilent research group modified two MTA instruments, combining them to form a single 4-channel instrument. This modified MTA was used as the basis of a large signal measurement architecture known as the NLVNA.

Such large signal waveform measurement architectures have proved to be very useful tools in the optimisation of device performance [5,14,15], and in the generation of accurate non-linear CAD models [16]. Having said this, they collectively lack the ability to measure complete multi-tone behaviour.

CW measurements of carriers and their harmonics now play an important role in the characterisation of devices and in the generation of CAD models, however, the complexity of new generation modulation schemes have highlighted shortcomings in the CAD models generated using such techniques. Gharaibeh et al. discuss the problem in [17], where they suggest that the traditional CW and even simple two-tone measurements are inadequate for the accurate estimation of in-band distortion. They also show how multi-tone signals with random phases enable evaluation of in band distortion for real communication signals. It is therefore clear that accurate measurement of device behaviour whilst being driven by multi-tone stimulus is required to produce models that truly predict the behaviour of the DUT in its final application. Such measurements would inherently uncover effects of memory and distortion.

2.2.3 Existing Multi-Tone Measurement Solutions

As has been mentioned, the systems discussed above have various advantages and limitations; they have proved to be a very useful design and characterisation tools, but are limited when used to approximate the complexity introduced through modulated stimulus.

Today the majority of multi-tone measurement architectures are based around the Spectrum Analyser (SA). This instrument has excellent dynamic range due to its swept frequency, narrow-band nature. However, measurements made using a spectrum analyser do not contain any phase information. Therefore, although the spectrum analyser based architectures are a useful tool in deciding how linear a particular device or system is, or in determining the presence of memory, the instrument does not supply enough measurement information to determine the cause of memory or non-linearity. These limitations have led in many cases to an iterative design process. Until recently, this problem has remained largely unaddressed with a general lack of measurement instruments or even measurement concepts available to perform the required analysis. An initial attempt to extend the capabilities of the MTA based time domain measurement system into the modulated domain is presented by Williams et al. [18]. The capabilities of the architecture are

extended through the integration of a low frequency test set and low frequency oscilloscope. The architecture employed is shown in figure 2.9.

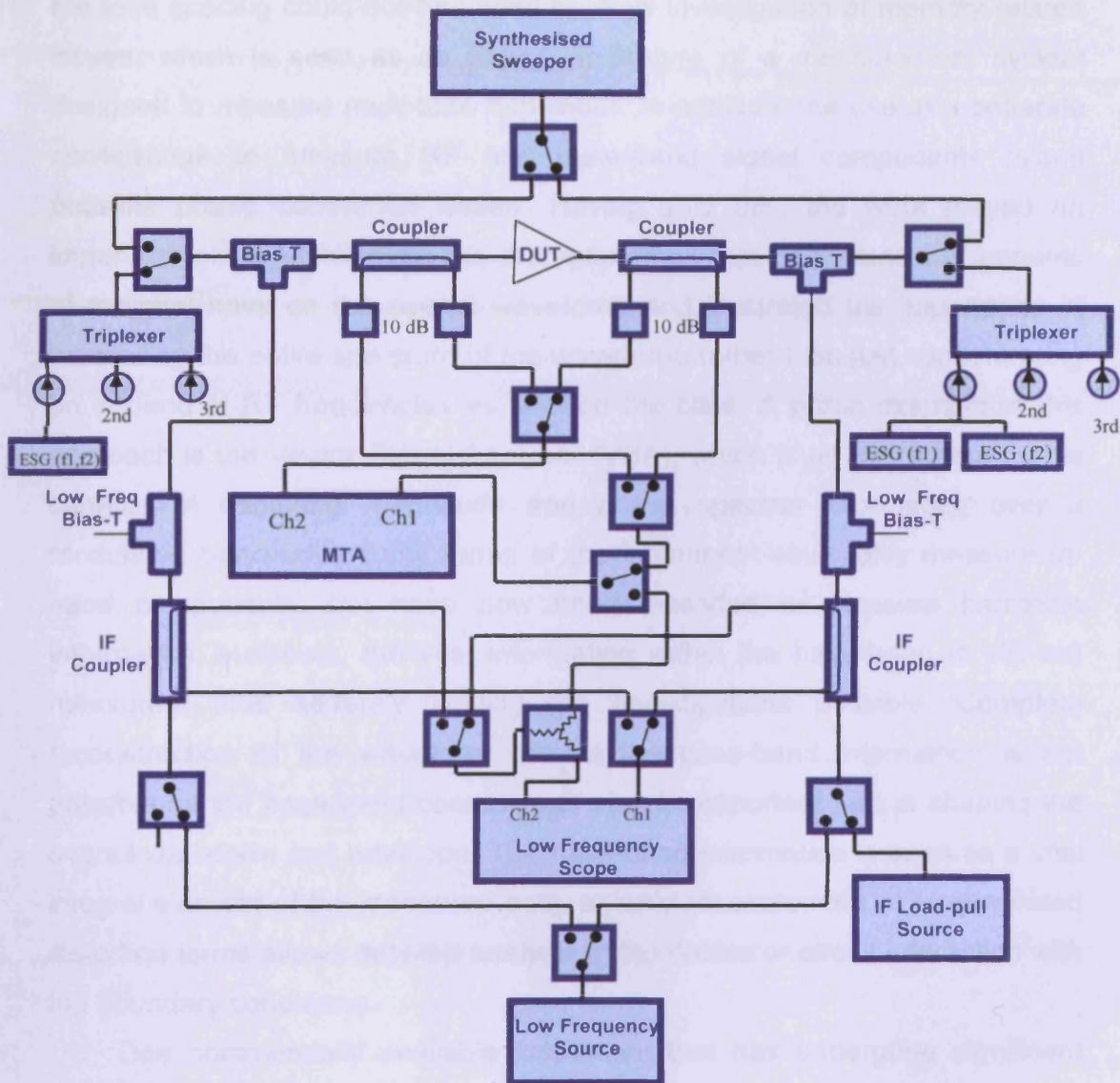


Figure 2.9 – 2-Tone Waveform Measurement system Based around the MTA presented by Williams et al [18]

The system proved useful in investigating the effects of base-band impedance on the linearity of devices and specifically third-order in-band distortion product asymmetry, with characterisation focusing upon simple two-tone modulation. However, the implemented sampling approach limited the excitation to a single tone spacing of 10 MHz and provided only a limited harmonic resolution. This is due to inherent problems in capturing

harmonically related multi-tone signals using a sampling oscilloscope, which led to the collection of many unnecessary data points. This problem will be discussed in more detail later in this chapter, but in summary, this meant that the tone spacing could not be varied to allow investigation of memory related issues, which is seen as an important feature of a measurement system designed to measure multi-tone behaviour. In addition, the use of a separate oscilloscope to measure RF and base-band signal components raised possible phase coherence issues. Having said this, the work played an important role in highlighting the dramatic effect that base-band components of a signal have on the overall waveform, and illustrated the importance of measuring the entire spectrum of the waveform, rather than just concentrating on in-band at RF frequencies as is often the case. A prime example of this approach is the Vector Signal Analyser (VSA), which is an instrument that is capable of capturing magnitude and phase spectral information over a modulated bandwidth. Early forms of the instrument could only measure in-band components, but have now been extended to measure harmonic information. However, the vital information within the base-band is still not measured, thus severely limiting the investigations possible. Complete reconstruction of the waveform without the base-band information is not possible as the base-band components play an important part in shaping the overall waveform and envelope. The base-band information is seen as a vital integral element of the measured data, as only measurement of all generated distortion terms allows detailed analysis of the device or circuit interaction with the boundary conditions.

One commercially available instrument that has undergone significant development as the work presented in this thesis was undertaken is the Large Signal Network Analyser (LSNA)¹, which stemmed from the evolution of the NLVNA discussed earlier. This development leads directly from systems based around the MTA; in fact the system receiver used is simply two MTA instruments combined to make a 4 channel receiver. The development of the

¹ However, it is important to note that in order to avoid confusion the term LSNA is now widely used to describe any time domain large signal measurement system. For discussion in this chapter LSNA will be used to refer to the commercially available product produced by Maury Microwave and NMDG Engineering under licence from Agilent.

LSNA was first presented in 1995 by Verspecht et al. [19] and this initial system was capable of only CW measurements. The important extension to allow measurement of multi-tone waveforms was presented in 2000 [20]. In this publication, the measurement of a signal that statistically describes a 'CDMA like' signal is presented with application to large signal modelling. However, the LSNA however lacks the ability to capture all of the information as the base-band distortion terms are again neglected. This prevents true reconstruction of the waveforms and overlooks the important effects of the generated base band components on distortion and memory investigations, as outlined in [21,22]. The LSNA also suffers from the fact that the receiver is not thought to be a perfect phase receiver, thus a phase calibration must be completed. This is achieved by measuring the 'well known' phase relationship of harmonics generated by a device such as a step recovery diode. The problem here is that as we move towards multi-tone signals it is necessary to calibrate on a grid related to the tone-spacing. Thus for example if we want to have a 1 MHz modulation then the diode would need to be stimulated with a 1MHz signal and produce enough harmonics to cover the desired measurement window, which can be very difficult. However it will be shown in the system validation in chapter 3, where comparisons are made between the CSA8000, LSNA and MTA based systems that (at least at the frequencies measured) there is no observed problem in the accurate measurement of phase even without calibration of the sampling instrument.

More recently, advances in the bandwidth of real time sampling oscilloscopes (particularly in terms of receiver bandwidth) have made it realistic to base waveform measurement systems around real time oscilloscopes. One such system was presented in 2006 by Macraigne et al. [23]. The system setup shown in figure 2.10 is based around a real-time digital oscilloscope that samples at 2Ms/s. An Arbitrary Waveform Generator (AWG) is used to generate modulated base-band signals, which are then fed into an I-Q modulator to produce the stimulus. Mixers are employed before the samplers to down-convert the complex time varying envelope of the fundamental carriers, both incident and reflected, at the input and output of the device. Significantly, the harmonics are filtered and are not taken into

account, so the system does not capture all of the relevant information. The base-band information is also neglected, limiting the usefulness of the captured data.

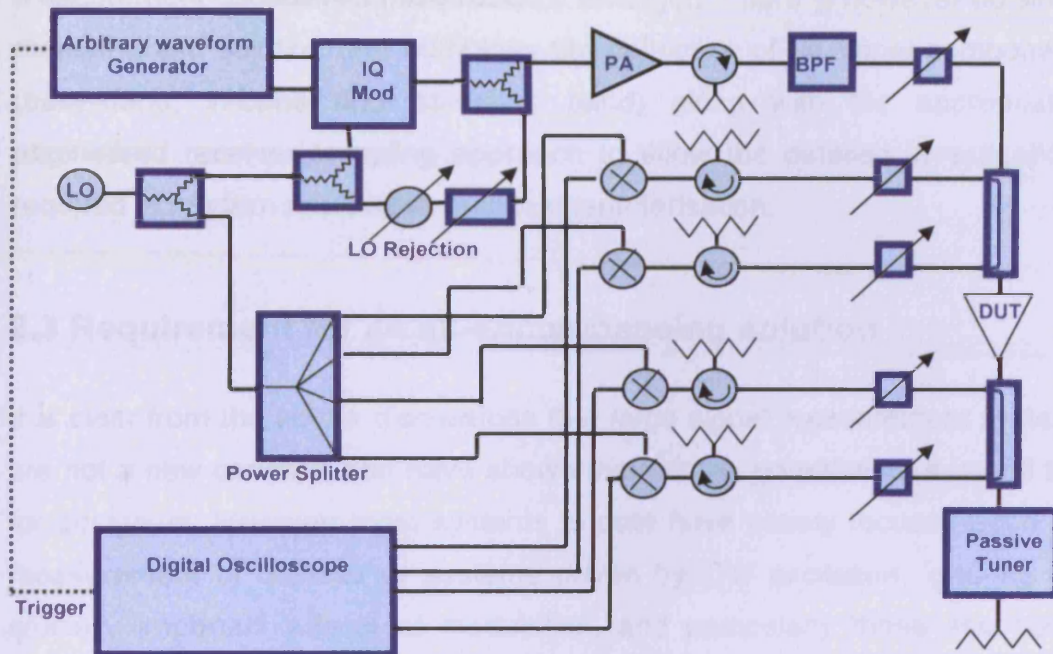


Figure 2.10 – multi-Tone envelope waveform measurement system Based around a real time digital oscilloscope, Macraigne et al. [23]

Although real-time oscilloscopes offer a number of advantages over sub-sampling oscilloscopes, such as increased memory depth allowing measurement of more complex modulated signals, and the ability to capture non-repetitive signals along with simplified triggering architectures, there is also a significant down side. Bandwidths of real time oscilloscopes are orders of magnitude smaller than sampling oscilloscopes; for example, the architecture presented here is limited in operation to 4 GHz. However there are real-time oscilloscopes available today that have bandwidths as high as 20 GHz (Tektronix DPO 70000) [24]. Although such instruments lend themselves to RF waveform measurement applications, there remains a significant drawback; due to the high sampling rate, the resolution of the digital to analogue converter (DAC) is typically limited to only 8 bits, which has

a significant effect on overall dynamic range and the ability to look at in-band and out-of-band distortion terms, which are typically at very different power levels to the carriers.

To summarise, a number of systems offering modulated large-signal measurement capabilities have recently emerged. There is however no single measurement solution that combines the collection of all signal components (base-band, in-band and harmonic band) along with the appropriately engineered receiver sampling approach to allow the detailed investigations required in modern microwave device characterisation.

2.3 Requirement for an all-encompassing solution

It is clear from the above discussions that large signal measurement systems are not a new concept, and have shown their strong potential as a useful tool for designers. However most systems to date have mainly focused upon the measurement of devices or systems driven by CW excitation, ignoring the crucially important effects of modulation, and particularly those associated with base-band components and memory. All have a major influence on linearity investigations and investigations into the suitability of pre-distortion techniques to linearise amplifier performance. A solution has been presented that can measure simple two-tone modulation, but this is limited to a tone-spacing of 10 MHz and can not be varied and has a limited harmonic resolution. This is due to the sampling architecture employed, and has limited the application of the system. For example, the ability to sweep the tone spacing is vital if we wish to uncover the time constants upon which memory occurs.

The inability to measure more complex modulation with variable tone-spacing has occurred due to a lack of suitable measurement concepts that combine the required engineered sampling approach with the collection of both RF and base-band signal components. The architecture presented in this work therefore looks to build upon the developed large signal CW and two-tone systems, extending capabilities into the multi-tone domain.

The main limiting factor that has prevented the previous systems from employing multi-tone stimulus are the unique issues surrounding the sampling of such waveforms. The issues along with proposed solutions are presented in this chapter. The problems have been overcome through the application of novel sampling techniques, which are detailed later in this chapter. Novel waveform alignment algorithms have been applied to enable software averaging of the multi-tone signals, significantly increasing the quality of the measurements and the achievable Signal to Noise Ratio (SNR).

The key requirements of the desired measurement system are noted below.

- The system should be based around a commercially available instrument, allowing easy take-up of the measurement approach.
- The system should be able to measure the multi-tone time domain voltage and current waveforms, that exist at the DUT plane.
- The system should allow for measurement of stimulus that allow characterisation to accurately predict device performance under current modulation schemes, and should be adaptable to future schemes.
- All significant components present in the spectrum should be measured and phase coherence should be maintained between them.
- Accuracy of the measurement system should be at least comparable to existing large signal measurement systems.
- The system should be flexible, allowing for expansion to include some impedance emulation architecture(s) for a more complete and intuitive design approach.

2.4 Realised CW Measurement Architecture

There was a desire to ensure that the hardware configuration of the new measurement system could exploit the developments that have occurred over the years on existing CW large-signal measurement systems presented and discussed earlier in this chapter. An interim step therefore was to build up a new system for the measurement of CW waveforms that could then be adapted for multi-tone signals. The MTA sampling instrument, used in iterations of the CW system architecture is now obsolete and although a mixer

based sampling architecture, would be desirable as discussed earlier, no such instrument is currently manufactured. Therefore the MTA was replaced in this measurement system with a high frequency sampling oscilloscope: the Tektronix CSA8000. As noted earlier, sampling oscilloscopes have improved dramatically over recent years in terms of reduced trigger jitter, resolution and speed of integrated ADC's, allowing much better dynamic range at higher sample rates to be achieved. In fact, tests conducted as part of this research show that if sufficient averaging is employed, the performance of the CSA8000 sampling-oscilloscope is comparable to that of the mixer based architecture of the MTA. The mainframe of the CSA8000 was fitted with two, dual-channel 80E03 sampling heads each offering a bandwidth of 12 GHz. It is worth noting that sampling modules are now available that would extend the instrument capabilities up to 60 GHz. As the sampling oscilloscope has 4 channels compared to the 2 channels of the MTA, the need for complex multiplexing and software control algorithms required to measure all four time synchronised incident and reflected travelling waves is removed, thus simplifying the design and removing any measurement ambiguity relating to the relative phase measured at the input and output of the DUT. The measurement time is also dramatically reduced since only a single measurement is required to capture the necessary four travelling waves instead of the 3 measurements required with the two-channel MTA.

Once the system was constructed, the CW performance was compared to the existing MTA. Measurements shown in the next chapter indicate that the dynamic range of the sampling oscilloscope and the MTA are similar. Waveform measurements from the new sampling-scope based system showed excellent agreement with those measured with two established, existing systems, one based around the MTA and the other around an LSNA; again results will be presented in chapter 3. This investigation proved that the realised system truly is a viable measurement solution.

The CW measurement system architecture using the new Tektronix CSA8000 employed as a development platform during this research is shown in figure 2.11. The system uses two broad-band directional couplers to simultaneously measure all four incident and reflected waves. DC biasing of

the device is achieved using bias-tees. As the DC component of the waveforms cannot be measured by the couplers, a computer controlled DC source is used to both supply and measure DC voltage and current. The full voltage and current waveforms are then constructed by inserting DC information into the measured voltage and current waveforms. The system is fully calibrated and controlled through a PC, via a GPIB instrument bus. Software and hardware are available to add source and load-pull capabilities.

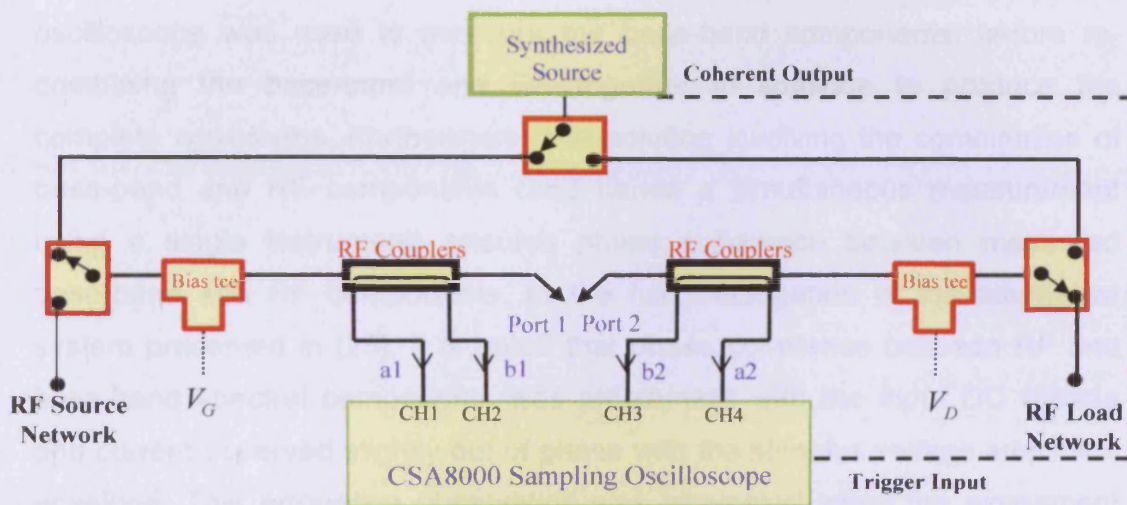


Figure 2.11 – CW mode of operation, Employed Using the CSA8000 Sampling Oscilloscope

2.4.1 Realised Multi-Tone Measurement Architecture

After initial tests were conducted to establish the viability of the sampling instrument and the general RF test-set architecture, it was necessary to redesign the test-set to incorporate base-band capabilities. It is important to remember that mixing induced in the device when multi-tone signals are applied will lead to the generation of in-band components at harmonic frequencies and at base-band frequencies. For example, in the two-tone case, base-band components are generated at $(\omega_2 - \omega_1)$, $2(\omega_2 - \omega_1)$ etc, and these base-band frequencies cannot be measured by the RF couplers as they are not within the relevant bandwidth. The final test-set incorporating fully integrated base-band and RF test-sets is shown in figure 2.12 with the IF

signal path shown in green and the RF signal path shown in blue. As the DC and base-band components of the signal cannot be measured through the RF couplers, the signal path is split at the bias tee, which acts as a diplexer. The incident and reflected base-band components are then measured by two base-band couplers, the outputs from the RF and base-band couplers are finally re-combined again using diplexers, before being measured by the sampling oscilloscope. The solution presented here is more compact and time-efficient than that used previously in [18], where a low frequency oscilloscope was used to measure the base-band components, before re-combining the base-band and RF together in software to produce the complete waveforms. Furthermore, this solution involving the combination of base-band and RF components (and hence a simultaneous measurement using a single instrument) ensures phase coherence between measured base-band and RF components. In the full investigation of the alternative system presented in [25], it is noted that phase coherence between RF and base-band spectral components was problematic with the input DC voltage and current observed slightly out of phase with the stimulus voltage amplitude envelope. This erroneous observation was eliminated when the experiment was repeated with the new measurement architecture, as shown in chapter 3 of the thesis, where (as expected), the base-band and RF envelopes are observed to be in phase.

The RF test set components allowed measurement of signals between 1 and 26.5 GHz, although the top end was limited by the receiver to 12 GHz. Two existing base-band test-sets were employed in this measurement system configuration. The first of these was constructed from off-the-shelf components, and was employed for the measurement of low power devices up to 5 Watts. This test set allowed for measurement of base-band waveforms from 200 KHz up to 5 MHz, the bandwidth being determined by the base-band couplers employed. The second test set was designed in-house [26] and employs a combination of off-the-shelf and custom-made components allowing application at much higher power levels, in excess of 100 W. This test-set allowed measurement of base-band waveforms from 100 kHz to 10 MHz.

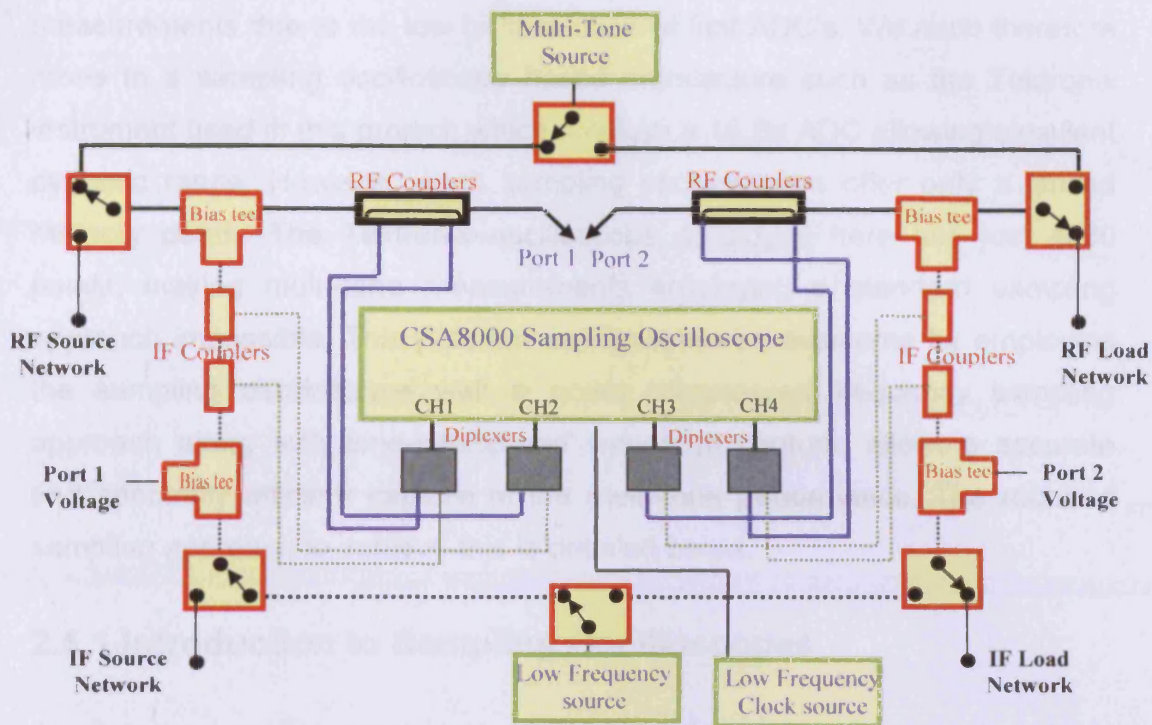


Figure 2.12 – Final measurement System Architecture, with Integrated RF and IF Capabilities

2.5 Multi-tone Sampling Implementation

As outlined in the introduction of this thesis, when we wish to sample multi-tone waveforms it is necessary to capture a significantly fine frequency grid. This grid must stretch from the lowest frequency of the base-band right up to the highest frequency of the highest harmonic band in order to capture all of the significant generated distortion terms. As the modulation frequency is typically many orders of magnitude smaller than the carrier frequency, if we employ the standard sampling approach and capture the signal on a frequency grid defined by the modulation frequency, tens of thousands frequency points are required to capture all the base-band, fundamental-band and harmonic-band information. Furthermore, as the distortion terms are generally significantly smaller than the excitation tones themselves, sufficient dynamic range is required to accurately capture the information.

As discussed in the literature review earlier in this chapter, the dynamic range of high-frequency real-time oscilloscopes is not sufficient for such

measurements due to the low bit resolution of fast ADC's. We must therefore move to a sampling oscilloscope based architecture such as the Tektronix instrument used in this project, which employs a 16 Bit ADC allowing excellent dynamic range. However, such sampling oscilloscopes offer only a limited memory depth. The Tektronix oscilloscope employed here has just 4000 points, making multi-tone measurements employing a standard sampling approach impossible. This problem can however be overcome by employing the sampling oscilloscope with a novel compressed frequency sampling approach along with time-interleaved waveform capture, allowing accurate and spectrally efficient capture of the multi-tone performance. The required sampling approach to achieve this is detailed below.

2.5.1 Introduction to Sampling Oscilloscopes

As discussed earlier, most large-signal, time domain measurement systems developed in the past 10 years have moved away from sample-and-hold based sampling oscilloscopes, in favour of the mixer based Microwave Transition Analyzer (MTA). However, recent advances in sampling oscilloscope technology mean that these instruments can no longer be ignored as viable alternative measurement instruments. Oscilloscopes now have excellent dynamic range and importantly have a larger number of samplers available. As mentioned in the previous section, this offers a significant advantage over two-channel instruments as all four travelling waves can be measured simultaneously, removing the need for multiplexing and phase handover measurements required to maintain a constant time reference. For these reasons the system presented here is based around a Tektronix CSA8000 sampling oscilloscope, providing the instrument required for a cost effective, yet high quality, time domain measurement system.

The Tektronix CSA8000 oscilloscope was used for the duration of this project. It is a sampling oscilloscope that can capture repetitive signals up to 12 GHz employing a sample-and-hold approach. The basic building blocks of a sampling oscilloscope are shown in figure 2.13. The most important part of the system is the sampling circuitry, and this will be discussed in more detail later in this chapter. This sampling circuit takes the input signal and effectively

down-converts it to a frequency that can be captured using an Analogue to Digital Converter (ADC). The signal conditioning block is then used to filter unwanted frequency components from the sampled signal and scale the amplitude to ensure the full dynamic range of the A/D is utilised. The digitised signal is then stored in memory before being processed by the Digital Signal Processor (DSP). The measured signal can then be displayed on the screen of the oscilloscope, or downloaded to a PC for post-processing.

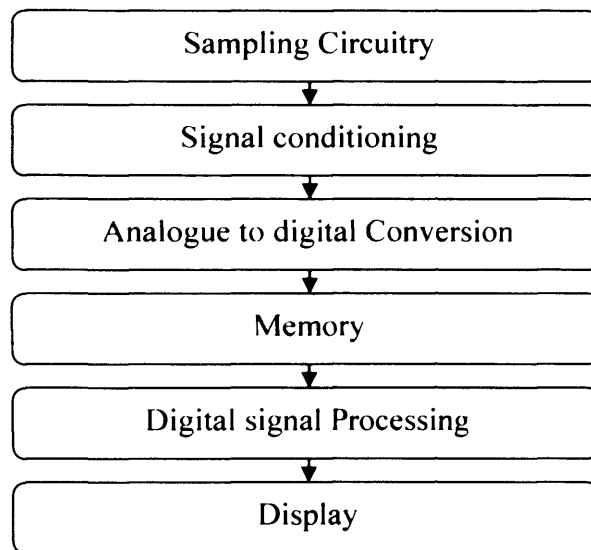


Figure 2.13 – Building Blocks of a sampling Oscilloscope

Figure 2.14 shows a simplified electrical model of a two-diode sampling circuit [27]. The two diodes shown in the model are nominally held in a high-impedance, reverse biased state, except when a strobe signal is fired. Each time the strobe fires, the two diodes are caused to conduct, lowering their impedance for a short time. While the diodes are conducting, any nonzero voltage at the input port will cause a charge to flow from the input port through the diodes to the hold capacitors. This net injected charge is proportional to the voltage at the input port when the strobe was fired. A differential arrangement is used to ensure that the differential strobe signals cancel and only the signal applied to the input is digitized.

It is important to note the sample rate of the oscilloscope is generally far lower than the RF frequency of the measured signal, thus only repetitive signals can

be measured by the oscilloscope. This is termed “equivalent-time” sampling, which effectively down-converts a measured input by capturing a single, consecutive point from different cycles of a repetitive input signal, thus building up a replica of the input signal, only at a much lower frequency.

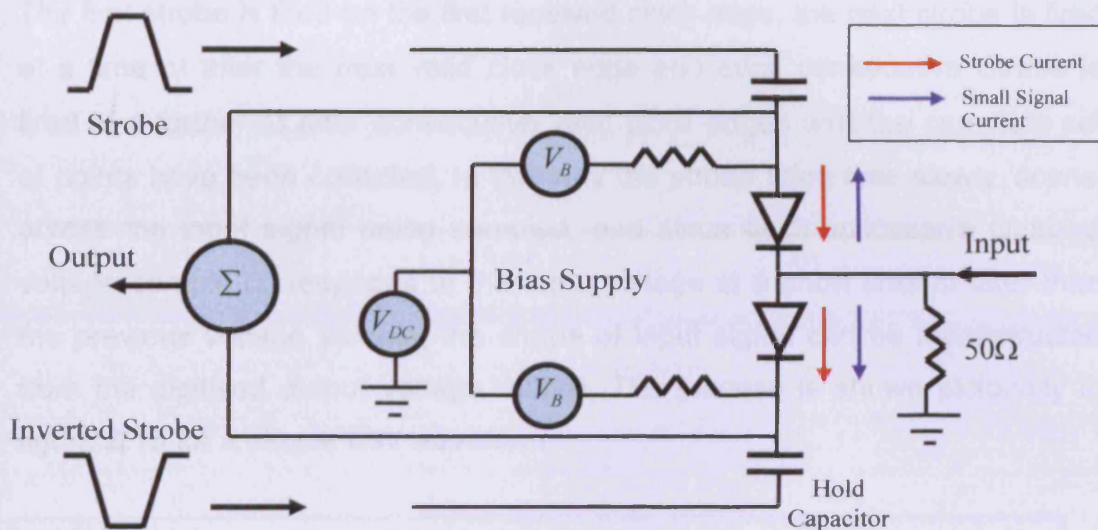


Figure 2.14 – Simplified model of sampling circuit

2.5.2 Standard Sampling Approach

Sampling oscilloscopes require an external clock signal in order to arrange collection of a particular point at the desired time interval. Typically, the stimulus signal can be split to achieve a coherent trigger signal, provided the signal repeats on each rising edge, as is the case for CW signals.

Trigger circuitry is used to generate the strobe pulses as shown in figure 2.14. Provided the trigger circuit is armed, a rising edge on the clock input results in the generation of a strobe pulse. Clearly if the measured signal is a high frequency signal and is used as the clock input, a number of clock pulses will be missed by the trigger circuit as the trigger is deployed and re-armed. A normal measurement procedure is described below –

The measurement window display time ($T_{Display}$) and number of points (P) to be collected must be set by the user. These must be carefully selected to avoid

aliasing. From these values, a step time (Δt) time can be calculated using equation 1.

$$\Delta t = \left(\frac{1}{P} \right) T_{Display} \quad (1)$$

The first strobe is fired on the first received clock edge, the next strobe is fired at a time Δt after the next valid clock edge and each consecutive Strobe is fired at a further Δt after consecutive valid clock edges until the complete set of points have been collected. In this way the strobe firing time slowly 'scans' across the input signal being sampled, and since each successive digitized voltage sample corresponds to the input voltage at a short time Δt later than the previous voltage sample, the shape of input signal can be reconstructed from the digitised output voltage record. The process is shown pictorially in figure 2.15 for a simple CW waveform.

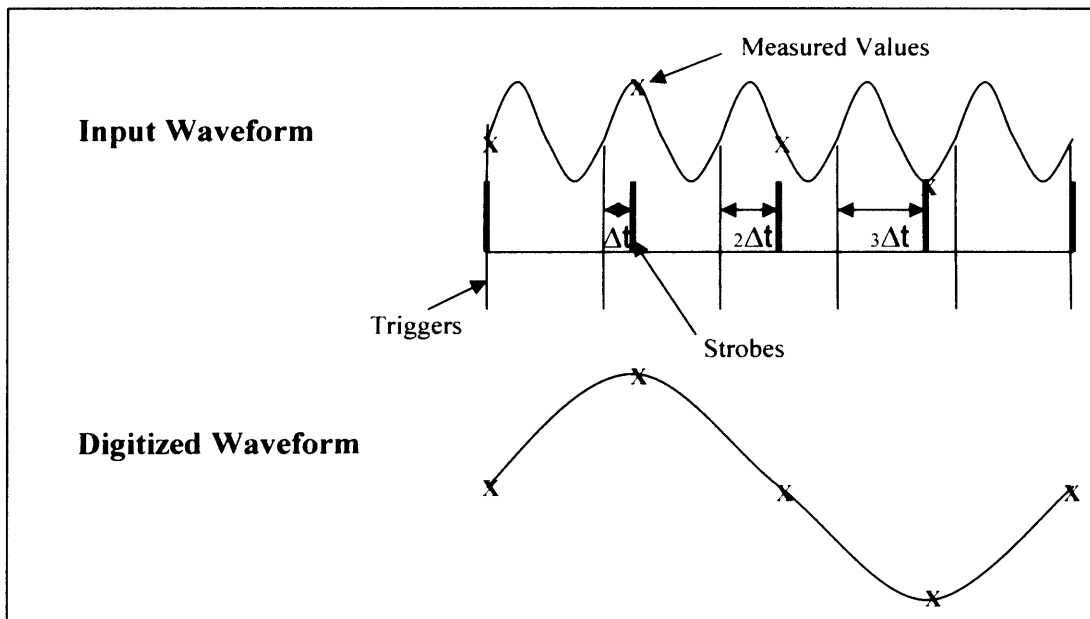


Figure 2.15 – Equivalent time Sampling, employed by sampling oscilloscopes to sample high frequency waveforms at much lower frequencies

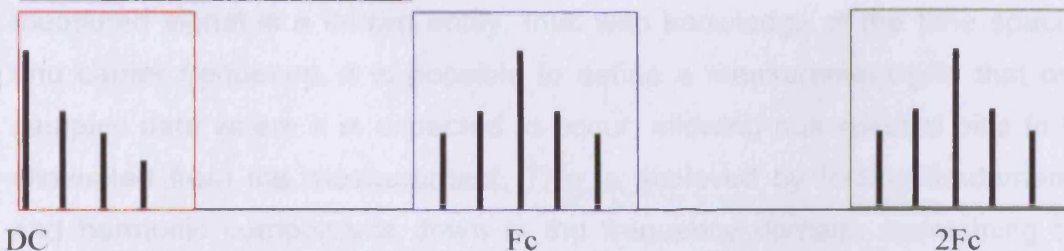
2.5.3 Compressed frequency sampling approach

Triggering from the input signal becomes impractical when we move away from CW stimulus and wish to sample multi-tone signals. The problem is that for modulated signals, each cycle of RF is no longer identical, thus the stimulus signal can no longer be used to trigger the measurement as the pattern no longer repeats on each rising edge. In order to capture the multi-tone signal using a standard sampling approach, a trigger would have to be provided at the repetition rate of the modulated sequence. Furthermore, as discussed the CSA8000 has only 4000 measurement points available, allowing for collection of only 2000 frequency component making a standard sampling approach impractical.

A novel compressed frequency approach has been developed which offers a solution to this problem. The major benefit of the sampling technique employed is that it allows multi-tone waveforms to be captured in a spectrally efficient way. This solution means that standard sampling oscilloscopes, which have only a limited memory depth, are now able to capture multi-tone waveforms in detail. A diagrammatic description of the compressed frequency sampling approach is shown in figure 2.16(a-c), where figure 2.16(a) shows the spectrum of the signal to be sampled. The spectral information is confined to specific frequency regions; at base-band, around the carrier and around harmonics of the carrier. Figure 2.16(b) shows the effect of a standard sub-sampling approach, where the frequency components are simply down converted in frequency and maintain an identical spectral pattern. Figure 2.16(c) shows the effect of the employed frequency compressed sampling where the frequencies are not only down converted but in addition the spectrum is compressed by removing the null spectral information between the bands of relevant information.

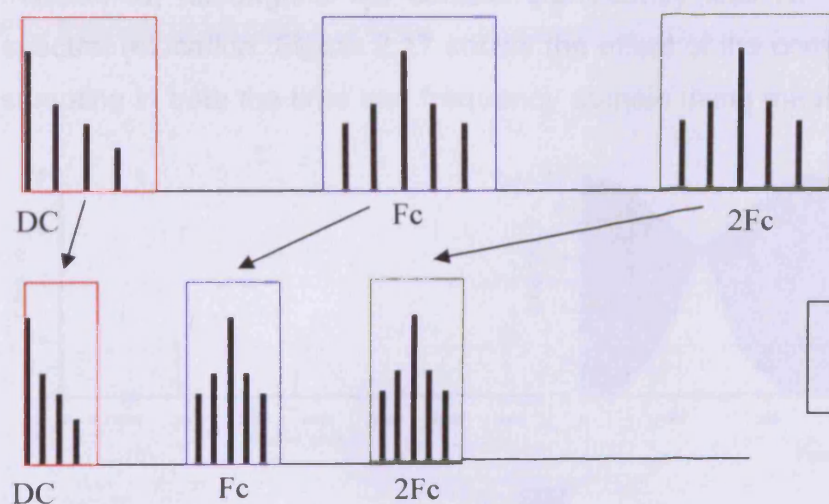
It can be seen that the employed compressed frequency approach offers significant improvement over the standard sampling case, where the down converted spectral pattern is identical to that of the sampled signal, thus resulting in a spectrally sparse collected data set with many null frequency bins between each 'block' of relevant data.

(a) Signal to be Measured



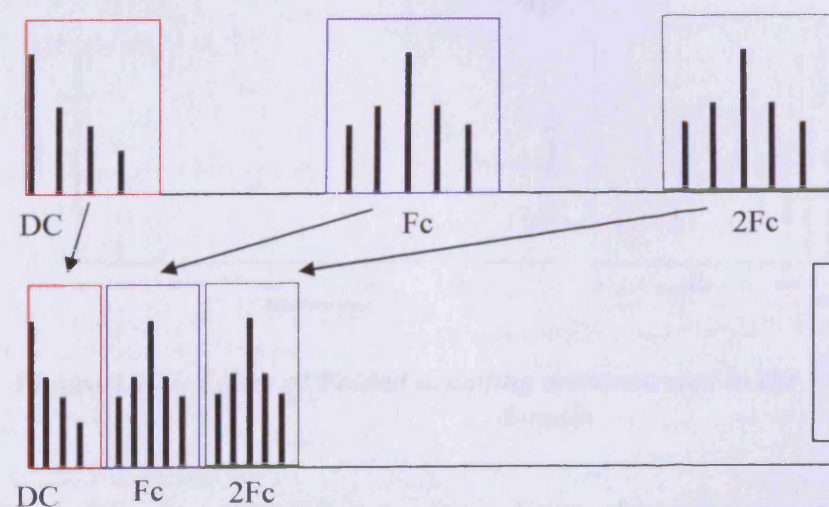
Shown Above is the signal to be sampled, all spectral information is confined to specific frequency regions in the diagram. The red box contains the base-band information, the blue box contains information around the carrier and the green box shows information around the second harmonic.

(b) - Conventional Sampling Approach



Spectral pattern is maintained, frequency components are down converted.

(c) Compressed Sampling Approach



Order of the spectral components is maintained, frequency components are down converted and compressed to remove nulls

Figure 2.16 Diagram showing the effect of standard sampling and compressed sampling on the frequency domain spectrum.

The compressed frequency approach takes advantage of the fact that the measured signal is a known entity, thus with knowledge of the tone spacing and carrier frequency, it is possible to define a measurement grid that only samples data where it is expected to occur, allowing null spectral bins to be eliminated from the measurement. This is achieved by folding fundamental and harmonic components down in the frequency domain, maintaining the sequence of the spectral components while removing null frequency bins. It is important to note that if we analyse waveforms collected using the compressed frequency sampling approach in the time domain, the modulation envelope is correct as the correct order of the spectral components has been maintained, although it will contain significantly less RF cycles due to the spectral relocation. Figure 2.17 shows the effect of the compressed frequency sampling in both the time and frequency domain using measured waveforms.

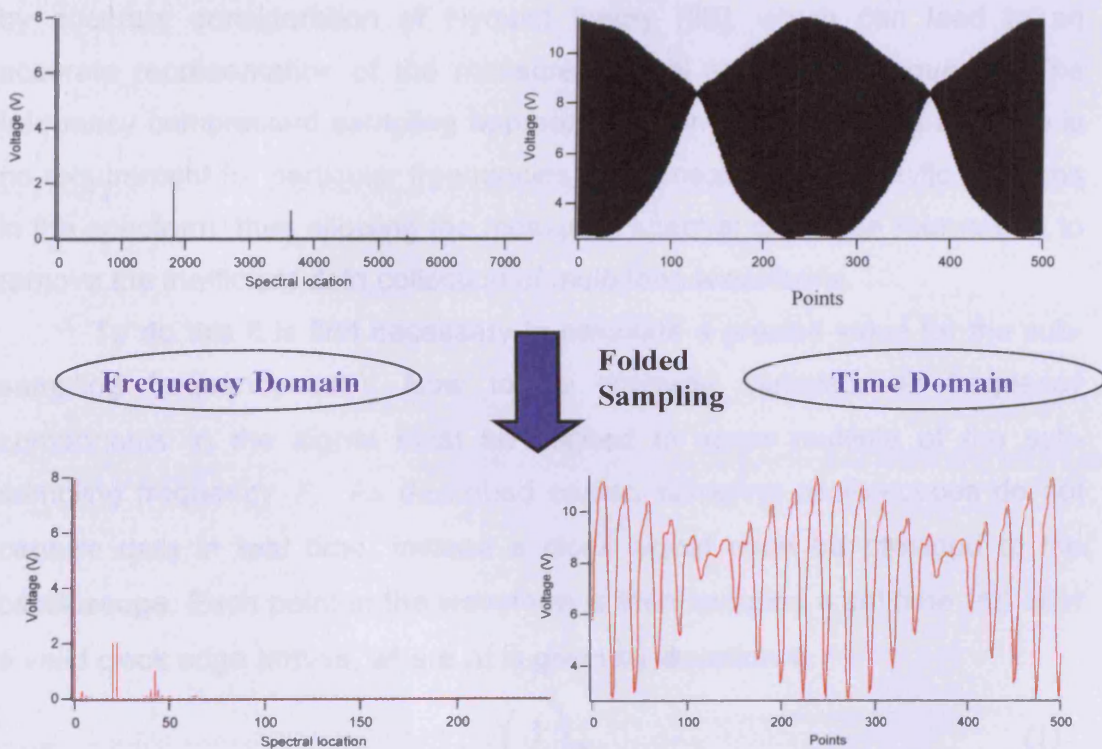


Figure 2.17 – Effect of Folded sampling demonstrated in the Frequency and Time domain

It can be seen that this compressed time domain representation is a useful way to view waveforms as effects on the envelope and on the RF carrier can

be seen simultaneously. The true waveforms can however be restored if desired, by simply uncompressing the spectrum in the frequency domain, hence shifting the measured components to the appropriate positions in the true spectrum. Using this approach, it is clear that far less measured points are required to collect the same spectral information compared to the standard sampling approach. This allows sampling-oscilloscopes with limited memory depth to capture multi-tone waveforms in great detail, including all significant generated components in all significant frequency bands.

2.5.3 Theory of Compressed frequency sampling approach

It is well known that sampling oscilloscopes employ aliasing to capture signals that are well above the sampling rate of the instrument. This can be achieved by accurate consideration of Nyquist theory [28], which can lead to an accurate representation of the measured signal at a lower frequency. The frequency compressed sampling approach further utilises aliasing as there is no requirement for particular frequencies to be measured at specific locations in the spectrum, thus allowing the measured spectral grid to be rearranged to remove the inefficient data collection of multi-tone waveforms.

To do this it is first necessary to calculate a precise value for the sub-sampling frequency (F_S). Now to be correctly sampled, all frequency components in the signal must be aligned to some multiple of the sub-sampling frequency F_S . As described earlier, sampling oscilloscopes do not capture data in real time, instead a clock signal must be provided to the oscilloscope. Each point in the waveform is then sampled a set time (Δt) after a valid clock edge arrives, where Δt is given by equation 1.

$$\Delta t = \left(\frac{1}{P} \right) T_{Display} \quad (1)$$

A valid trigger occurs when a clock edge arrives at the trigger port of the oscilloscope while the trigger is in armed mode. This process will by definition result in an effective sub-sampling period T_S or sampling frequency F_S , as shown pictorially in figure 2.18.

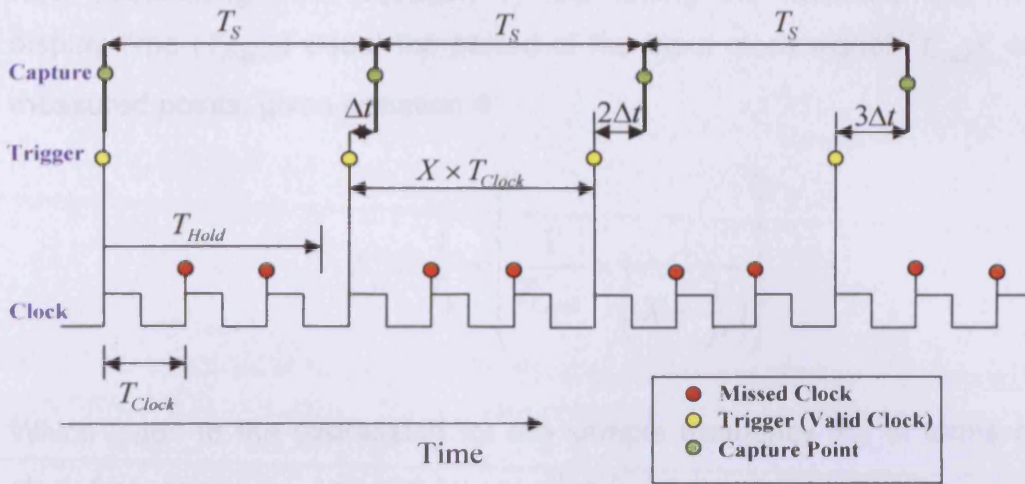


Figure 2.18 – Timing Diagram allowing Calculation of the sampling frequency

It should be noted that a consistent sampling frequency is only maintained for relatively low frequency input clocks, which is discussed in further detail in the application issues section of this chapter.

The formulation below will allow a stimulus to be engineered, which will ensure that all components in the device output will lie on the sampled grid. In order to calculate the sub-sampling frequency (F_s), the trigger re-arm time must be known or calculated. The re-arm time is the time the trigger circuitry is effectively disabled. For the Tektronix CSA 8000, used in this project, the minimum trigger re-arm time (T_{Hold}) was quoted in the literature as $5\mu S$ [29]. Using this value and the period of the clock signal (T_{Clock}) applied to the oscilloscope, it is possible to calculate the number of 'missed' clock edges (X) that occur while the circuit is being re-armed, as shown in equation 2.

$$X = \frac{T_{Hold}}{T_{Clock}} \quad (\text{Where } x \text{ is rounded up to nearest integer value}) \quad (2)$$

Clearly the sample time (T_s) must then be given by equation 3.

$$T_S = (X \times T_{Clock}) + \Delta t \quad (3)$$

Now substituting from equation 1, and letting the measurement window display time ($T_{display}$) equal the period of the input clock signal (T_{clock}), with P measured points, gives equation 4.

$$F_S = \frac{1}{T_S} = \left(\frac{1}{T_{clock}} \times \frac{1}{\left(X + \frac{1}{P} \right)} \right) \quad (4)$$

Which leads to the expression for the sample frequency F_S , in terms of the clock frequency (F_{clock}) shown by equation 5.

$$F_S = \left(\frac{P}{1 + XP} \right) F_{clock} \quad (5)$$

Thus the sampling window must then begin at multiples of the sample frequency (F_S). The spectral measurement window can then be broken down into a number of locations with spacing (δF), which define the location of that particular frequency component within the measurement grid. The location is then simply dictated by the multiple of δF . if P is defined as the number of measured points, an equation for δF is given by equation 6.

$$\delta F = \left(\frac{1}{P} \right) F_S \quad (6)$$

It is therefore possible to engineer the stimulus in terms of carrier frequency and tone spacing in order to manipulate their location in the measured down-converted spectrum. This is shown pictorially in figure 2.19, where the carrier is engineered to become (F_c') and thus lie at location 8 in the measured grid. The mathematical relationships used to engineer the stimulus frequencies are outlined below.

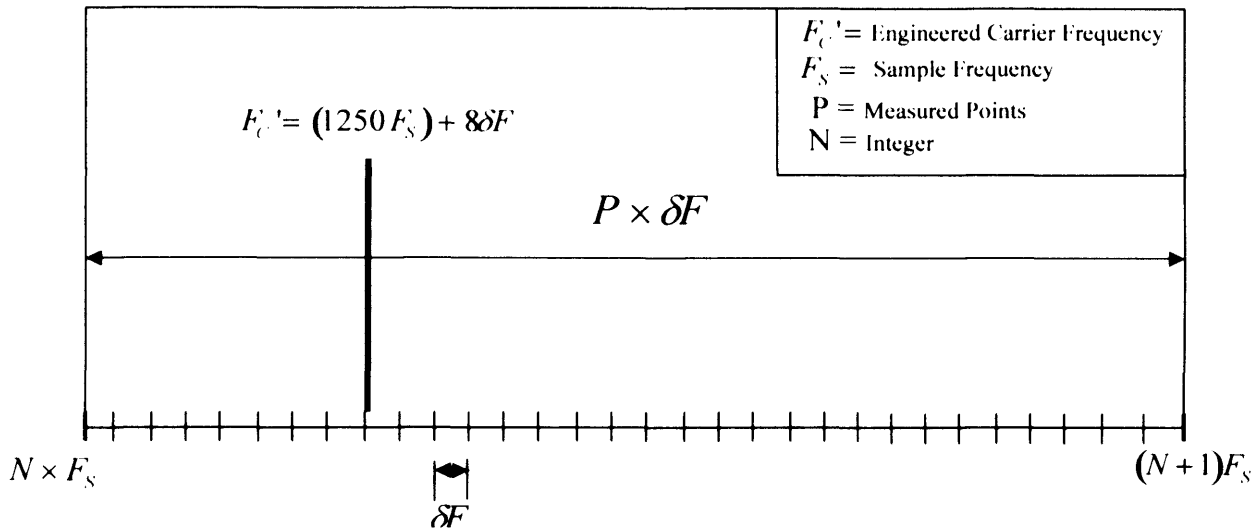


Figure 2.19 – Engineering the location of frequency components in the down-converted spectrum

In order to correctly sample the carrier, its frequency must be aligned to some multiple of F_s . It can be seen that the closest multiple M of F_s to a given desired carrier frequency F_c is given by the following equation –

$$M = \frac{F_c}{F_s} \tag{7}$$

(Where M is truncated to the nearest integer)

As we are measuring multi-tone waveforms, there is a need to measure many frequency components to analyse mixing and distortion terms at base-band and RF frequencies. Thus if we define ‘Order’ as the desired number of spectral locations to be measured at the base-band, and either side of the carrier and harmonic centre frequencies, then it is clear that the desired location (L) of the carrier in the spectrum is given by the following equation –

$$L = 2 \times \text{Order} + 1 \tag{8}$$

Therefore the carrier frequency can be engineered using equation 9, thus allowing the carrier to be measured at the correct location in the spectral grid.

$$F_c' = (M \times F_s) + (L \times \delta F) \tag{9}$$

Substitution from equation 5 and subsequent re-arrangement leads to a final equation for the engineered carrier frequency as shown in equation 10.

$$F_{c'} = \left(M + \frac{L}{P} \right) \times F_s \quad (10)$$

To ensure efficient use of the spectrum, we require that $F_{c'} - F_{M'}$ (the lower tone) appears in the same measurement window, but at location (L-1). Therefore we must again find the closest multiple of the sub-sampling frequency (N) to the required modulation frequency. N can be calculated using equation 11.

$$N = \left(\frac{F_M}{F_s} \right) \quad (11)$$

Substituting for N into equation 10 gives equation 12, for the required engineered tone spacing.

$$F_{c'} - F_{M'} = (M - N)F_s + ((L - 1)\delta F) \quad (12)$$

Substitution for δF , $F_{c'}$, and N from equations 5,9 and 11 respectively, gives equation 13 for calculation of ($F_{M'}$).

$$F_{M'} = \left(N + \frac{1}{P} \right) F_s \quad (13)$$

Using a target carrier frequency (F_c), target tone spacing (F_M) and Order, the above equations can thus be used to calculate the engineered carrier frequency ($F_{c'}$) and engineered tone spacing ($F_{M'}$), which will ensure that all frequency components will lie on the measured grid and at the desired locations in the spectrum. From the above analysis it can be seen that the

generic equation to engineer any given frequency F_x , to be measured at a particular location (Z) in the spectrum, the new frequency F_x' must be given by the following equation –

$$F_x' = \left(Y + \frac{Z}{P} \right) F_s \quad (14)$$

where Y is the closest multiple of the sampling frequency F_s to the desired frequency F_x , given by equation 15.

$$Y = \frac{F_x}{F_s} \quad (15)$$

2.6 Compressed Frequency Sampling Application Issues

2.6.1 Spectral Overflow and Folding

Appropriate consideration of the expected distortion products is vital to avoid misinterpretation of measured data when employing the compressed frequency sampling approach. A user must then take care in selection of the required order, to avoid spectral overflow. If the number of significant (i.e. above the noise floor) distortion terms is greater than the selected order then these distortion terms will be misinterpreted as distortion in a different band. Additionally care is also required in the selection of the number of measured points in order to avoid unwanted spectral folding. If too few points are used then higher frequency distortion terms will fold back down on top of other spectral components. This issue is discussed in more detail in appendix 1, where worked examples are shown.

2.6.2 Limited Tone Spacing grid

By analysis of equation 13, it becomes clear that only certain tone spacing values can be measured by the system when using the folded sampling algorithm. This can be shown by incrementing the value of Y , with Z set to 1. As an example, table 1 shows the tone spacing obtainable with the oscilloscope set up to capture 500 points and assuming a sub-sampling

frequency (F_s) of 200 kHz. It can be seen in the table that the 'permitted' grid of tone-spacing is effectively defined by the sampling frequency, so the tone spacing can be set on a 200 kHz grid starting from 400Hz. This is adequate for most investigations although there are certain measurements that require a fine degree of control such as investigation into thermally induced memory, which occurs for tone spacing in the kHz range. Although it is possible to alter the number of points and the number of cycles of modulation collected to perturbate the measurement grid, this does not offer the degree of flexibility required.

Y	Tone Spacing
0	400 Hz
1	200.4 kHz
2	400.4 kHz
3	600.4 kHz
4	800.4 kHz
5	1.0004 MHz
6	1.2004 MHz
7	1.4004 MHz
8	1.6004 MHz
9	1.8004 MHz
10	2.0004 MHz

Table 1 - Indication of the tone spacing achievable using the folded sampling approach.

This problem has been overcome through the development of a time interleaved sampling approach that can be combined with the frequency folded sampling. This sampling approach is similar in principle to that described in an application brief on Coherent Interleaved Sampling (CIS) from Lecroy [30,31], where a time interleave is employed to increase measurement speed in their NRO 9000 sampling oscilloscope.

The sampling solution presented in this section involves interleaving measured time domain data points during measurement, before removing the time-interleave in software during post-processing on the measurement PC. Combining an interleaved sampling approach with the novel frequency folded

sampling approach results in a much finer resolution of the tone spacing that can be employed.

Interleaved sampling takes advantage of the fact that there is no necessity to employ the folded sampling approach while sampling across a single cycle of modulation. In fact, provided the number of modulated cycles we sample across is prime and the number of measured points is not a direct multiple of this prime number, the same information can be gathered over many modulated cycles allowing a much finer grid of 'allowable' tone spacing to be generated.

Provided data points are collected over a prime number of modulation cycles, the same time domain data points will be collected as if sampling across a single cycle; however the points will no longer be collected in the correct order, or in other words, the time samples become interleaved. This means that the collected data in the time domain may no longer look meaningful and the data must be post-processed by re-ordering the collected points in time to get back to the original time domain representation. The reason the sampling must occur over a prime number of modulated cycles becomes clear if we examine this sampling approach more closely. For example, if we sample over 5 modulated cycles, the first point to be collected would be the same as the first point if collected over 1 modulated cycle, the next point however would correspond to the 5th point, and the next the 10th point and so on until all points have been collected. It is important to note that only by selecting a prime number of cycles will result in unique measurement points.

A pictorial representation of the interleaved sampling process is shown in figure 2.20, where arrows indicate the true location of the measured points in the collected waveform. Arrows are only used for the first 2 modulation cycles to avoid complication. It becomes clear that by the time all 49 points are collected we have 49 unique measurement points that correspond to the 49 points that would have been collected should we have sampled at a faster rate over a single modulation cycle. It is important to reiterate that this is only the case if the number of cycles we capture the data over is prime and the points to be collected is not a multiple of this prime number. Any other solution

will result in only part of the data being collected with repetition of some of the measured points.

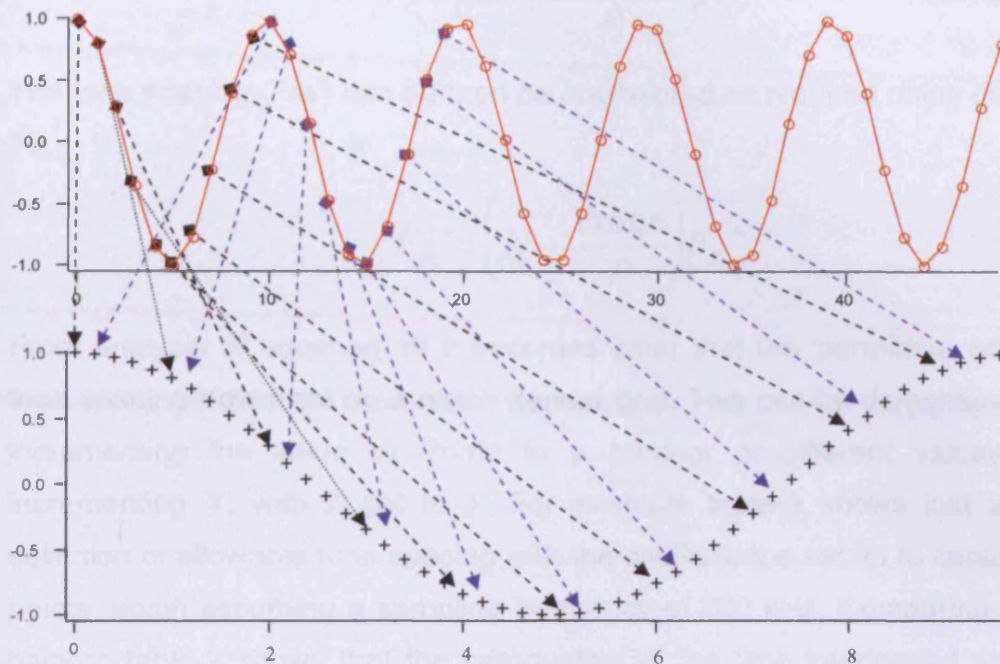


Figure 2.20 - Pictorial Representation of interleaved sampling - using of a prime number of sampled cycles.

The combination of the frequency compressed sampling with the time interleaved sampling, therefore, not only allows engineering of the Fourier locations of spectral components, but also the ability to engineer the order in which the time domain data is collected. Combining the two approaches gives the following modified equations required to calculate the new carrier frequency and tone spacing required to ensure all components in the desired spectral location. Equation 14 for the engineered frequency is replaced with equation 16, where Y is the closest multiple of the sampling frequency (F_s) to the desired frequency (F_x). The number of modulated cycles the data is captured over is a prime number (Prime).

$$F_x' = \left(Y + \frac{Z \times \text{Prime}}{P} \right) F_s \tag{16}$$

It can therefore be seen that it is possible to engineer the carrier (F_c') to be located at spectral location L using equation 17.

$$F_c' = \left(M + \frac{L \times \text{Prime}}{P} \right) F_s \tag{17}$$

The tone spacing (F_m') can be then be engineered as required using equation 18.

$$F_m' = \left(N + \frac{\text{Prime}}{P} \right) F_s \tag{18}$$

From analysis of equation 16 it becomes clear that the 'permitted' values of tone spacing now exist on a much denser grid. This can be demonstrated by incrementing the value of *Prime* to a number of different values while incrementing *Y*, with *Z* set to 1. For example table-3 shows just a small selection of allowable tone spacing with the oscilloscope set up to capture 500 points, again assuming a sampling frequency of 200 kHz. Comparing table-3 back to table-2 shows that the introduction of the time interleaved sampling process provides far greater flexibility in the 'permitted' tone spacing, allowing far more detailed investigations.

Prime	Y	Tone Spacing
1	0	200.002 Hz
3	0	600.601 Hz
5	0	1.001 kHz
7	0	1.4014 kHz
11	0	2.2002 kHz
13	0	2.603 kHz
17	0	3.403 kHz
19	0	3.804 kHz
.....
1	1	200.4008 kHz
3	1	201.2024 kHz
5	1	202.004 kHz
7	1	202.8056 kHz
11	1	204.4088 kHz
13	1	205.2104 kHz
17	1	206.8136 kHz
19	1	207.6152 kHz

Table 3 - Indication of the tone spacing achievable using the folded sampling approach combined with an interleaved sampling approach.

2.6.3 Error on the Trigger Re-Arm Time

When an external clock is used to trigger measurements on the CSA 8000, the user has the ability to select the hold time (T_{Hold}) of the trigger circuitry. The hold time is defined as the time before the trigger is ready to accept the next input clock pulse. This value is limited however by a minimum re-arm time of the trigger circuitry, which is quoted in the instrument's literature as 5 μs [29]. It would be logical to assume therefore that the best solution would be to set this hold time to its minimum value, as this would give the fastest measurement time. However due to an inherent variation or jitter in this re-arm time (\varnothing), a possible problem arises, as it can lead to an unexpected trigger event, as illustrated in figure 2.21.

This does not cause a problem if triggering is via the measured signal as is the case with CW measurements, as the signal is then repetitive on each rising edge. This variation however causes major issues when employing the frequency compressed sampling method described earlier. This is because a constant sampling frequency (F_S) is required throughout the measurement, and the approach will fail if this is not the case.

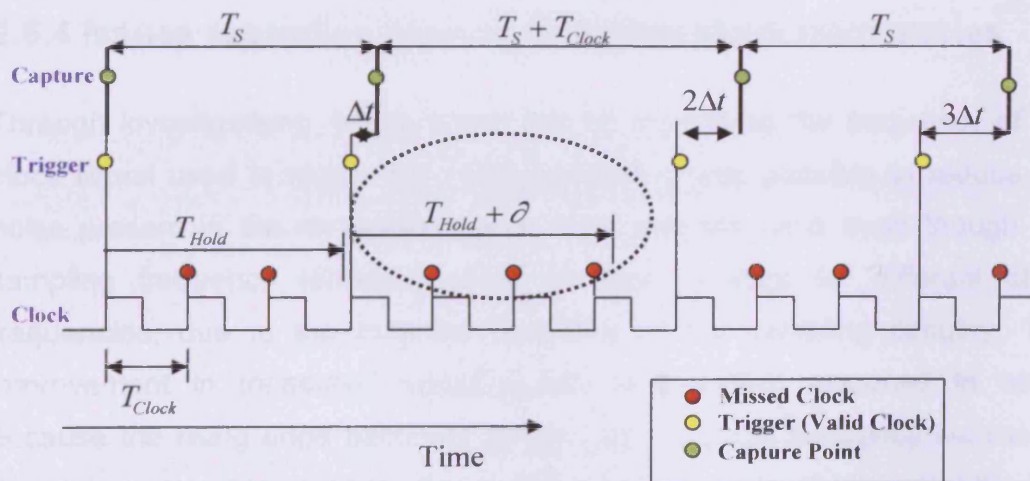


Figure 2.21 – Timing Diagram – Highlighting problem caused by jitter on trigger re-arm time

Provided the jitter is small compared with the clock period, the solution is to extend the hold time (T_{Hold}') to occur in the middle of received clock pulses thus negating the effect of any jitter on the hold time. This is shown in figure 2.22.

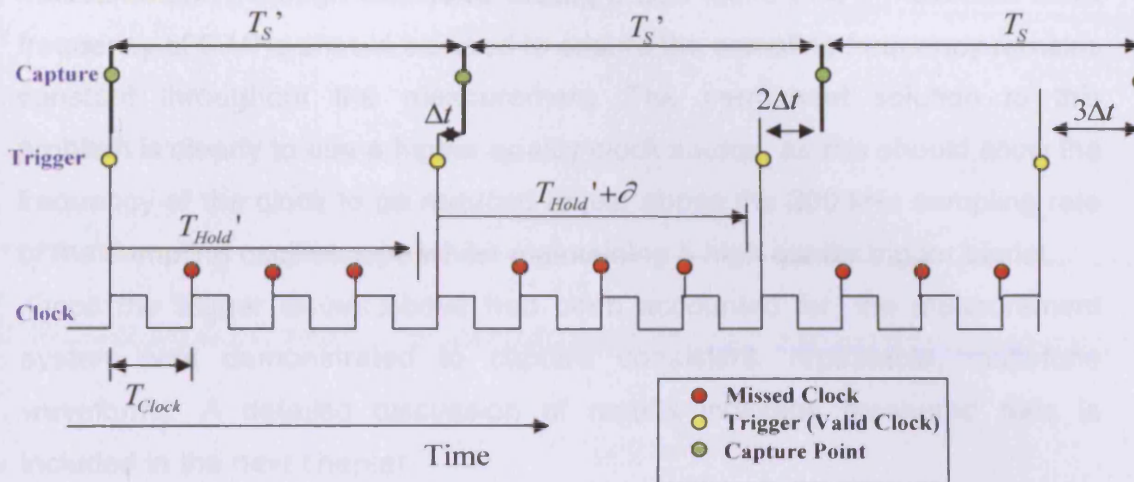


Figure 2.22 – Timing Diagram - Solution to noise on trigger re-arm time application issue

2.6.4 Issues regarding moving to higher clock frequencies

Through investigations, it was found that by increasing the frequency of the clock signal used to trigger the measurements it was possible to reduce the noise present in the measured signal. This was the case even though the sampling frequency remained more or less constant for different clock frequencies, due to the invariant hold-time of the sampling circuitry. The improvement in measured signal quality is therefore assumed to occur because the rising edge becomes steeper as the clock frequency increases, thus introducing less trigger jitter in the measurements. If this conjecture is correct, similar improvements in the measurement noise would be expected from a higher quality clock source.

There is however a problem as we move to higher clock frequencies: as the clock frequency is increased, the time between consecutive clock pulses is reduced. As noted earlier in this chapter, if there is small inherent

jitter on the hold time of the trigger circuitry, as the frequency of the clock is increased, the time between consecutive rising edges is clearly reduced. At some stage if we continue to increase the frequency, the possibility of a misinterpreted clock edge is again possible, causing varying F_s over the measurement. Through extensive testing it was found that a maximum clock frequency of 5 MHz should be used to ensure the sampling frequency remains constant throughout the measurement. The permanent solution to this problem is clearly to use a higher quality clock source, as this should allow the frequency of the clock to be reduced to just above the 200 kHz sampling rate of the sampling oscilloscope whilst maintaining a high quality trigger signal.

Once the trigger issues above had been accounted for, the measurement system was demonstrated to capture consistent, repeatable, multi-tone waveforms. A detailed discussion of results including measured data is included in the next chapter.

2.7 Multi-tone Software Time Alignment

One significant issue when employing the frequency compressed sampling technique is an inability to 'freeze' the display of the sampling-oscilloscope. The collection of each new multi-tone waveform is, in itself a valid measurement and captures all of the relevant information; however, consecutive measurements do not occur with a coherent time reference. This transpires because although the oscilloscope coherently samples across the selected time window, when the end of the time window is reached the data must be processed and displayed. This leads to an unknown and unpredictable number of clock edges being ignored, thus each new waveform collection begins at a different time-point in the repetitive waveform. This means that the on-board averaging of the oscilloscope cannot be employed.

This section deals with the software post-processing required to accurately time align the collected waveforms in order to allow averaging that is necessary to improve the overall quality of the measurements to an acceptable level. The required software processing is relatively trivial for a sampled CW signal as each consecutive captured waveform is simply a time-

shifted version of its predecessor. In this case, averaging can be achieved by simply using the first waveform as a reference with all other waveforms time-shifted to align. This approach allows for simple yet effective time-domain averaging. However, as soon as we modulate the excitation, a simple time shift is no longer sufficient as the RF and Modulation naturally have different down-conversion ratios, which means that consecutive waveform collections are no longer just time shifted versions of each other. The envelope changes and RF changes occur on totally different time scales. This is illustrated in figure 2.23 below, which shows two instances of a captured two-tone waveform. From this illustration it is clear that it is no longer possible to just time shift waveforms to align them.

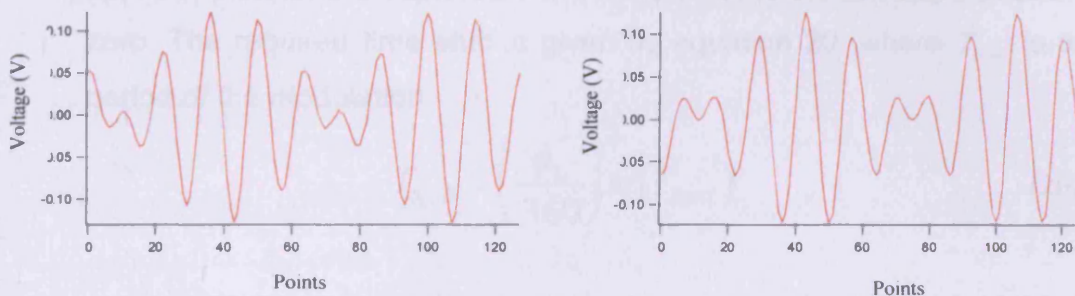


Figure 2.23 – Two consecutive multi-tone waveform captures

The software alignment algorithm is written in the IGOR² software environment, which also provides the interface with the instruments, along with the ability to set up measurements and to collect data. The concept is to align all subsequent waveform captures to an original data set, thus giving the ability to consistently average multiple multi-tone waveforms. The alignment process involves two stages, a first to align the modulation envelopes, then a second to align the RF cycles within the envelope as outlined in the steps below.

- A waveform is collected, and an FFT is completed to convert the information into the frequency domain using IGOR's in-built FFT function. This information is then converted into a polar format to give the

² IGOR is a programming language used for instrument control and data processing the software environment is produced by Wavemetrics.

magnitude and phase information for each spectral component. Using this data set the phase of the envelope ϕ_e is calculated by considering the phase of the upper sideband ϕ_u and lower sideband ϕ_l as shown in equation 19.

$$\phi_E = (\phi_U) - (\phi_L) \quad (19)$$

- This envelope phase is then compared to the envelope phase of the reference waveform. Once the required phase of the envelope is known, it is possible to calculate an equivalent time-shift (T_{Shift}) that will be applied to the entire captured waveform, to force the envelope phase to zero. The required time shift is given by equation 20, where T_{Mod} is the period of the modulation.

$$T_{Shift} = \left(\frac{\phi_E}{360} \right) \times (T_{Mod}) \quad (20)$$

- To apply the time shift, the data is left in the frequency domain and each spectral component is multiplied by a complex function determined by its frequency (F_{Loc}). The required phase shift (A_x) to provide the correct time shift is shown in equation 21 but must be converted into the rectangular domain before multiplication with the original spectral information –

$$A_x = -2\pi F_{Loc} T_{Shift} \quad (21)$$

At this point, a check is completed to ensure the envelopes have indeed been aligned. This step is included to account for issues encountered when applying this method to suppressed carrier modulation schemes. When this approach is applied to a suppressed carrier multi-tone there are two zero crossings in any modulation cycle. The mathematics above therefore only ensures that consecutive samples are either correctly aligned or are in anti-phase. The method chosen to decide if waveforms were accurately aligned was to subtract the fundamental envelope of the collected signal from the

original. The average value of the data-set is then compared against some chosen reference level and if envelopes are found to be misaligned then a further 180 degree phase shift is applied.

At this stage, although the modulated envelopes have been successfully aligned to the reference waveform, it is very difficult to achieve perfect alignment of the RF phase purely using a time shift calculated from the envelope phase alone. This problem is caused by inaccuracies in calculating the envelope time shift and it is clear that a small inaccuracy in the calculation of the envelope time shift calculation will be scaled by many thousands of times when applied to the RF cycles. Analysis shows that the initial envelope alignment is sufficient to align consecutive waveforms to within one RF period, so in order to overcome this problem, a similar process is employed to ensure alignment of the RF Phase. The required time shift to align the RF cycles is calculated by directly extracting the carrier phase.

By firstly correcting the phase of the envelope, the subsequent shift in envelope phase caused by the alignment of the RF is negligible. This approach is fully validated in the next chapter.

2.8 System Calibration

A calibration procedure is required to account for any errors introduced due to losses, mismatches and imperfect directivities in the system, thus allowing for the measurement of the complete multi-tone voltage and current waveforms and impedances that exist at the DUT plane.

The calibration employs a well-established calibration presented in detail in [4,32]. This calibration procedure has been successfully implemented and utilised on various previous iterations of measurement systems developed at Cardiff University. For this reason, only the additions and alterations made to allow calibrations on a multi-tone grid will be presented in this thesis.

In order to calibrate for a multi-tone measurement, it is necessary to apply the calibration procedure outlined in [4,32] both at base-band and at RF frequencies covering fundamental and significant harmonic bands. The base-band and RF calibration results can then be combined to create a single

calibration file containing all necessary error coefficients for application during waveform measurement. Due to the nature of the sampling employed, all expected frequency components are known, thus a calibration grid is engineered that covers all of the frequency components contained in the compressed spectrum, ensuring that only relevant components are calibrated.

The ability to vary the tone-spacing during a measurement is a common requirement when performing multi-tone measurements. For example, we may wish to consider the effect of the different modulation rates on transistor performance in order to investigate various memory phenomena. If the calibration grid is defined in the same way as the measurement grid then a new calibration must be completed for each change in tone spacing, which makes measurements rather time consuming. To overcome this potential problem an interpolated calibration procedure has been utilised.

Obviously an interpolation process is only viable if the error coefficients are reasonably well behaved across the entire measurement bandwidth. This is shown to be the case in appendix 2, where the error coefficients are plotted at base-band, fundamental-band and harmonic bands up to the 5th harmonic. The measurements indicate that the error coefficients are well behaved in each of the measured bands and as such can be easily interpolated. Thus, rather than using the desired measurement grid as the calibration grid, the user calibrates with a reasonable resolution over bandwidth at base-band, fundamental-band and around each harmonic band. An interpolation function within the IGOR programming environment is then used to generate the appropriate error coefficients for the desired tone spacing. The error coefficients for each band are then combined to form a calibration file for use in the waveform measurement software.

2.9 Chapter Summary

A literature review into current large signal measurement systems has been undertaken, and revealed that there were no existing measurement solutions that allowed the capture of all of the relevant information contained within a device input and output signal when driven with a multi-tone stimulus. This led

to the requirement for the optimum measurement architecture presented in this chapter.

The realised optimum hardware architecture has been presented. This required integration of base-band and RF test-sets, allowing base-band and RF signals to be coupled separately before being recombined for measurement by the sampling oscilloscope, ensuring phase coherence of the measured components. The test-sets employed followed a standard configuration of components used in previous iterations of the measurement system. The resulting hardware allows measurement of RF signal components between 1 GHz and 12 GHz, and IF components between 200 kHz and 5 MHz when using the low power IF test set, and between 100 kHz and 10 MHz when employing the high power IF test set.

The next section of the chapter detailed the required novel sampling architecture required to allow a sampling oscilloscope with limited memory depth to capture sufficient information to accurately describe a non-linear device's response to a multi-tone signal, including all of the significant distortion terms. The presented solution of a frequency folded sampling process allowed for spectrally efficient capture of repetitive multi-tone signals. A section detailing the application issues that occur when using the new measurement system followed, and where appropriate, solutions were offered. The two main issues were; firstly a limited tone-spacing resolution, which was solved by combining the frequency-folded sampling approach with time-interleaved sampling; and secondly the inability to freeze the multi-tone signals on the sampling-oscilloscope, which was solved through an algorithm that allowed time alignment of consecutive waveform captures, thus allowing for a post-processing and averaging procedure to increase the quality of the measurements.

The final section of the chapter discussed additions to the calibration software that allowed for efficient calibration for multi-tone measurements.

In summary it is believed that the presented measurement system offers the optimum solution, measuring all components contained within a wide-band multi-tone signal including base-band, in-band and harmonic-band distortion terms. The frequency compressed sampling technique employed

combined with the time interleaved collection approach ensures the collection is performed in the most spectral and time efficient manner. Accuracy of the measurement system has been dramatically improved through software alignment and averaging algorithms. The calibration process has also been optimised to ensure the fastest solution without compromising on the accuracy of the measurements.

2.10 References

1. S.A. Maas "*Nonlinear Microwave Circuits Second Edition*" Artech House Microwave Library 2003, ISBN 1-58053-484-8
2. Bossche, Marc Vanden; Verbeyst, Frans; Verspecht, Jan. "*The Three Musketeers of Large Signal RF and Microwave Design-Measurement, Modeling and CAE*" 53rd ARFTG Conference Digest-Spring, Volume 35, June 1999 Page(s):1 - 8
3. N. O. Sokal and A. D. Sokal, "*Class E — A New Class of High-Efficiency Tuned Single-Ended Switching Power Amplifiers*", *IEEE Journal of Solid-State Circuits*, vol. SC-10, pp. 168–176, June 1975.
4. Benedikt, J.; Gaddi, R.; Tasker, P.J.; Goss, M. "*High-power time-domain measurement system with active harmonic load-pull for high-efficiency base-station amplifier design*" *IEEE Transactions on Microwave Theory and Techniques*, Volume 48, Issue 12, Dec. 2000 Page(s):2617 – 2624 .
5. Roff, Chris; Benedikt, Johannes; Tasker, Paul J. "*Design Approach for Realization of Very High Efficiency Power Amplifiers*" *IEEE/MTT-S International Microwave Symposium Digest 2007* Page(s):143 - 146
6. Sipila, M.; Lehtinen, K.; Porra, V. "*High-frequency periodic time-domain waveform measurement system*" *IEEE Transactions on Microwave Theory and Techniques*, , Volume 36, Issue 10, Oct. 1988 Page(s):1397 - 1405
7. Lott, U. "*Measurement of magnitude and phase of harmonics generated in nonlinear microwave two-ports*" *IEEE Transactions on Microwave Theory and Techniques*, Volume 37, Issue 10, Oct. 1989 Page(s):1506 - 1511
8. Barataud, D.; Arnaud, C.; Thibaud, B.; Campovecchio, M.; Nebus, J.-M.; Villotte, J.P. "*Measurements of time-domain voltage/current waveforms at RF and microwave frequencies based on the use of a vector network analyzer for the characterization of nonlinear devices-application to high-efficiency power amplifiers and frequency-multipliers optimization*" *IEEE Transactions on Instrumentation and Measurement*, Volume 47, Issue 5, Oct. 1998 Page(s):1259 – 1264.
9. Agilent Technical Data Sheet "*PNA-X Series Network Analyser*", (<http://cp.literature.agilent.com/litweb/pdf/N5242-90007.pdf>). Accessed Dec. 07
10. Kompa, G.; van Raay, F. "*Error-corrected large-signal waveform measurement system combining network analyzer and sampling oscilloscope capabilities*" *IEEE Transactions on Microwave Theory and Techniques*, Volume 38, Issue 4, April 1990 Page(s):358 - 365
11. Van Raay, F.; Kompa, G. "*A new on-wafer large-signal waveform measurement system with 40 GHz harmonic bandwidth*" *IEEE/MTT-S International Microwave Symposium Digest 1992*, vol.3, Page(s):1435 – 1438.

12. Demmler, M.; Tasker, P. J.; Schlechtweg, M. "***A Vector Corrected High Power On-Wafer Measurement System with a Frequency Range for the Higher Harmonics up to 40 GHz***" 24th European Microwave Conference 1994, Volume 2, Page(s):1367-1372.
13. J. Benedikt, "***Novel High Frequency Power Amplifier Design System***" Ph.D. thesis, University of Wales, Cardiff, September 2002.
14. Lees, J.; Benedikt, J.; Hilton, K.P.; Powell, J.; Balmer, R.S.; Uren, M.J.; Martin, T.; Tasker, P.J. "***Characterisation of an experimental gallium nitride microwave Doherty amplifier***" 2005 European Microwave Conference, Volume 2, 4-6 Oct. 2005.
15. McGovern, P.; Benedikt, J.; Tasker, P.J.; Powell, J.; Hilton, K.P.; Glasper, J.L.; Balmer, R.S.; Martin, T.; Uren, M.J. "***Analysis of DC-RF dispersion in AlGaIn/GaN HFETs using pulsed I-V and time-domain waveform measurements***" IEEE/MTT-S International Microwave Symposium Digest 2005.
16. Qi, Hao; Benedikt, Johannes; Tasker, Paul J. "***Novel Nonlinear Model for Rapid Waveform-based Extraction Enabling Accurate High Power PA Design***" IEEE/MTT-S International Microwave Symposium Digest 2007, Page(s):2019 - 2022
17. Gharaibeh, K.M.; Gard, K.; Steer, M.B. "***Characterization of in-band distortion in RF front-ends using multi-sine excitation***" 2006 IEEE Radio and Wireless Symposium, 17-19 Jan. 2006 Page(s):487 – 490.
18. Williams, D.J.; Leckey, J.; Tasker, P.J. "***A study of the effect of envelope impedance on intermodulation asymmetry using a two-tone time domain measurement system***" IEEE/MTT-S International Microwave Symposium Digest 2002, Volume 3, 2-7 June 2002 Page(s):1841 – 1844.
19. Verspecht, J.; Debie, P.; Barel, A.; Martens, L. "***Accurate on wafer measurement of phase and amplitude of the spectral components of incident and scattered voltage waves at the signal ports of a nonlinear microwave device***" IEEE/MTT-S International Microwave Symposium Digest 1995, Vol.3, Page(s):1029 – 1032.
20. Verspecht, Jan; Verbeyst, Frans; Bossche, Marc Vanden "***Network Analysis Beyond S-parameters: Characterizing and Modeling Component Behaviour under Modulated Large-Signal Operating Conditions***" 30th European Microwave Conference Oct. 2000 Page(s):1 – 4.
21. Vuolevi, J.H.K.; Rahkonen, T.; Manninen, J.P.A. "***Measurement technique for characterizing memory effects in RF power amplifiers***" IEEE Transactions on Microwave Theory and Techniques, Volume 49, Issue 8, Aug. 2001 Page(s):1383 – 1389.
22. Abdulrahman Alghanim; Jonathan Lees; Tudor Williams; Johannes Benedikt, Paul Tasker "***Using active IF load-pull to investigate electrical base-band memory***"

effects in high-power LDMOS transistors” IEEE Asia-Pacific Microwave Conference 2007.

23. Macraigne, F.; Reveyrand, T.; Neveux, G.; Barataud, D.; Nebus, J.-M.; Soury, A.; NGoya, E. “*Time-domain envelope measurements for characterization and behavioral modeling of nonlinear devices with memory*” IEEE Transactions on Microwave Theory and Techniques, Volume 54, Issue 8, Aug. 2006 Page(s):3219 – 3226.

24. *Data Sheet DPO70000 Series Digital Phosphor Oscilloscopes and Digital Serial Analyzers* (http://www.tek.com/site/ps/4H-19377/pdfs/4HW_19377.pdf). Accessed June 2008.

25. Williams, D.J. (2003) *Non-Linear Measurement System and Techniques for RF Power Amplifier Design*. PhD thesis. Cardiff University.

26. Alghanim, A.; Benedikt, J.; Tasker, P.; “*A measurement test-set for characterisation of high power LDMOS transistors including memory effects*” High Frequency Postgraduate Student Colloquium, 2005, 5-6 Sept. 2005 Page(s):29 – 32.

27. Remley, K.A.; Williams, D.F. “*Sampling oscilloscope models and calibrations*” IEEE/MTT-S International Microwave Symposium Digest 1995 Volume 3, Page(s):1507 – 1510.

28. Luke, H.D. “*The origins of the sampling theorem*” IEEE Communications Magazine, Volume 37, Issue 4, April 1999 Page(s):106 – 108.

29. *DSA8000 Digital Serial Analyzer Specifications and Performance Verification 071-2048-01* (<http://www2.tek.com/cmswpt/mafinder.lotr?cn=dsa8200&lc=EN>). Accessed May 2008.

30. Lecroy Corporation Application Note “*Coherent interleaved sampling and FFT*” http://www.lecroy.com/tm/Library/LABs/PDF/LAB_WE770.pdf. Accessed June 2008.

31. Lauterbach. M, Schnecker. M. “*Capturing and Evaluating High-Frequency Signals*”EvaluationEngineering.com; http://archive.evaluationengineering.com/archive/articles/0106/0106capturing_evaluating.asp. Accessed June 2008.

32. R. Gaddi, “*Characterisation and Modelling of Silicon RF LDMOS Transistors*” Ph.D. thesis, University of Wales Cardiff, January 2002.

Chapter 3 – Validation of the Non-Linear Multi-tone Waveform Measurement System

3.1 Introduction

The previous chapter outlined the conceived multi-tone non-linear waveform measurement architecture, along with the required sampling, time alignment and averaging required to capture high quality multi-tone information. The system is based around an off-the-shelf Tektronix 8000 series sampling oscilloscope, and provides the ability to measure multi-tone time-domain voltage and current waveforms, calibrated to the DUT plane. The system allows large signal measurements to be completed with stimuli that more closely represent the signals used in current communication systems. Furthermore the approach taken is adaptable to future modulation schemes. All significant components present in the spectrum are captured and phase coherence between all measured components is consistently maintained. The system allows for expansion to include impedance emulation architecture, which will be discussed in the following chapters of the thesis.

The purpose of this chapter is to validate all of the concepts discussed in the previous chapter. This is not a straightforward task due to the unique nature of the presented system, which results in a lack of similar measurement concepts with which to compare and contrast results. The validation process has therefore been split into a number of validation steps outlined in the sections below. Firstly a CW comparison is conducted using two well-established large-signal measurement systems, providing the fundamental evidence that the system is measuring magnitude and phase information accurately over a sufficiently large dynamic range. The same CW comparison is then repeated, but with the system set up in its multi-tone measurement configuration, thus verifying the multi-tone sampling approach outlined in the previous chapter. Finally a spectrum analyser is used to validate the measurement system under multi-tone drive, with measurements conducted over the entire dynamic range of the new measurement system. Further to the system comparisons, throughout the chapter, theory is used to confirm that the system is operating correctly.

3.2 Small Signal and CW Waveform Verification

In this section, two completely different and established large-signal measurement systems are used to validate the CW measurement capabilities of the new measurement architecture. The two reference measurement systems are an MTA based measurement system used for the investigations presented in [1-3], currently in use at Cardiff University, and an LSNA based system used in the investigations presented in [4-5] currently in use in the Universidade de Vigo, Spain. Comparisons will be made by analysing measured s-parameters, measured power performance and finally by overlaying measured voltage and current waveforms. The waveforms are perhaps the most important validation as they contain all of the magnitude and phase information contained in the device output.

These investigations allow for detailed analysis of the new measurement system's ability to accurately measure large signal vectoral information. In these initial investigations, the Tektronix CSA8000 based system was set up in its standard CW mode of operation as shown in figure

3.1 and discussed in the previous chapter. Standard open-loop load-pull control was integrated to allow, if necessary, the control of the load impedance at fundamental and harmonic frequencies, although initial investigations were conducted into the nominal $50\ \Omega$ impedance environments of the three measurement systems.

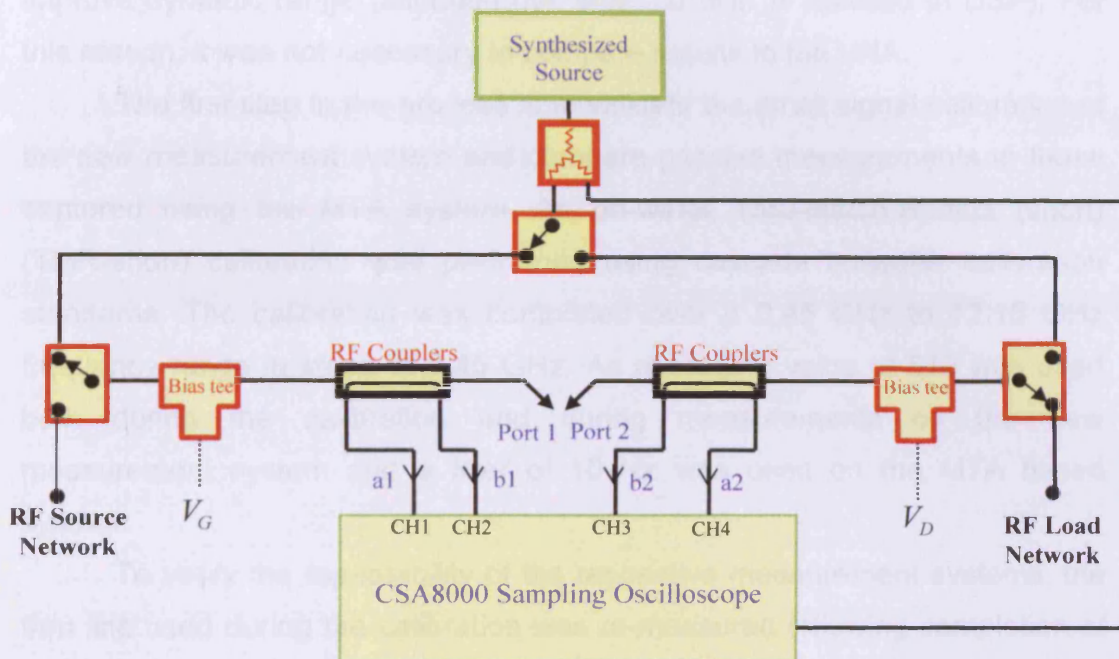


Figure 3.1 Measurement Set-up Employed For CW Measurement Verification

3.2.1 Small Signal Validation

The ability to measure s-parameters is fundamental to the successful operation of the measurement system. During calibration, s-parameter measurements are used to determine the error coefficients, and so any inaccuracies in the measured s-parameters will lead to inaccuracies in the error coefficients determined, in turn effecting the quality of large signal waveform measurements. For this reason, the first step in the validation of the new measurement system is to compare the ability of the new measurement system to measure s-parameters referenced to an established MTA based system.

The most widely used instrument for the measurement of s-parameters is the VNA, which allows very accurate measurement of s-parameter data due

to the swept, narrow-band nature of the instrument. A narrow-band tuneable filter is employed at the receiver to limit the receiver bandwidth, hence limiting noise and increasing the dynamic range. The MTA used in these comparisons however has a fully functional VNA mode, which is employed when the instrument measures s-parameters. It also employs a narrow-band filter to improve dynamic range (although this time the filter is realised in DSP). For this reason, it was not necessary to compare results to the VNA.

The first step in the process is to validate the small signal calibration of the new measurement system and compare passive measurements to those captured using the MTA system. An on-wafer Thru-Match-Reflect (short) (TMR-short) calibration was performed using cascade on-wafer calibration standards. The calibration was completed over a 0.45 GHz to 12.15 GHz frequency range in steps of 0.45 GHz. An averaging value of 512 was used both during the calibration and during measurements on the new measurement system and a filter of 10 Hz was used on the MTA based system.

To verify the repeatability of the respective measurement systems, the thru line used during the calibration was re-measured following completion of the calibration. The resulting plots showing magnitude of all 4 measured s-parameters are presented in figure 3.2(a) for the new measurement system, and in 3.2(b) for the MTA based system.

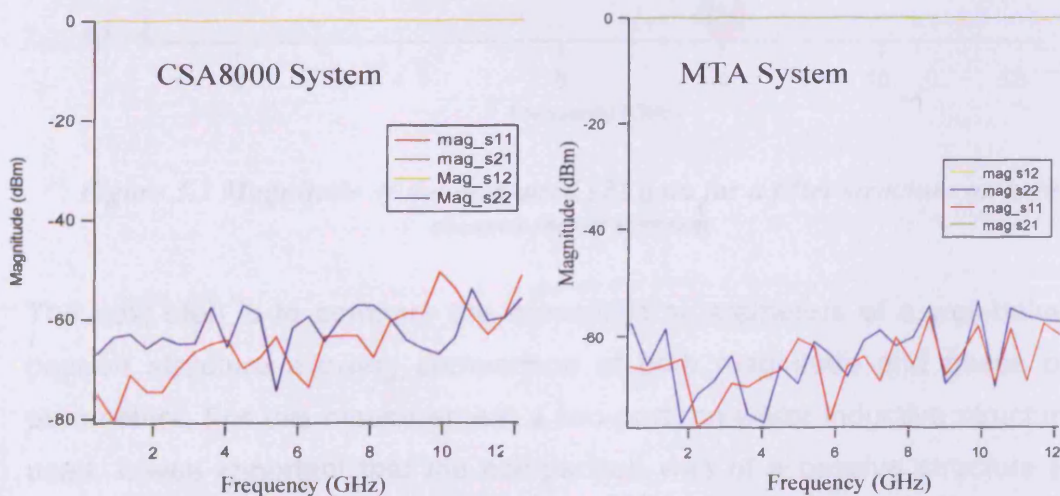


Figure 3.2(a) magnitude of the measured s-parameter data for a Thru-line using new measurement system and (b) for the MTA Based System

The plots indicate good repeatability in measurements in both cases, with the new measurement system showing a dynamic range of around 55 dB across the 12 GHz bandwidth, compared to a dynamic range of around 60 dB across the bandwidth for the MTA based system. The dynamic range achieved by the new measurement system is impressive considering that the MTA is a narrow band receiver when in s-parameter mode, while the new measurement system always operates over the full 12 GHz bandwidth. Some care should however be taken in interpretation of these results as the thru-line formed part of the calibration. Thus in order to fully validate the calibrations, a passive filter structure was measured on both measurement systems, the measured s-parameters are shown in figure 3.3. The plot shows the excellent agreement in measured s_{21} , across 12 GHz bandwidth, over a dynamic range of around 60 dB.

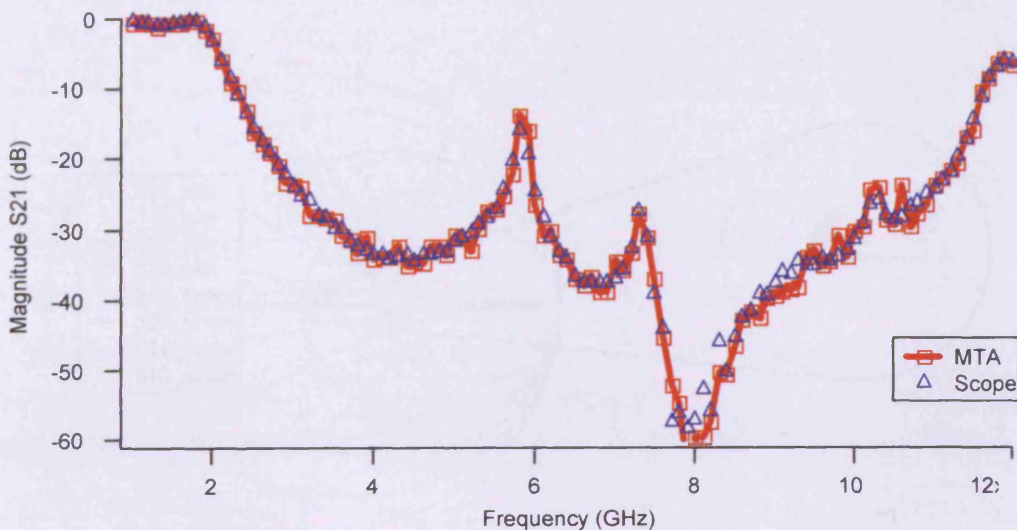


Figure 3.3 Magnitude of the measured s_{21} data for a filter structure on both measurement systems

The next step is to compare the measured s-parameters of a well-behaved passive structure allowing comparison of both magnitude and phase of s-parameters. For this measurement a two-port, on-wafer inductive structure is used. It was important that the comparison was of a passive structure as it avoided any differences that could be introduced due to bias, temperature or impedance environment, as would be the case for an active device. The

measured s-parameters of the inductive structure for both systems are shown in figures 3.4(a) and (b) and on the Smith chart in figure 3.5.

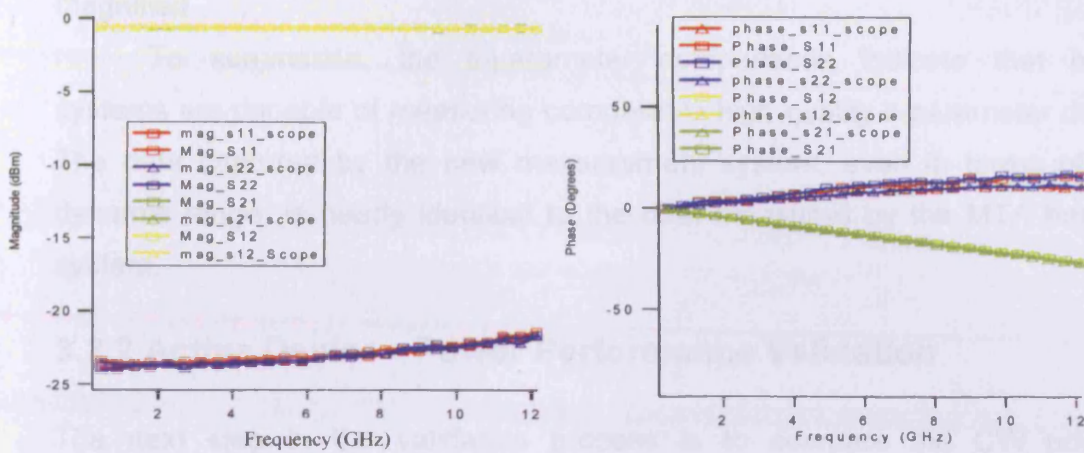


Figure 3.4(a) magnitude of the measured s-parameters for the passive structure, (b) Phase information for both measurement systems

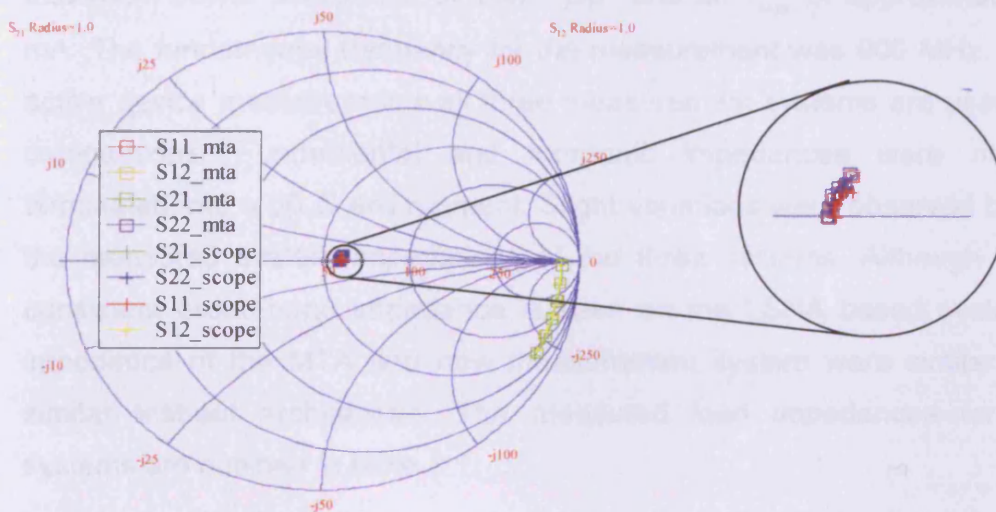


Figure 3.5 Measured s-parameter data for the passive structure shown on the Smith chart

The plots show excellent agreement in the measured s-parameters. The only visible difference can be seen in the phase of s11 and s22 when we compare between systems, but it is thought that this difference is caused by the probe positions being slightly different between measurements. This is likely to be the case as we see the phase difference between the two systems increase linearly with frequency as seen in figure 3.4(b), indicating that the structure

has a different length in each case. This small difference is put into perspective when the Smith chart shown in figure 3.5 is analysed, as the magnitude of s_{11} and s_{22} are very small any difference in the phase is greatly magnified.

To summarise, the s-parameter comparisons indicate that both systems are capable of measuring comparable high quality s-parameter data. The data captured by the new measurement system, even in terms of its dynamic range, is nearly identical to the data measured by the MTA based system.

3.2.2 Active Device - Power Performance Validation

The next step in the validation process is to compare the CW power performance of an active device using the different measurement systems. The device used for comparisons was an on-wafer $240 \mu\text{m}^2$ HBT, with a maximum power dissipation of $1 \text{ mW} / \mu\text{m}^2$ and an I_{Max} of approximately 120 mA. The fundamental frequency for the measurement was 900 MHz. For the active device measurements all three measurement systems are used in the comparisons. Fundamental and harmonic impedances were nominally terminated into a 50Ω environment. Slight variations were observed between the measured system impedances of the three systems. Although a more consistent broad-band impedance is seen on the LSNA based system, the impedance of the MTA and new measurement system were similar due to similar test-set architecture. The measured load impedances for the 3 systems are outlined in table 3.1.

Harmonic	CSA8000		MTA		LSNA	
	Real (Ω)	Imag (Ω)	Real (Ω)	Imag (Ω)	Real (Ω)	Imag (Ω)
F0	50,15	-4,58	50,82	-4,64	49,57	3,69
2f0	52,24	2,17	53,14	-0,45	47,78	4,49
3f0	40,62	-4,69	41,37	2,79	49,25	1,2
4f0	43,01	-6,42	46,45	3,48	50,59	-0,42
5f0	40,91	-4,33	63,85	0,15	50,57	-1,92

Table 3.1 – Comparison of Load impedances measured on the three systems

Great care was taken to ensure a constant impedance environment was maintained at the device input, on all systems and for all measurements. In order to achieve this, the same physical input structure was shipped to all locations along with the devices. This comprised an isolator and 6 dB attenuator, and was effective in standardizing the impedance environment, removing unwanted source harmonics, as well as improving stability.

The first set of power sweeps were conducted with the device biased in class A-B, with a base (V_b) of 1.28 V and a collector voltage (V_c) of 6V. The measured data for the 3 systems is shown in figure 3.6, which shows (a) the output power versus input power and (b) the measured gain profile of the device versus input power.

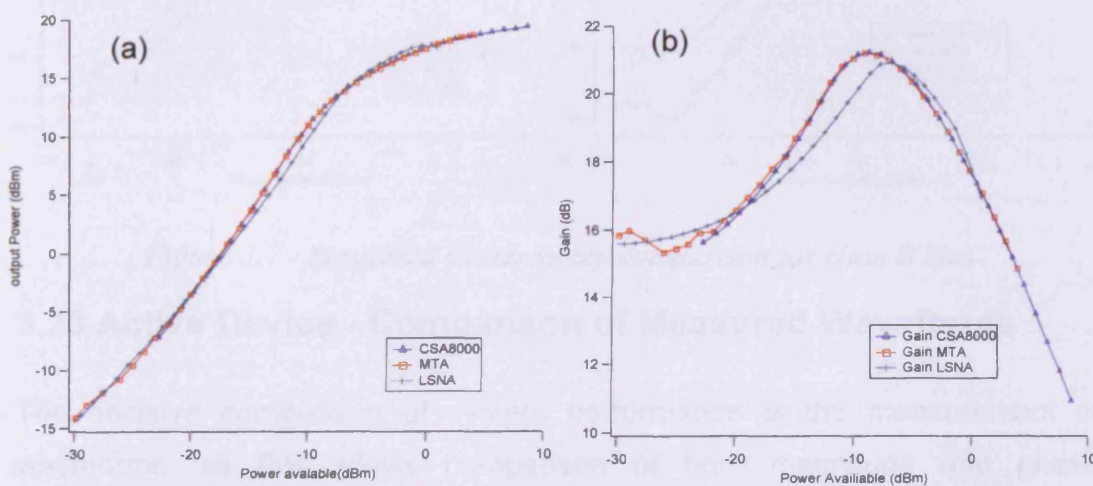


Figure 3.6 - Measured Power Sweep and Gain Comparison for Class A-B Bias

The plots show excellent agreement in the captured power performance between the new CSA8000 based measurement system and the established MTA based system, with some small differences observed between the data collected using the LSNA. These observed differences are directly attributed to the difference in impedance environment for this system. It should be noted that the LSNA based system actually offers a more broad-band 50 Ω impedance environment as it does not contain structures required for load pull such as circulators and triplexers, which add additional discontinuities.

Figure 3.7 shows the power performance in a class B bias with $V_b=1.2$ V and $V_c=6$ V. Again the MTA and CSA8000 based systems show excellent agreement over the entire 50 dB range of output power, with the LSNA based system showing the largest differences. Again it is believed that this results from the difference in impedance environment between this system and the others, with the harmonics being more important in this case.

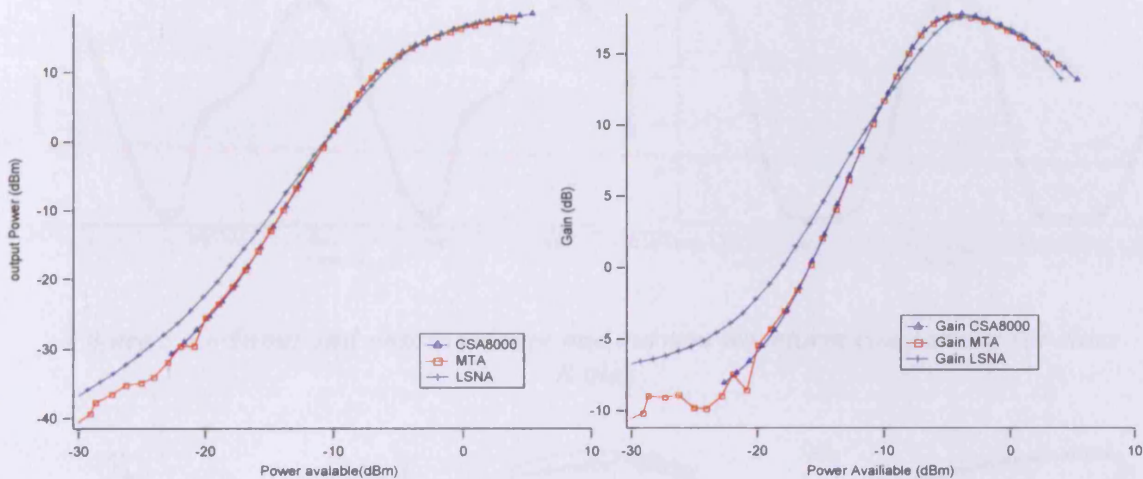


Figure 3.7 - Measured Power sweep comparison for class B bias

3.23 Active Device - Comparison of Measured Waveforms

The decisive comparison of system performance is the measurement of waveforms, as this allows comparison of both magnitude and phase information. The same HBT device as described earlier was used for these comparisons. The measurements were again made at a fundamental frequency of 0.9GHz, with the device biased in class A-B. Measurements were conducted at three different power levels, increasing the drive level each time, thus increasing harmonic content in the waveforms. Only the highest drive levels are presented here. No load-pull was employed during the measurements, although again the same physical input network was used on all measurement systems. Figure 3.8 shows the current and voltage waveforms at the input and output of the device. Differences in load impedance were outlined in table 3.1 earlier in this chapter. Figure 3.9 shows the current transfer characteristic, input characteristic and the dynamic RF load-lines for the three systems.

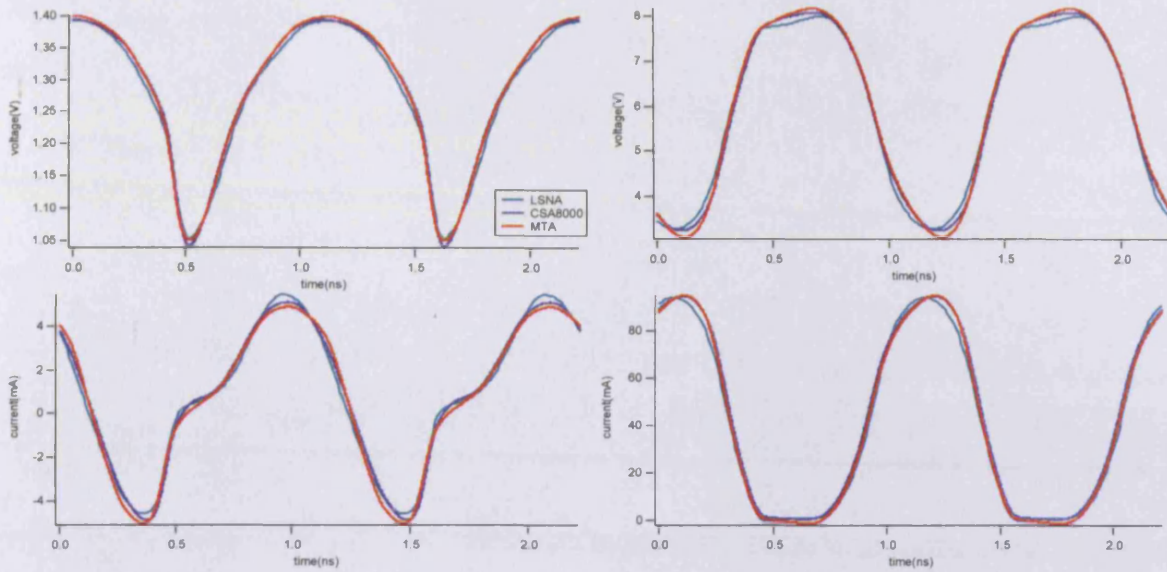


Figure 3.8 – Input and output voltage and current waveform comparison for class B bias

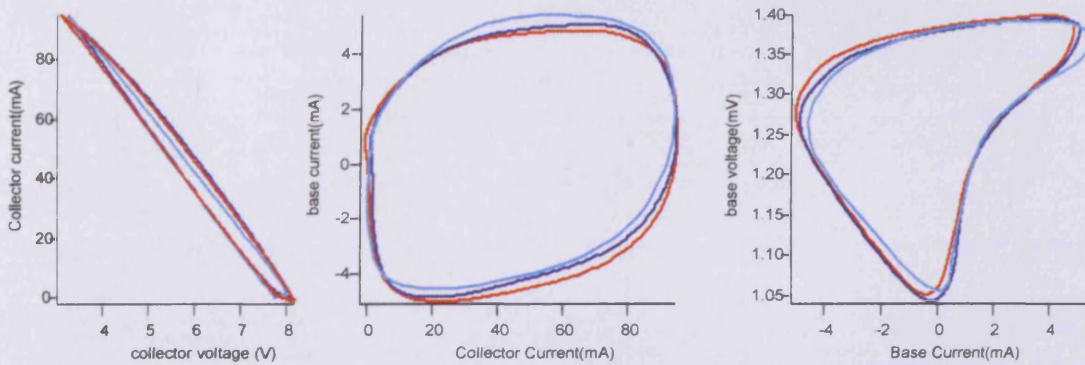


Figure 3.9 – a) Dynamic load line, b) current transfer characteristic, c) current transfer characteristic

The agreement shown in the current and voltage waveforms at this power level is impressive as they contain significant harmonic content. The benefit of using a data set where a device is driven into compression is that as the waveforms become increasingly harmonically rich, the visual effect of small inaccuracies in measured current and voltage become increasingly obvious, allowing for easier visual comparison. These plots indicate excellent agreement between the MTA and CSA8000 based architectures, and even the LSNA based system shows very good agreement. The origin of the

difference between the LSNA and the other systems is variation in output impedance seen by the device. Note that it is the output voltage waveform that exhibits the most significant difference. The current transfer characteristic, input characteristic and the dynamic RF load-lines for the three systems also confirm the agreement between the measurement systems, with only small differences observed in the characteristics measured by the LSNA.

The spectral information can also be extracted from the measured waveforms, enabling direct comparison of the measured magnitude and phase information. This is a useful step as it highlights for example the case where a system compares well in measured magnitude, but not in phase. The measured magnitude and phase components of the carrier and first 4 harmonics are shown in figure 3.10, again for the highest drive level.

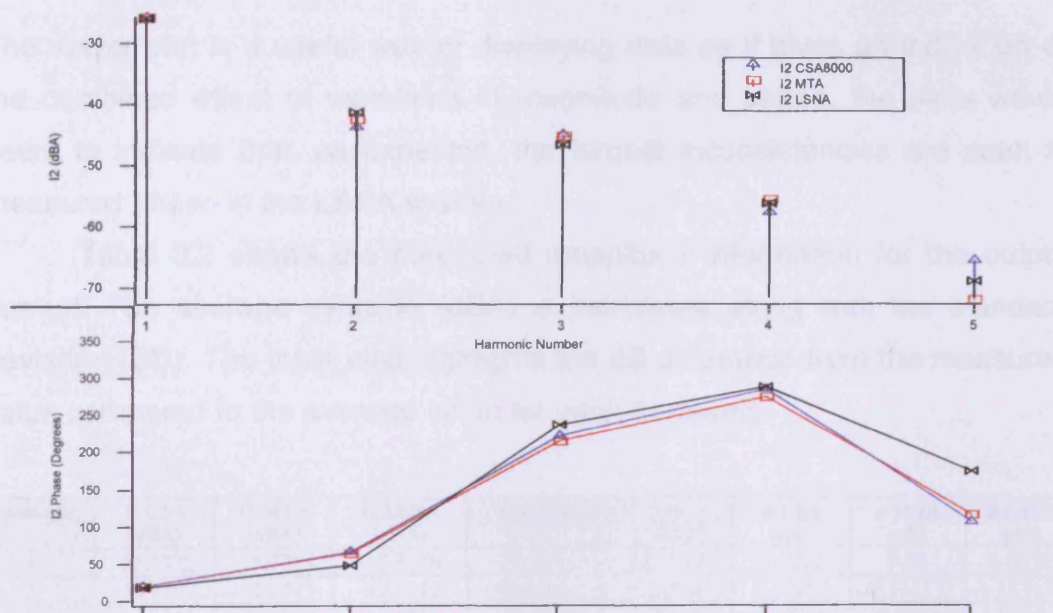


Figure 3.10 – Magnitude and Phase Information of I_2

The plot shows that a good agreement is achieved between all measurement systems although it is a little difficult to determine absolute error when magnitude and phase are plotted separately. This issue is resolved by plotting the vector information in figure 3.11. The vector analysis is limited to the fundamental and first 2 harmonics to avoid crowding the vector plot.

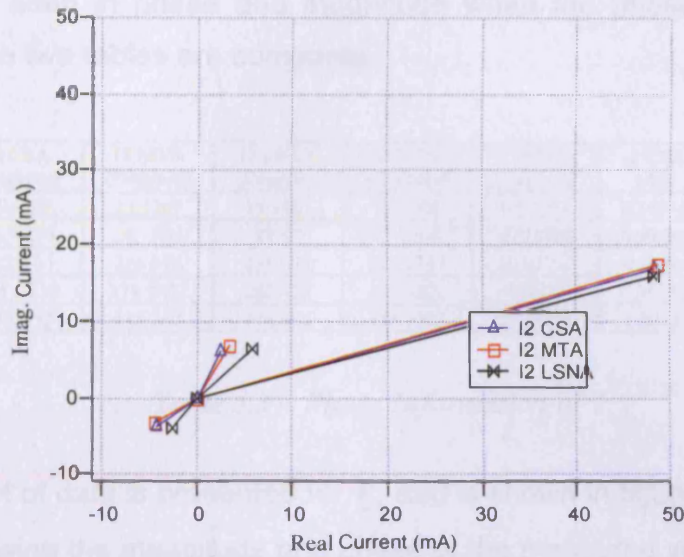


Figure 3.11 – Vector comparison of I_2 for Third power level

The vector plot is a useful way of displaying data as it gives an indication of the combined effect of variations in magnitude and phase, the plots would seem to indicate that, as expected, the largest inconsistencies are seen in measured phase in the LSNA system.

Table 3.2 shows the measured magnitude information for the output current. The average value in (dBA) is calculated along with the standard deviation (SD). The table also highlights the dB difference from the measured value compared to the average value for each harmonic.

Harmonic	I2 CSA (dBA)	I2 MTA (dBA)	I2 LSNA (dBA)	I2 AVG (dBA)	S.D (dBA)	Δ CSA (dB)	Δ MTA (dB)	Δ LSNA (dB)
1	-25.7922	-25.7254	-25.8686	-25.7954	0.07165	0.0032	0.07	0.0732
2	-43.7272	-42.2775	-41.2212	-42.40863	1.25814	1.31857	0.13113	1.187433
3	-44.9311	-45.2345	-46.5888	-45.5848	0.88262	0.6537	0.3503	1.004
4	-57.7577	-55.5682	-56.1908	-56.5056	1.12818	1.25213	0.93737	0.31477
5	-65.5570	-72.0232	-69.1144	-68.8982	3.23852	3.3412	3.125	0.2162

Table 3.2 – Magnitude Information of I_2

The table indicates very good agreement between systems at the fundamental, which degrades slightly when we analyse the harmonics. It is important to remember that for the harmonics, the magnitudes become significantly smaller, resulting in larger percentage errors. A similar table presented for phase (Table 3.3) again shows good agreement with similar

differences seen in phase and magnitude when the phase is converted to dB's and the two tables are compared.

Harmonic	I2 CSA (Degrees)	I2 MTA (Degrees)	I2 LSNA (Degrees)	I2 AVG (Degrees)	S.D (Degrees)	Δ CSA (dB)	Δ MTA (dB)	Δ LSNA (dB)
1	19.483	19.7267	18.1827	19.1308	0.83007	0.15845	0.26643	-0.44150
2	66.9684	64.1908	47.99	59.7164	10.24988	0.99553	0.62758	-1.89886
3	222.763	216.076	236.697	225.1787	10.52060	-0.09368	-0.35841	0.43331
4	284.8316	274.9082	288.450	282.7300	7.01131	0.06433	-0.24368	0.17398
5	106.795	115.332	173.662	131.9297	36.39246	-1.83583	-1.16785	2.38725

Table 3.3 – Phase Information of I_2

A similar set of data is presented for V_2 and is shown in figure 3.12 and 3.13.

Tables showing the magnitude and phase of the measured voltage are also presented in table 3.4 and 3.5, respectively.

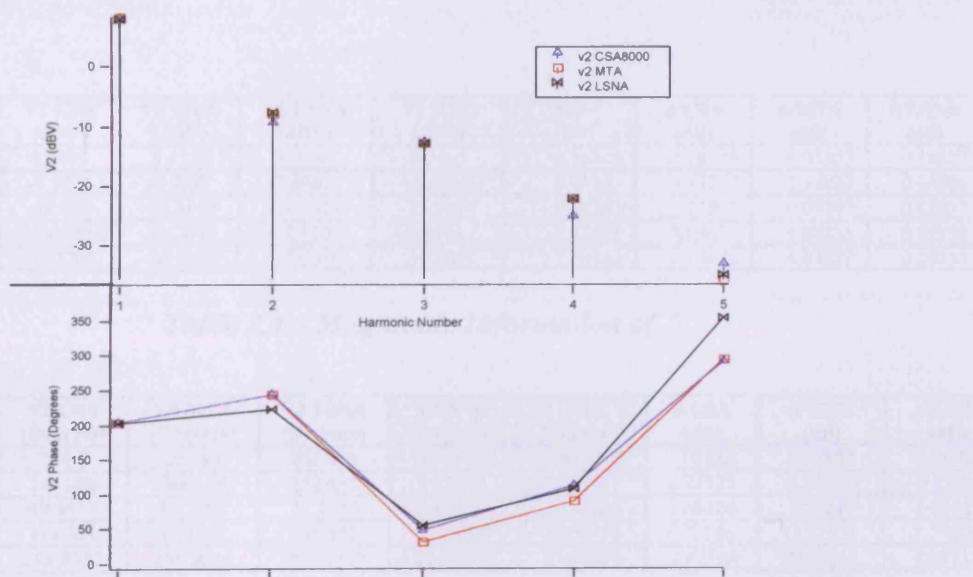


Figure 3.12 – Magnitude and Phase spectral Information of V_2

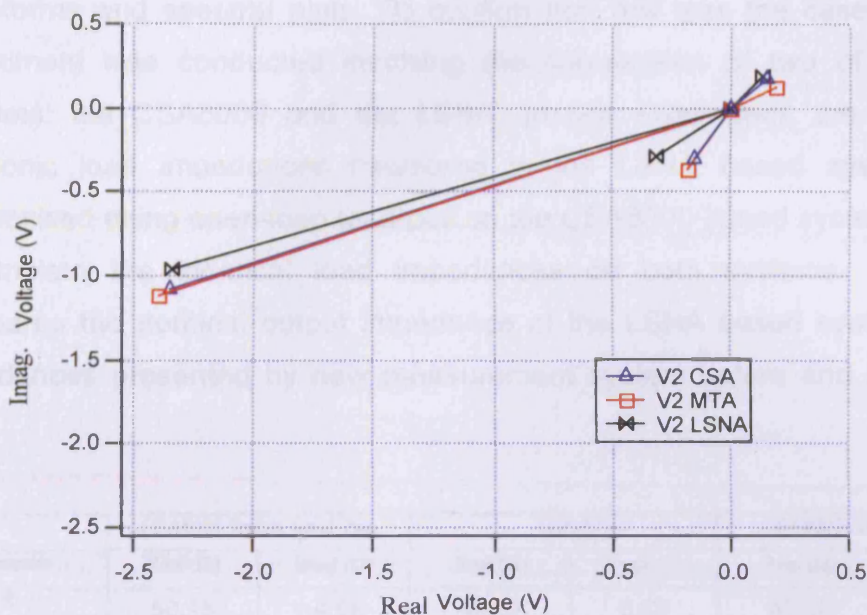


Figure 3.13 – Vector comparison of V_2

Harmonic	V2 CSA (dBV)	V2 MTA (dBV)	V2 LSNA (dBV)	V2 AVG (dBV)	S.D (dBV)	Δ CSA (dB)	Δ MTA (dB)	Δ LSNA (dB)
1	8.2499	8.4321	8.0586	8.2469	0.15248	0.18523	0.00303	0.18827
2	-9.3601	-7.7691	-7.59611	-8.2418	0.79393	0.47267	1.11833	0.64566
3	-12.698	-12.8813	-12.7321	-12.7705	0.07962	0.11083	0.07247	0.03837
4	-24.990	-22.2049	-22.1101	-23.1017	1.33581	0.89677	1.88833	0.99157
5	-33.2708	-35.9197	-35.0386	-34.7431	1.10145	1.17673	1.47227	0.29553

Table 3.4 – Magnitude Information of V_2

Harmonic	V2 CSA (Degrees)	V2 MTA (Degrees)	V2 LSNA (Degrees)	V2 AVG (Degrees)	S.D (Degrees)	Δ CSA (dB)	Δ MTA (dB)	Δ LSNA (dB)
1	204.7	204.94	202.426	204.022	1.387376	0.02882	0.03899	-0.10721
2	244.586	244.676	222.632	237.298	12.70121	0.26275	0.26595	-0.82008
3	49.3533	32.2203	55.3176	45.6304	11.99026	0.68124	3.02249	4.69467
4	113.328	90.6292	108.885	104.2807	12.02948	0.72266	-1.21872	1.59400
5	292.8322	295.2015	355.61829	314.5506	35.58533	-0.62144	-0.55144	1.61731

Table 3.5 – Phase Information of V_2

As was the case for current comparisons, similar comparisons of voltage are presented, with excellent agreement between the MTA and CSA8000 based architectures. Again, small variations are seen, particularly in measured phase between the LSNA and other systems. As outlined earlier in this chapter, small variations in impedance environments between the systems are considered to be the root cause of the differences observed in the measured

waveforms and spectral plots. To confirm that this was the case, a further experiment was conducted involving the comparison of two of the three systems: the CSA8000 and the LSNA. In this experiment, the first three harmonic load impedances measured in the LSNA based system were synthesised using open-loop load-pull on the CSA8000 based system in order to emulate the identical load impedances on both systems. Table 3.6 compares the nominal output impedance of the LSNA based system to the impedances presented by new measurement system before and after load-pull.

Harmonic	CSA8000 Before Load-Pull		LSNA		CSA8000 After Load-Pull	
	Real (Ω)	Imag (Ω)	Real (Ω)	Imag (Ω)	Real (Ω)	Imag (Ω)
f_0	50,15	-4,58	49,57	3,69	49.56	3.66
$2f_0$	52,24	2,17	47,78	4,49	47.95	4.31
$3f_0$	40,62	-4,69	49,25	1,2	49.45	1.30
$4f_0$	43,01	-6,42	50,59	-0,42	48.59	0.69
$5f_0$	40,91	-4,33	50,57	-1,92	50.98	2.00

Table 3.6 – Comparison of Load impedances measured on the LSNA system and CSA8000 System Before and After Load-Pull

Figure 3.14 shows the output voltage and figure 3.15 the output current waveform compared to those captured by the LSNA, before and after load-pull.

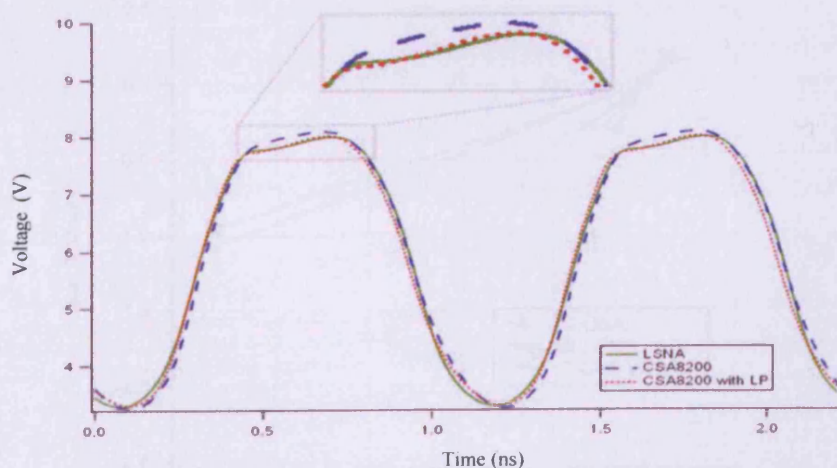


Figure 3.14 – Comparison of Output Voltage Waveform Before and after Load-pull

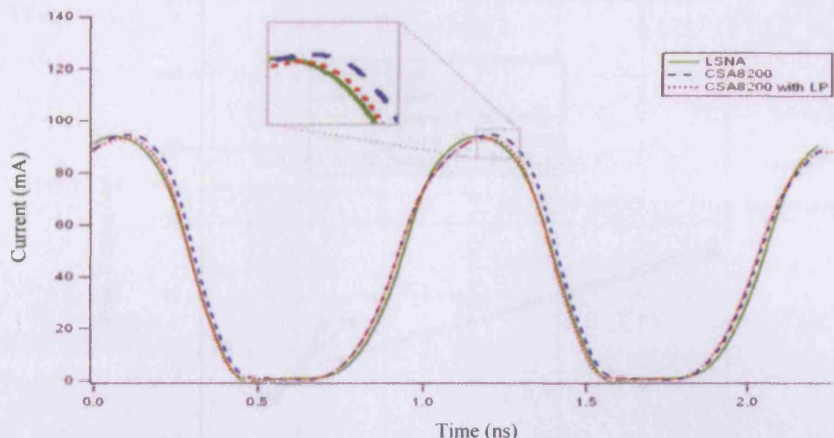


Figure 3.15 – Comparison of Output Current Waveform Before and after Load-pull

The waveforms indicate that provided the output impedances between systems are aligned, excellent agreement can be obtained between the two completely different measurement architectures, thus highlighting the importance of having identical system impedance environments for any direct comparison of waveforms. This approach is considered to be more applicable than the previously suggested approach of using a reference device, which must be accompanied with an accurate, large-signal model [6].

The final step was to compare the vectoral information before and after load-pull of the CSA based systems. Vector plots of the output voltage and current are shown in figure 3.16 and 3.17, respectively.

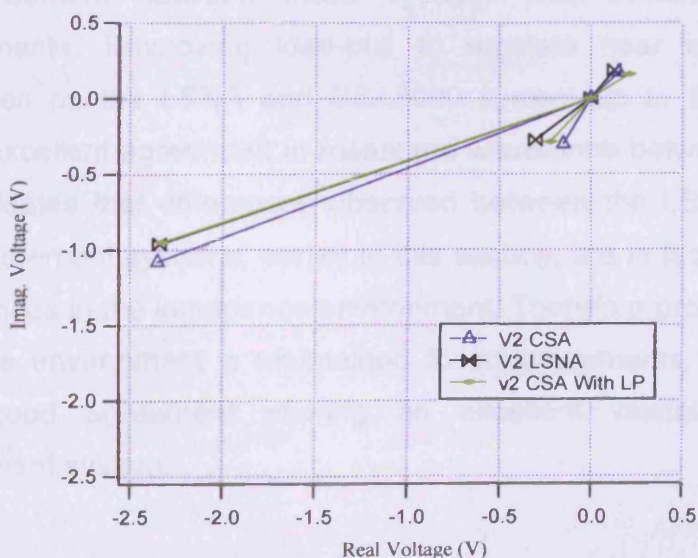


Figure 3.16 – Comparison of Vectoral information of the Output Voltage Before and after Load-pull

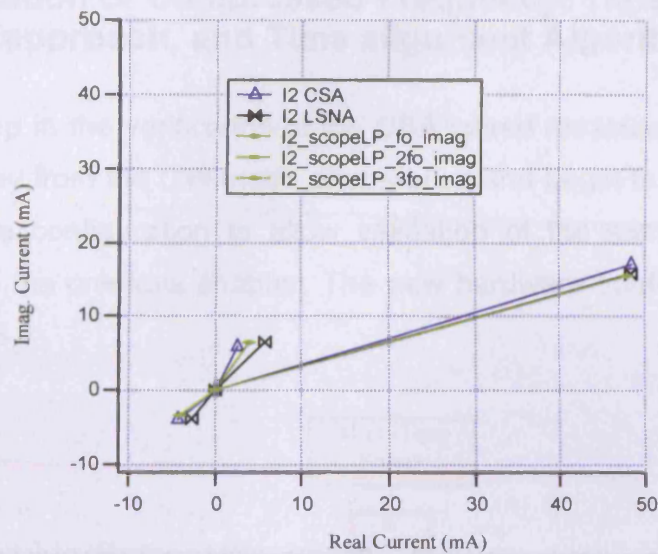


Figure 3.17 – Comparison of Vectorial information of the Output Current Before and after Load-pull

It is clear from these plots that the load-pull corrects the original differences seen in the captured vector information from the two systems. The effect of the load-pull is particularly noticeable in the case of the fundamental signal component where, following load-pull, excellent agreement is observed in both voltage and current.

To summarise, results in this section show that as similar nominal impedance environments were observed for the MTA and CSA 8000 systems, good agreement between these systems was evident throughout the measurements. Employing load-pull to emulate near identical harmonic impedances on the LSNA and CSA8000 system up to the third harmonic leads to excellent agreement in measured waveforms between systems. This result indicates that differences observed between the LSNA and the other two measurement systems, earlier in this section, are in fact primarily caused by differences in the impedance environment. Therefore provided a consistent impedance environment is maintained for measurements, all three systems are in good agreement offering an excellent validation of the new measurement system.

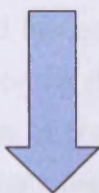
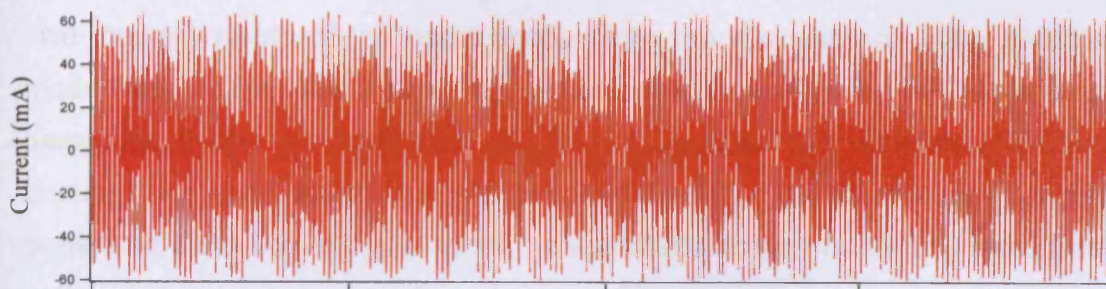
fine grid of 'permitted' tone-spacing values, and finally the post-processing time-alignment required to allow averaging of the measured data.

3.3.1 Validation of the Time Interleave Sampling

The first step in the validation of the multi-tone sampling approaches is to verify the correct operation of the time interleaved sampling approach. As described in the previous chapter, time interleaved sampling involves capturing points out of order, over a number of modulation cycles. The collected time-points can then be rearranged to recreate the measured waveform. This approach is employed together with the folded frequency sampling approach, also outlined in the previous chapter, which allows the efficient capture of multi-tone waveforms without the need to collect a large number of empty spectral bins. As explained in the previous chapter, this approach unfortunately means that the on-board averaging of the sampling oscilloscope cannot be employed as there is no consistent time reference between successive waveform collections. However, as the sampling oscilloscope has a maximum of 4000 measurement time points available, it is often possible to sample a number of modulated cycles on the screen at any one time to enable some FFT averaging to occur in a single capture. This at least goes some way to solve the time taken to download data, required to enable averaging in the software.

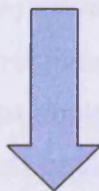
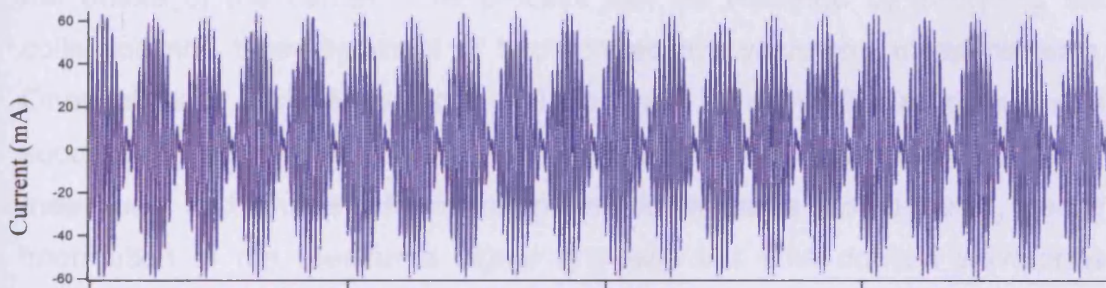
Figure 3.19 shows the waveform collection process using measured data. The first (red) trace is the time-interleaved signal captured by the sampling oscilloscope, the second (blue) trace shows the waveform after the time-interleave has been mathematically removed. Finally the third (black) waveform shows the result after the spectral locations have been re-arranged to allow the FFT averaging. It is this waveform that is then vector corrected using the error coefficients from the calibration. These plots indicate that it is possible to successfully remove the time-interleave, and shows that the capture of multiple modulation cycles can be used to perform some FFT averaging during the waveform capture.

Interleaved as collected by sampling oscilloscope



**Unwind
Time
Interleave**

Signal is now un-wound but still contains multiple modulation cycles



**FFT
Averaging**

The result after re-locating spectral grid is one 'averaged' cycle of modulation

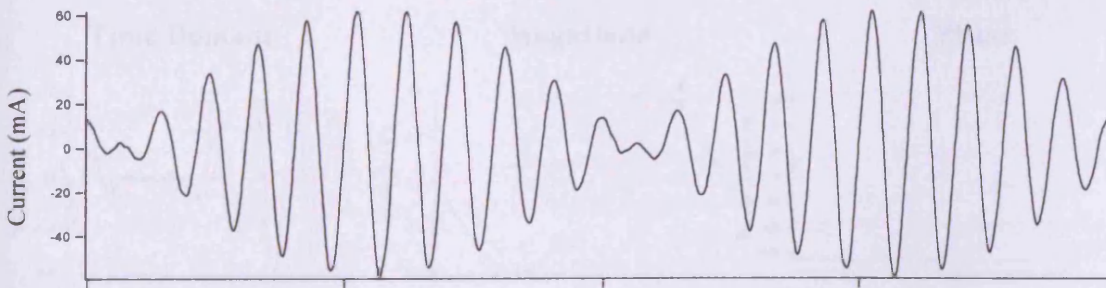


Figure 3.19 – Unwinding the time interleaved signal and FFT averaging to give the desired outcome of one modulation cycle

3.32 Validation of the Software waveform Alignment

The memory depth of the oscilloscope limits the approach of using multiple modulation cycles on the sampling oscilloscope to perform the FFT averaging discussed in the previous section. This is because the user must always ensure there are enough points in each modulation cycle to capture all of the generated distortion terms to avoid the spectral leakage and folding discussed in the application issues section of the previous chapter.

The full averaging solution, described in detail in the previous chapter, is to average data in software, after collection by the sampling oscilloscope, where all collected data is aligned to the first 'reference' data-set. As discussed in chapter 2, this is a two-stage process; first the delay of the envelope is calculated and corrected, then a second stage correction is applied to align the phase of the carrier. This process can be validated by analysing the collection and time-alignment of two consecutive waveform measurements. Once aligned, various methods will be used to show the alignment was successful, which will include the analysis in the envelope domain of magnitude and phase information of the fundamental components, vector information of the measured signal and also the time domain waveforms themselves. Figure 3.20 shows the two consecutive waveform measurements of a three-tone signal, along with the magnitude and phase of the fundamental envelope with the reference waveform shown in red and the next waveform collection shown in black. It is clear that both the envelope and the RF itself is misaligned.

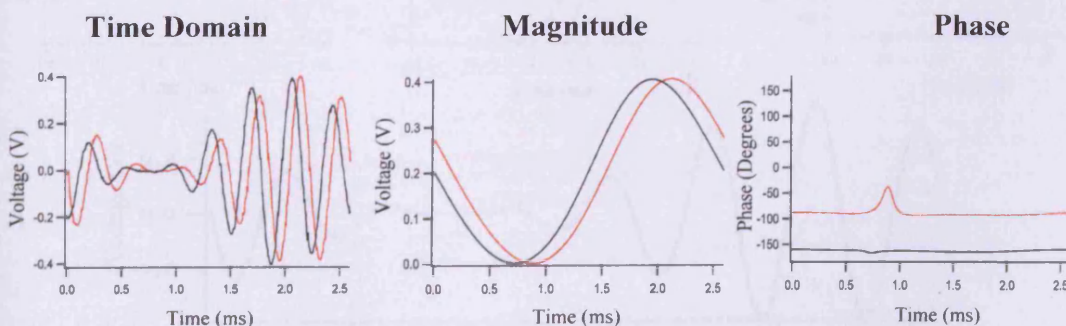


Figure 3.20 – Two consecutive waveforms captured by the system, shown in time-domain and magnitude and phase in envelope domain

The first step is to calculate a value for the time-shift between the two waveforms using the phase difference in the envelopes. Applying this correction results in the new corrected waveform shown in blue, in figure 3.21. It can be seen that although the envelopes of the original and corrected waveforms are now aligned, however there is also a phase component that still has an offset. This relates to the phase difference at RF, which can also be seen in the measured time domain waveforms.

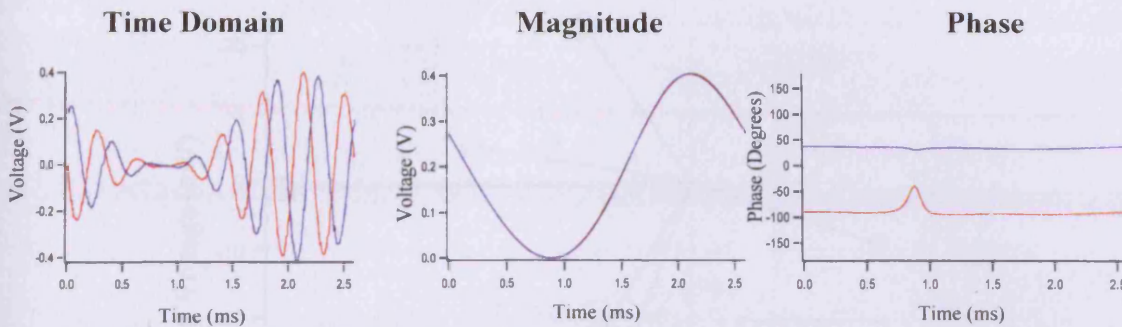


Figure 3.21 – Comparison of reference waveform and waveforms after initial correction process

The final correction involves calculating the phase difference at RF. Again this is used to calculate the required time-shift to align the signals. The fully corrected, 'aligned' waveform is shown in figure 3.22. This is compared back to the reference waveform, where a zoomed view of the time domain comparison is also included.

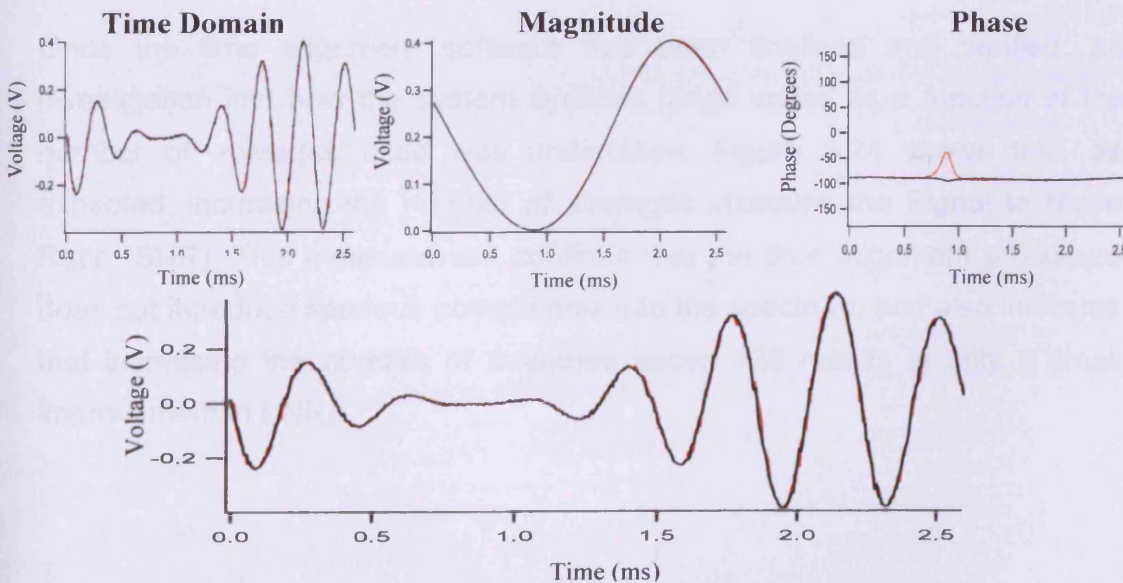


Figure 3.22 – Comparison of reference waveforms and waveforms after full correction process

After the final correction has occurred, it is clear that the alignment process has been successful. The envelope domain magnitude and phase are now in perfect alignment, as are the time domain waveforms. Successful alignment is further confirmed when we look at the vectors of three-tones for the original, new and corrected signals shown in figure 3.23. This time alignment process therefore means that multiple waveforms can be collected and averaging can be simply performed on the time domain waveforms in the standard way.

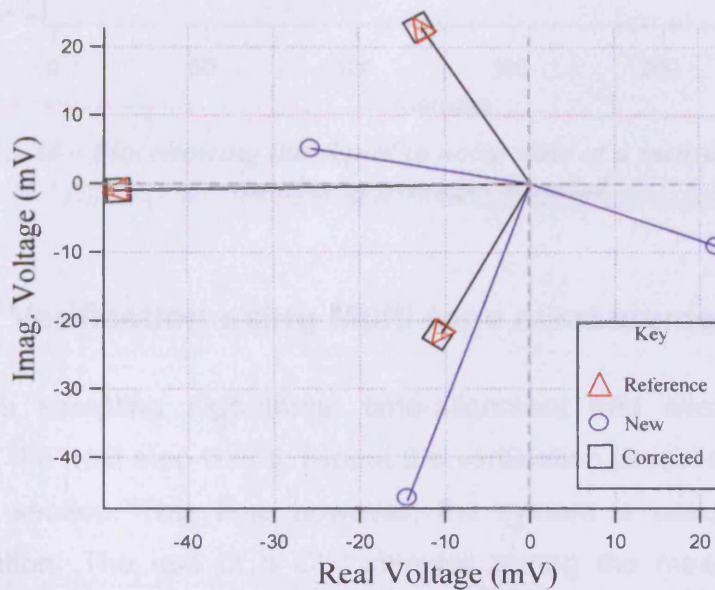


Figure 3.23 – Comparison of Three-tone vectors of reference waveform, new waveform and waveform after full correction process

Once the time alignment software had been finalised and verified, an investigation into how the system dynamic range varied as a function of the number of averages used was undertaken. Figure 3.24 shows that, as expected, increasing the number of averages improves the Signal to Noise Ratio (SNR). This measurement confirms that the time alignment procedure does not introduce spurious components into the spectrum, and also indicates that increasing the number of averages above 128 results in only a small improvement in SNR.

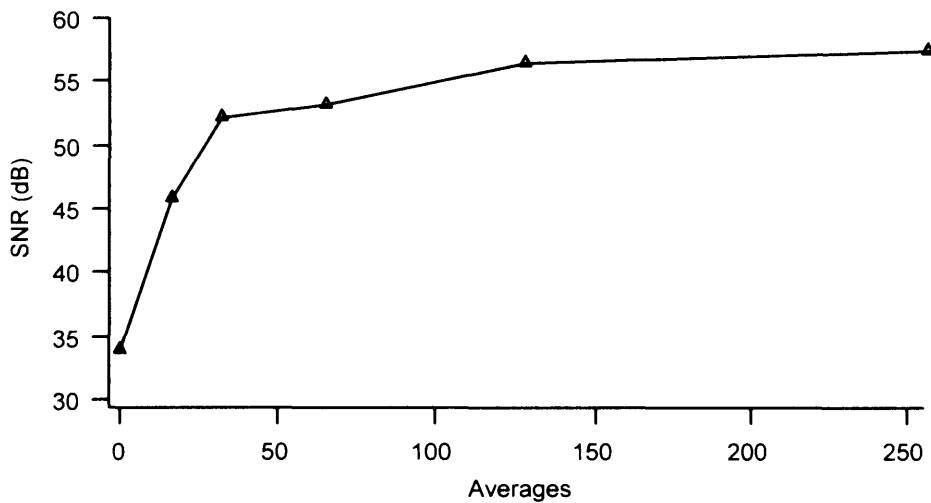


Figure 3.24 – Plot showing the signal to noise ratio of a measured signal as the number of averages is varied

3.4 CW Verification using Multi-tone measurement set-up

Once the sampling algorithms, time-alignment and averaging had been checked, the next step was to repeat the verification process, presented in the previous section. This time however, the system is used in its multi-tone configuration. The use of a CW stimulus during the measurements allows comparison back to previous measurements. This approach will still, by definition, validate the multi-tone configuration.

As described in the previous chapter, when the multi-tone mode of operation is employed, the sampling oscilloscope is setup to capture a single cycle of modulation. Due to the compressed frequency approach, the 'envelope time-domain' waveform captured will not be a true representation of the measured signal. Although it will have the correct envelope shape, there will be a reduced number of RF cycles. To conduct the CW experiment, the system can be established as if it were to be used to collect a 3-tone signal. The two sidebands can then be suppressed to leave only the carrier. Clearly, as we are only sampling a CW signal, the 'tone-spacing' and 'order' are completely arbitrary and were set to 1 MHz and 10 respectively. This meant that the carrier would now lie at location 22 in the captured folded frequency domain spectrum. Figure 3.25 shows collected input and output, voltage and current 'envelope time-domain' waveforms, which contain 22 cycles of the

captured CW waveforms. The black trace then shows one extracted cycle of RF. This is achieved by moving the carrier and the harmonic spectral components to the appropriate locations in the spectrum.

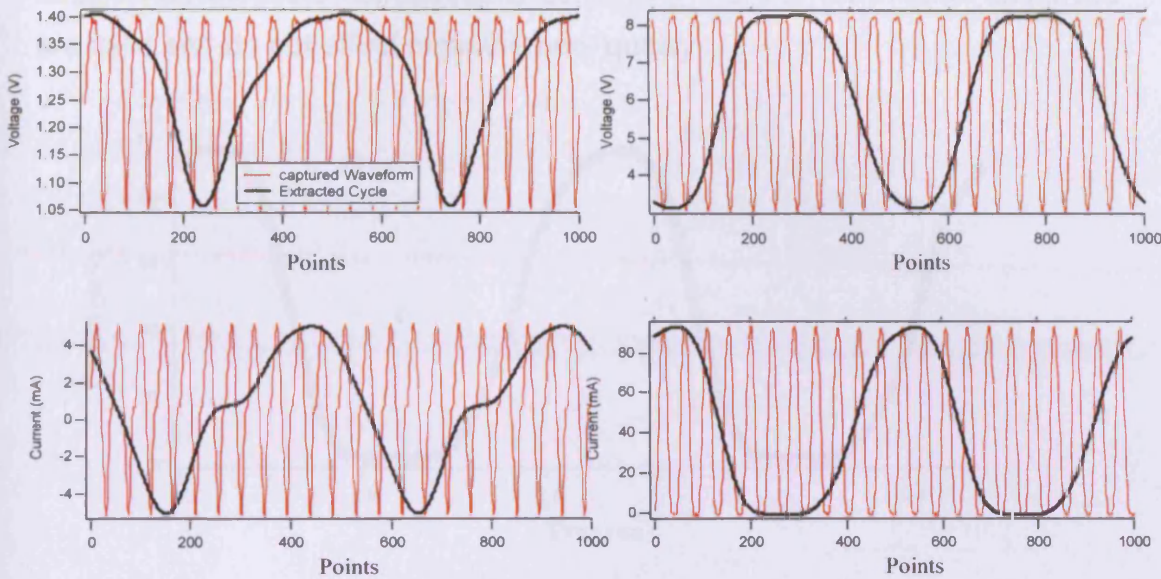


Figure 3.25 –CW Waveforms captured using the multi-tone configuration along with an extracted Single Cycle

Once it had been demonstrated that CW waveforms could easily be extracted from the data collected using the multi-tone system configuration, the CW comparison of the HBT measurements demonstrated earlier in the chapter were repeated. In this section, the waveforms captured by the CSA8000 in its CW configuration are used as the reference. An identical measurement procedure was repeated, this time using the multi-tone hardware and software configurations.

Excellent agreement was seen between waveforms captured using the CW architecture and those captured using the multi-tone architecture, although load-pull was again required in order to maintain a consistent load impedance between measurements. Figure 3.26 a) and 3.26 b) show the output voltage and current respectively for the class A-B bias condition ($V_b=1.28V$, $V_c=6V$). The waveforms before and after load-pull give a further indication of the importance of standardisation of system impedance before comparing waveforms. The results indicate that the various sampling approaches

employed do not have any detrimental effect on the ability of the system to measure high quality, vector corrected magnitude and phase information. The waveforms captured using the new sampling approach have also been referenced back to the measurements from two completely different, well established measurement systems confirming that the techniques employed are valid and do not effect measurement quality.

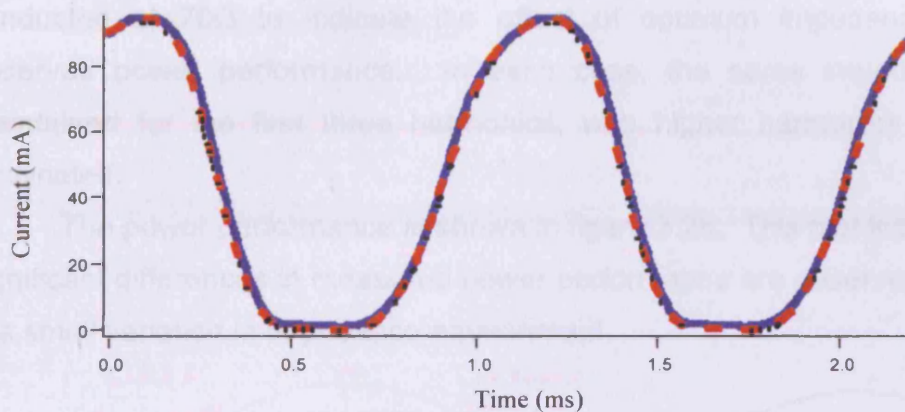


Figure 3.26 – a) Output Current captured using the multi-tone system with and without Load-pull, compared to waveforms captured using the CW configuration

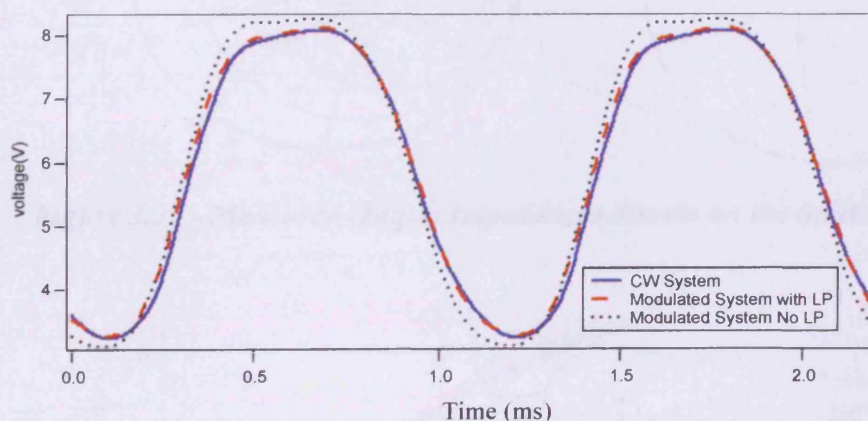


Figure 3.26 – b) Output Voltage captured using the multi-tone system with and without Load-pull, compared to waveforms captured using the CW configuration

3.5 System impedance sensitivity analysis

As the impedance clearly plays an important role in the system comparison measurements outlined above, a further investigation was undertaken to

quantify the effect of small differences in nominal system impedance on measured power performance and waveforms. The power performance of the same HBT device used in the previous investigations was measured for 6 different output impedances, with harmonic active load-pull. All impedances (fundamental and harmonics up to the third harmonic) were swept together around a 5Ω circle, centred at 50Ω . The impedances at the measured points are shown on the Smith chart in figure 3.27. A final measurement was conducted at 70Ω to indicate the effect of optimum impedance on the observed power performance. In each case, the same impedance was maintained for the first three harmonics, with higher harmonics nominally terminated.

The power performance is shown in figure 3.28. This plot indicates that significant differences in measured power performance are observed, even for this small variation in impedance environment.

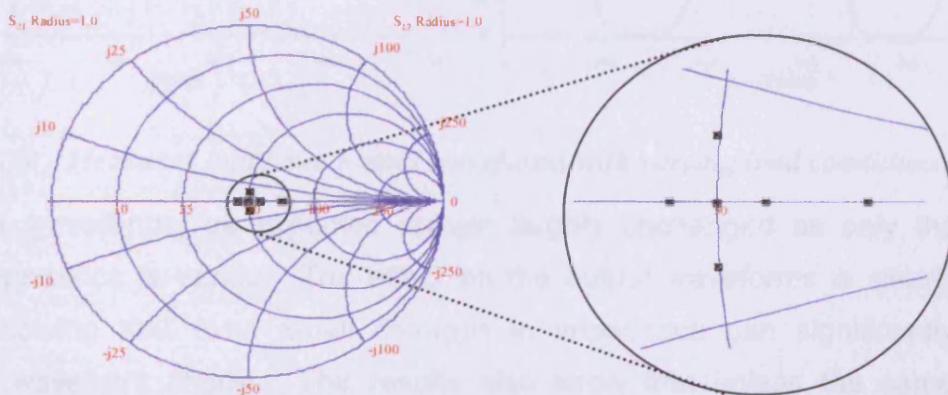


Figure 3.27 - Measured Output Impedances Shown on the Smith Chart

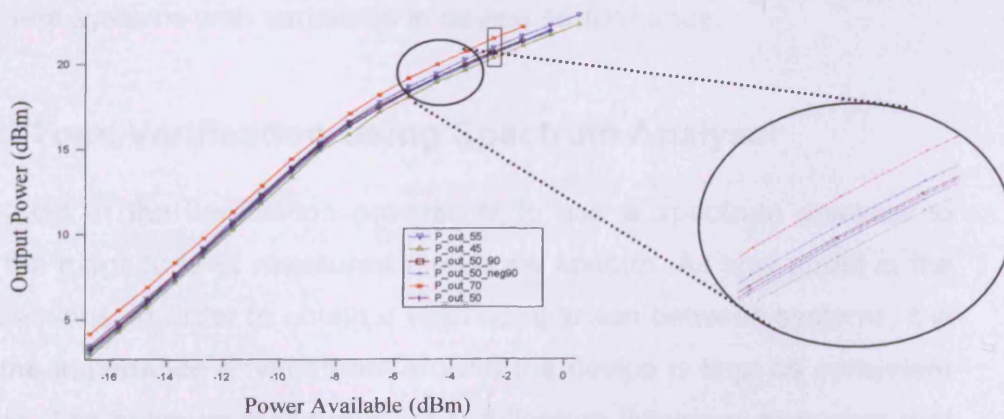


Figure 3.28 - Measured Power sweep with varying load conditions

The same data-set was used to show the effect of the differences in measured waveforms. To achieve this, the 1dB compression point was chosen as a reference case. Waveforms are shown for the 45, 50 and 55 Ω impedances and the input and output waveforms are shown in figure 3.29.

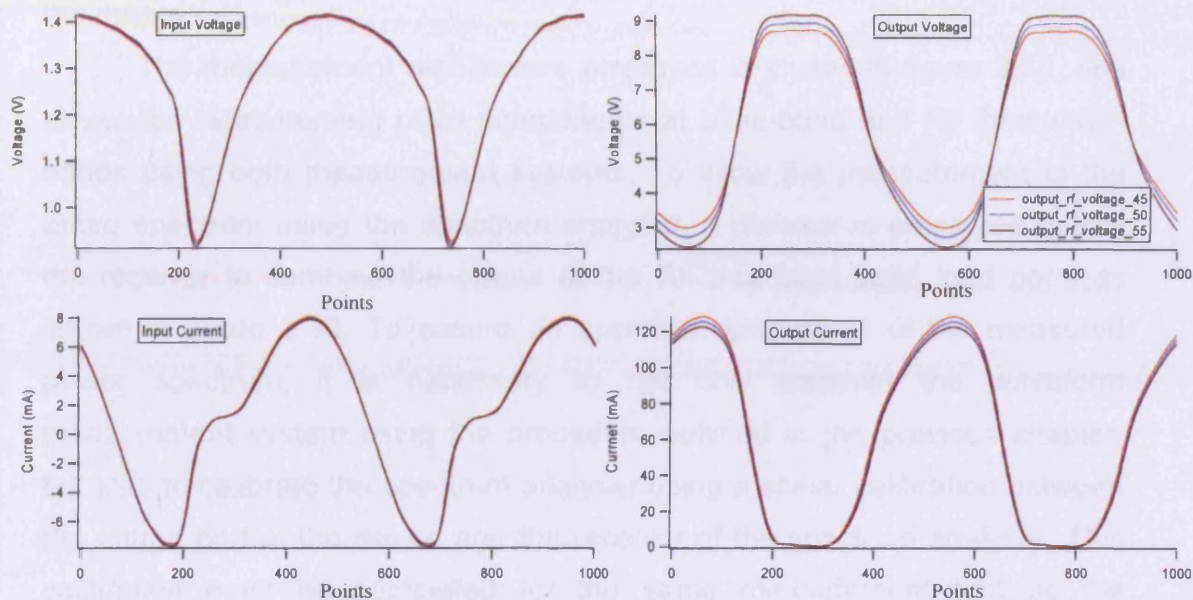


Figure 3.29 - Measured input and output waveforms with varying load conditions

The input waveforms, as expected remain largely unchanged as only the output impedance is varied. The effect on the output waveforms is clearly visible, showing that even small changes in impedance can significantly influence waveform shape. The results also show that unless the same fundamental and harmonic impedance are maintained, it would be easy to confuse the effects of very small differences in system impedance between measurement systems with variations in device performance.

3.6 Multi-Tone Verification Using Spectrum Analyser

The next step in the verification process is to use a spectrum analyser to compare the magnitude of measured multi-tone spectra. As was noted in the previous sections, in order to obtain a valid comparison between systems, it is vital that the impedance environment around the device is kept as consistent as possible. The optimum measurement architecture therefore, to ensure that a constant impedance environment is maintained when comparing the two

measurements, is to incorporate the spectrum analyser directly into the new multi-tone waveform measurement system. This allows comparisons to be made when the device is operating into identical input and output impedance conditions, as the spectrum analyser provides the load impedance seen by the device.

The measurement architecture employed is shown in figure 3.30. and allows for measurement of all components at base-band and RF frequency-bands using both measurement systems. To allow the measurement of the entire spectrum using the spectrum analyser, a diplexer is employed before the receiver to combine the output of the RF and base-band load ports as shown in figure 3.30. To ensure an accurate comparison of the measured power spectrum, it is necessary to not only calibrate the waveform measurement system using the procedure outlined in the previous chapter, but also to calibrate the spectrum analyser using a scalar calibration between the output port of the device and the receiver of the spectrum analyser. This calibration must be completed for the same measurement grid as the waveform measurement system to include correction for all base-band and RF frequency components. To do this, a VNA was used at the end of the cable connecting the spectrum analyser to look back into the system. With a short-circuit calibration standard at the probe tip, s_{11} was measured across the spectrum. This value of s_{11} provided a value of the two way loss between the spectrum analyser and probe tip, therefore dividing this loss by 2 gave the loss between probe-tip and spectrum analyser. Using this approach it was possible to generate a frequency grid with corresponding scalar correction factors.

It was found that a full one-port calibration was not required as the approach using a single calibration standard yielded an almost identical value for the loss. Therefore following the above calibration step, all RF and base-band components could be fully corrected in magnitude, thus base-band fundamental band and harmonic band frequencies measured by the two systems could be directly compared.

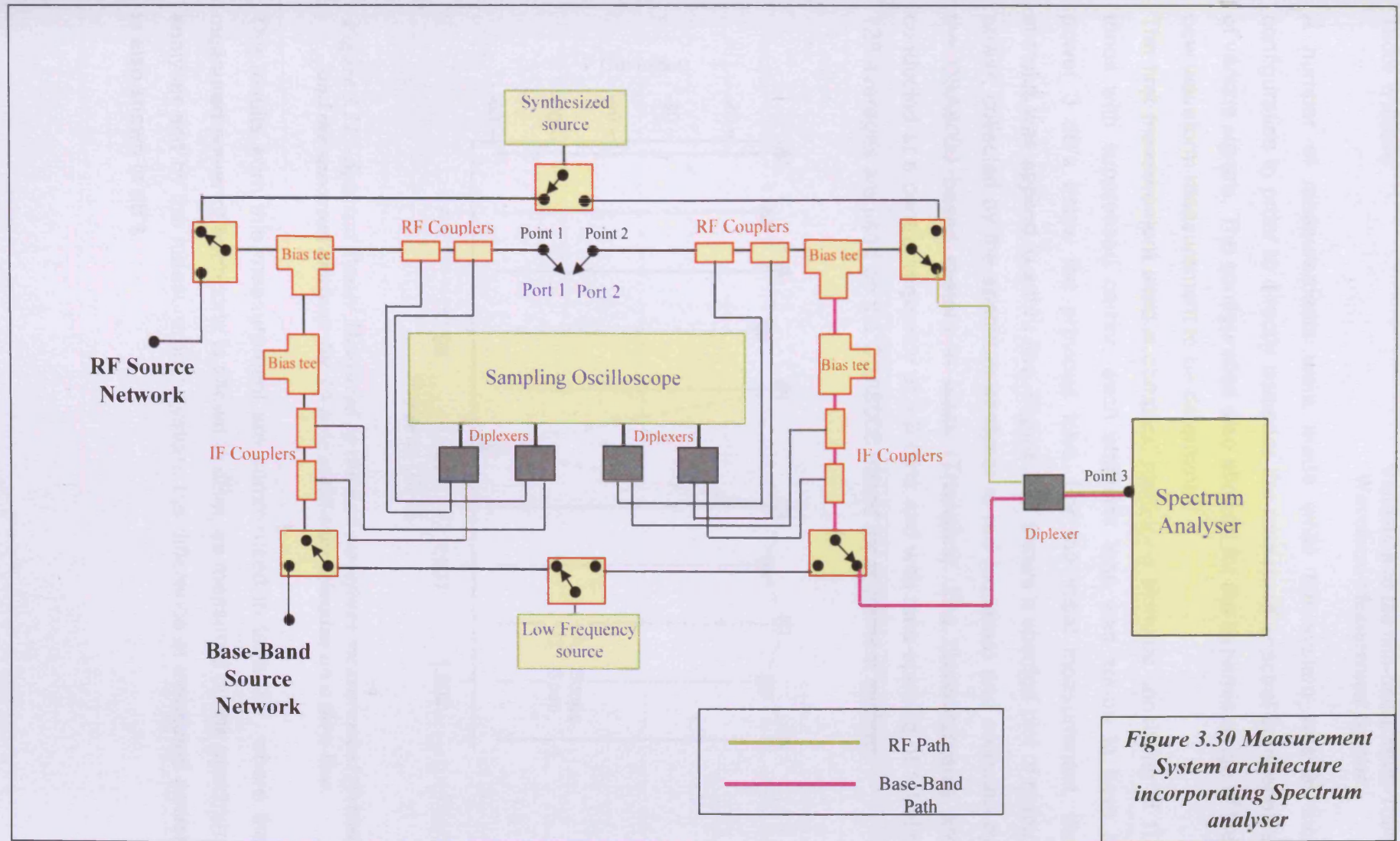


Figure 3.30 Measurement System architecture incorporating Spectrum analyser

A number of measurements were made while the system was in this configuration in order to directly compare the measured spectral components of various signals. The configuration also allowed for the dynamic range of the new waveform measurement to be determined.

The first measurement used a complex, multi-tone stimulus consisting of 10 tones with suppressed carrier, each alternate tone was set-up to have a power 3 dB's below the previous tone. For the initial measurement, the stimulus was applied to a thru line. Figure 3.31 shows a spectral plot of output power, collected by the spectrum analyser in red (squares) and collected by the CSA8000 based system in black (Triangles). The measurements are conducted at a centre frequency of 1.8 GHz and with tone-spacing of 1 MHz, 128 averages are used on the CSA8000 based measurement system.

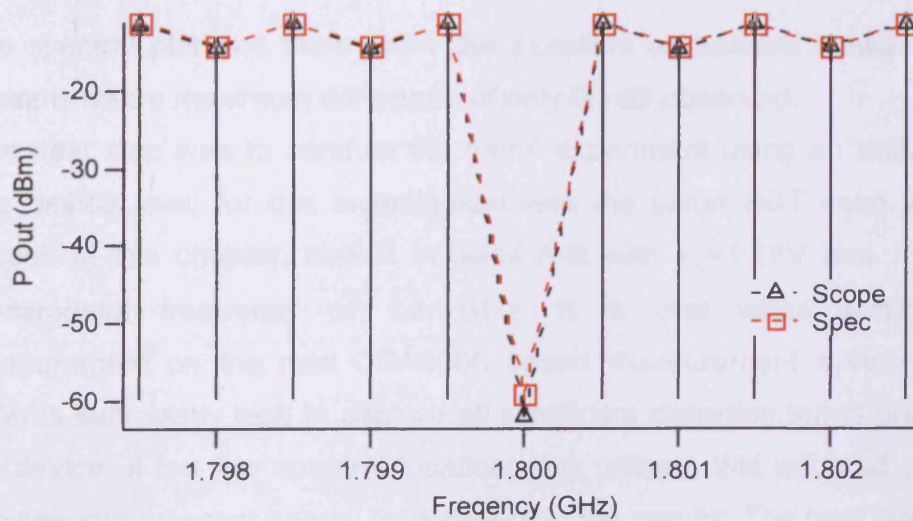


Figure 3.31 – Spectral Power Measured by the new waveform measurement system and the spectrum analyser for 10-tone multi-tone stimulus on a thru line

The results from this measurement are summarised in table 3.7, where the measured power of each tone is shown in dBm, as measured by the spectrum analyser and by the measurement system; the difference in measured power is also shown in dB's.

Tone	Power Spectrum Analyser (dBm)	Power Sampling Scope (dBm)	Delta Power (dB)
-1	-11.3919	-11.381	0.0109
-2	-14.3922	-14.353	0.0392
-3	-11.3290	-11.343	-0.0140
-4	-14.3262	-14.322	0.0420
-5	-11.2519	-11.278	-0.0261
1	-11.2425	-11.267	-0.0245
2	-14.2819	-14.311	0.0627
3	-11.2483	-11.310	-0.0617
4	-14.2243	-14.328	-0.1037
5	-11.2153	-11.319	-0.1038

Table 3.7 – Measured power from spectrum analyser and sampling oscilloscope for 10-tone signal

The spectral plot and table show the excellent agreement between the two systems with a maximum difference of only 0.1dB observed.

The next step was to conduct the same experiment using an active device. The device used for this investigation was the same HBT used in the first section of this chapter, biased in class A-B with $V_b=1.28V$ and $V_c=6V$ at a fundamental frequency of 1.8 GHz. It is vital when setting-up the measurement on the new CSA8000 based measurement system, that the order is sufficiently high to capture all significant distortion terms produced by the device. If too few spectral locations are utilised, this will lead to spectral leakage into adjacent bands, thus distorting the results. The best way to avoid this is to gradually increase the order until there are a number of spectral locations between each band that reach the noise floor, whilst driving the device at maximum power. In this case, an order of 20 was used.

The measured spectrum at the base-band, fundamental-band and harmonic bands (up to the third harmonic) are shown in figures 3.32-3.35 below. Direct comparisons are made between spectrum analyser and those captured with the new measurement system. The measured signal had components ranging in power between 20 and -40 dBm.

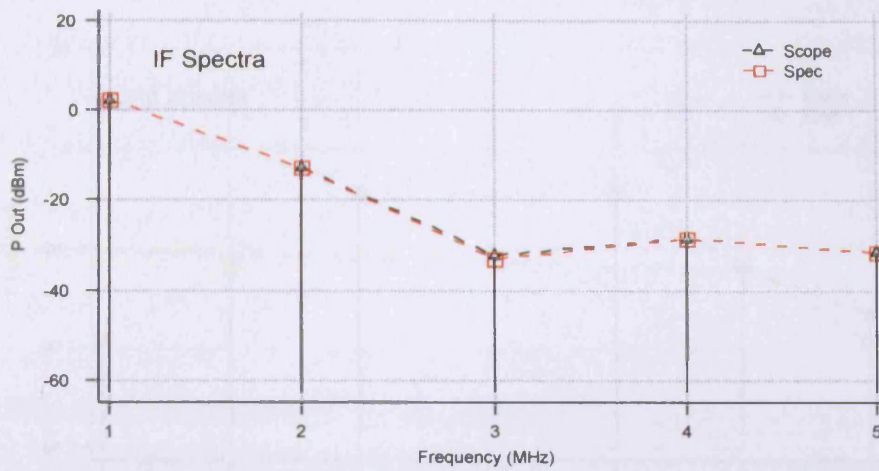


Figure 3.32 – Comparison of Spectral Power in the IF-band

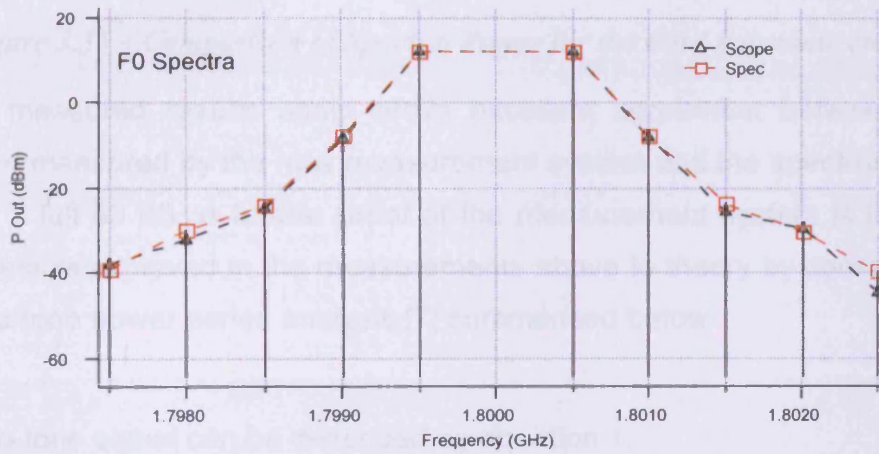


Figure 3.33 – Comparison of Spectral Power for the fundamental components

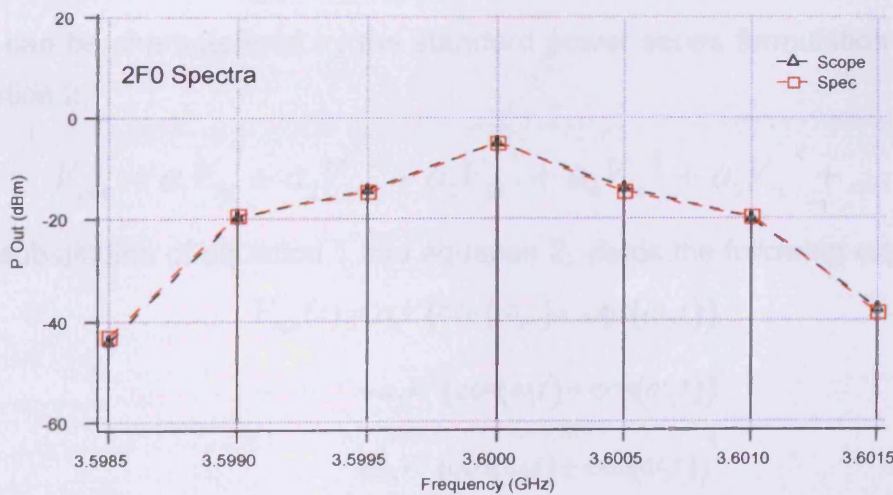


Figure 3.34 – Comparison of Spectral Power for the second harmonic components

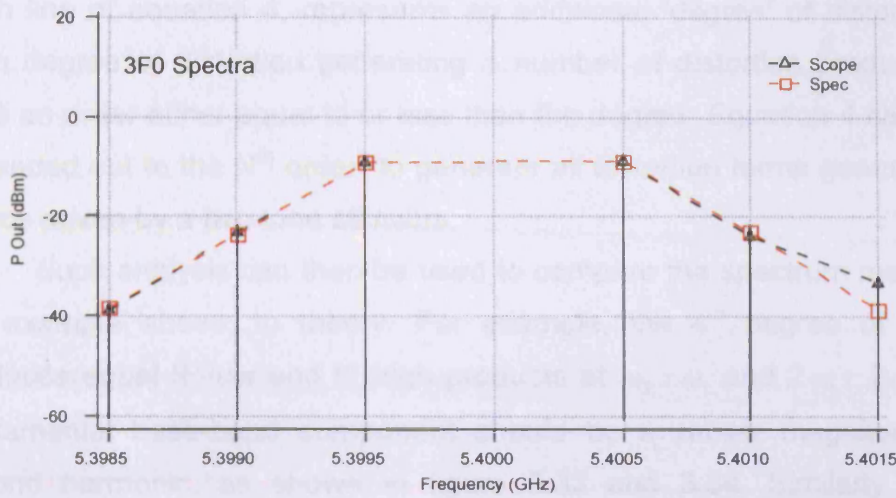


Figure 3.35 – Comparison of Spectral Power for the third harmonic components

The measured results again prove excellent agreement between spectral power measured by the new measurement system and the spectrum analyser over a full 60 dB. A further proof of the measurement system is to compare the results achieved in the measurements above to theory by consideration of a two-tone power series analysis [7] summarised below.

A two-tone signal can be described by equation 1.

$$V_{in}(t) = V \cos(\omega_1 t) + V \cos(\omega_2 t) \tag{1}$$

This can be characterised by the standard power series formulation shown in equation 2.

$$V_{out} = a_1 V_{in} + a_2 V_{in}^2 + a_3 V_{in}^3 + a_4 V_{in}^4 + a_5 V_{in}^5 + \dots \tag{2}$$

The substitution of equation 1 into equation 2, yields the following expansion.

$$\begin{aligned} V_{out}(t) = & a_1 V (\cos(\omega_1 t) + \cos(\omega_2 t)) \tag{3} \\ & + a_2 V^2 (\cos(\omega_1 t) + \cos(\omega_2 t))^2 \\ & + a_3 V^3 (\cos(\omega_1 t) + \cos(\omega_2 t))^3 \\ & + a_4 V^4 (\cos(\omega_1 t) + \cos(\omega_2 t))^4 \\ & + a_5 V^5 (\cos(\omega_1 t) + \cos(\omega_2 t))^5 \\ & + \dots \end{aligned}$$

Each line of equation 4, represents an additional 'degree' of distortion, with each degree of distortion generating a number of distortion products which have an order either equal to or less than the degree. Equation 4 can thus be expanded out to the N^{th} order, to generate all distortion terms generated by a device driven by a two tone stimulus.

Such analysis can then be used to compare the spectrum measured in the example above, to theory. For example, the 4th degree of distortion produces equal IF-low and IF-high products at $\omega_2 \pm \omega_1$ and $2\omega_1 + 2\omega_2$, so the fundamental base-band component should be a similar magnitude to the second harmonic, as shown in figure 3.32 and 3.34. Similarly 3rd order distortion produces equal magnitude components in-band around the fundamental at $2\omega_1 - \omega_2$ and $2\omega_2 - \omega_1$ termed IM3 low and high respectively. Analysis of figure 3.33 confirms as expected that these components have the same magnitude. Thus an analysis against theory offers further confidence in the performance of the system.

The measured output time domain current waveform that was used to generate the spectral plots above is shown in figure 3.36(a), whilst figure 3.36(b) shows the current generated by the base-band components.

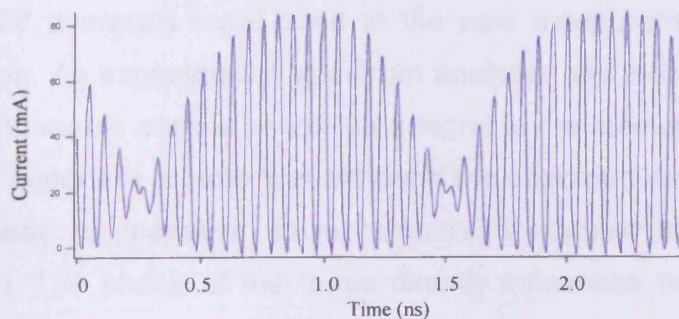


Figure 3.36(a) – Time domain Output Current and voltage waveforms captured by the new waveform measurement system

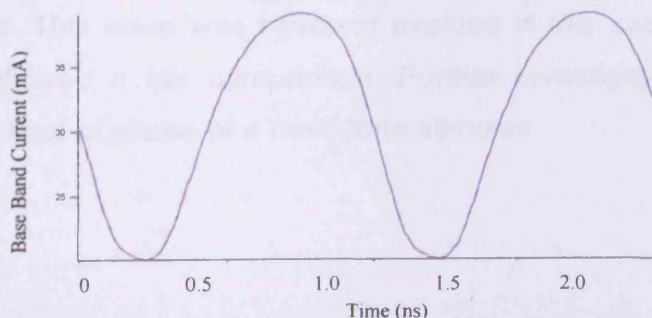


Figure 3.36(b) – Time domain base-band output Current and voltage waveforms captured by the new waveform measurement system

These measured waveforms themselves offer a further validation of the measurement system. Firstly, the class A-B operation of the amplifier is confirmed, the output current clearly pinches off at 0 mA, and the upper portion of the current waveform is more rounded. This offers some evidence that the phase relationship between fundamental and harmonic components have been correctly measured. Evidence of phase coherence between base-band and RF components can be seen when we isolate the base-band components and compare these back to the modulated 'envelope', where it can clearly be seen that the base-band and modulated 'envelope' are in-phase, as expected.

The final experiment in this section compares the measurement of the power sweep from a device driven with a two-tone signal. The two-tones and the IM3 products were measured by the two systems. A plot showing measured power in the lower tone and lower IM3 product versus input drive is shown in figure 3.37(a) with the power in the upper tone and upper IM3 product is shown in figure 3.37(b). The aim of this experiment was to give further indication of the agreement between the systems and most importantly to give an indication of the dynamic range of the new multi-tone measurement system. 128 averages were used in the new measurement system for the investigation. As expected the spectrum analyser has a larger dynamic range due to the tuneable narrow band filter integral to the receiver.

It is important to note that although the spectrum analyser offers a very accurate way to measure power spectra, it cannot measure the phase information. The phase of the tones directly influences the envelope shape, which in turn will excite the device in different ways. Such things are impossible to see using the spectrum analyser due to the lack of phase information. This issue was however avoided in this section, since the same stimulus allowed a fair comparison. Further investigation in chapter 6 will show the effect of phase of a multi-tone stimulus.

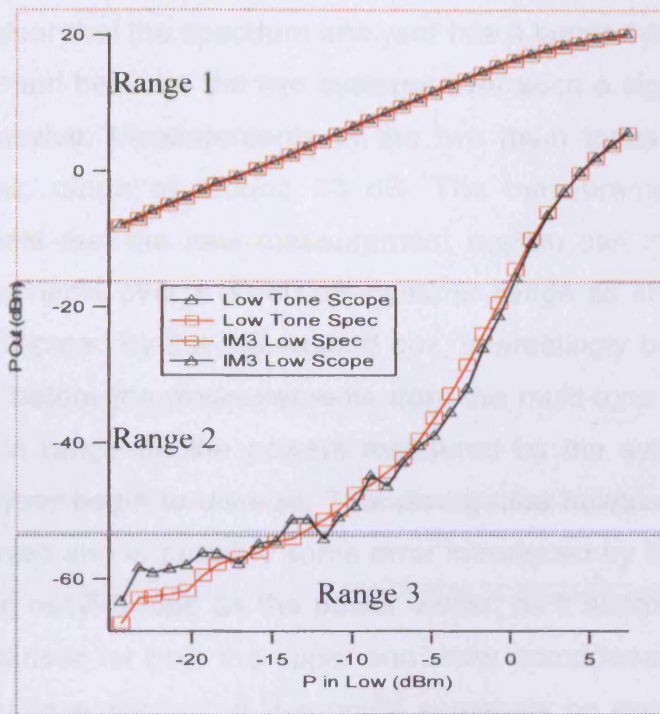


Figure 3.37(a) – Comparison of spectral Power in lower tone and generated IM3-low components as a power sweep is conducted

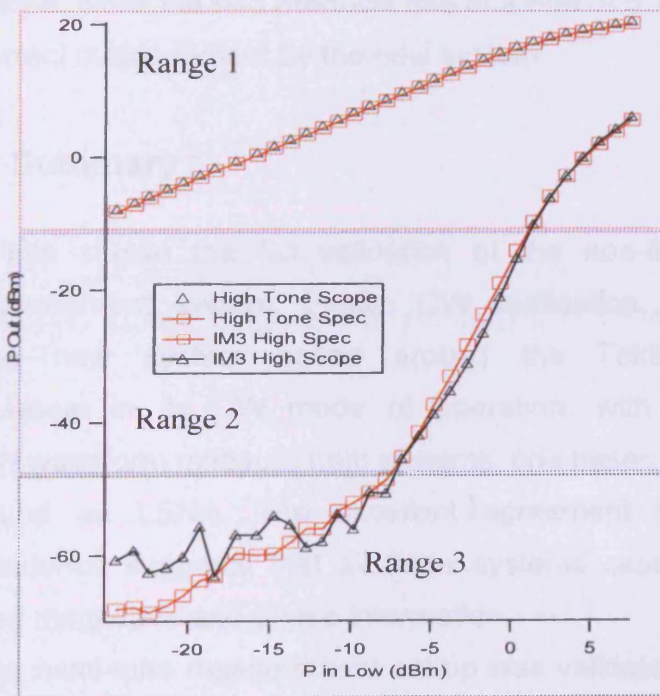


Figure 3.37(b) – Comparison of spectral Power in upper tone and generated IM3-high components as a power sweep is conducted

Although it is clear that the spectrum analyser has a larger dynamic range, the level of agreement between the two systems over such a significant dynamic range is impressive. Measurements of the two main tones overlay exactly over a dynamic range of around 30 dB. The measurements of the IM3 products suggest that the new measurement system can in fact accurately measure components over a 35-40 dB dynamic range as shown by range 1 on the plots, indicated by the red dashed box. Interestingly below this level in range 2, even before the measurements from the multi-tone system become noisy (shown in range 3), the powers measured by the system and by the spectrum analyser begin to diverge. This divergence however appears to be very well behaved and is possibly some error introduced by the A/D converter of the sampling oscilloscope as the power varies, as it seems to have a very similar characteristic for both the upper and lower components. This however requires further investigation. If this could somehow be corrected, the plots would suggest that the dynamic range could be extended to 65-70 dB. The plots also indicate, as predicted by theory, that the fundamental components rise on a 1:1 slope, while the IM3 products rise at a rate of 5:1, offering further evidence of correct measurement by the new system.

3.7 Chapter Summary

This chapter has shown the full validation of the non-linear, multi-tone waveform measurement system. Firstly, CW verification was completed, comparing the new system based around the Tektronix CSA8000 oscilloscope, set-up in its CW mode of operation, with two other well established CW waveform measurement systems: one based around the MTA and one around an LSNA. The excellent agreement shown between measured waveforms suggests that all three systems capture high quality vector corrected magnitude and phase information.

Next, the multi-tone measurement set-up was validated. This involved verification of the required sampling techniques, including the frequency folded sampling, time interleaved sampling and waveform alignment process. The CW comparison process was then repeated with the system established in its multi-tone mode of operation. This successful comparison between the

two modes of operation of the new measurement system confirmed that the combined approach utilising time interleaved, folded-frequency sampling, along with the modifications to the triggering architecture, were successfully implemented and did not degrade measurement quality.

As a final verification, a scalar comparison was made using multi-tone measurement data from the new measurement architecture referenced to a scalar calibrated spectrum analyser system. This allowed comparison of the magnitude of frequency domain spectra captured by the two measurement systems at all frequencies of interest. Measured results demonstrate a impressive agreement, showing that almost perfect agreement was achieved over a dynamic range of around 35 dB.

Further to the system comparisons, theory was used throughout the chapter to offer further confidence that the system is operating correctly.

3.8 References

1. Lees, J.; Benedikt, J.; Hilton, K.P.; Powell, J.; Balmer, R.S.; Uren, M.J.; Martin, T.; Tasker, P.J. "*Characterisation of an experimental gallium nitride microwave Doherty amplifier*" 2005 European Microwave Conference, Volume 2, 4-6 Oct. 2005.
2. McGovern, P.; Benedikt, J.; Tasker, P.J.; Powell, J.; Hilton, K.P.; Glasper, J.L.; Balmer, R.S.; Martin, T.; Uren, M.J. "*Analysis of DC-RF dispersion in AlGaIn/GaN HFETs using pulsed I-V and time-domain waveform measurements*" IEEE/MTT-S International Microwave Symposium Digest 2005.
3. Qi, Hao; Benedikt, Johannes; Tasker, Paul J. "*Novel Nonlinear Model for Rapid Waveform-based Extraction Enabling Accurate High Power PA Design*" IEEE/MTT-S International Microwave Symposium Digest 2007, Page(s):2019 - 2022
4. Fernandez-Barciela, M.; Tasker, P.J.; Campos-Roca, Y.; Demmler, M.; Massler, H.; Sanchez, E.; Curras-Francos, M.C.; Schlechtweg, M. "*A simplified broad-band large-signal nonquasi-static table-based FET model*" IEEE Transactions on Microwave Theory and Techniques, Volume 48, Issue 3, March 2000 Page(s):395 – 405
5. Curras-Francos, M.C.; Tasker, P.J.; Fernandez-Barciela, M.; O'Keefe, S.S.; Campos-Roca, Y.; Sanchez, E. "*Direct extraction of nonlinear FET I-V functions from time domain large signal measurements*" Electronics Letters, Volume 34, Issue 21, 15 Oct. 1998 Page(s):1993 – 1994
6. Remley, K.A, DeGroot, D.C, Jargon, J.A, Gupta, K.C. "*A Method to Compare Vector Nonlinear Network Analyzers*" IEEE/MTT-S International Microwave Symposium Digest 2001 Page(s):1667 – 1670.
7. Steve C. Cripps "*RF Power Amplifiers for wireless communications*" Second Edition Artech House Microwave Library 2006 ISBN 1-59693-018-7

Chapter 4 - Realisation of Impedance Control architectures for multi-tone Measurements

4.1 Motivation

Once we begin to measure the large signal performance of a non-linear device or circuit, it is important to realise that it is no longer possible to predict how the DUT will perform when operated in different impedance environments. Instead, the only way to predict the performance is to perform the large signal measurement in the impedance environment into which the DUT will be placed in the final application.

Although it was true that impedance control architectures existed at RF frequencies, there were no fully realised solutions that could deal with multi-tone signals, where the impedance control architecture or load-pull system is required to present specific impedances across a modulation bandwidth, presenting specific impedances to a number of different frequency components around the fundamental and harmonics. Furthermore, mixing

leads to the generation of significant components at base-band frequencies where control of the impedance environment is just as important.

The aim of this work is therefore to build upon existing load-pull architectures, which have proven a very effective tool in the design process, and extend their operation into the multi-tone domain. This will allow a device to be measured in an impedance environment that closely resembles the environment into which it will ultimately be placed. For example, it is then possible to present specific, broad-band impedances at the fundamental and harmonic bands, as well as at the base-band, that would closely emulate the impedance presented by the matching and bias insertion circuits respectively. Furthermore, the architecture will naturally lend itself to novel applications where injection is used to present negative impedance to the DUT to improve device performance. One such application that could make good use of such a measurement system is in the design of an Envelope Tracking (ET) type power amplifier such as that presented in [1] where base-band injection is used to significantly improve the efficiency of the DUT.

4.2 Impedance Control and Waveform Engineering

The ability to control impedance is vital in the full large signal characterisation of a device or circuit. As soon as we move away from linear measurements, it is no longer possible to predict the performance of a device or circuit purely from measurements conducted in a 50 Ω environment. Load-pull therefore plays an integral component in any measurement system designed to characterise and investigate non-linear performance. As the majority of systems designed to uncover large-signal RF performance have focused around CW characterisation, it is therefore not surprising that impedance control architectures, that have usually been designed in parallel, only apply to CW signals. Such systems however, play a significant role in the design process of modern communication systems, and have highlighted the importance of not only fundamental, but also harmonic impedances on device performance. The strategies employed range from simple load-pull sweeps, used to capture optimum impedances for a required specification, to waveform engineering where the waveform shape is engineered by

terminating the different generated components into specific impedances, allowing optimisation of device performance through a more calculated approach. The power of waveform engineering is demonstrated by Benedikt et al. in [2], where fundamental and harmonic impedance control is used to directly engineer the voltage waveforms, and indirectly to engineer the current waveforms; the latter is being achieved through control of the load-line interaction with the device boundary conditions. Further examples are given by Lees et al. in [3], where waveform engineering is employed to design and optimise a GaN Doherty Power Amplifier (PA) structure, and also by Barataud et al. in [4], where waveform engineering is used to optimise the PA design process for high efficiency. It is clear that the new large-signal multi-tone measurement concept presented in Chapter 2, and validated in Chapter 3 of this thesis, must include waveform engineering capabilities at fundamental and significant harmonic bands in order to allow the progression seen in the CW design process to be employed instead, with modulated stimulus. In addition, the use of modulation during the characterisation process also introduces a new band of components generated at base-band frequencies. Research has shown that control of the impedances presented to these components forms an integral part of the PA optimisation process [5,6]. This chapter therefore discusses and suggests possible impedance control and engineering solutions that can be employed alongside the realised measurement architecture to allow full engineering of multi-tone signals. One significant advantage of the new design approach using multi-tone stimulus is the ability to directly engineer for linearity and the removal of electrical memory effects.

4.3 Existing Impedance Control Solutions

Tuning the impedance environment around a device can in turn result in improved device performance. For example gain, power, efficiency and linearity are all reliant on the design of the correct impedance matching network. In order to analyse the effect of impedance matching, it is necessary therefore to vary the impedance either at the input (source-pull) or at the output (load-pull) of the device, and to measure the resulting performance. For

full optimisation, it is necessary to simultaneously control the impedance at the fundamental and significant harmonics, both at the input and at the output. Such systems are termed harmonic source and load-pull.

The load reflection coefficient (Γ_L) can be described in terms of incident and reflected travelling waves. Analysis is often considered in a similar way to s-parameters, using the analogous names a_1 , b_1 , a_2 and b_2 for the forward and reverse travelling waves, where a_1 is the incident travelling wave, b_1 is the travelling wave reflected at the device input, b_2 is the output of the device and a_2 is the travelling wave reflected off the load. From this, it is clear that the load and source reflection coefficients are given by the ratios shown in equation 1 and 2 respectively.

$$\Gamma_L = \frac{a_2}{b_2} \quad (1)$$

$$\Gamma_S = \frac{b_1}{a_1} \quad (2)$$

Using this fundamental theorem, measurement systems have evolved to emulate the impedance seen by the device by changing the reflected power injected into the device output port. This can be achieved either passively or actively.

Traditionally, load-pull or ‘emulation’ of load impedance has been achieved using passive techniques, such as line stretchers and phase shifters. This is clearly a very manually intensive approach where a skilled engineer is required to tune an amplifier’s performance. Passive architectures have however evolved, and there are now a number of commercially available mechanical tuners that are fully automated, such as those produced by Focus [7]. Focus’ latest generation tuner (the ‘iTuner’) is a fully automatic mechanical tuner for fundamental and harmonic impedances. Similar tuners are also offered commercially by Maury Microwave [8]. Even these automated measurement solutions have limitations however: firstly, losses in the measurement system become a major issue as any loss between the DUT and the tuner reduces the maximum reflection coefficient obtainable. This

problem is highlighted for example when measuring high-power (100W) LDMOS devices such as those used in power amplifiers for base station transmitters. The typical optimum output impedance of such a device is less than 1Ω . Realistically, such low impedances requiring such high reflection coefficient cannot be achieved using purely passive systems. The problem of loss is compounded when we wish to measure waveforms as additional passive structures such as directional couplers are needed to measure the travelling waves, thus adding additional loss to the measurement system and further reducing the reflection coefficient that can be presented. Furthermore, passive systems require extensive and time-consuming calibration of the mechanical tuners. This can take a significant amount of time if a large area of the Smith chart is to be calibrated and is further compounded if harmonic impedances also need to be tuned. This often limits their application to collection of only small data sets. Perhaps the biggest problem with regards to the application of passive tuners to multi-tone signals is that the set load reflection coefficient is only maintained over a small bandwidth. Additionally, such tuners do not lend themselves to applications at base-band frequencies. A further consideration is cost, as the mechanical precision required to accurately and repeatedly emulate loads in such systems result in a solution that is very expensive.

To overcome the issue of loss within the measurement system, active load-pull has evolved where emulation of load impedance is achieved by injecting an amplified signal of specific magnitude and phase into the DUT output, emulating the reflected travelling wave (a_2). Active load-pull systems have the ability to compensate for any losses in the system allowing the load reflection impedance to be set anywhere within, or even outside the Smith chart. Active systems typically have either a closed-loop or an open-loop architecture. Active load-pull has been accepted as a valid measurement and design approach and comparisons between passive and active measurements, such as those presented by Deshours et al. in [9] confirm coherence of the measurements achieved by both methods.

The first closed-loop active load-pull architecture was presented by Bava in 1982 [10]. In this closed-loop architecture shown in figure 4.1, a direct

RF feedback loop is employed. The output of the device is passed through a circulator and is then attenuated and phase-shifted to emulate the desired impedance, before being amplified to overcome any losses in the system. This means that the injected signal is a directly related, modified version of the DUT output signal. This ensures the emulated load impedance is independent of drive level and any changes in phase of the device output, typically caused by AM-PM. Such an architecture is also useful for application to modulated waveforms as a constant impedance can be maintained across a modulation bandwidth, since all tones present in the output spectra of the carrier are thus terminated into a constant impedance environment.

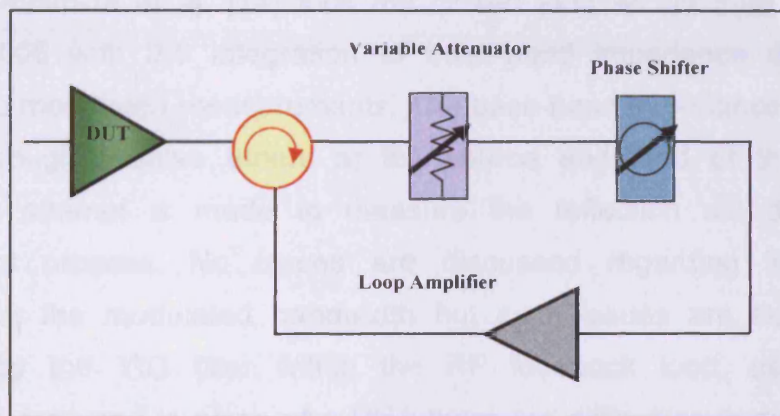


Figure 4.1 – Closed-loop Active load-pull Architecture first Proposed by Bava [10]

Research has however uncovered a major problem with the architecture in that it is prone to instability, due to the closed RF loop employed. Such oscillations are particularly dangerous as they not only destroy the device but could also destroy any measurement equipment in the test set due to maximum input powers of the instruments being exceeded.

An attempt to solve the oscillation problem is presented by Hughes et al. in 1992 [11], where a tuneable barium YIG filter is incorporated into the active closed loop to limit the possibility of oscillation, although caution is required to ensure the losses of the loop introduced by the filter do not lead to a requirement for large amplification in the active loop, which could again introduce the possibility of oscillation. The filter will also clearly limit the bandwidth of signals that can pass around the loop. Furthermore, the architecture no longer presents a broad-band impedance across a modulated

bandwidth due to the filter characteristic. Ferrero et al. present a further improvement in 2006 [12] where the losses of the test set are minimised through the introduction of ultra-low loss couplers, termed a 'double head'. This novel coupling device is shown to be nearly transparent up to 15 GHz, which has large implications for both passive load-pull architectures and for closed-loop active load-pull architectures where losses must be limited to avoid oscillations. Other attempts have also been made to minimise loss within the system, and one such example is presented by De Groote et al. in [13] where a loop of coaxial cable is used to couple the RF in a non-invasive way, thus dramatically reducing the loss when compared to the standard approach. Bensmida et al. [14] took the closed loop architecture one step further in 2006 with the integration of base-band impedance control for application to modulated measurements. The base-band impedance control is achieved through passive tuners at the source and load of the device, however no attempt is made to measure the reflection set during the measurement process. No issues are discussed regarding impedance variation over the modulated bandwidth but such issues are likely to be introduced by the YIG filter within the RF feedback loop, as six port reflectometers are used in place of a VNA there are difficulties in determining the reflection coefficient at individual tones within the spectrum.

Due to the inherent oscillation problems associated with closed-loop architectures, much of the microwave community continue to employ active load-pull systems in open-loop configurations. The open-loop architecture was first demonstrated in 1976 by Takayama [15]. In the architecture shown in figure 4.2, the input signal is equally split and one half used to drive the device, while the other half is phase shifted, attenuated and injected into the output port of the device.

By its nature, this method avoids the stability problems associated with closed-loop feedback architectures, as there is no longer a direct RF feedback path. There is however no longer any relationship between the device output and input-derived load-pull signals. Any change in the reflected power wave changes the output state of the device, thus changing the achieved load impedance. This leads to an iterative process where a number of magnitude

and phase adjustments of the injected signal are required to maintain the target reflection coefficient.

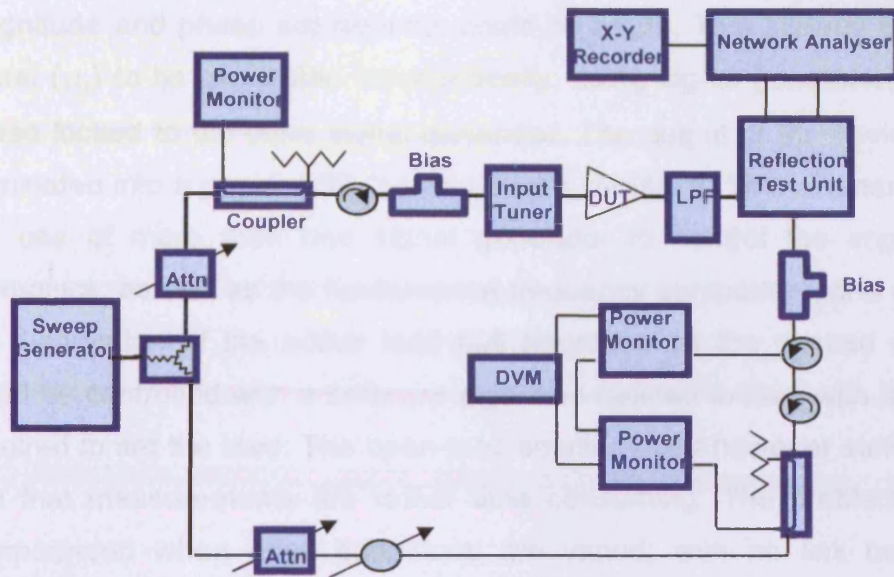


Figure 4.2 – Open-loop Active load-pull Architecture Proposed by Takayama [15]

Poulin et al. improved the open-loop architecture in 1992 [16] by replacing the variable attenuator and line stretcher used to alter magnitude and phase with an electronic approach using an I-Q Vector modulator, thus providing a solution that was both easier to automate and less susceptible to mechanical wear. A further extension of the architecture presented by Benedikt et al. [2] shown in figure 4.3 came with the introduction of microwave signal generators with phase lock-capabilities.

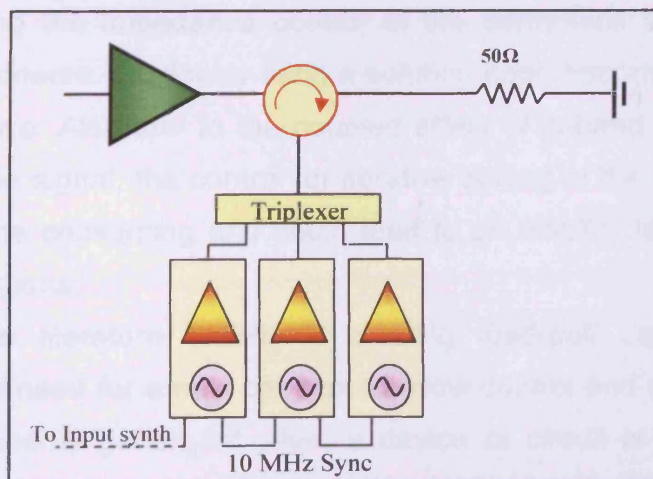


Figure 4.3 – Multi-Harmonic Open-loop Active load-pull Architecture, Benedikt [2]

The ability to phase lock signal generators using a 10 MHz reference signal allowed multiple signal generators to be locked together which meant relative magnitude and phase adjustments could be made. This allowed the injected signal (a_2) to be generated independently, using signal generator(s) that are phase locked to the input signal generator. The output of the device is again terminated into a passive 50 Ω load using a circulator. This extension allowed the use of more than one signal generator to control the impedance of harmonics, as well as the fundamental frequency component, and allowed for full automation of the active load pull approach as the desired impedance could be controlled with a software algorithm defined to deal with the iteration required to set the load. The open-loop solution does however suffer from the fact that measurements are rather time consuming. The problem is further compounded when drive conditions are varied; with no link between the device output and injected signal, any change in the input signal leads to a further round of iteration to re-establish the required load. The biggest problem with respect to this work is that the architecture becomes unrealistic for the impedance control of multi-tone signals as load-pulling each generated tone in the device output would require a separate signal generator. Thus, even for simple modulation schemes such as the two-tone excitation often used in linearity investigations, control would be required for at least the two tones, plus significant in-band intermodulation products such as the IM3, IM5 and IM7 products, leading to a requirement for 8 signal generators, and that is before considering the impedance control of the harmonics and generated base-band components. Obviously such a solution soon becomes impractical and cost prohibitive. Also due to the coupled effect of in-band and harmonic components of the signal, the control for iterative setting of the load becomes very complex, time consuming and could lead to an inability to converge on certain load conditions.

The above literature review of existing load-pull capabilities has demonstrated the need for a new concept to allow control and engineering of frequency components generated when a device or circuit is driven with a multi-tone stimulus. Passive solutions have been ruled out as they do not offer a constant impedance across a modulated bandwidth. In addition they have

an inability to reach all required load impedances and are time consuming to calibrate. Active systems seem to overcome many of the issues associated with passive architectures as losses in the test-set are no longer an issue. However, the existing active architectures also have associated problems. Closed-loop architectures suffer from stability problems, and when filters are employed to control the oscillation risk, the architecture becomes impractical for multi-tone operation due to limited bandwidth and a non-constant impedance across the band. Open-loop architectures are slow, iterative and are impractical for use with modulated signals. Clearly a solution is required for the active impedance control of devices driven with modulated stimulus.

The impedance control required for multi-tone measurements can be broken down into two distinct sections: frequency components generated at RF frequencies and frequency components generated at base-band frequencies. As was explained in chapter 2, the test set architecture was designed in such a way that base-band and RF components were separate, with the base-band and RF signal components recombined for measurement by the sampling oscilloscope. This architecture also ensures that there are separate load networks for base-band and RF frequencies, allowing different approaches to be adopted for each. The following sections will detail the architectures employed in each case.

4.4 Base-band Impedance control

The base-band impedance control architecture employed builds upon an existing active open-loop baseband load-pull architecture presented by Williams et al. in 2002 [17]. As the literature review suggests, existing architectures make little effort to control or even measure generated base-band components. However the impedance presented to the base-band components can in fact have a dramatic effect on the overall measured waveforms. If a generated base-band current component is presented with a high impedance then it will naturally generate voltage. This generated voltage manifests itself as modulation on the bias lines of the device. This modulation is a common cause of electrical memory, which is probably the most common

memory effect exhibited. Furthermore, as measurements of modulated signals are often conducted with spectrum analysers that give only scalar information, such electrical effects usually occur as a device is driven close to compression, and can be misinterpreted as device related memory, when in fact, they are due to the impedance environment presented at the base-band. Any modulation on the drain voltage supplied can result in the dynamic characteristic interacting with the device's boundary conditions, causing additional distortion. This is highlighted in figure 4.4(a) where a device is operated in a backed off state. The plot shows the DC-IV performance with an example RF load-line appended in blue. It is clear that in this case a modulation of 2 Volts on the drain would not dramatically effect the performance of the device as there will be no interaction with the device boundary conditions. However, if the device is operated closer to compression, as shown by the black load-line in figure 4.4 (b), a modulation of 2 Volts on the drain voltage would clearly cause interaction with the knee boundary and thus introduce electrical memory. As the modulation on the bias caused by the generated base-band components is generally regarded as a problem, it is standard practice to attempt to short these generated base-band components. However this becomes particularly difficult as operational bandwidths become larger.

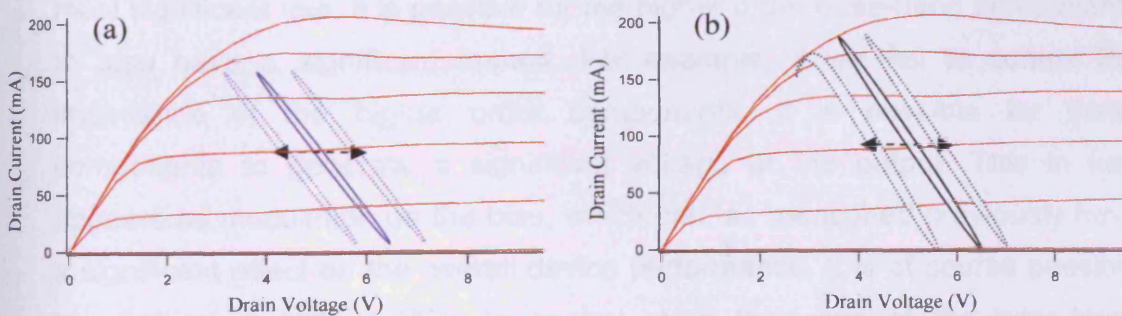


Figure 4.4 – Load line appended to DC measurements highlighting the possible implications of bias modulation

Additionally, it is sometimes possible in the design process to use bias modulation to actually improve device performance. For example, a growing

number of companies and universities are investigating the development of Envelope Tracking PAs [1,18]. These architectures use a variable voltage power supply, sometimes called a DC-DC converter or Modulator, which is dynamically adjusted to track the envelope of the applied modulation. In this way a designer can ensure that the amplifier always operates close to compression, even when operating at reduced output power level, therefore greatly improving the average efficiency. The presented system would allow a clear measurement of device performance under such a mode of operation and is therefore seen as a key tool in any such investigations, allowing a direct measurement and manipulation of the entire base-band spectrum, combined with the ability to view and analyse the resulting effect on RF performance.

The base-band load-pull employed takes the form of an open-loop active architecture similar to that depicted in figure 4.3. Instead of signal generators to control harmonic impedances, an Arbitrary Waveform Generator (AWG) is used to control impedances at the base-band. Initially, only the impedance of the fundamental base-band impedance generated was controlled, highlighting the importance of measuring and controlling the impedance of the base-band components. This will be revisited in chapter 6 of the thesis where applications of the measurement system will be discussed. It was however noted that although the fundamental component played the most significant role, it is possible for the higher order base-band components to also have a significant impact. For example, if we fail to control the impedance of the higher order components, it is possible for these components to generate a significant voltage at the output. This in turn appears as modulation on the bias, which can, as mentioned previously have a significant effect on the overall device performance. It is of course possible to combine multiple AWG's to control more than one of the base-band impedances. However, it is difficult to source combiners, isolators and triplexers at base-band frequencies and it is therefore necessary to design multiplexers in house.

This solution however soon becomes impractical, as any change in tone spacing would lead to a requirement for new diplexers, with additional

components required for each required tone spacing, so clearly this is not an optimum solution. One possible solution is suggested in the future work section where the measured base-band information is used to generate a modulated base-band signal using the AWG to control more than one frequency component simultaneously. This architecture is also an ideal tool for investigations into envelope tracking as the envelope of the output can be measured and the base-band recreated to modulate the bias and improve overall efficiency.

4.5 RF Impedance control

Although there has been substantial research into optimal load-pull architectures, as discussed in the literature review, the architectures all focus upon CW stimulus and the control of fundamental and harmonic impedances only. This work however looks to measure and characterise devices using multi-tone signals, therefore the required load-pull architecture becomes more complex as we now need to maintain impedance over a wide bandwidth, and at fundamental and harmonic frequencies. This rules out the use of the majority of existing architectures, the only possibility being some form of closed-loop active load pull architecture. However, as mentioned, these have associated problems: firstly filters are required in the feedback loop to control oscillation problems, and these in turn limit the bandwidth of the signals that can pass through the loop and cause a variation in impedance across the modulated band. Furthermore, such systems still suffer from the possibility of potentially destructive RF oscillations. This section proposes an architecture to solve the problems associated with existing load pull systems and allow load-pull of multi-tone signals. The architecture has been termed envelope load-pull, and is illustrated in figure 4.5. The architecture incorporates a quasi closed-loop approach, where the feedback loop exists only at the envelope or modulation frequency, and not at RF frequencies. This means there is no longer a problem with RF stability and the destructive RF oscillation issues associated with existing closed-loop architectures. Additionally, the architecture maintains the same advantages as the classical, closed-loop architecture, as the loop can for example react to changes in the device

output. For this reason, no iteration is required, making the system much faster than open-loop counterparts. Furthermore, as all in-band impedance components can be controlled by the loop, even under varying drive conditions, the system is ideal for application to multi-tone stimulus. The controllable bandwidth of the loop is only limited by the bandwidth of the control electronics along with the induced group delay around the loop. The new architecture effectively couples the advantages of the classical open-loop architectures, and closed-loop while removing the disadvantages of these architectures.

4.5.1 Theory of operation

The proposed architecture is shown in figure 4.5. The device output is fed into a circulator, the signal is then demodulated into its in-phase (I) and quadrature (Q) components which exist at the modulation or envelope repetition rate. It is important to note that the architecture works equally well for CW and modulated stimuli. The down conversion creates either DC, or time varying I and Q components, which describe completely the magnitude and phase information of the RF signal over time. The I and Q signals from the demodulator are then fed through an electronic control block, that has a number of functions, the first of which is to correct any errors introduced by the demodulator. The main function of the analogue control block is to set the impedance seen by the DUT. This is achieved through a complex multiplication process with control signals X and Y used to manipulate the I and Q signals. This, in turn, results in a magnitude and phase shift compared to the demodulated signal, which will result in the appropriate injected signal a_2 . The final step is to feed these 'processed' I and Q signals (termed I' and Q') into another electronic block that has the function of pre-distorting any errors that will be introduced by the modulator. The signals are then up-converted by the I-Q modulator to form the signal that is re-injected into the output of the device, setting the load impedance.

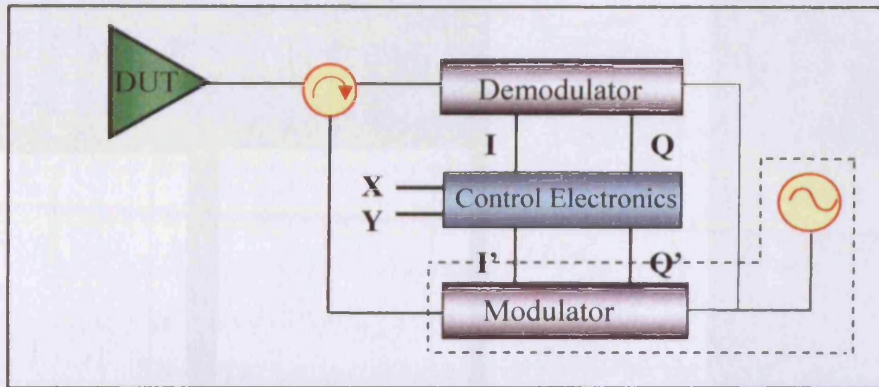


Figure 4.5 – Proposed Envelope Load Pull Architecture

The flow diagram shown in figure 4.6 highlights in more detail how the load impedance is set. In this case, the intention is to present a broadband reflection coefficient with magnitude of 0.5 and phase of 180 degrees.

A simulation of the system using Agilent's Advanced Design System (ADS) proved the successful operation of the architecture using ideal components. The next step was to characterise each of the components within the loop to ensure an optimum design. The architecture can be split into 3 distinct sections: the demodulator (down-converter), the control circuitry used to alter the vector described by the base band signals and the modulator (up-converter). The following sections will detail the characterisation process along with discussion of the results, followed by the final design.

4.5.2 Control Electronics

The prime objective of the control electronics is to control the impedance seen by the device by manipulation of the demodulated device output I and Q signals. The control circuitry also includes conditioning electronics associated with the removal of errors introduced by the modulator and demodulator. This section will deal with the ability to set the impedance and the conditioning will be discussed later in the chapter, after the errors introduced by the modulator and demodulator have been outlined.

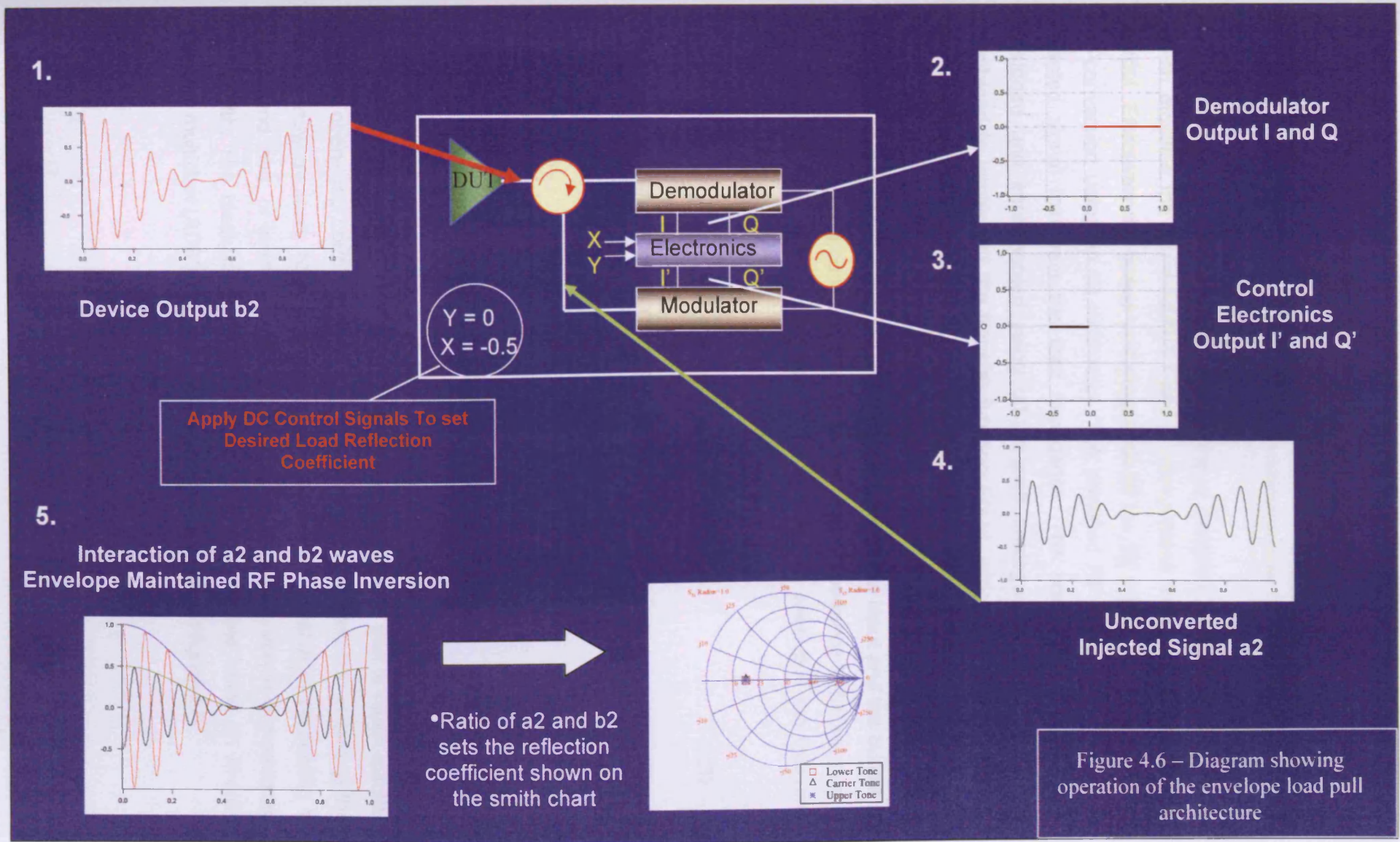


Figure 4.6 – Diagram showing operation of the envelope load pull architecture

Impedance control is achieved using a complex multiplication function which modifies the demodulated I and Q components that exist at the device output. Effectively the phase and magnitude of the RF signal are varied before up-conversion using an IQ modulator. This modified RF signal then forms the injected signal that sets the load impedance. The control electronics were designed and implemented using off-the-shelf analogue circuitry, which are combined to implement the transfer function $F(x,y)$, which is derived below. A block diagram of the realised electronics module is shown in figure 4.7.

In order to provide an impedance that does not change with drive condition, it is imperative that the relationship between the input and the output of the load-pull loop is a constant, and as we want the impedance to be set purely by the input value of control signals X and Y, it can be seen that the following relationship is required;

$$(I' + jQ')/(I + jQ) = Z = X + jY \quad (3)$$

Re-arranging to put in terms of the output I' and Q' gives;

$$I' + jQ' = (X + jY)(I + jQ) \quad (4)$$

Leading to the following transfer function;

$$F(x,y) = I' + jQ' = (XI - YQ) + j(XQ + YI) \quad (5)$$

This formulation ensures a drive level independent emulated load, quantified by the user defined values of X and Y, thus making a system that is much quicker than its open-loop counterpart for CW measurements as iteration in setting the load is now avoided. More importantly, the system is capable of presenting a broadband load, or even varying load impedance if desired, across a modulated bandwidth. The block diagram shown in fig 4.7 was realized using an Analog Devices multiplier (AD633JN), as shown in the photograph of figure 4.8.

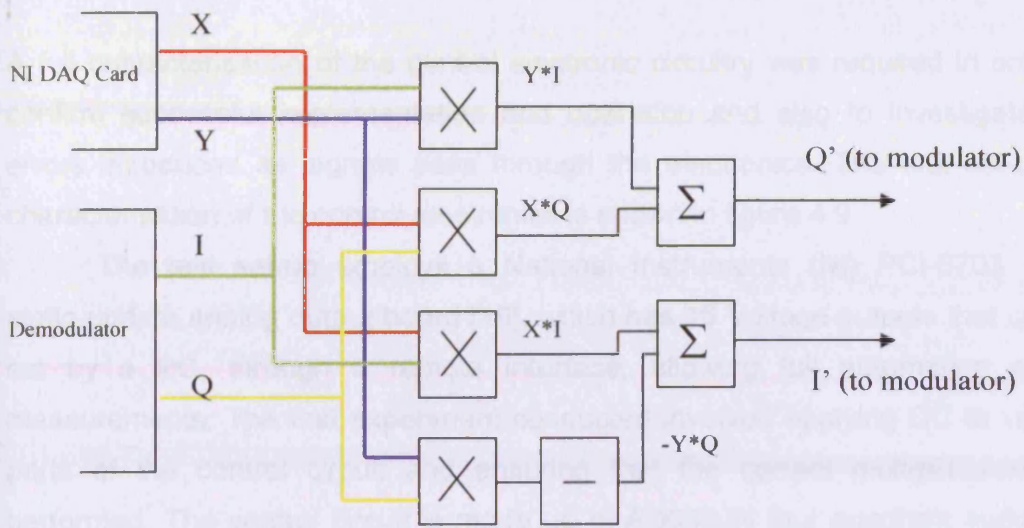


Figure 4.7 – Block Diagram of the Control Electronics block

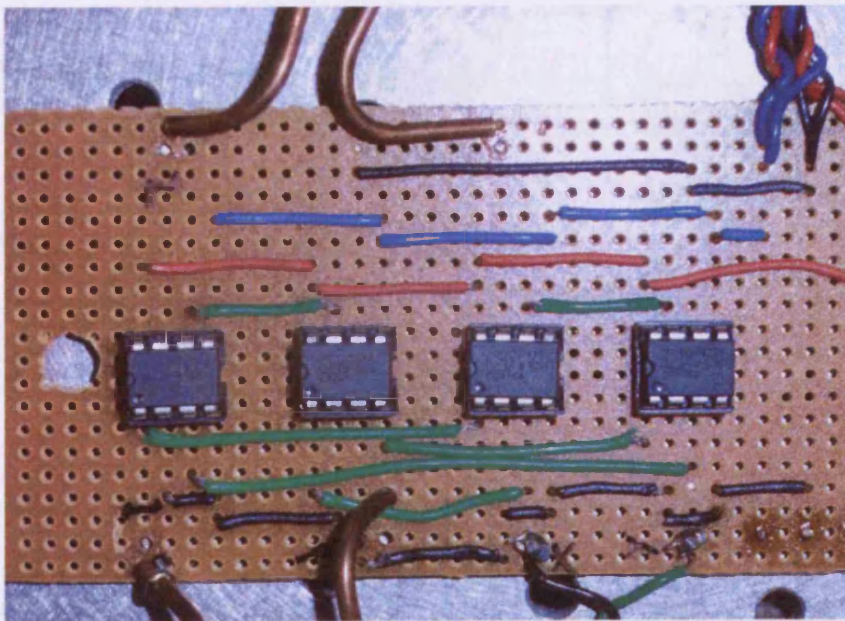


Figure 4.8 – Photograph of the realised Control Electronics block

4.5.2.1 Characterisation of Control Electronics

A full characterisation of the control electronic circuitry was required in order to confirm successful implementation and operation and also to investigate any errors introduced as signals pass through the electronics. The test set-up for characterisation of the control electronics is shown in figure 4.9.

The test set-up employs a National Instruments (NI) PCI-6703 16-bit static-update analog output board [19], which has 16 Voltage outputs that can be set by a PC, through a remote interface, allowing full automation of the measurements. The first experiment conducted involved applying DC to various ports of the control circuit and ensuring that the correct multiplication was performed. The control circuit is made up of AD633JN four quadrant multipliers that include integrated addition capabilities. Further information can be found in the data sheet [20].

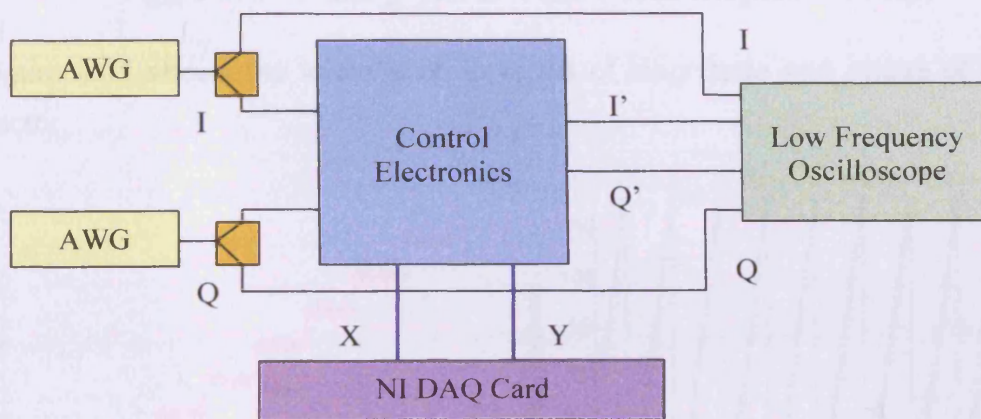


Figure 4.9 – Test set-up for characterisation of the control electronics

With 1 Volt DC applied to the I input, and 0 Volts applied to the Q input the values of X and Y were varied to alter the magnitude and phase of the original input vector. Figure 4.10 shows the resulting plot in the polar domain as magnitude is swept from 0 to 1.2 in steps of 0.15 and the phase is swept in steps

of 10 degrees. The plot highlights the very linear and accurate performance of the circuit, with predicted and measured value overlaying, with no visible errors such as DC offset or quadrature skew introduced by the circuit.

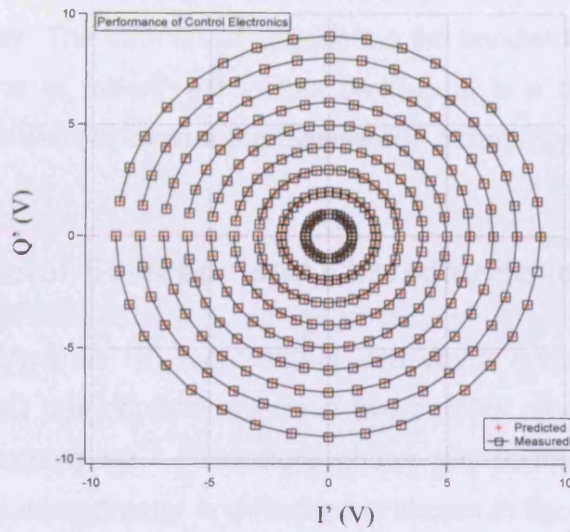


Figure 4.10 – I' and Q' plot as X and Y control signals are swept

Figure 4.11 shows the information in terms of magnitude and phase of the I-Q vector.

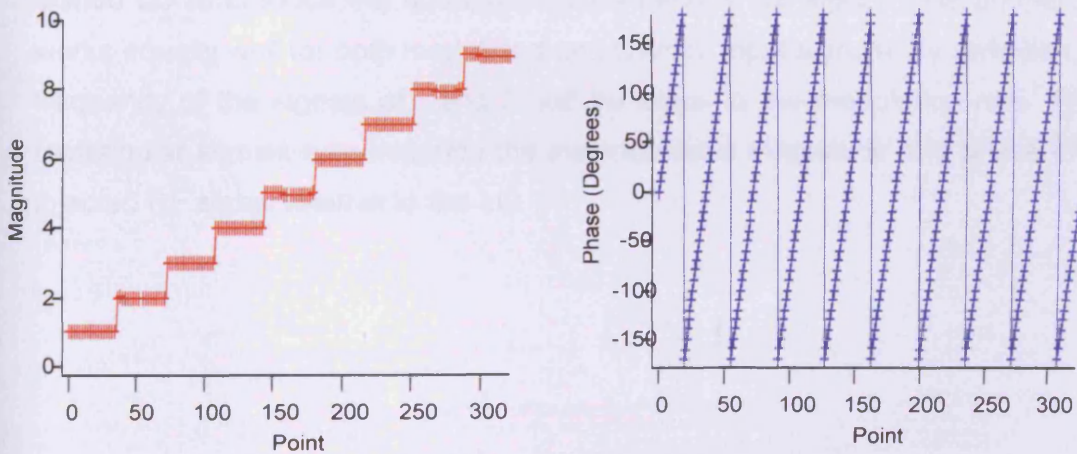


Figure 4.11 – Magnitude and Phase of I-Q vector as the X and Y signals are swept

Figure 4.11 shows the performance of the control circuit in terms of the magnitude and phase of the measured I and Q vector. Again, the plot indicates excellent performance. The bandwidth of the configuration can be found by analysis of the data sheet [20], as the entire architecture consists of the same AD633JN multiplier. The data sheet suggests a flat bandwidth of at least 400 kHz before gain begins to roll-off. While this bandwidth is a little limited, solutions exist that could be used to extend this bandwidth, potentially to tens of MHz.

4.5.3 Demodulator Selection and Characterisation

A demodulator takes an RF input signal and down converts it to base-band frequencies. An I-Q demodulator will have two outputs: one containing in-phase (I), and one containing 90 ° quadrature phase (Q) components of the carrier signal. The typical demodulator architecture is shown in figure 4.12. It consists of power splitters, mixers and low pass filters. The RF input signal is split at the input and sent to two mixers. The first mixer creates the product of the RF input and the un-modulated carrier or local oscillator (LO). The output is the in-phase component or 'I' base-band signal. The second mixer uses a 90 degree phase shifted LO to produce the quadrature base-band or 'Q' signal. This architecture works equally well for both modulated and CW RF input signals. By definition, the frequency of the signals of I and Q will be equal to the modulation rate. These rectangular signals fully describe the instantaneous magnitude and phase of the injected RF signal relative to the LO.

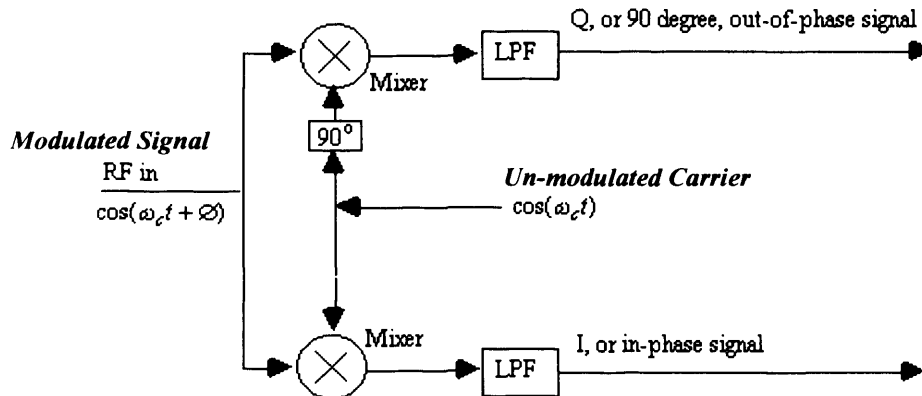


Figure 4.12 Quadrature demodulator architecture

The selection of an appropriate demodulator was critical to the success of the overall envelope load-pull architecture, as any errors introduced by the demodulator that could not be corrected using simple conditioning electronics would directly impact the overall performance of the load-pull architecture. There are various demodulator products available, which can generally be divided into passive and active architectures. Passive architectures have an advantage that any errors introduced will be drive independent, however passive structures by their nature can only be designed to work over a very narrow band, which would severely limit application of the new load-pull architecture. Active demodulators can introduce errors that vary depending upon the operating conditions, such as input drive, temperature and bias. Such variations make correcting errors more difficult. This said, such circuits often offer some form of on-chip conditioning to correct errors and offer a much larger operational bandwidth. Both passive and active demodulators were characterised and a decision was made to employ an active device, as the errors introduced were small compared to the benefit achieved from the larger operational bandwidth. Common errors introduced by demodulators are outlined below –

- **DC offsets on the I and Q channels** – often DC offsets occur with active demodulators as they are designed to run off a single polarity supply. These offsets are easily corrected using conditioning electronics,

although issues occur if the DC offsets change with drive level, frequency of operation or temperature.

- **Unbalanced I and Q gain** – can be a problem, for example, if the I and Q signals have some internal amplification that is (or becomes) unbalanced. One simple method to analyse this problem is to apply phase modulation at the RF input, which can be achieved by slightly offsetting the input frequency relative to the LO frequency. Plotting the resulting I and Q signals in the polar domain should define a circle. Any imbalance will result in elliptical behaviour in either the X or Y plane. This can again be corrected easily using simple electronics.
- **I and Q Phase imbalance** – arises from unequal time delays in the I/Q signal paths, inaccuracy in the LO quadrature generator, and from port-to-port coupling. This results in RF phase being incorrectly mapped down to the base-band, for example a phase change of 50 degrees in the input RF signal may only result in a 49 degree change at the base-band; these errors are difficult to correct. Sweeping the phase of the input RF signal and measuring the result at the base-band can highlight the problem. There is no simple conditioning solution.
- **RF Linearity** – the performance is likely to change with centre frequency. It is however important that the performance is linear across a modulation bandwidth, or there will be significant problems in the application of the envelope load-pull architecture. There is no simple conditioning solution.
- **Base-band linearity** – the base-band performance should be relatively linear until the base-band bandwidth of the demodulator is approached. There is no simple conditioning solution.
- **Dynamic Range** – problems can occur if the performance of the demodulator is not maintained over a large enough dynamic range. This would become a very important parameter should we wish to apply the envelope load-pull to complex modulation that may have amplitude changes over a large dynamic range. Again there is no simple conditioning solution to rectify this issue.

Once the possible issues had been decided, a measurement setup for the characterisation of demodulators was created allowing analysis based around the known issues. This allowed for continuous improvement throughout the project, as new and improved demodulators came online.

4.5.3.1 Demodulator characterisation

Various demodulators were characterised throughout the duration of the project, including passive and active technologies. The chosen demodulator for the final design iteration was a Linear Technology LT5575 demodulator (a photograph is shown in figure 4.13). This demodulator exhibited the best performance of all the demodulators tested. Detailed specifications are included in the data sheet [21].

The Linear Technology LT5575 Demodulator is an active demodulator. To aid the design process, an evaluation board was purchased and this was used as the basis for all characterisation of the demodulator. It was also employed in the final application of the envelope load-pull loop. The demodulator can be operated with either single-ended or differential I and Q outputs, although driving the demodulator differentially offered slightly superior noise performance. For this reason, during the characterisation process the demodulator was operated in differential mode with the mathematical subtraction of I and I-, Q and Q-performed in software after collection.

To characterise the demodulators, the test set-up shown in figure 4.14 was used. Software was written to automate the measurement, allowing new demodulators to be easily characterised, ensuring a smooth integration of future demodulator components into the measurement architecture.

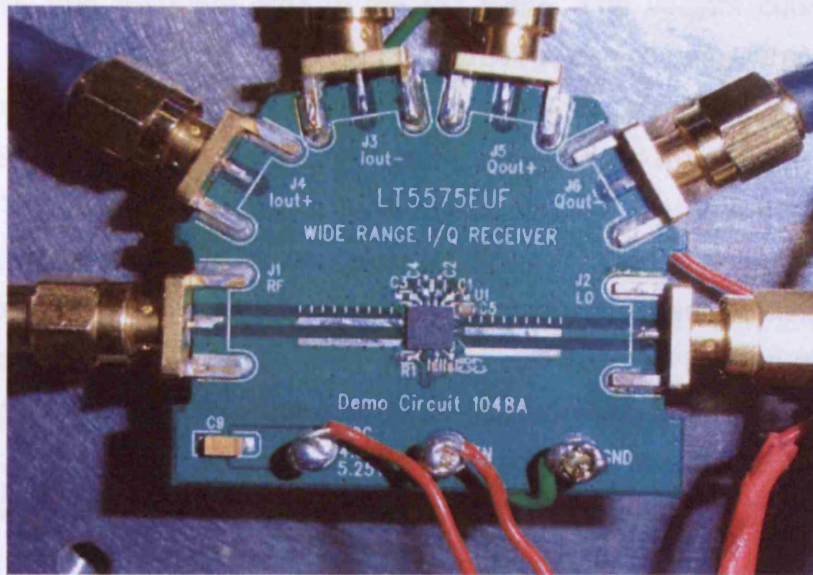


Figure 4.13 – Photograph of chosen LT5575 demodulator on evaluation board

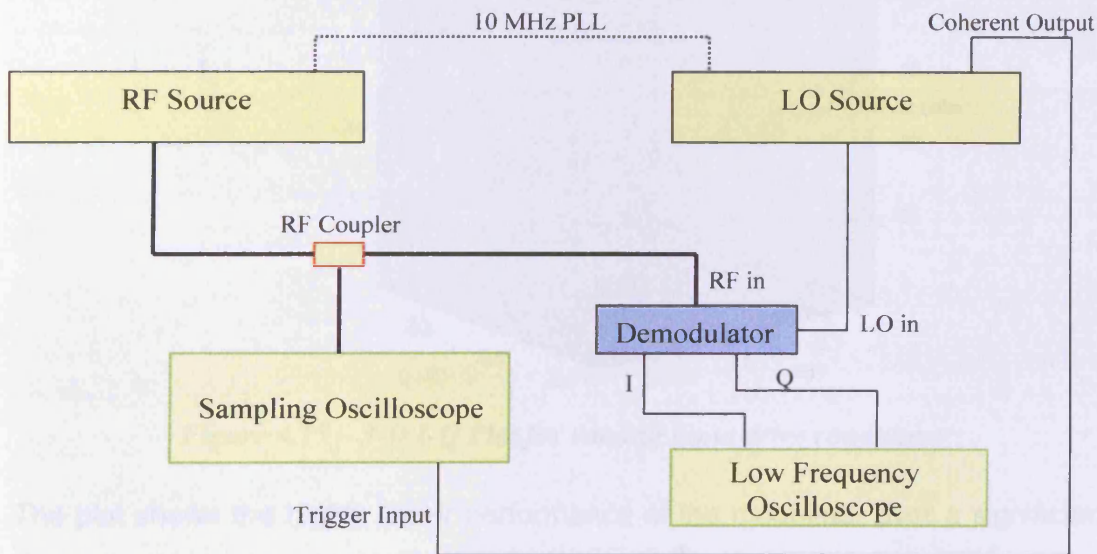


Figure 4.14 – Test set-up for characterisation of demodulators

In the first experiment, a source signal generator was used to generate a CW signal at a fixed frequency equal to the frequency of the LO (1.8GHz), whilst the phase of this signal was varied in steps of 10 degrees. This vectorally mapped a

circle at RF and therefore also in the I-Q plane. The vectors could then be compared to investigate the accuracy of a particular demodulator. The magnitude of the input signal generator was also swept with the same phase sweep conducted for each power level. The power was stepped from -31 to -8 dBm in steps of 1 dB. This would give a good confirmation of the achievable dynamic range and would highlight, in particular, any drive level dependent errors, which are the most difficult to deal with. Figure 4.15 shows the results obtained for the characterisation of the LT5575. The graph is displayed as a three-dimensional plot showing the result of phase and magnitude variation at the RF input on the measured I and Q in the polar-plane. As mentioned the differential I and Q signals have been converted to single ended values in software.

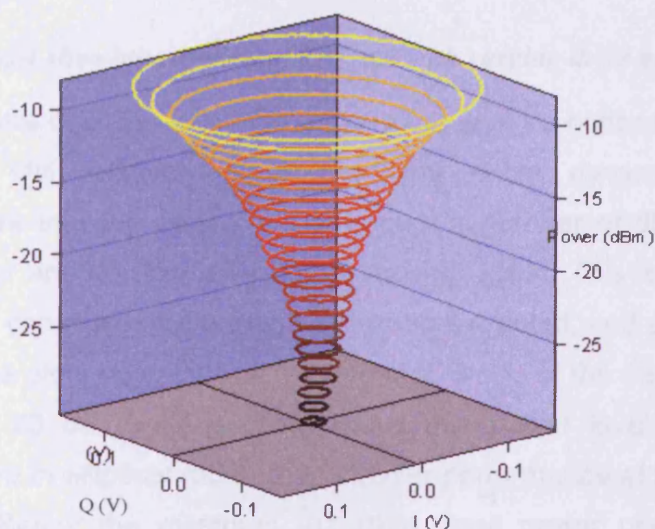


Figure 4.15 – 3-D I-Q Plot for varying input drive conditions

The plot shows the highly linear performance of the modulator over a significant dynamic range; the only problem would appear to be a small variation in the centre as the power increases, which becomes more evident when we look at the plot shown in Figure 4.15 which shows a top view of this plot shown in figure 4.16.

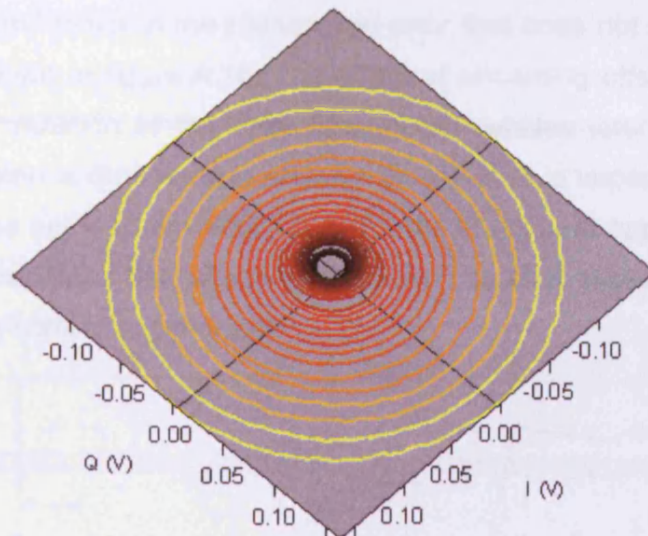


Figure 4.16 – Graph showing top view of I-Q plot with varying drive power

The change in the centre over the entire dynamic range is more noticeable in this plot, although it is still relatively small over the entire dynamic range. Interestingly, it appears that the centre is stable over a number of dB's before moving, then stable for another few dB's before moving again. This is shown in figure 4.17, where the centres of the circles have been extracted, and are plotted against drive level. The plots suggest that the dynamic range of the demodulator is excellent over the 23 dB range shown. Above this power level distortion occurred which resulted in elliptical rather than circular performance at the output of the demodulator. Below the minimum -31 dBm input power used in this experiment, measurements of I and Q became noisy. It is assumed that the majority of the noise originated from the measurement itself as the low voltage levels approached the lower limit of the low frequency oscilloscope used. The only real problem therefore is the offsets seen in the centres of the circles, which are typically simple to deal with in electronics. As mentioned however, in this case the offset moves with drive level, making correction difficult. It is possible to optimise the architecture over a given dynamic range. For example, if we take the top end of the dynamic range from -21 to -8 dBm, it is possible to apply an

optimum offset to minimise the maximum percentage error in the I-Q vector. In this case this would result in the percentage error that does not exceed 6% over the range, as shown in figure 4.18. The effect of remaining offsets is discussed further in the formulation of the error flow model detailed later in this chapter, where a formulation is derived that allows calculation. It is important to note that small errors in the set load are acceptable for the majority of applications, as the system always measures the reflection coefficient, so each measurement can be referenced to the correct impedance.

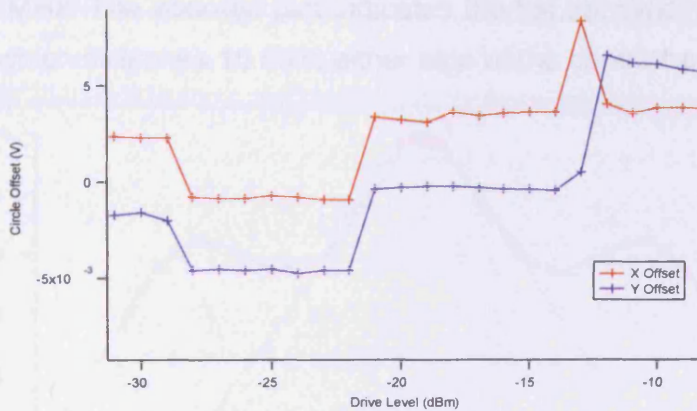


Figure 4.17 – Plot showing how centre of I-Q circle varies with drive power

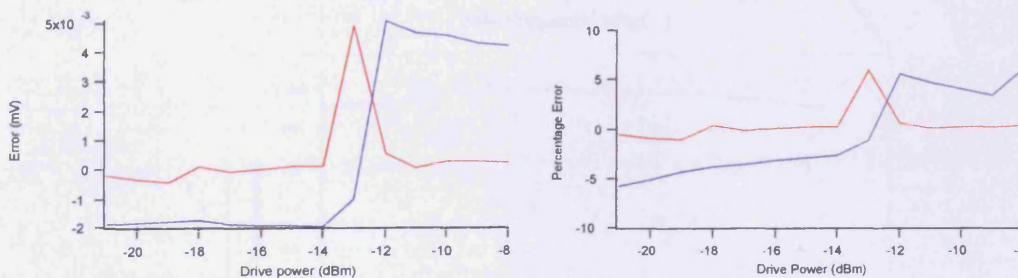


Figure 4.18 –Results Achieved applying optimum offset to minimise percentage error

The final experiment aimed to determine the base-band bandwidth of the demodulator, along with its linearity across this bandwidth. This measurement was conducted using the same experimental set-up shown in figure 4.10, although only the low frequency oscilloscope was required for measurements.

An input RF power level of -10 dBm was used in the investigation. The frequency of the RF source was then swept either side of the centre frequency of 1.8 GHz relative to the local oscillator. As soon as the frequency is moved away from the centre frequency, we effectively set up phase modulation that results in the generation of sinusoidal I and Q signals that are in quadrature. Figure 4.19 shows the magnitude of the generated I signal as the frequency is swept. The result has been converted to dB's referenced to the lowest modulation frequency (100 Hz). The demodulator shows a typical roll-off with side lobes appearing at around 60 MHz. The zoomed plot indicates the flat bandwidth, with less than 0.2 dB ripple, which stretches 10 MHz either side of the centre frequency.

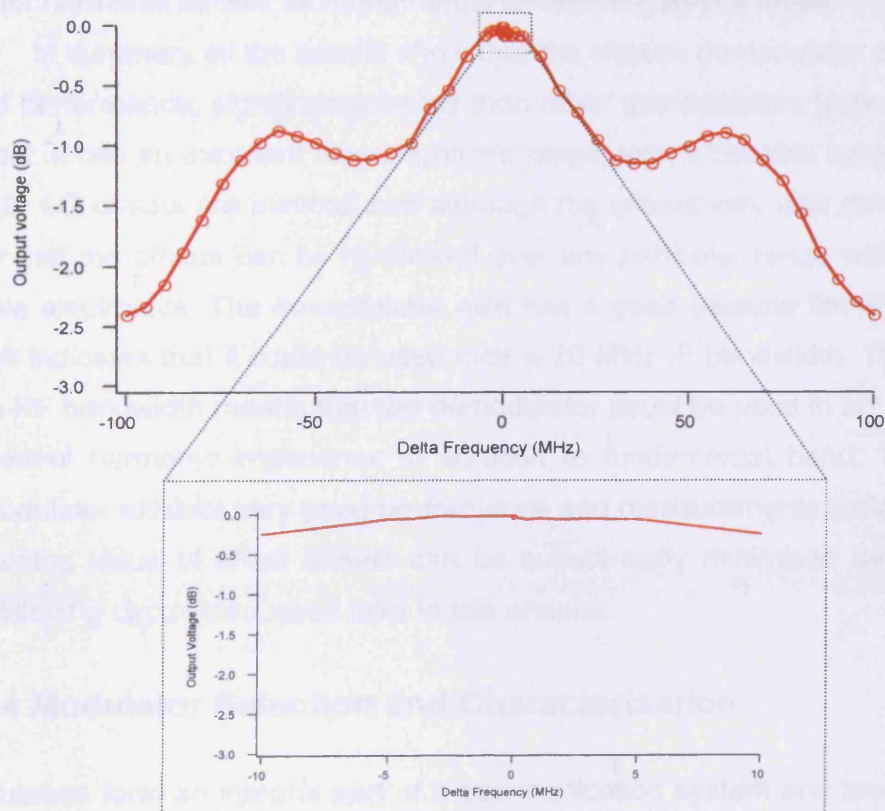


Figure 4.19 – Plot highlighting base-band bandwidth and linearity of the demodulator

The previously mentioned ideal simulation of the envelope load-pull system was altered to predict the effect of a 0.2 dB magnitude ripple across a modulated bandwidth. This simulation indicates that a 0.2 dB change across the band would cause a corresponding 4.5% variation in set load impedance. However this simulation does not deal with the group delay introduced by the demodulator, which for a multi-tone signal would cause the impedance of the tones to split apart. The effect of delay around the envelope loop will be discussed in more detail in the next chapter, when the entire architecture is characterised.

Although measurements here were only presented at a single carrier frequency, the RF bandwidth of the demodulator is 800 MHz to 2.7 GHz, allowing use for harmonic as well as fundamental envelope load-pull loops.

In summary all the results show that the chosen demodulator exhibits very good performance, significantly better than other demodulators tested during the project. It has an excellent linear dynamic range, with a useable range of around 23 dB, I-Q offsets are minimal and although the offsets vary with drive level, it is clear that the offsets can be minimised over any particular range with the use of simple electronics. The demodulator also has a good useable flat IF bandwidth, which indicates that it could be used over a 20 MHz IF bandwidth. The relatively wide RF bandwidth means that the demodulator could be used in an architecture to control harmonic impedance in addition to fundamental band. The chosen demodulator exhibits very good performance and measurements indicate that the remaining issue of small offsets can be substantially minimised by the simple conditioning circuit discussed later in this chapter.

4.5.4 Modulator Selection and Characterisation

Modulators form an integral part of a communication system and are used to up convert the data contained within base-band signals on to the carrier for transmission. In this case, the modulator is to be used within the envelope load pull loop to up-convert the modified I and Q signals to form the injected signal that is used to load pull the device. The typical modulator architecture is shown in figure 4.20.

The 'I' signal (which can be mathematically described by equation 6), is multiplied by the LO signal. The 'Q' signal (mathematically described by equation 7) is multiplied by the LO signal, phase shifted by 90 degrees. The resultant mixing products are then summed to produce the final RF output signal RF(t) described by equation 8.

$$I(t) = A \cos(\omega t) + D \tag{6}$$

(Where A is the magnitude and D is the DC offset on the I channel)

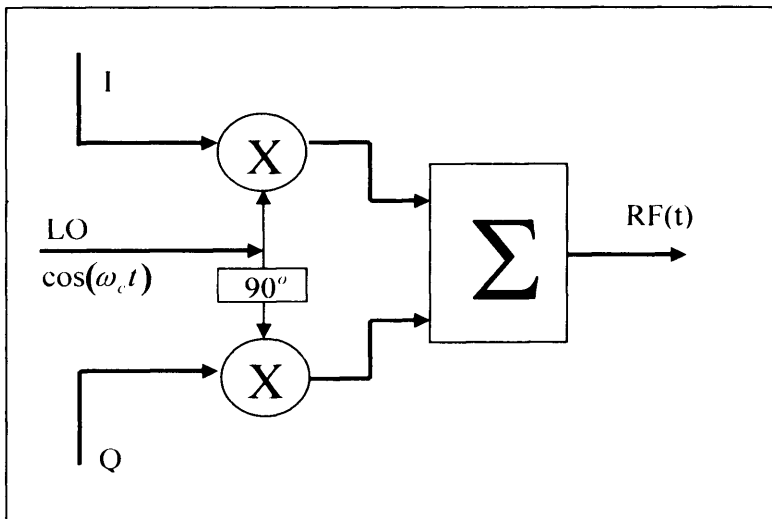


Figure 4.20 – Figure 4.6 Quadrature Modulator architecture

$$Q(t) = B \cos(\omega t + 90^\circ) + E \tag{7}$$

(Where B is the magnitude and E is the DC offset on the Q channel)

$$RF(t) = A \cos(\omega t) \cos(\omega_c t) + D \cos(\omega_c t) - B \sin(\omega_c t) \cos(\omega t + 90^\circ) - E \sin(\omega_c t) \tag{8}$$

The modulator, as is the case for the demodulator, is a critical component within the envelope loop, and any errors introduced will have a large impact if not corrected. The following are common issues encountered in modulators -

- **LO Leakage** – caused by DC offsets on I and/or Q input channels, these offsets are easily pre-corrected using conditioning electronics, although again issues occur if the DC offsets change with drive level, frequency of operation or temperature. For a modulator, base-band DC signals are directly mixed up to the LO frequency. This was one of the major issues faced during the project, particularly when the envelope load-pull was applied to CW signals as any DC offsets then directly corrupt the feedback signal.
- **Unbalanced I and Q gain** – caused by imbalance during the mixing process. Any imbalance can again be corrected easily using simple electronics.
- **LO Phase imbalance** – this results in the phase of the base-band vector being incorrectly mapped up to RF frequencies. These errors are difficult to correct. Sweeping the phase of the input base-band signal and measuring the result at RF can highlight the problem. There is no simple conditioning solution.
- **Mixing Linearity** – the performance will always change with centre frequency. However it is important that the performance is linear across a modulation bandwidth, or there will be significant problems in the application of the envelope load-pull architecture. There is no simple conditioning solution.
- **Base-band linearity** – the base-band performance should be relatively linear until the base-band bandwidth of the modulator is approached. The solution to overcome any issue would be to use a variable gain amplifier, although this was considered out of the scope of this project.
- **Dynamic Range** – problems can occur if the performance of the modulator is not maintained over a large enough dynamic range. This would become a very important parameter should we wish to apply the

envelope load-pull to complex modulation that may have amplitude changes over a significant dynamic range. Again, there is no simple conditioning solution to rectify any issues.

4.5.4.1 Modulator Characterisation

Within the first instance, and for reasons of simplicity, the internal modulator of an Agilent ESG4433 signal generator was used rather than using an external modulator. It was found that the performance of this modulator was far superior to any existing stand alone modulator module tested, and although various modulators were tested, this modulator was therefore used for the remainder of the project. More information on the specification of the internal modulator can be found in the data sheet for the ESG4433 [22]. To characterise the modulators, the test set-up shown in figure 4.21 was used. Software was again written to automate the measurement allowing new demodulators to be easily characterised, if and when they become available.

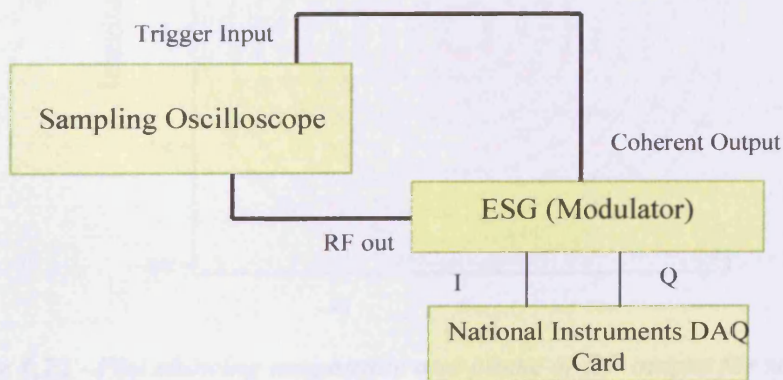


Figure 4.21 – Test set-up for characterisation of Modulators

The first experiment involved varying the values of I and Q to vectorally sweep circles of varying magnitude in a polar plane. The output of the modulator, which in this case was the output of the signal generator, was then measured using the high frequency oscilloscope, which was triggered using the coherent output. The

modulator within the signal generator required some pre-calibration, which involved defining the maximum I and Q levels that would be used during the measurements. It was possible to either use a predefined 0.5 V level set internally within the signal source or to apply a signal externally to become the new maximum level. This allowed the maximum possible dynamic range of the modulator to be achieved for all measurements by selecting the most suitable I and Q maximum levels. Figure 4.22 shows the magnitude and phase of the output RF signal obtained while the values of the input I and Q vector was swept in between 0.1 and 0.5 volts in magnitude and in phase steps of 10 degrees. For the results shown, a centre frequency of 1.8 GHz was chosen, although measured results confirmed identical linear operation independent of RF frequency.

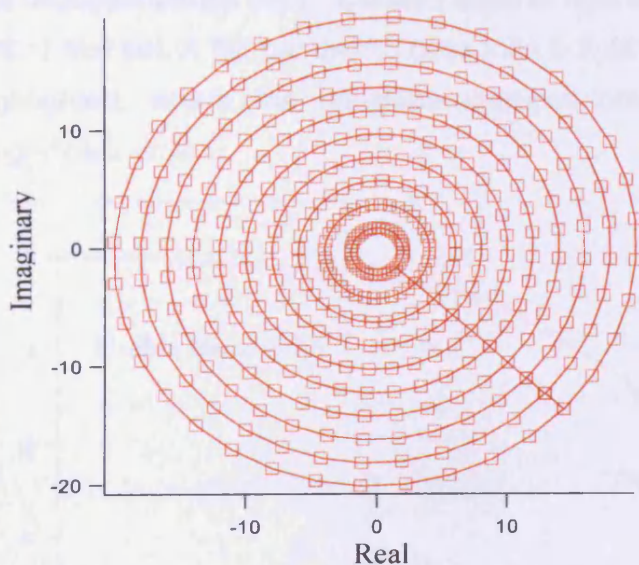


Figure 4.22 –Plot showing magnitude and phase of RF output for varying input drive conditions

The graph is displayed as a polar plot showing the result of varying the phase and magnitude at the base-band inputs on the measured magnitude and phase of the up-converted RF signal. The graph indicates that the performance of the modulator is excellent. Great care has been taken by the manufacturer of the signal generator to ensure optimum performance of the up-converter. There are

no issues with linearity, dynamic range or with DC-offsets. The modulator is virtually ideal and as such needs no correction.

The second experiment looked to uncover the linearity of the modulator performance across the base-band bandwidth. To achieve this, a sinusoidal signal biased around 0 Volts with peak-to-peak voltage of 200mV, was applied to the I input of the modulator while the Q input of the modulator was grounded. With the sinusoidal signal kept at a constant magnitude, the base-band frequency of the applied I signal was varied. Figure 4.23 shows the magnitude of the resultant vector after up conversion, and conversion to dB's referenced to the smallest modulation frequency (100 Hz). This plot indicates a good useable base-band bandwidth, with a steady roll-off giving a 3 dB bandwidth of around 20 MHz. As previously stated however, simulation suggests that a variation of less than 0.2 dB is required across the modulated band to maintain a load impedance to within 4.5% of that set. A flat bandwidth (less than 0.2 dB) of around 10 MHz is therefore highlighted, where the envelope load-pull could be used without introducing significant error.

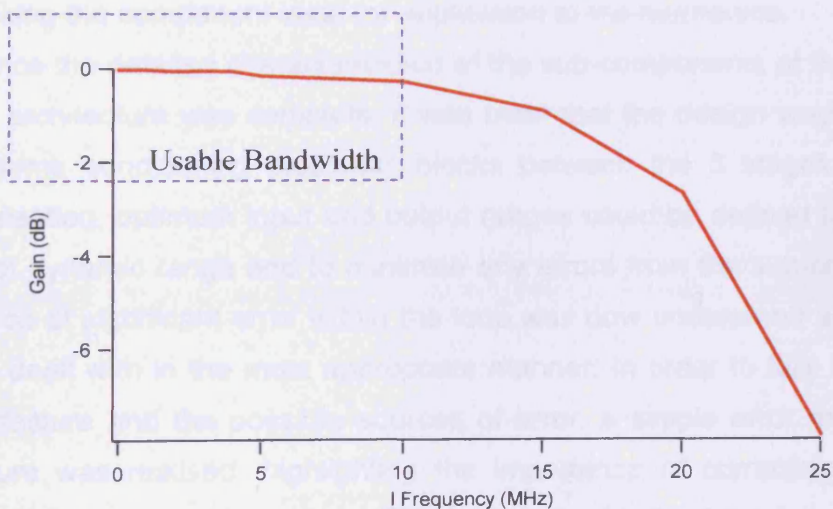


Figure 4.23 – Plot of modulator base-band bandwidth

Although a flat bandwidth of 10 MHz is reasonable, it is important to note, that the bandwidth must cover all generated in-band distortion terms to ensure a broad-band impedance is presented across the band. Thus if we now allow for an order of 10, to measure sufficient distortion terms, then this would lead to a maximum tone-spacing of only 1 MHz, to ensure all terms see the same impedance.

The RF bandwidth of the modulator is significant, ranging from 250 kHz up to 4 GHz, allowing the modulator to be employed at harmonic frequencies. Additionally, recently acquired Agilent PSG E8267D signal generators offer similar performance over a much wider base-band bandwidth of 160 MHz, and RF bandwidth up to 44 GHz [23].

In summary, all the results show that the chosen modulator exhibits virtually ideal performance. It has an excellent linear dynamic range and there are virtually no I-Q offsets. The modulator also has a good, useable flat base-band bandwidth, which indicates that it could be used over a 10 MHz IF bandwidth, in addition to a very wide RF bandwidth ranging from 250 kHz up to 4 GHz, making the component ideal for application to the harmonics.

Once the detailed characterisation of the sub-components of the envelope load-pull architecture was complete, it was clear that the design would not work without some conditioning electronic blocks between the 3 stages. From the characterisation, optimum input and output ranges could be defined to maximise the use of dynamic range and to minimise any errors from the sub-components. Any source of significant error within the loop was now understood and as such could be dealt with in the most appropriate manner. In order to fully understand the architecture and the possible sources of error, a simple error model of the architecture was realised, highlighting the importance of correcting for errors introduced within the envelope loop. This is described in the following section.

4.6 Error Flow Model of the Envelope Load Pull Loop

The purpose of producing an error flow model for the architecture is to enhance understanding of the effects that sources of error have on the architecture, thus

allowing conditioning electronics to be employed to correct, or partially correct for these errors, resulting in a more accurate operation of the envelope load-pull loop. Figure 4.24 shows a simple flow model for the envelope loop. To keep the model as simple as possible, small errors introduced by loss and directivity of passive components have been neglected.

In the model, Γ_0 represents the system impedance, T_D represents the transfer function of the demodulator, D represents the DC offset induced by the demodulator, and Γ is the transfer function of the control electronics given in equation 9, which in an ideal system is solely responsible for setting the desired impedance. M is the DC offset induced by the modulator and T_M is the transfer function of the modulator.

$$\Gamma = X + jY \tag{9}$$

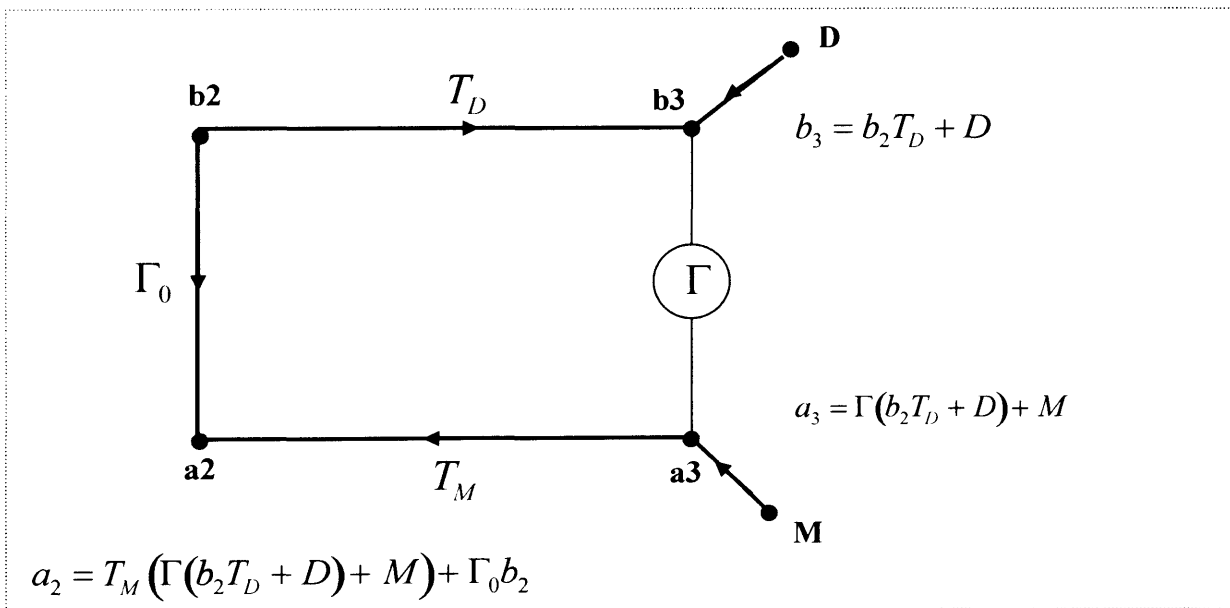


Figure 4.24 – Simple Error flow model of the Envelope Load Pull Loop

From the error flow model, it is clear that the injected signal a_2 is given by equation 10 -

$$a_2 = T_M (\Gamma (b_2 T_D + D) + M) + \Gamma_0 b_2 \quad (10)$$

From this expression it can be seen that the biggest issue is error introduced by DC offsets generated by the modulator (M) and demodulator (D), as these terms become independent of the signal generated by the device b_2 . Thus, as the drive conditions change, this causes a change to the output signal b_2 . Since the offsets do not change in proportion, a_2 fails to track b_2 and the impedance set by the control electronics, governed by Γ , will not equal that set. It is therefore vital that such errors be countered as far as is possible through the use of conditioning electronics. It is clear from the characterisation of the demodulator that D cannot simply be removed as the offset has drive dependence, so it is important to fully quantify the load error that occurs due to such offsets. The percentage error associated with any remaining DC offsets from the demodulator and modulator is therefore derived below.

Although the other sources of error scale with b_2 , it is still important to deal with these errors to ensure that the impedance set will be the impedance achieved. The offset that results from the system impedance, Γ_0 , can easily be calibrated out by employing a constant offset in the generated X and Y control signals, reducing the expression for a_2 given by equation 11.

$$a_2 = T_M (\Gamma (b_2 T_D + D) + M) \quad (11)$$

As the characterisation of the demodulator and modulator showed that the transfer functions T_D and T_M are linear within the flat bandwidth, we can assume these are equal to 1, thus reducing the expression to equation 12.

$$a_2 = (\Gamma b_2 + \Gamma D + M) \quad (12)$$

If we now assume that there are remaining errors from DC offsets in the system, where D remains due to the drive dependent offset of the demodulator, and M results from any small remaining DC error introduced by the combination of the control circuit and modulator, the load set is given by equation 13.

$$\Gamma_{Set} = \frac{a_2}{b_2} = \Gamma + \left[\frac{\Gamma D}{b_2} + \frac{M}{b_2} \right] \quad (13)$$

As the load should be purely dependent upon Γ , the percentage error in the set load is clearly given by equation 14.

$$\%Error(\Gamma) = \left[\frac{D}{b_2} + \frac{M}{b_2\Gamma} \right] \times 100 \quad (14)$$

It is important to note that D , M , Γ and b_2 are complex quantities, which describe the magnitude and phase of the respective vectors. Therefore it is possible for these errors to add or subtract, depending upon the relative phase of these vectors.

Clearly, only an ideal case where all errors are dynamically corrected would result in a_2 being given by equation 15, by setting the remaining errors D and M to zero.

$$a_2 = b_2(\Gamma) \quad (15)$$

The only case where impedance could be directly set by the user-entered reflection coefficient, Γ , is a case where all errors are removed. In this case, the reflection coefficient is set only by the user-entered values of X and Y , as shown in equation 16.

$$\Gamma_{Set} = \frac{a_2}{b_2} = \Gamma = (X + jY) \quad (16)$$

The characterisation of the various components within the envelope loop indicates that it will not be practical to correct for all of the sources of error using an analogue electronic solution. However, the above analysis does highlight the importance of minimising sources of DC offset in the loop as these errors will lead to constant offset vectors that do not vary with the drive conditions, making the load set drive dependent at the centre frequency. The following section will describe the conditioning electronics employed to bring the operation of the

envelope load pull loop as close as possible to the ideal case outlined in equations 13 and 14 above.

4.7 Final Electronics Block with Conditioning Electronics

It is clear from the generation of the error model that the final electronics block should contain three distinct sections. Firstly, demodulator conditioning deals with the correction of errors introduced by the demodulator as well as the scaling of the I and Q signals to the appropriate levels. The conditioning block effectively becomes part of the demodulator and the I and Q produced from this block are corrected. Secondly, the control block is the original control circuitry and thirdly, the modulator conditioning block effectively corrects for small errors introduced by the modulator and control circuitry, and again scales the I and Q signals to the appropriate levels. The block diagram of the final electronics block is shown in figure 4.25.

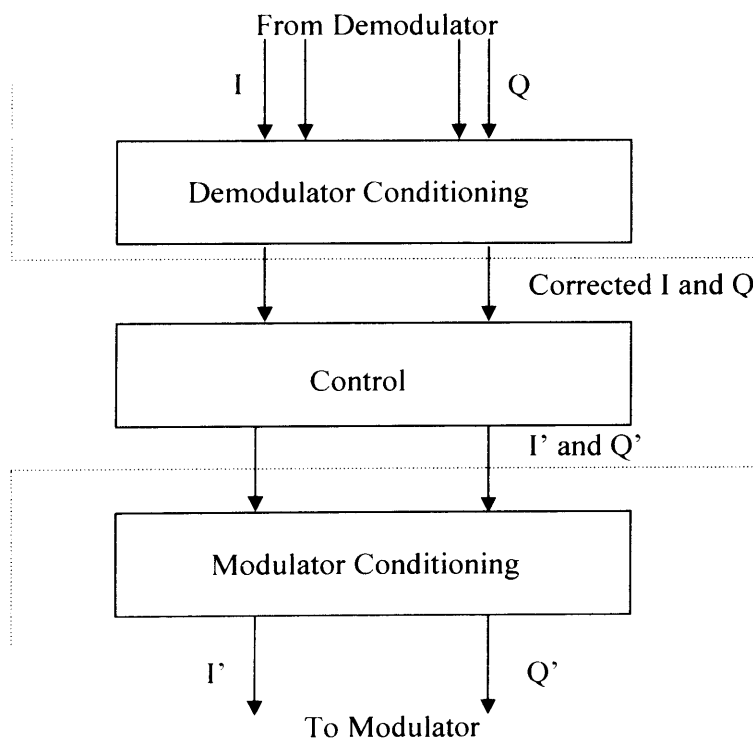


Figure 4.25 – Simple flow graph of the Envelope Load Pull Loop

The following sections will describe in detail the architectures employed in the demodulator and modulator conditioning blocks, and then uncover the final design of the realised electronics block.

4.7.1 Demodulator Conditioning Block

This block contains electronics to convert the differential I and Q signals from the demodulator into single ended I and Q. These signals are then processed to remove the two main common errors introduced by the demodulator. Namely the correction of errors associated with slight uneven channel gain and DC offsets added to the channels by the demodulator.

Uneven channel gain is solved by the inclusion of variable gain stages on the output of both I and Q, thus allowing the correction of any imbalance. The second error that can be corrected is miss-centred demodulators, and this can be combated by applying DC offsets to the output I and Q signals. The schematic of the demodulator condition block is shown in figure 4.26 and includes eight operational amplifiers, with a photograph shown in figure 4.27.

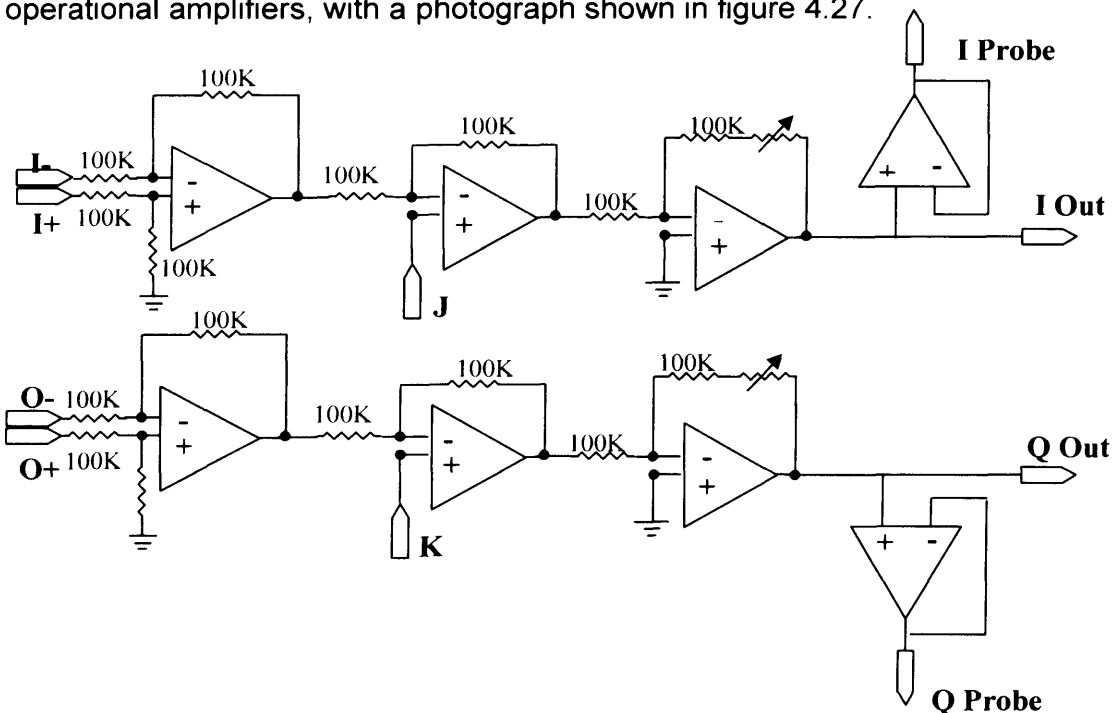


Figure 4.26 Schematic of the realised Demodulator Conditioning Block

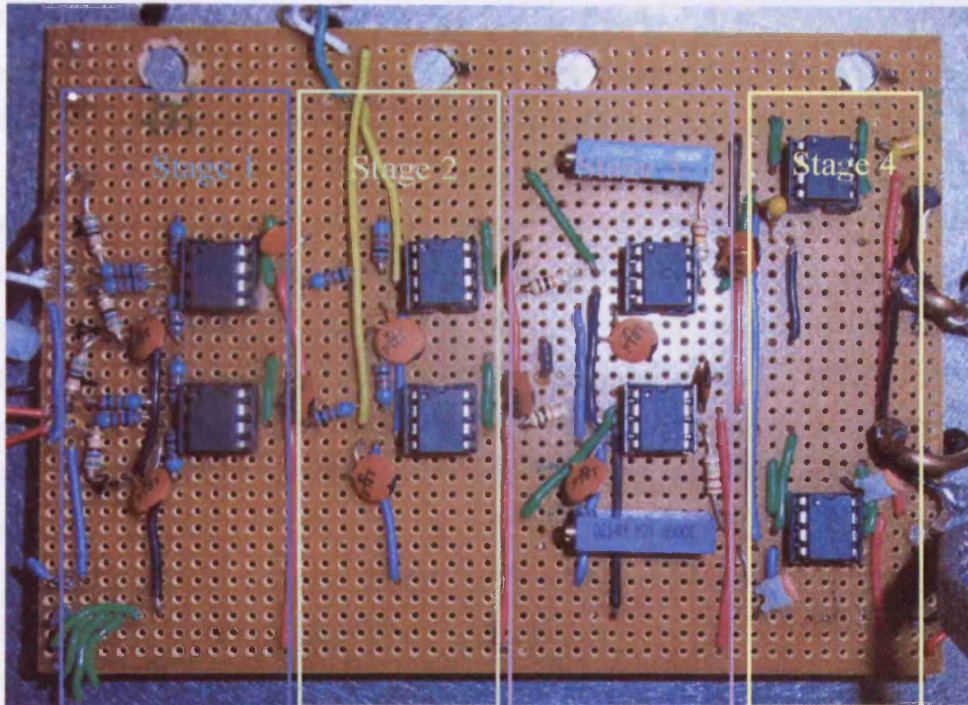


Figure 4.27 Photograph of the realised Demodulator Conditioning Block

Stage 1 - is an op-amp configuration used to convert the differential output of the demodulator to single ended I and Q. This stage has no gain.

Stage 2 - is an inverting op-amp configuration where the non-inverting op-amp input is used to apply a DC offset, to counter any offsets induced in the demodulator.

Stage 3 - is a variable gain stage, again employing an inverting op-amp configuration. Variable gain is achieved through the use of a variable resistor in series with the feedback resistor.

Stage 4 - is a buffer stage. Two buffer amplifiers are included to avoid loading the circuit when attempting to probe within the envelope load-pull loop.

All stages employ an OP177 Ultra-Precision Operational Amplifier produced by Analog Electronics. More details on these devices can be found in the data sheet [24]. Clearly this solution does not correct all of the errors introduced by the

demodulator. However, electronics to deal with any of the other error sources would be too complex and would be better dealt with digitally, which will be discussed in the future work. Furthermore, results presented below suggest that dealing with these two main error sources is sufficient for a good operation.

Combining the demodulator with conditioning block and repeating the experiment conducted in the demodulator characterisation section highlights the removal of the major sources of error. The presented result shows the optimisation of performance over a given dynamic range, to overcome the problem of the drive dependent DC offsets. Importantly the DC offsets have been dramatically reduced in this case over a 10 dB dynamic range, ensuring that the problems associated with this have been nullified. Figure 4.28a shows the 3 dimensional I-Q plot for varying drive conditions. Appropriate correction has been applied to J and K in order to centre the circles around 0 V. figure 4.28b shows the same information looking vertically, highlighting the lack of drive dependence. It is clear that the circles produced by sweeping the phase of the RF input signal are now circular and are centred around a centre point located at 0 V.

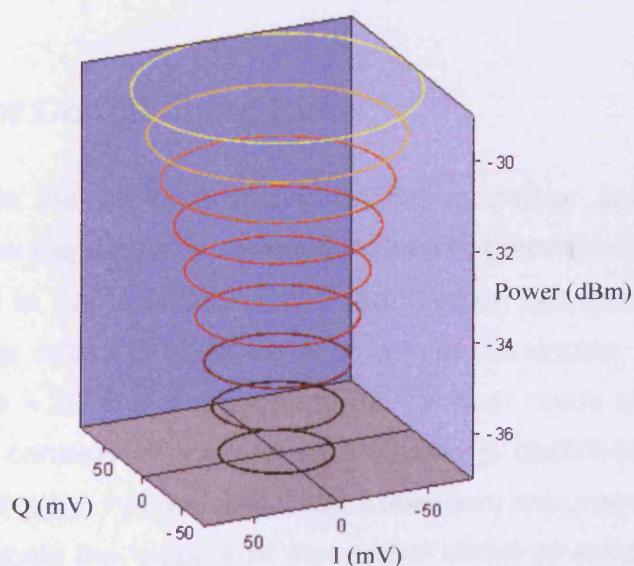


Figure 4.28(a) 3-D plot of I and Q as input to demodulator is varied in magnitude and phase

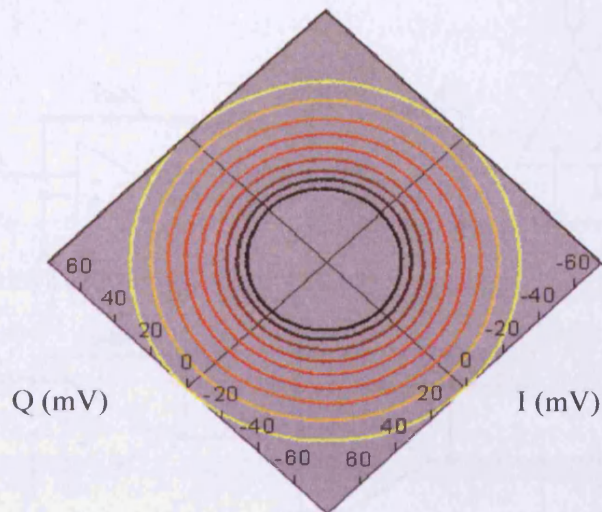


Figure 4.28(a) 2-D plot of I and Q as input to demodulator is varied in magnitude and phase

The bandwidth of the combined demodulator and conditioning will now of course be limited by the op-amps used in the conditioning block. From analysis of the data sheet [24], this bandwidth will be at least 100 kHz before gain roll off.

4.7.2 Modulator Conditioning Block

The third block is the pre-conditioning for the modulator and has the same functionality as the demodulator conditioning block; other than there is no need for the differential to single ended conversion. It again has gain control for each signal path and the option to offset either or both of the signals. A circuit diagram is shown in figure 4.29 and a photograph of the final circuit is shown in figure 4.30. The board consists of the stages 2, 3 and 4 described above. As the internal ESG modulator needed very little correction, the main purpose of this board was to re-scale the outputs of the control circuit to extract the maximum dynamic range for the modulator. DC offset control was kept in place to allow for future expansion towards alternative modulators, which could well require additional DC offset control.

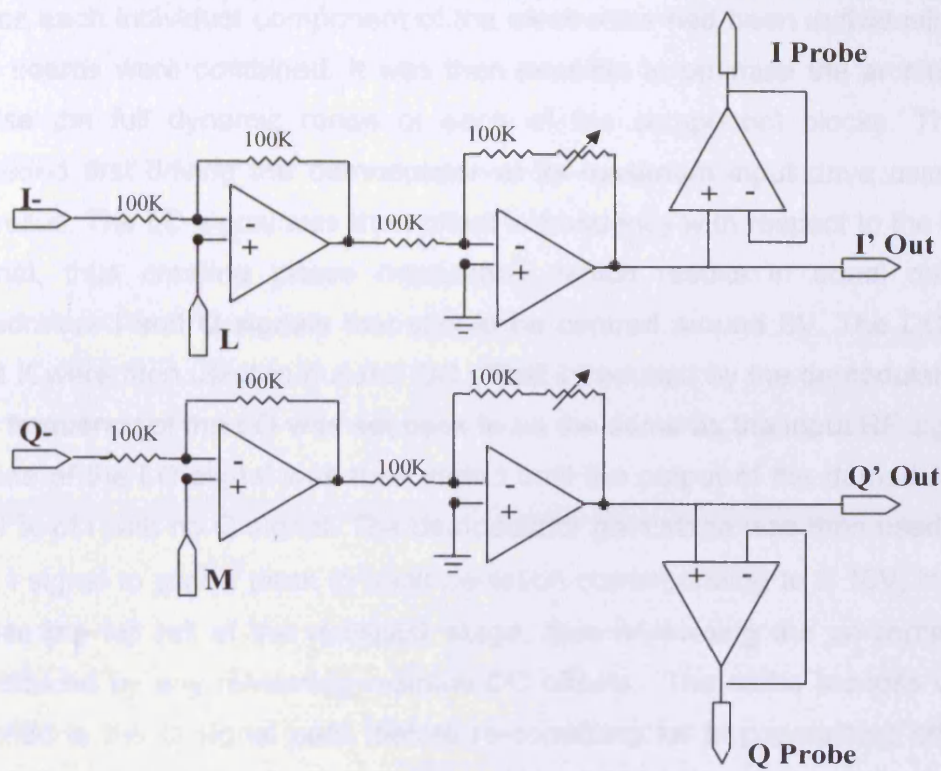


Figure 4.29 Circuit Diagram of Modulator Conditioning Block

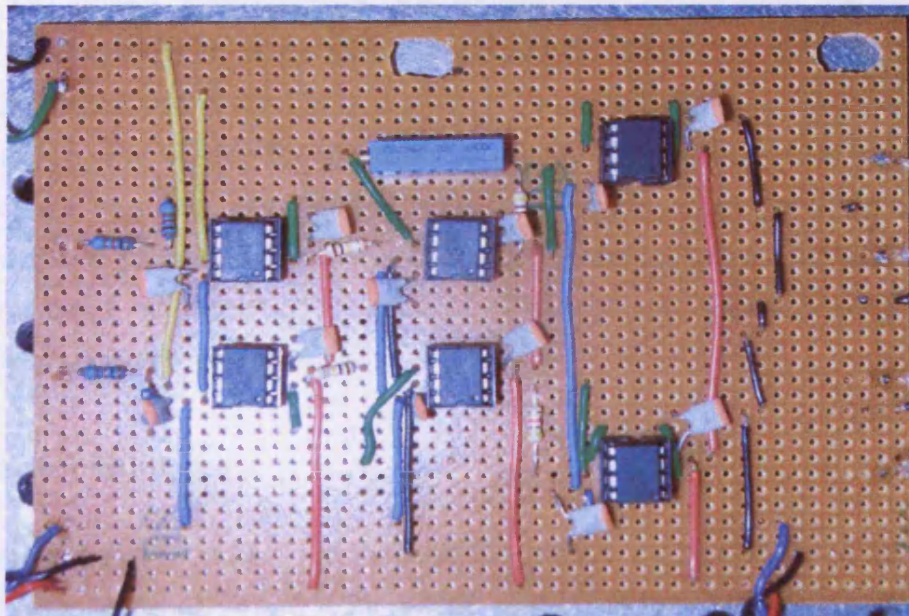


Figure 4.30 Photograph of the realised Modulator Conditioning Block

Once each individual component of the electronics had been individually tested, the boards were combined. It was then possible to optimise the architecture to utilise the full dynamic range of each of the component blocks. The setup included first driving the demodulator at its maximum input drive using a CW stimulus. The LO signal was then offset in frequency with respect to the input RF signal, thus creating phase modulation, which results in equal magnitude, quadrature I and Q signals that should be centred around 0V. The DC offset J and K were then used to null the DC offset introduced by the demodulator. Next, the frequency of the LO was set back to be the same as the input RF signal. The phase of the LO signal was then varied until the output of the demodulator was 100 % of I with no Q signal. The demodulator gain stage was then used to scale the I signal to give a peak to peak deviation corresponding to $\pm 10V$, in order to utilise the full rail of the multiplier stage, thus minimising the percentage error introduced by any remaining residual DC offsets. The same process was then applied to the Q signal path, before re-correcting for any remaining offset. The multiplier stage was set with $X = 1 V$ and $Y = 0 V$, which should simply reproduce the input on the output. DC offset signals L and M were used to remove any minimal DC offsets introduced by the multiplication stage from the I and Q signals. Finally, the gain stage of the modulator conditioning board was used to reduce the magnitude of the I and Q signals to meet the maximum input range of the modulator, which using the standard value quoted in literature [22] was 0.5 V. The envelope loop had now been optimised for the optimum performance and was ready for a full test with the measurement system. The next chapter of the thesis provides a validation of the envelope load-pull architecture, through a full test of the architectures capabilities.

4.8 Chapter Summary

This chapter has presented solutions to the unique problems that arise when load-pull is to be employed in a multi-tone system. When multi-tone stimuli are employed, additional distortion components arise in-band at the fundamental, at

harmonic-bands and also at the base-band. Any impedance control solution therefore has to be capable of controlling impedance across a bandwidth at both base-band and RF frequencies to ensure control of all significant components. A two-stage approach was adopted, where one architecture was used to control base-band components and a second architecture was used to deal with RF components. This was simplified by the fact that there is a natural split in the measurement of these components, as discussed in chapter 2.

At the base-band, a standard open-loop active load-pull approach is adopted, offering control of all significant components through the use of multiple signal generators. At RF frequencies, there was no available solution, so a new approach termed envelope load-pull was realised. This is similar in nature to closed-loop active load-pull; however the RF signal is down-converted within the feedback loop. The base-band I and Q signals are then engineered in order to set the impedance seen at RF. This approach offers the benefits of a closed-loop approach without the RF stability issues noted earlier in this chapter. The ability to hold a constant load under varying drive conditions and across bandwidth means the architecture is ideal for use over a modulated bandwidth.

Each sub-component in the envelope load-pull loop has been fully characterised and solutions have been realised to attempt to deal with any errors introduced. The components have been integrated to form the full envelope load-pull loop and all components have been tuned to operate in their optimum range. Table 4.1 summarises the various components used in the envelope load-pull architecture.

Component	Base-Band Flat Bandwidth	RF Bandwidth	Dynamic Range	Offset Issues
Demodulator	20 MHz	0.8-2.7 GHz	Good (23 dB)	Yes
Modulator	10 MHz	0.025-4 GHz	Excellent	No
Op-Amps	100 kHz	N/A	Excellent	No
Multipliers	400 kHz	N/A	Excellent	No

Table 1 – Summary of Components used in the Envelope Load-pull Architecture

The table shows that the current capabilities of the components used in the envelope load-pull loop. Clearly, the base-band bandwidth is limited at present by the operational amplifiers and the multipliers. However the fundamental aim of this work is to prove the concept of the envelope load-pull and as such, at least in this initial investigation, the limited bandwidth was not such an issue. Even with limited bandwidth, the system lends itself to one of the major applications; to perform ultra-fast CW characterisation using slow modulation. The future work section discusses the options available to increase the base-band bandwidth to allow the impedance control to be employed over wider band.

The RF bandwidth of both the demodulator and the modulator is excellent with scope to use the envelope load-pull to control harmonic-band impedance as well as the fundamental-band impedance. The dynamic range of all components is good and is more than sufficient for the application. Drive level dependent offsets are still present in the demodulator as discussed earlier in the chapter, although these do not cause too much of an issue. This will be demonstrated through measurement in the next chapter.

4.9 References

1. Feipeng Wang; Yang, A.H.; Kimball, D.F.; Larson, L.E.; Asbeck, P.M. “*Design of wide-bandwidth envelope-tracking power amplifiers for OFDM applications*” IEEE Transactions on Microwave Theory and Techniques, Volume 53, Issue 4, Part 1, April 2005 Page(s):1244 – 1255.
2. Benedikt, J.; Gaddi, R.; Tasker, P.J.; Goss, M. “*High-power time-domain measurement system with active harmonic load-pull for high-efficiency base-station amplifier design*” IEEE Transactions on Microwave Theory and Techniques, Volume 48, Issue 12, Dec. 2000 Page(s):2617 – 2624.
3. Lees, J.; Benedikt, J.; Hilton, K.P.; Powell, J.; Balmer, R.S.; Uren, M.J.; Martin, T.; Tasker, P.J. “*Characterisation of an experimental gallium nitride microwave Doherty amplifier*” 2005 European Microwave Conference, Volume 2, 4-6 Oct. 2005.
4. Barataud, D.; Campovecchio, M.; Nebus, J.-M. “*Optimum design of very high-efficiency microwave power amplifiers based on time-domain harmonic load-pull measurements*” IEEE Transactions on Microwave Theory and Techniques, Volume 49, Issue 6, Part 1, June 2001 Page(s):1107 – 1112.
5. Vuolevi, J.H.K.; Rahkonen, T.; Manninen, J.P.A. “*Measurement technique for characterizing memory effects in RF power amplifiers*” IEEE Transactions on Microwave Theory and Techniques, Volume 49, Issue 8, Aug. 2001 Page(s):1383 – 1389.
6. Abdulrahman Alghanim; Jonathan Lees; Tudor Williams; Johannes Benedikt, Paul Tasker “*Using active IF load-pull to investigate electrical base-band memory effects in high-power LDMOS transistors*” IEEE Asia-Pacific Microwave Conference 2007
7. Technical data sheet “*Intelligent Computer Controlled Microwave Tuner iCCMT-1808*” (<http://www.focus-microwaves.com/template.php?unique=237>). Accessed Jan. 2007.
8. Technical data sheet 4T-070 Maury Microwave. “High-Gamma Automated Tuners (HGTTM)” Accessed Jan. 2007.
9. Deshours, F.; Bergeault, E.; Blache, F.; Villotte, J.-P.; Villeforceix, B. “*Experimental comparison of load-pull measurement systems for nonlinear power transistor characterization*” IEEE Transactions on Instrumentation and Measurement, Volume 46, Issue 6, Dec. 1997 Page(s):1251 – 1255.
10. Bava, G.P.; Pisani, U.; Pozzolo, V. “*Active load technique for load-pull characterisation at microwave frequencies*” Electronics Letters, Volume 18, Issue 4, February 18 1982 Page(s):178 – 180.

11. Hughes, B.; Ferrero, A.; Cognata, A. “**Accurate on-wafer power and harmonic measurements of MM-wave amplifiers and devices**”, IEEE/MTT-S International Microwave Symposium Digest 1992 vol.2, Page(s):1019 - 1022.
12. Ferrero, A.; Teppati, V.; Pisani, U. “**Recent Improvements in Real-Time Load-Pull Systems**” Proceedings of the IEEE Instrumentation and Measurement Technology Conference, 2006. IMTC 2006, April 2006 Page(s):448 – 451.
13. De Groote, F.; Verspecht, J.; Barataud, D.; Teyssier, J.-P. “**An improved coupling method for time domain load-pull measurements**” 2005 European Microwave Conference Volume 1.
14. Bensmida, S.; Bergeault, E.; Abib, G. I.; Huyart, B. “Power Amplifier Characterization: An Active Load-Pull System Based on Six-Port Reflectometer Using Complex Modulated Carrier” IEEE Transactions on Microwave Theory and Techniques, Vol. 54, NO 6, June 2006, Page(s):2707-2712.
15. Takayama, Y. “**A New Load-Pull Characterization Method for Microwave Power Transistors**” MTT-S International Microwave Symposium Digest 1976, Volume 76, Issue 1, Page(s):218 – 220.
16. Poulin, D.D.; Mahon, J.R.; Lanteri, J.-P. “**A high power on-wafer pulsed active load pull system**” MTT-S International Microwave Symposium Digest 1976, Volume 76, Issue 1, vol.3, Page(s):1431 - 1434
17. Williams, D.J.; Leckey, J.; Tasker, P.J. “**A study of the effect of envelope impedance on intermodulation asymmetry using a two-tone time domain measurement system**” IEEE/MTT-S International Microwave Symposium Digest 2002, Volume 3, 2-7 June 2002 Page(s):1841 – 1844.
18. Asbeck, P.; Larson, L.; Kimball, D.; Yu Zhao; Feipeng Wang; Dongjiang Qiao “**High dynamic range, high efficiency power amplifiers for wireless communications**” Proceedings of Bipolar/BiCMOS Circuits and Technology Meeting, 2005. 9-11 Oct. 2005 Page(s):103 – 107.
19. Technical data sheet, National Instruments “**NI PCI-6703 Card Static Analog Voltage Output**” (http://www.ni.com/pdf/products/us/4daqsc362_366-367_373_368.pdf) Accessed March 2006.
20. Technical data sheet, Analog devices “**AD633 Low Cost Multiplier**” (http://www.analog.com/UploadedFiles/Data_Sheets/AD633.pdf) Accessed April 2006.
21. Technical data sheet, linear Technology “**LT5575 “800MHz to 2.7GHz High Linearity Direct Conversion Quadrature Demodulator”**”

(<http://www.linear.com/pc/productDetail.jsp?navId=H0,C1,C1011,C1725,P36240>)
Accessed March 2007.

22. Agilent E4433B ESG Signal Generators User's Guide
(<http://cp.literature.agilent.com/litweb/pdf/E4400-90323.pdf>) Accessed March 2006.

23. Agilent E8267D PSG Signal Generators Data Sheet
(<http://cp.literature.agilent.com/litweb/pdf/5989-0697EN.pdf>) Accessed March 2006.

24. Technical data sheet, Analog Devices “**OP177 Ultra-Precision Operational Amplifier**” (http://www.analog.com/en/prod/0,,759_786_OP177,00.html) Accessed Feb. 2006.

Chapter 5 – Validation of the envelope Load-Pull Architecture

5.1 Introduction

The developed envelope load-pull architecture described in the previous chapter and presented in [1-3] will be validated in this chapter. The loop consists of an I-Q demodulator, conditioning and control circuitry and an I-Q modulator. The control circuit allows any impedance to be synthesised on the Smith chart using control signals (X and Y). Furthermore the architecture ensures that a constant load is maintained for varying RF magnitude and phase.

This chapter will use measurements performed on both passive and active structures to validate the performance of the optimised envelope load-pull architecture. CW measurements will be used to fully validate the control and accuracy of the synthesised impedance, before using stepped CW measurements to validate the system's ability to maintain constant impedance under varying drive conditions (magnitude and phase). Finally, multi-tone

measurements will be used to show the useable bandwidth of the envelope load-pull architecture.

As discussed in detail in the previous chapter, by far the most significant source of error introduced by the envelope load-pull loop are introduced by DC-offsets. Although every effort has been made to remove this source of error, it is virtually impossible with the current configuration to completely remove the DC offsets. For this reason, this chapter will also examine the impact these offsets have upon the final presented impedance.

5.2 Optimised configuration of the Envelope Load-pull Architecture

The flow chart shown in figure 5.1 shows the components that make up the envelope load-pull architecture. In each case the desired operational range for optimum performance is shown.

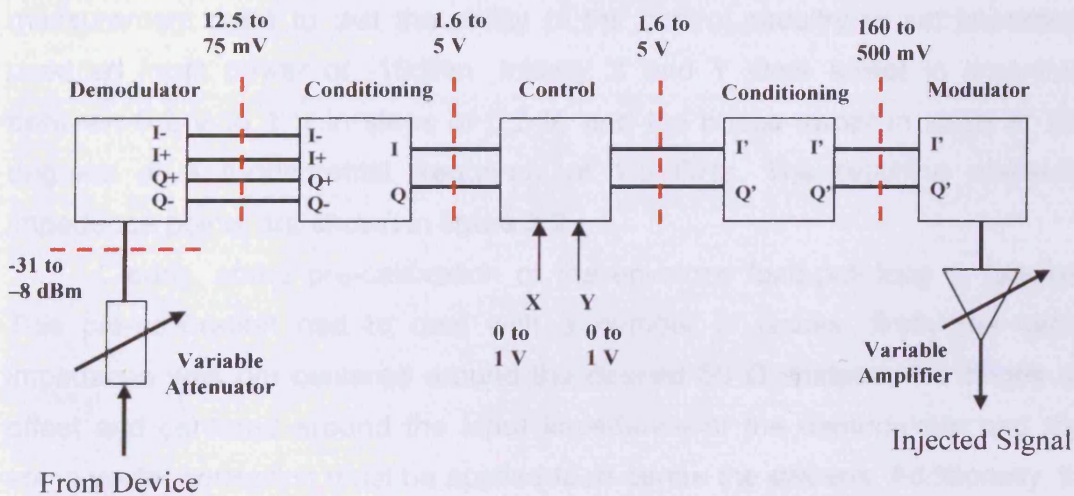


Figure 5.1 – Flow Graph of the optimized Envelope Load-pull Architecture

It is important to note, as shown in figure 5.1, that for optimum performance it is essential to include a variable attenuator before the demodulator to ensure that whatever the output power of the DUT, the demodulator always operates in its

linear range. At the output, an amplifier is required to allow the injected signal to be at the correct power to achieve the required load.

5.3 Verification of X-Y Control

The first step in the verification of the envelope load-pull architecture is to analyse the impedance control that can be achieved using the X and Y control signals. This will also allow for a calibration process to be defined, ensuring that the impedance achieved is as close as possible to impedance required.

Initial measurements were conducted using a thru line in place of the DUT. As described in the previous chapter, steps were taken to ensure all components within the envelope load-pull loop are used over their optimum ranges. To ensure linearity, the maximum input power to the demodulator was limited to -8 dBm. The maximum range of the multipliers and op-amps was $\pm 5V$ and the maximum input voltage to the modulator was 0.5V. The initial measurement used to test the ability of the control circuitry to set impedance used an input power of -10dBm. Initially X and Y were swept in magnitude between 0.2 V to 1 V in steps of 0.2 V, and the phase swept in steps of 22.5 degrees at a fundamental frequency of 1.8 GHz. The resulting measured impedance points are shown in figure 5.2.

Clearly, some pre-calibration of the envelope load-pull loop is required. This pre-calibration had to deal with a number of issues: firstly the centre impedance was not centered around the desired 50 Ω ; instead, the circles are offset and centered around the input impedance of the demodulator and thus some vector correction must be applied to re-centre the sweeps. Additionally, the starting phase of the sweeps is random and depends arbitrarily upon the phase length of connecting cables. This offset must therefore be measured and a correction applied. Finally the variable amplifier must be used to scale the injected signal such that a set magnitude of 1 results in impedance at the edge of the Smith chart.

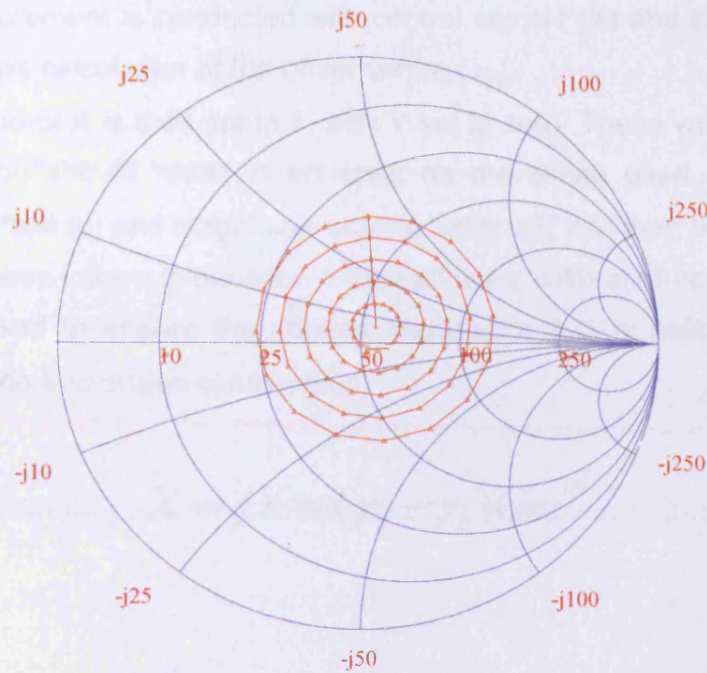


Figure 5.2 – Initial un-calibrated performance of the envelope load-pull impedance control

In order to fully analyze these results, it is first necessary to compensate for the offset centre. To achieve this, the centre point was found and the difference in the real and imaginary plain was calculated; this value was then subtracted from each point in the sweep. Although the envelope load-pull is not yet calibrated it is however, already clear that it is operating successfully. Table 1 and Table 2 show the predicted and measured phase difference for the two largest circles, indicating that circles of constant magnitude are achieved and that the correct phase steps are seen.

The tables indicate that the control is working well, with phase steps that are correct to within less than a degree. The next step is to calibrate the loop to correct for the centre of the sweeps along with the phase offset and magnitude scaling. An automated calibration procedure was formulated allowing calibration of the envelope load-pull at the press of a button. The calibration process can be described by the following steps.

1. A measurement is conducted with control signals (X) and (Y) set to zero, this allows calculation of the offset centre (γ_c).
2. The value of X is then set to 1, with Y set to zero. These values, following calibration should result in an open on the Smith chart. The required phase offset (θ) and magnitude-scaling factor (G) can then be obtained.
3. Using these values in equation 1 then allows a calibrated value of X and Y to be used to ensure the chosen impedance (γ_s) is calibrated for any magnitude and phase combination.

$$X + jY = (\gamma_s - \gamma_c)Ge^{j\theta} \quad (1)$$

Circle	Point	Measured Phase (Degrees)	Phase Change (Degrees)	Expected Phase Change (Degrees)	Phase Change Error (Degrees)
4	1	93.9449	n/a	n/a	n/a
4	2	116.295	22.350	22.5	-0.150
4	3	138.601	22.306	22.5	-0.194
4	4	160.855	22.254	22.5	-0.246
4	5	-176.897	22.248	22.5	-0.252
4	6	-154.629	22.268	22.5	-0.232
4	7	-132.183	22.446	22.5	-0.054
4	8	-109.350	22.833	22.5	0.333
4	9	-86.161	23.190	22.5	0.689
4	10	-62.925	23.236	22.5	0.736
4	11	-39.8838	22.769	22.5	0.541
4	12	-17.115	22.450	22.5	0.269
4	13	5.335	22.180	22.5	-0.050
4	14	27.513	22.062	22.5	-0.322
4	15	49.575	22.150	22.5	-0.438
4	16	71.725	22.282	22.5	-0.350

Table 1 – Predicted and measured Phase change between points in the sweep for circle

4

<i>Circle</i>	<i>Point</i>	<i>Measured Phase (Degrees)</i>	<i>Phase Change (Degrees)</i>	<i>Expected Phase Change (Degrees)</i>	<i>Phase Change Error (Degrees)</i>
5	1	93.847	n/a	n/a	n/a
5	2	116.097	22.251	22.5	-0.250
5	3	138.300	22.203	22.5	-0.297
5	4	160.512	22.212	22.5	-0.288
5	5	-177.250	22.238	22.5	-0.262
5	6	-154.985	22.265	22.5	-0.235
5	7	-132.458	22.527	22.5	0.027
5	8	-109.480	22.978	22.5	0.478
5	9	-86.142	23.338	22.5	0.838
5	10	-62.821	23.320	22.5	0.820
5	11	-39.725	23.097	22.5	0.587
5	12	-16.914	22.811	22.5	0.311
5	13	5.522	22.435	22.5	-0.065
5	14	27.638	22.116	22.5	-0.384
5	15	49.640	22.002	22.5	-0.498
5	16	71.741	22.101	22.5	-0.399

Table 2 – Predicted and measured Phase change between points in the sweep for circle 5

After calibration, it is clear that the centre of the collected sweeps has been normalized to 50Ω . Phase has been re-aligned to start at zero and the magnitude has been normalized to 1. The same impedance sweep was conducted after calibration by varying the X and Y control signals, again employing a CW stimulus with centre frequency of 1.8 GHz. The results are shown in figure 5.3. Whilst the plot highlights that the system is operating well, it also shows that there are some remaining issues with the loop operation. This performance is however seen as the optimum that can be obtained using a simple analogue electronics approach adopted in this project, with remaining errors likely to be caused by drive dependent DC offsets. The future work section of this thesis will discuss the possibility of further improvements. Tables 3 and 4 show the measured and predicted magnitude and phase of the set reflection coefficient, along with the observed errors for the two largest circles. It is important to note at this point that some of the errors appear quite large on the Smith chart. This is compounded by the fact that the entire Smith chart is covered for this impedance sweep, which will very rarely be the case for a real

device characterization, where a much smaller area is typically swept (as will be seen in the next section where devices are characterised).

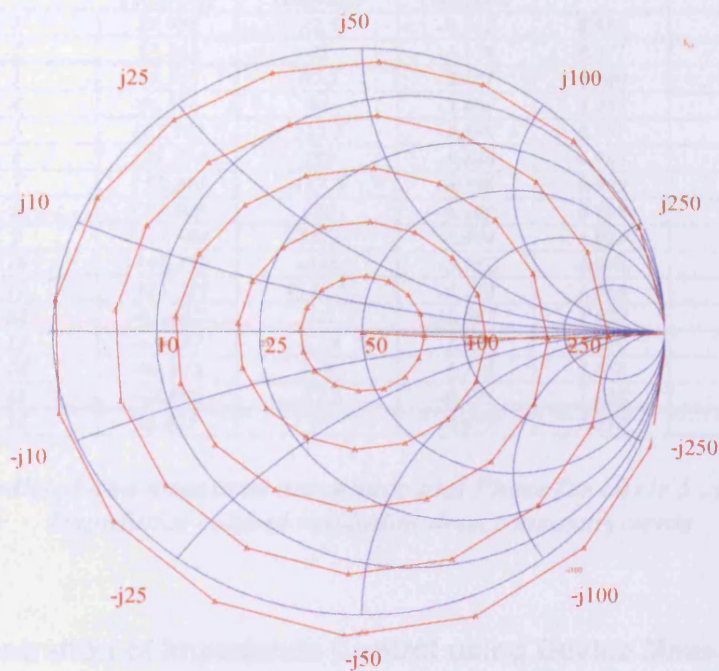


Figure 5.3 – Calibrated Performance of the envelope load-pull loop

Circle	Point	Measured Phase (Degrees)	Expected Phase (Degrees)	Phase Error (Degrees)	Measured Magnitude	Expected Magnitude	Magnitude Error
4	1	20.704	22.5	-1.796	0.798	0.8	-0.002
4	2	42.578	45	-2.422	0.782	0.8	-0.018
4	3	64.391	67.5	-3.110	0.770	0.8	-0.030
4	4	86.244	90	-3.757	0.765	0.8	-0.035
4	5	108.078	112.5	-4.220	0.767	0.8	-0.033
4	6	129.944	135	-5.056	0.777	0.8	-0.023
4	7	151.861	157.5	-5.639	0.791	0.8	-0.009
4	8	174.465	180	-5.535	0.802	0.8	0.002
4	9	-162.610	-157.5	-5.110	0.818	0.8	0.018
4	10	-139.464	-135	-4.464	0.836	0.8	0.036
4	11	-116.245	-112.5	-3.745	0.851	0.8	0.050
4	12	-92.955	-90	-2.956	0.857	0.8	0.057
4	13	-69.653	-67.5	-2.153	0.855	0.8	0.055
4	14	-46.534	-45	-1.534	0.845	0.8	0.045
4	15	-23.682	-22.5	-1.182	0.830	0.8	0.030
4	16	-1.006	0	-1.006	0.8112	0.8	0.012

Table 3 – Predicted and measured magnitude and Phase for circle 4 after calibration

Circle	Point	Measured Phase (Degrees)	Expected Phase (Degrees)	Phase Error (Degrees)	Measured Magnitude	Expected Magnitude	Magnitude Error
5	1	21.988	22.5	-0.512	0.988	1	-0.012
5	2	43.862	45	-1.138	0.971	1	-0.029
5	3	65.345	67.5	-2.151	0.960	1	-0.040
5	4	86.596	90	-3.404	0.955	1	-0.045
5	5	107.901	112.5	-4.599	0.957	1	-0.043
5	6	129.354	135	-5.646	0.965	1	-0.035
5	7	151.204	157.5	-6.296	0.979	1	-0.021
5	8	173.599	180	-6.401	0.998	1	-0.002
5	9	-163.504	-157.5	-6.004	1.022	1	0.022
5	10	-140.232	-135	-5.232	1.046	1	0.046
5	11	-116.729	-112.5	-4.229	1.066	1	0.066
5	12	-93.087	-90	-3.087	1.074	1	0.074
5	13	-69.487	-67.5	-1.990	1.072	1	0.072
5	14	-46.116	-45	-1.116	1.058	1	0.578
5	15	-23.095	-22.5	-0.595	1.035	1	0.035
5	16	-0.421	0	-0.451	1.010	1	0.009

**Table 4 – Predicted and measured magnitude and Phase for circle 5 after calibration
Impedance control validation device measurements**

5.3.1 Demonstration of Impedance Control using Device Measurements

This section contains measurements conducted using a GaAs HBT device. The device is on wafer, possesses an I_{Max} of 120mA, and all measurements are completed at 1.8 GHz. The first measurement conducted used the control signals to sweep load circles around 50 Ω with reflection coefficient magnitudes of 0.1, 0.2 and 0.3 respectively, and phase in steps of 22.5 degrees. This measurement is a good gauge of system performance because as we move towards device characterisation and sweep output impedance, this results in a change in the output power of the device. This means that the required load circles will only be achieved if the envelope load-pull both sets the correct impedance and then correctly tracks any change in power. The Smith chart shown in figure 5.4 shows the predicted and measured performance.

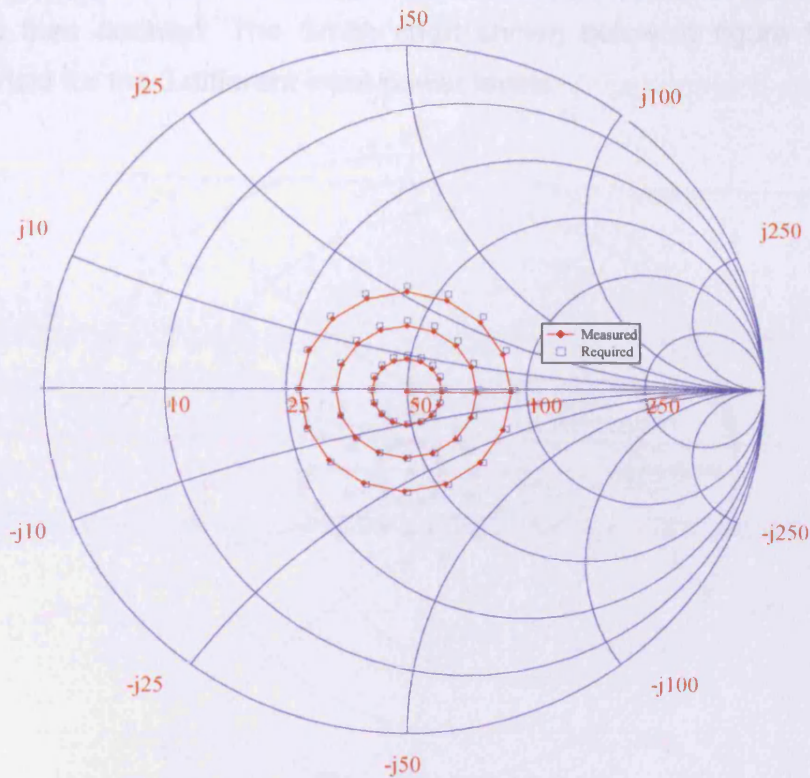


Figure 5.4 – Predicted and measured results for the load impedance presented to the HBT as the load impedance is swept using the control signals in circles around 50Ω

The plot indicates the successful operation of the architecture with only small errors observed between predicted and measured impedances. It is important to reiterate at this point that the small errors would not effect any generation of a load-pull contours or models for a device as we still know the measured impedances, even if they are a little different to the required value. If, however, for any reason, a greater sensitivity in load impedance is required, it would be possible under CW operating conditions to combine the envelope load-pull loop with the iterative approach employed in an open loop system to achieve very tight control of the impedance. This would however impact on the speed of any load-pull sweeps. Clearly, under modulated operation, any such errors cannot be corrected.

As a further validation of the architecture, the same impedance sweep on the device was completed with varying input power, firstly with the input power

halved and then doubled. The Smith chart shown below in figure 5.5 shows results overlaid for the 3 different input power levels.

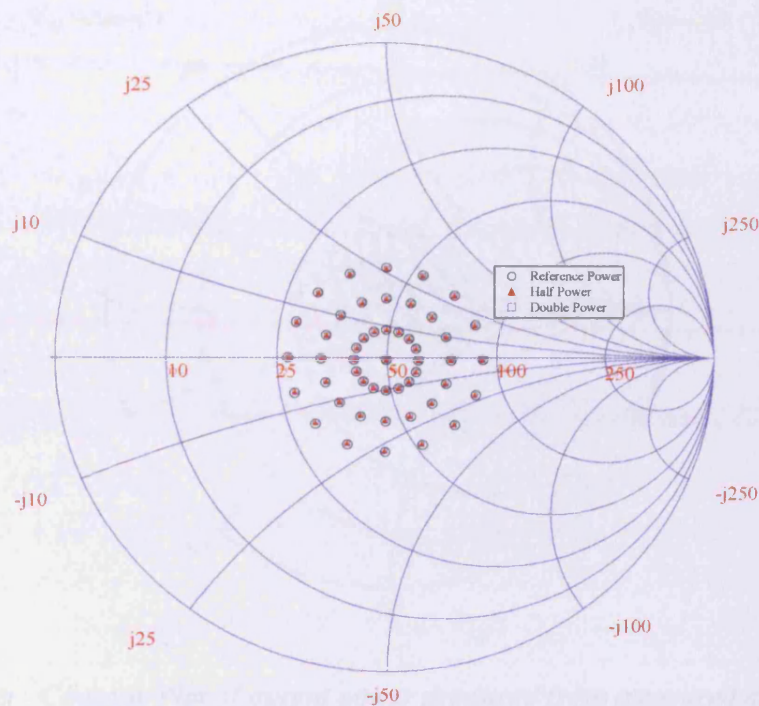


Figure 5.5 – Measured results for the load impedance presented to the HBT as the load impedance is swept using the control signals in circles around 50 Ω while input power is varied

The plot highlights excellent agreement in measured load impedance as the power is varied, offering a further indication that the envelope load-pull has been implemented and calibrated successfully. This kind of impedance sweep could be used for a variety of reasons; for example, it could be employed to create a lookup model of the device or to rapidly plot load pull contours of maximum power or efficiency. Figure 5.6 shows the extracted contours of output power versus fundamental load impedance when the device is driven with an input power of 0 dBm. The contour plot would suggest that the optimum impedance is not 50 Ω , as is typically the case for a power device. It would therefore be necessary to re-centre the load-pull sweep closer to the optimum impedance to achieve a more appropriate characterisation of the device. To do this, it is possible

to apply further DC offsets to X and Y to re-centre the sweep around the optimum impedance. This was completed and the resulting sweep is shown in figure 5.7.

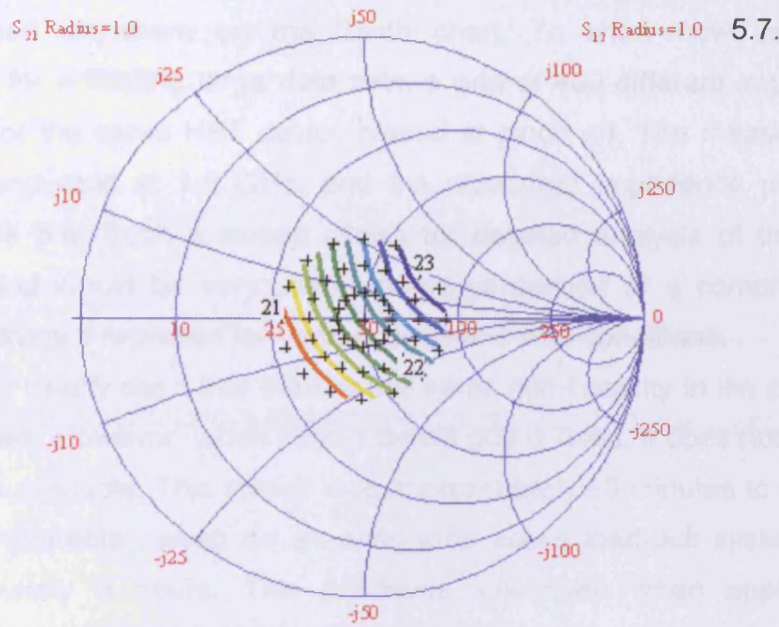


Figure 5.6 – Contour Plot of output power produced from measured data at the impedances shown in figure 5.7.

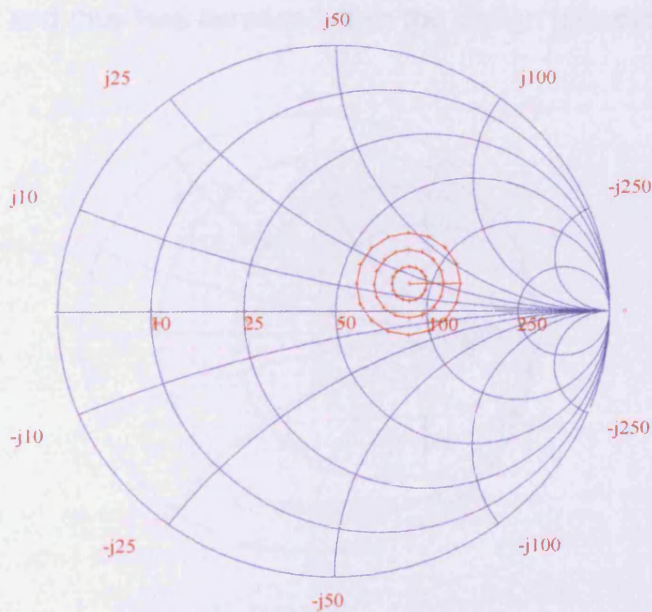


Figure 5.7 – Measured results for the load impedance presented to the HBT as the load impedance is swept using the control signals in circles around the optimum impedance

Although thus far the control signals have only been used to sweep circles of constant magnitude around a given load, it is possible to map any constellation of required load anywhere on the Smith chart. To show how useful this architecture is for collecting large data sets, a grid of 400 different impedances was mapped for the same HBT device biased at pinch off. The measurements were again conducted at 1.8 GHz, and the measured impedance points are shown in figure 5.8. Such a sweep allows for detailed analysis of the device performance and would be very useful in the generation of a comprehensive model of the device if repeated for various drive and bias conditions.

It can be clearly seen that there is still some non-linearity in the presented load-impedances. However, when such a dense grid is used, it does not degrade the information available. This sweep took approximately 40 minutes to complete whereas a comparable sweep on an open loop active load-pull system would take approximately 8 hours. This highlights that even when applying the envelope load-pull loop to more standard CW measurement applications, a massive time saving can be achieved. This would allow for much larger and finer grids to be used in device characterisation and modeling, leading to more accurate designs and thus less iteration within the design process.

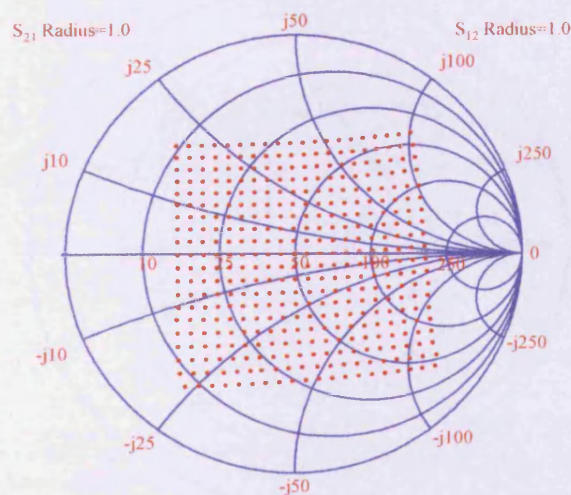


Figure 5.8 – Measured load impedance points presented to the HBT as the load impedance is swept using the control signals

Figure 5.9 shows a 3-D plot extracted from the measured grid, clearly indicating a surface of maximum power which could prove very useful in the design process. The same information is also presented in figure 5.10 where contours of constant power have been produced.

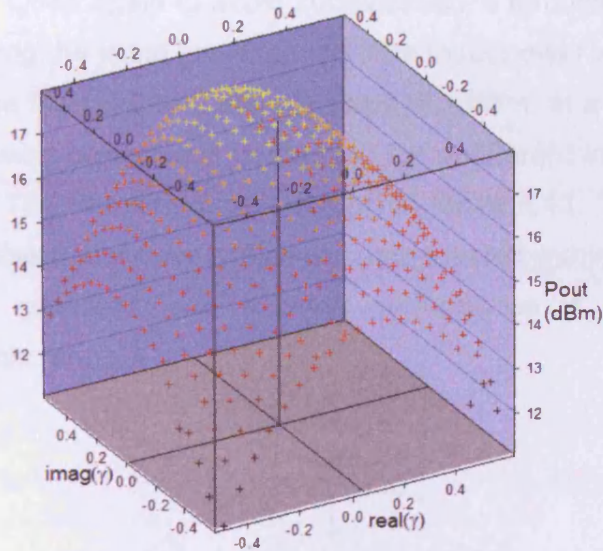


Figure 5.9 – Measured 3-D Plot showing output power from the device as the impedance is varied

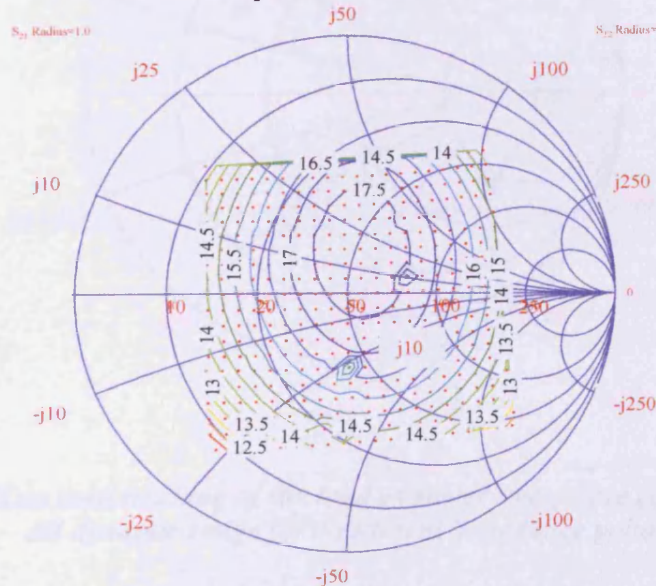


Figure 5.10 – Measured contours of maximum power in dBm as the impedance is swept

5.4 Verification of Architecture under Varying Input Power

This section aims to verify that the envelope load-pull loop can successfully track changes in the device output, thus allowing constant impedance to be presented to a device under varying drive conditions. The initial test considered changes in CW input power. Once again to avoid complication, a thru line was used in place of the device during the initial investigation. The input power was swept over a 27 dB dynamic range from -20 to 7 dBm in steps of 1 dBm, at a centre frequency of 1.8 GHz. The power sweep was conducted for 4 different impedance points on the Smith chart. The resulting plot is shown in figure 5.11. The plot shows that any remaining offsets that have not been compensated within the electronics are very small and excellent load tracking performance is obtained over this significant dynamic range.

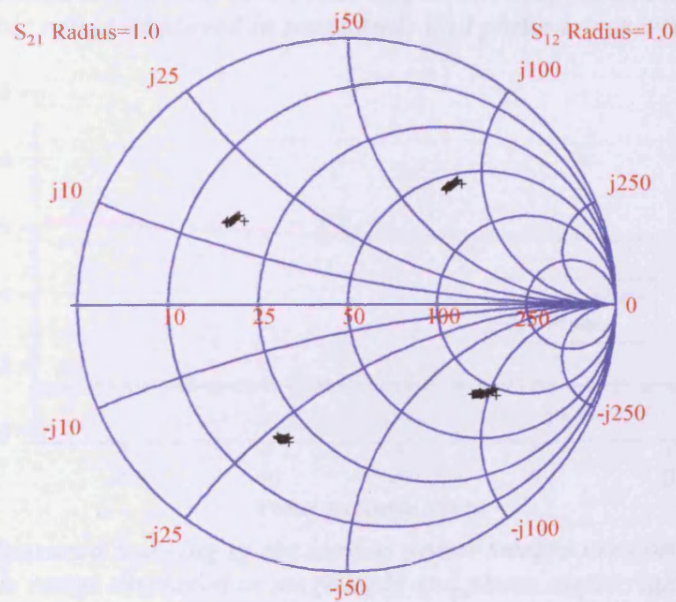


Figure 5.11 – Measured tracking of the load as power sweeps are conducted over a 27 dB dynamic range for 4 different impedance points

Figure 5.12 and 5.13 show the best and worst case extracted magnitude and phase of the measured load reflection coefficient as the power sweep is

conducted, for the load set in the lower left and upper right quadrants respectively. Again this highlights the impressive performance obtained, with even the worst case showing only very small deviations from the set load.

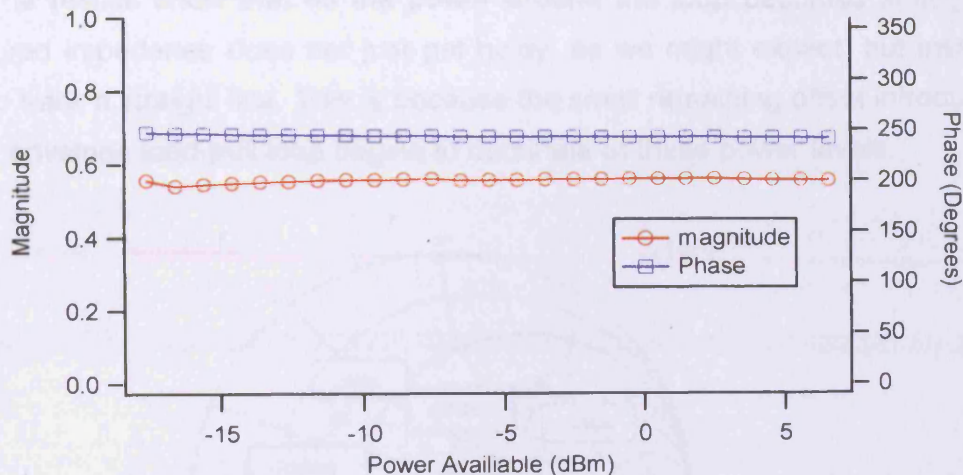


Figure 5.12 – Measured tracking of the load as power sweeps are conducted over a 27 dB dynamic range displayed in magnitude and phase lower left quadrant

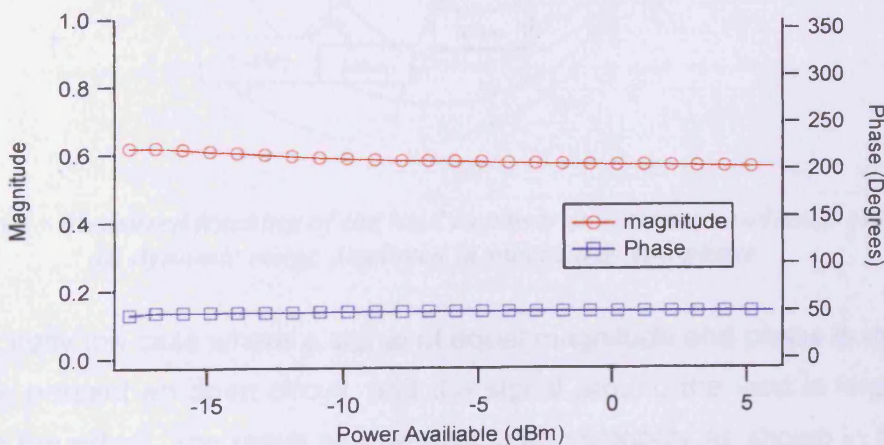


Figure 5.13 – Measured tracking of the load as power sweeps are conducted over a 27 dB dynamic range displayed in magnitude and phase upper right quadrant

The next step was to consider the effects of any small remaining DC offset induced in the envelope load-pull loop. To do this, the experiment was repeated, but this time the experiment was conducted over a larger dynamic range. At low power levels, the resulting error in the achieved load due any offset becomes large relative to the level of the signal. The plot shown in figure 5.14 is a repeat

of the power sweep performed in the previous example. This time however the power is swept over a 35 dB dynamic range. The performance over the original 27 dB dynamic range is also highlighted on the plot.

The results show that as the power around the loop becomes small, the measured impedance does not just get noisy, as we might expect, but instead start to track a straight line. This is because the small remaining offset introduced by the envelope load-pull loop begins to dominate at these power levels.

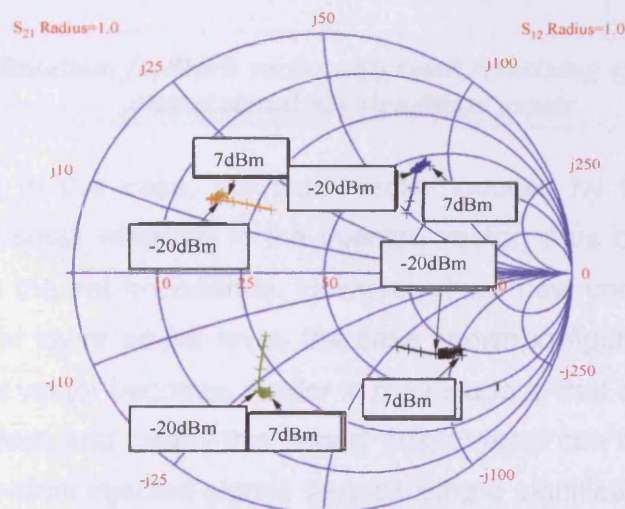


Figure 5.14 – Measured tracking of the load as power sweeps are conducted over a 35 dB dynamic range displayed in magnitude and phase

Consider firstly the case where a signal of equal magnitude and phase is injected in order to present an open circuit, and the signal around the loop is large with respect to the offset. The result can be described vectorally as shown in figures 5.15 and 5.16 below.

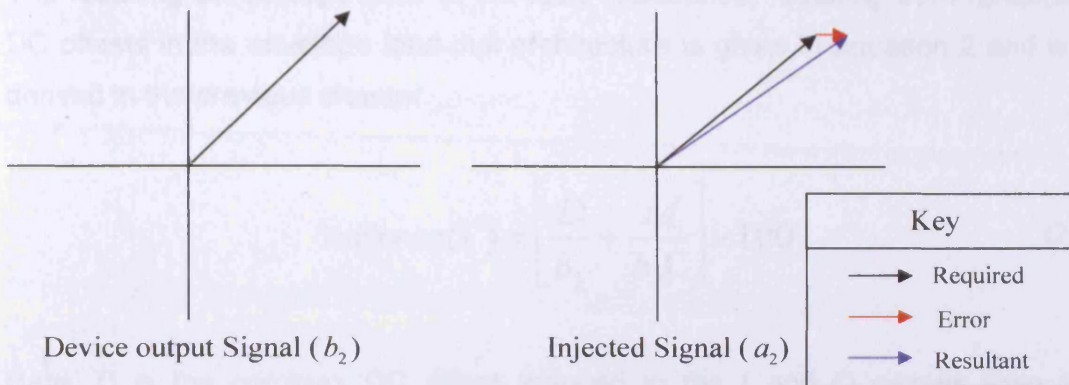


Figure 5.15 – Resultant feedback vector with small remaining offset when the device output signal has significant power

It is clear that in this case, the fixed vector induced by the remaining offset causes only a small variation in the injected vector, thus causing only a small perturbation in the set impedance. However, if we now consider a point in the power sweep at lower power level, the case shown in figure 5.16 applies. This time, the signal vector becomes similar in magnitude to that of the vector induced by the fixed offset, and clearly this “small” offset vector can now have a dramatic effect on the overall injected signal, thus causing a significant change in the set impedance. Obviously, as the offset vector becomes large with respect to the signal vector, it has a major influence on the set impedance. This means that as power changes the load varies.

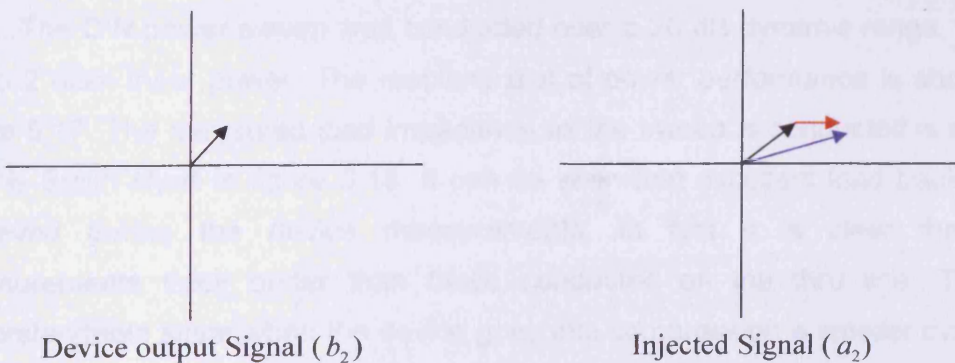


Figure 5.16 – Resultant feedback vector with small remaining offset when the device output signal has a significantly reduced power

The resulting percentage error in set load impedance, resulting from remaining DC offsets in the envelope load-pull architecture is given in equation 2 and was derived in the previous chapter.

$$\%Error(\Gamma) = \left[\frac{D}{b_2} + \frac{M}{b_2\Gamma} \right] \times 100 \quad (2)$$

Here, D is the complex DC offset induced in the I and Q signals from the demodulator, M is the complex DC offset induced by the control circuit and modulator and Γ is the set impedance.

5.4.1 Demonstration of Impedance tracking under varying power using Device Measurements

The next step is again to apply this approach to device characterisation; verifying the performance is vital as the power sweep is one of the most common measurements performed on a device and can be combined with load-pull sweeps to produce a model of a device. Furthermore, the ability to hold the load constant under varying power is imperative if the envelope load-pull is to be employed for amplitude modulated signals, such as two or three tone signals.

The same HBT device was used for these measurements as in the previous section; the device was biased in class A-B with a fundamental frequency of 1.8 GHz. The CW power sweep was conducted over a 20 dB dynamic range, from -18 to 2 dBm input power. The resulting plot of power performance is shown in figure 5.17. The measured load impedance as the sweep is conducted is shown on the Smith chart in figure 5.18. It can be seen that excellent load tracking is achieved during the device measurements. In fact it is clear that the measurements track better than those conducted on the thru line. This is understandable since when the device goes into compression a smaller dynamic range is required of the envelope load-pull.

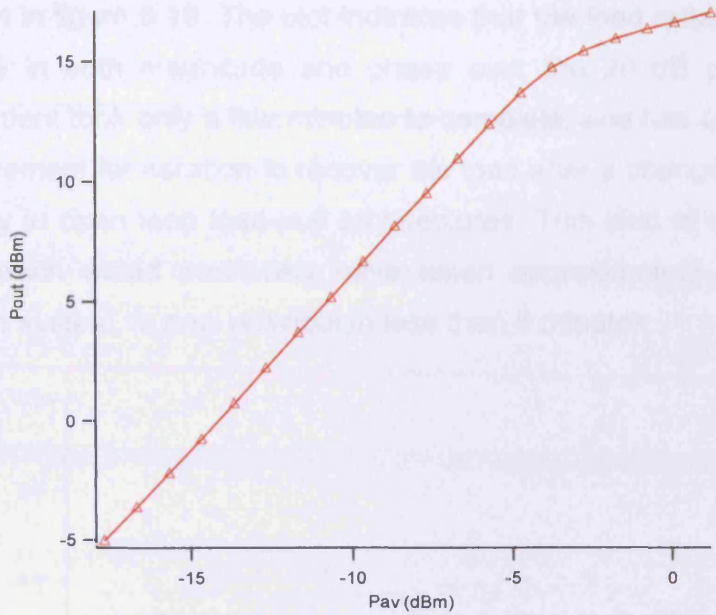


Figure 5.17 – Measured Power performance of the HBT while employing envelope load-pull to maintain a constant load

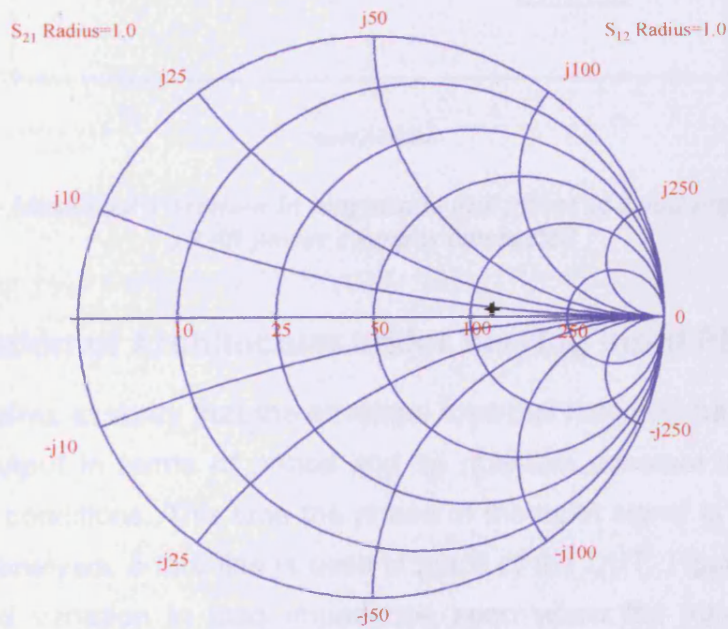


Figure 5.18 – Measured Variation in Load impedance as the 20 dB power sweep is conducted

The data is shown in terms of measured magnitude and phase of the reflection coefficient in figure 5.19. The plot indicates that the load reflection varies by less than 2 % in both magnitude and phase over the 20 dB power sweep. This measurement took only a few minutes to complete, and has completely removed the requirement for iteration to recover the load after a change in power that was necessary in open loop load-pull architectures. This kind of stepped CW power sweep, which would previously have taken approximately 40 minutes on an open-loop system, is now possible in less than 5 minutes.

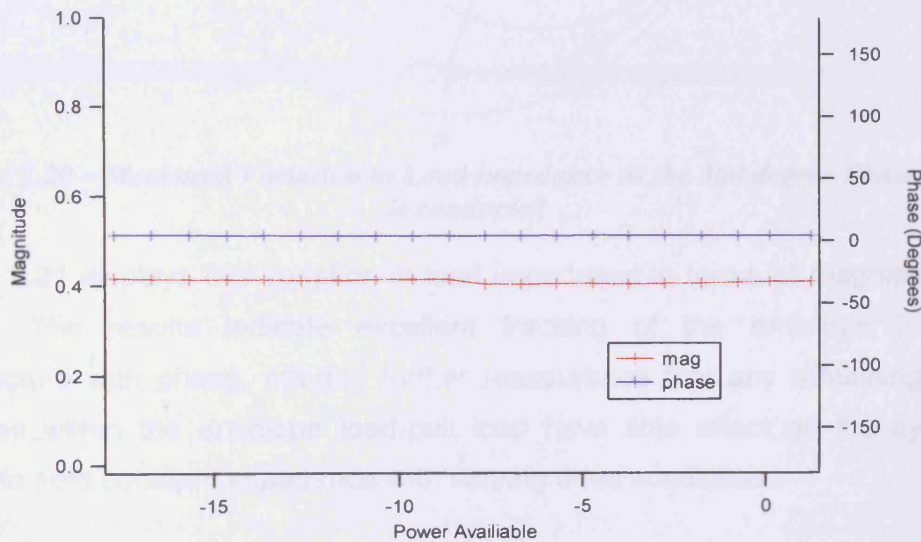


Figure 5.19 – Measured Variation in magnitude and phase of Load impedance as the 20 dB power sweep is conducted

5.5 Verification of Architecture under Varying Input Phase

This section aims to verify that the envelope load-pull loop can track changes in the device output in terms of phase and so maintain constant impedance for varying drive conditions. This time the phase of the input signal is swept. Again, for the initial analysis, a thru line is used in place of the DUT. Figure 5.20 shows the measured variation in load impedance seen when the input was swept around 360 degrees in steps of 10 degrees, with an input power of 0 dBm at a frequency of 1.8 GHz.

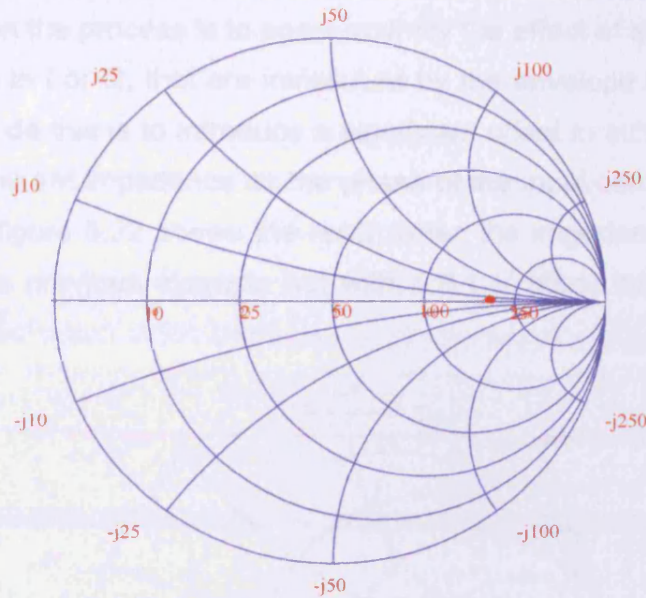


Figure 5.20 – Measured Variation in Load impedance as the 360 degree Phase sweep is conducted

Figure 5.21 displays this variation in load impedance in terms of magnitude and phase. The results indicate excellent tracking of the envelope load-pull architecture with phase, offering further reassurance that any remaining offset voltages within the envelope load-pull loop have little effect on the system's ability to hold constant impedance with varying drive conditions.

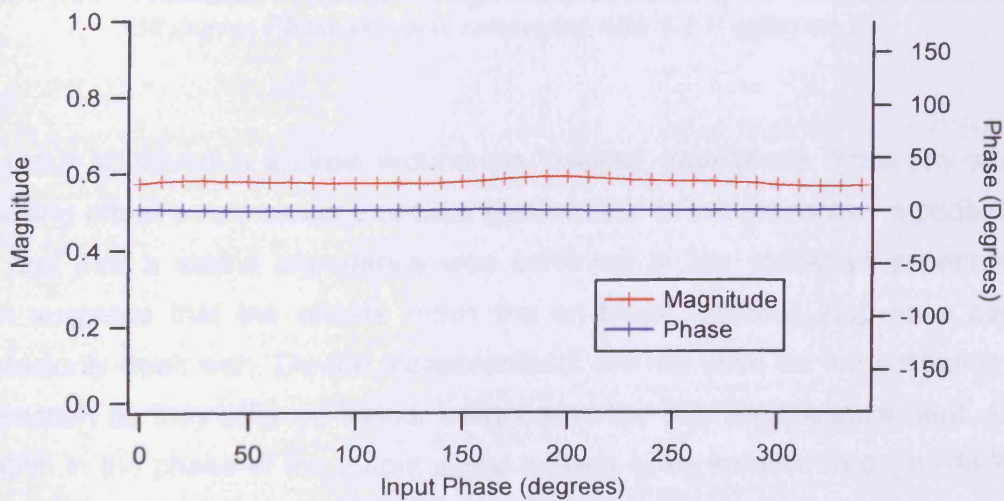


Figure 5.21 – Measured Variation in magnitude and phase of Load impedance as the 360 degree Phase sweep is conducted

The next step in the process is to again quantify the effect of any remaining small voltage offsets in I or Q, that are introduced by the envelope load-pull loop. The easiest way to do this is to introduce a significant offset in either I or Q and view the effect on the set impedance as the phase of the input stimulus is swept. The plot shown in figure 5.22 shows the result when the impedance is set to be the same as in the previous example but with a 0.1 V offset introduced into the I' signal.

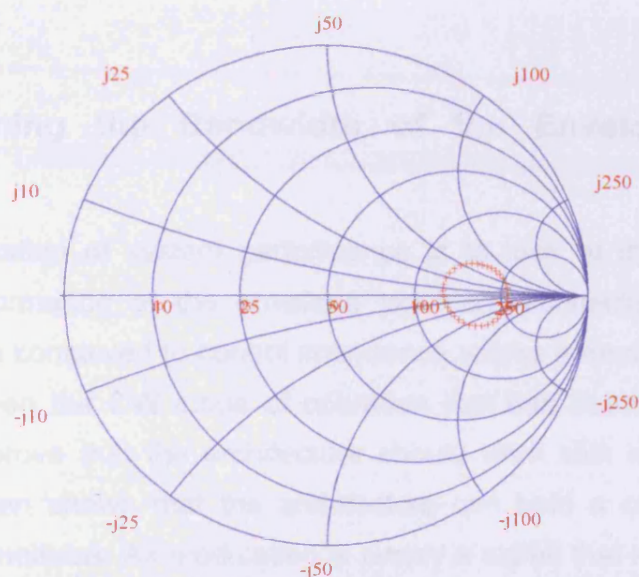


Figure 5.22 – Measured Variation in magnitude and phase of Load impedance as the 360 degree Phase sweep is conducted with 0.1 V offset on I'

The result achieved is a circle around the 'desired' impedance. Thus any small remaining offset would cause a circular perturbation of the presented impedance. The fact that a stable impedance was achieved in the validation experiment again suggests that the offsets within the envelope load-pull loop have been satisfactorily dealt with. Device measurements are not used for the validation in this section as they offer no further insight than the thru line measurement. Any variation in the phase of the output signal is likely to be induced through AM-PM of the device rather than the stimulus phase being changed. It is also important to note at this point that AM-PM would only vary the phase by a few degrees so

the test conducted in this section is a particularly aggressive test of the system performance.

Now it has been proven that we can accurately set impedance using the envelope load-pull architecture and that the system can maintain a constant impedance for varying drive conditions, the only remaining measurement was to determine the useable bandwidth of the system. This quantifies the performance that can be expected when used with multi-tone signals rather than the CW signals.

5.6 Determining the Bandwidth of the Envelope Load-pull Architecture

The final verification of system performance is to look at the in-situ useable bandwidth performance of the envelope load-pull architecture. Although the architecture was conceived to control impedance across a modulated bandwidth, so far it has been the CW mode of operation that has been validated. These results in fact prove that the architecture should work with modulated signals since it has been shown that the architecture can hold a constant load with varying drive conditions. As modulation is simply a signal that has dynamic drive conditions with time, it must therefore be true that the system is capable of maintaining constant impedance for multi-tone signals within the bandwidth of the load-pull architecture.

The experiment involved sweeping the tone spacing of a three-tone stimulus signal, thus sweeping the frequency of the X and Y signals that flow around the envelope load-pull loop. As the X and Y control signals are held at static DC values, the impedance at all three tones should ideally be identical. Any variation in the impedance seen by the three frequency components is a problem as it introduces a time varying load. The bandwidth of the demodulator and modulator were measured in the previous chapter and had 'flat bandwidth'¹ of 20 MHz and 10 MHz respectively. The OP177 operational amplifiers used in

¹ 'Flat Bandwidth' is defined as less than 0.2 dB across the bandwidth

the control circuitry have 'flat bandwidth' of only 100 kHz [4], thus it is op-amp component that is likely to limit the bandwidth performance of the entire architecture.

The plot of figure 5.23 shows the measured presented impedances to all three tones as the tone-spacing was stepped through the following values – 1kHz, 2kHz, 3kHz, 4kHz, 5kHz, 6kHz, 7Kkz, 8kHz, 9kHz, 10kHz, 15kHz, 20kHz, 25kHz, 30kHz, 40kHz, 50kHz, 75kHz, 100kHz, 200kHz.

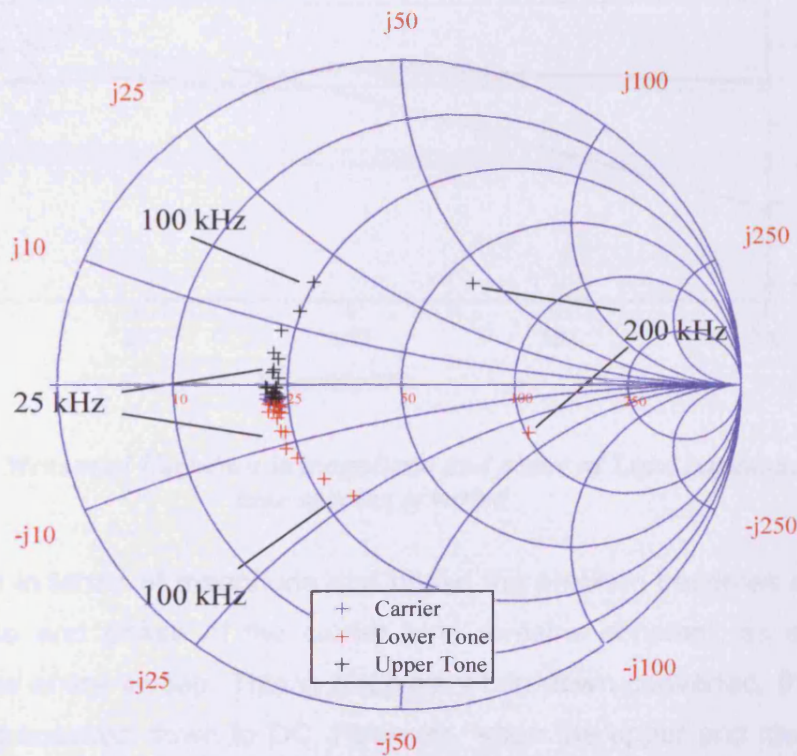


figure 5.23 – Measured Variation in load impedance as the tone spacing is varied

The architecture actually begins to fail at much lower frequency than predicted by the bandwidth of the op-amps used in the envelope load-pull loop. The measured useable range is actually only around 10 kHz. For higher frequencies, the phase of the impedance presented to the upper and lower tones split apart from the phase of the reflection coefficient set for the carrier. Figure 5.24 shows the measured magnitude and phase of the reflection coefficient of the three tones as the tone spacing is varied.

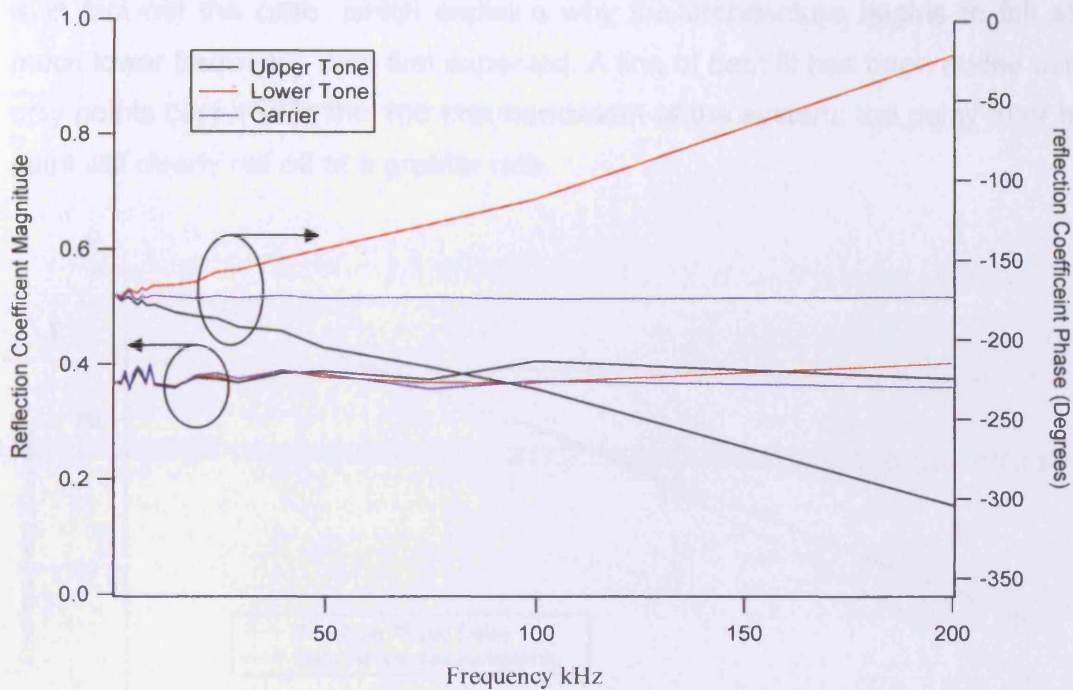


Figure 5.24 – Measured Variation in magnitude and phase of Load impedance as the tone spacing is varied

When viewed in terms of magnitude and phase the problem becomes apparent: the magnitude and phase of the carrier tone remains constant, as expected, throughout the entire sweep. This is because when down-converted, the carrier frequency is translated down to DC. However, when the upper and lower tones are analyzed, the magnitude remains constant throughout the sweep, but the phase of the two tones splits apart equally and linearly about the phase of the carrier tone. It becomes clear that the upper and lower tones are in fact tracking around a circle of constant magnitude as the tone spacing is increased. This would suggest that it is actually the delay of the envelope that results in the breakdown of the architecture and not the bandwidth of the components within the loop. This is again indicated as we look at the extracted envelope delay between a_2 and b_2 for the various tone spacing plotted in figure 5.25. For the envelope load-pull architecture to function correctly, it is imperative that the

envelopes of output and injected signals are aligned. However, it is clear that this is in fact not the case, which explains why the architecture begins to fail at a much lower frequency than first expected. A line of best fit has been added using only points captured in the 100 kHz bandwidth of the system; the delay after this point will clearly roll off at a greater rate.

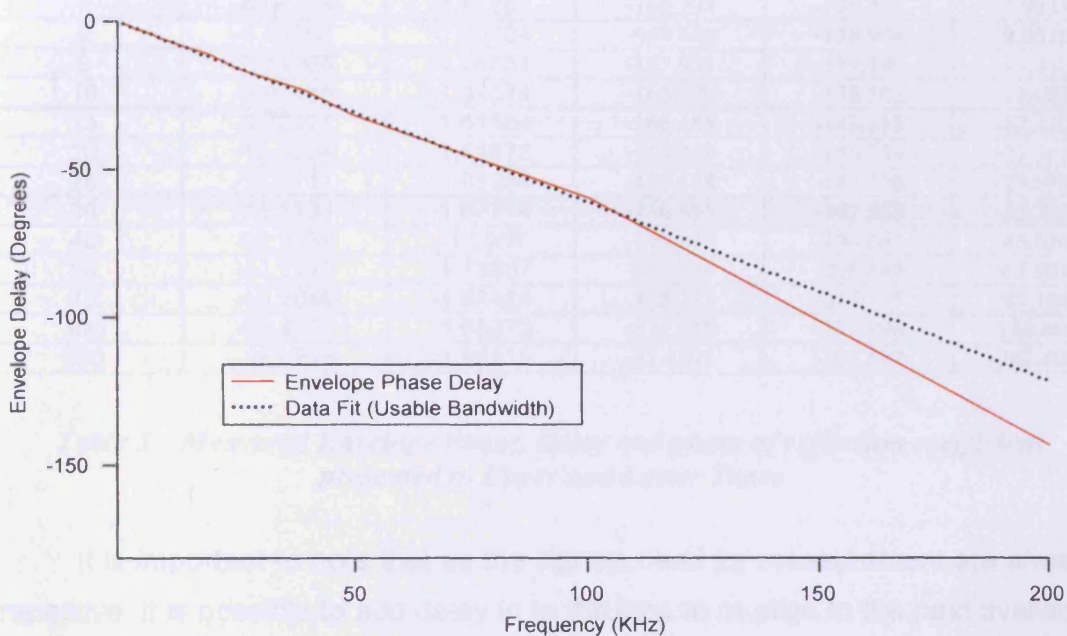


figure 5.25 – Measured Variation in envelope phase as the tone-spacing is swept

This plot of envelope phase delay can be directly referenced back to the impedance variation between upper and lower tones shown in figure 5.24. Table 5 shows the measured envelope phase delay in degrees and microseconds along with the phase difference between the upper and lower tones for each tone-spacing.

As predicted, a direct relationship is observed between the envelope delay and the phase difference observed between the upper and lower tone. The phase difference between tones is always double the envelope delay as the upper and lower tones split away in equal and opposite directions.

<i>Tone Spacing (kHz)</i>	<i>Envelope Phase Delay (Degrees)</i>	<i>Delay (μs)</i>	<i>Phase of Γ for Lower Tone (Degrees)</i>	<i>Phase of Γ for Upper Tone (Degrees)</i>	<i>Phase Difference (Degrees)</i>
1	-0.58142	-1.61506	-172.147	-173.33	-1.1827
2	-1.27819	-1.77527	-173.660	-176.192	-2.5324
3	-1.80799	-1.67407	-170.718	-174.277	-3.5590
4	-2.65416	-1.84317	-169.080	-174.240	-5.1591
5	-3.12729	-1.73738	-170.811	-176.961	-6.1497
6	-3.69862	-1.71232	-171.419	-178.681	-7.2611
7	-4.06434	-1.61283	-168.298	-176.233	-7.9355
8	-4.58566	-1.59224	-169.846	-178.908	-9.0616
9	-5.71968	-1.76531	-167.931	-179.140	-11.210
10	-5.92465	-1.64574	-166.979	-178.582	-11.603
15	-8.72121	-1.61504	-166.185	-183.317	-17.132
20	-10.9204	-1.51672	-164.258	-185.759	-21.501
25	-14.8711	-1.65234	-158.138	-187.216	-29.078
30	-18.1131	-1.67714	-156.855	-192.558	-35.703
40	-22.9939	-1.5968	-149.845	-194.861	-45.016
50	-31.2943	-1.73857	-143.585	-205.485	-61.901
75	-45.2046	-1.67424	-128.213	-217.377	-89.164
100	-59.4977	-1.65272	-112.316	-230.996	-118.680
200	-142.715	-1.98215	-21.4871	-303.887	-282.400

Table 5 – Measured Envelope Phase, Delay and phase of reflection coefficient presented to Upper and Lower Tones

It is important to note that as the signals used for measurement are always repetitive, it is possible to add delay in to the loop to re-align to the next available modulation envelope, which would mean that the architecture could be used comfortably within the 'flat bandwidth' of the electronics. This however is not that simple for the analog electronic solution presented in this thesis, but possible solutions are suggested in the future work section.

By definition, there must also be valid tone spacing values where the envelope delay through the envelope load pull architecture becomes a whole cycle, and at such frequencies the architecture would again operate correctly. However using points up to 100kHz (within the bandwidth of the op-amps), to calculate an average value for the delay of 1.672 μ s, suggests that the next usable solution, where the envelope delay will becomes one period would be 598kHz; unfortunately this is far above the operating limits of the control electronics.

5.7 Chapter Summary

This chapter has presented a validation of the new envelope load-pull architecture, also presented by the author in [1-3]. Verification showing the control and accuracy of the impedance set through the X and Y control signals of the envelope load-pull electronics showed good performance with only small errors introduced. It was shown that a pre-calibration of the loop is required in order to re-centre the system around 50Ω and to ensure correct phase and magnitude of the set load impedance; this has been derived and verified. Device measurements taken over a sizable area of the Smith chart show that the system is operating well and even in its CW mode of operation is a very useful tool in the characterisation process, offering the speed of a closed loop load-pull system without the usual stability issues.

The architecture has also been fully verified under varying drive conditions. This was an important step, as successful verification makes the envelope load-pull architecture immediately useful in its CW measurement mode, as measurements such as power sweeps become dramatically faster than traditional open-loop active load-pull. Furthermore, the ability to maintain constant impedance with varying drive conditions shows the suitability of the architecture to modulated operation. Validation was conducted under varying phase and power of the input stimulus. The results indicate near invariant load over the full 360 degree phase sweep and an impressive stable load over a 25 dB power sweep, which is more than enough to uncover the linear and non-linear power performance of any DUT. The effect of introducing significant offsets in both cases was also investigated, offering further proof that the offsets are in fact now under control and so do not significantly effect the operation of the system.

The bandwidth investigation showed a significant problem with group delay. Although the bandwidth was expected to be around 100 kHz from the bandwidth of the electronics used, a group delay of $1.672 \mu\text{s}$ meant that the useable bandwidth of the architecture was limited to around 10kHz. This does severely

limit the operation of the architecture, although it is still valid for slowly modulated multi-tone signals. Suggestions on solving the group delay issues are discussed in the future work section of the thesis, which would allow the same architecture to be utilized at much greater bandwidths.

In summary, the concept of envelope load-pull has been fully realised, demonstrated and verified, albeit at a limited bandwidth. The work presented suggests that simply adding delay in the load-pull loop would solve the group delay issue and make the architecture applicable to wider-band multi-tone signals. Even in its current state, the architecture is ideal for application in a CW measurement system and is also suitable for application to real-time measurements, which only utilise slow modulation. A selection of real time measurement applications will be presented in chapter 6 of the thesis.

5.8 References

1. Williams, T.; Benedikt, J.; Tasker, P.J.; “*Experimental evaluation of an active envelope load pull architecture for high speed device characterization*” IEEE/MTT-S International Microwave Symposium 2005.
2. Williams, T.; Benedikt, J.; Tasker, P.J.; “*Application of a novel active envelope load pull architecture in large signal device characterization*” 2005 European Microwave Conference, Volume 1, 4-6 Oct. 2005.
3. Williams, T.; Benedikt, J.; Tasker, P.J.; “*Fully Functional "Real Time" Non-Linear Device Characterization System Incorporating Active Load Control*” 2006 European Microwave Conference, Page(s):1610-1613.
4. Technical data sheet, Analog Devices “*OP177 Ultra-Precision Operational Amplifier*” (http://www.analog.com/en/prod/0,,759_786_OP177,00.html) accessed June 2004.

Chapter 6 – Application of the Waveform Measurement and Engineering System

6.1 Introduction

The primary aim of this research was to design, realise and validate a new multi-tone large-signal waveform measurement system, as presented in the preceding chapters. It is however important to highlight a number of measurements that become possible through the realisation of the new system. In this case, the presented results are not used to make observations or to fully characterise the DUT, but are used to demonstrate an assortment of measurements that have been made possible and that would be useful to others.

The first measurement section will consider novel applications of the system published in [1-3]. These involve the use of slowly modulated excitation or slowly modulated load-impedance, that allows for the ultra-rapid

collection of CW data sets. Such measurements have been termed 'real-time' large-signal measurements.

The next section describes an investigation into memory effects, made using the new system, presented in [4-5]. The investigation uses base-band load-pull to control the impedance of the two most significant base-band components, in an attempt to remove electrical memory from a 20 Watt LDMOS device, while sweeping the modulation rate. Once electrical memory has been removed, remaining memory related to the device can be uncovered.

The final section of this chapter discusses the depth of information that is contained within the multi-tone waveforms, and introduces the envelope domain as a very useful method of data display. It also discusses the importance of collecting all of the significant generated components, for a full understanding of device behaviour.

6.1.1 Envelope Domain Extraction

In this chapter, the envelope domain will be discussed as an alternative method of data display and interpretation. The envelope domain uses time domain and frequency domain techniques to perform an envelope analysis of the measured data. In this domain, a modulated signal is described as a complex time varying envelope containing magnitude and phase information for each Fourier coefficient [6]. Using this approach, it is possible to extract 'envelopes' for the fundamental and all harmonic bands. This process involves extracting time varying I and Q, or magnitude and phase components that are associated with each band. The method used to extract the envelope domain information from the measured waveforms is described below -

A Fourier transform is first conducted to transform the time domain multi-tone waveforms into the frequency domain. A new spectral representation is then created that contains only the spectral information related to that particular band, where the centre of the band is made to lie around DC. The cosine or In-phase (I) and Sine or quadrature (Q) time domain signals are then extracted from the spectrum, achieved by summing the

magnitude (ρ_i) and phase (ϕ_i) of each of the spectral location as we step between $-order$ and $order$ about the centre point as shown in equation (1) and (2), where F_{Mod} is the tone spacing.

$$I_n(t) = \sum_{i=-Order}^{Order} \rho_{n+1} \cos(i2\pi F_{Mod} - \phi_{n+1}) \quad (1)$$

$$Q_n(t) = \sum_{i=-m}^m -\rho_{n+1} \sin(i2\pi F_{Mod} - \phi_{n+1}) \quad (2)$$

These I and Q signals can then, if required, be converted into time varying magnitude and phase envelopes as shown in equation 3 and 4 respectively.

$$Mag(t) = \sqrt{I(t)^2 + Q(t)^2} \quad (3)$$

$$Phase(t) = \tan^{-1}\left(\frac{Q(t)}{I(t)}\right) \quad (4)$$

6.2 Introduction to Real Time Measurements

Large signal measurement systems are beginning to establish themselves as an integral part of the power amplifier design process, required to provide both improved device understanding and the data sets critical for successful power amplifier design [7-9]. A limitation of many large-signal measurement systems is that generally, irrespective of the use of passive or active load-pull, the measurements are time consuming. This usually results in the collection of only minimal data sets, restricting their use in the design process. The solution developed in this thesis overcomes this problem. It exploits the multi-tone waveform measurement system, discussed in chapter 2, combined with the envelope load-pull architecture, discussed in chapter 4, by using active

load-pull under slowly modulated conditions to uncover the CW performance of a device within a single waveform capture.

The work presented in chapter 4 and published in [1-3], demonstrated the feasibility of realising an active load-pull architecture; allowing for both electronic control of the load impedance and oscillation free self tracking. The active envelope load-pull architecture has been connected to the fully calibrated waveform measurement system, capable of measuring both CW and multi-tone signals presented in chapter 2 (see figure 6.1). Since the active envelope load-pull loop is capable of holding a constant load under varying drive conditions, it enables, for the first time, the utilization of active rather than passive load control during the application of a slowly modulated stimulus.

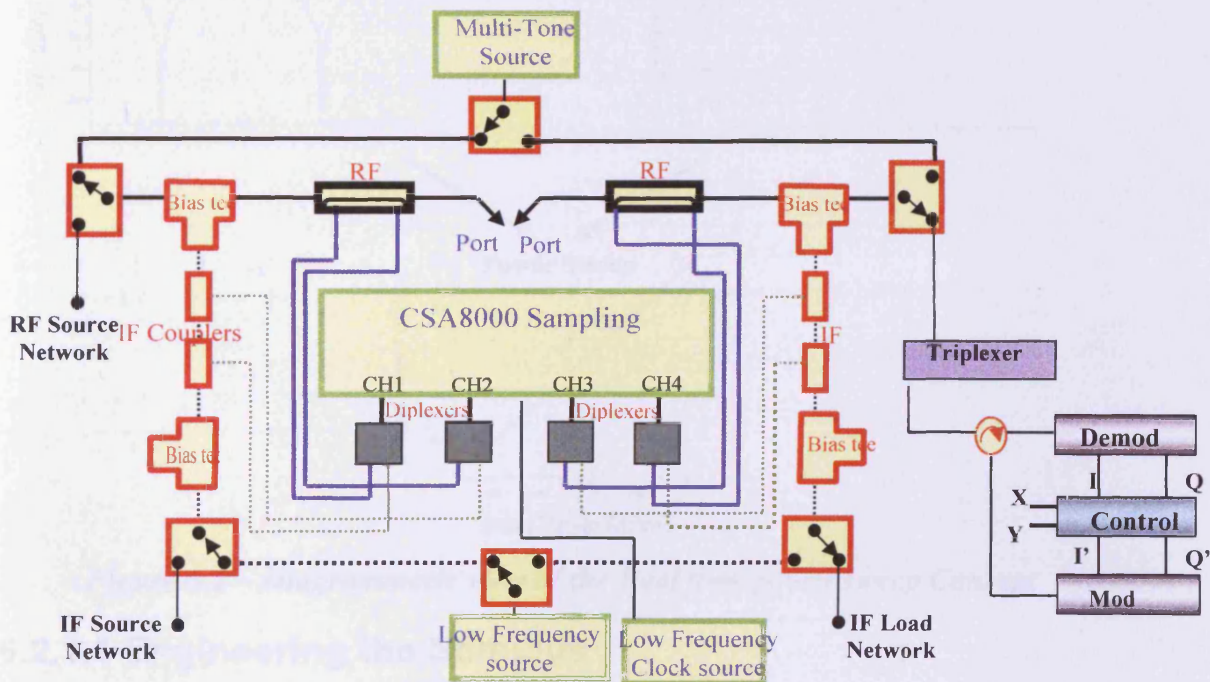


Figure 6.1 – Multi-tone large signal time-domain waveform measurement and engineering architecture

6.2.1 Real Time Power Sweeps

The real time power sweep concept looks to provide an alternative ultra-rapid method of capturing a CW power sweep, by slowly modulating the stimulus. If for example, we set up amplitude modulation as a stimulus, provided the

modulation rate is slow enough, we can assume the device is put into a quasi-CW state, where none of the device memory effects are excited. By measuring one cycle of modulation, a single waveform capture, all the information contained in a multi-point power sweep into a constant active load-impedance can be captured in 'real time'. A diagrammatic view of the approach is shown in figure 6.2.

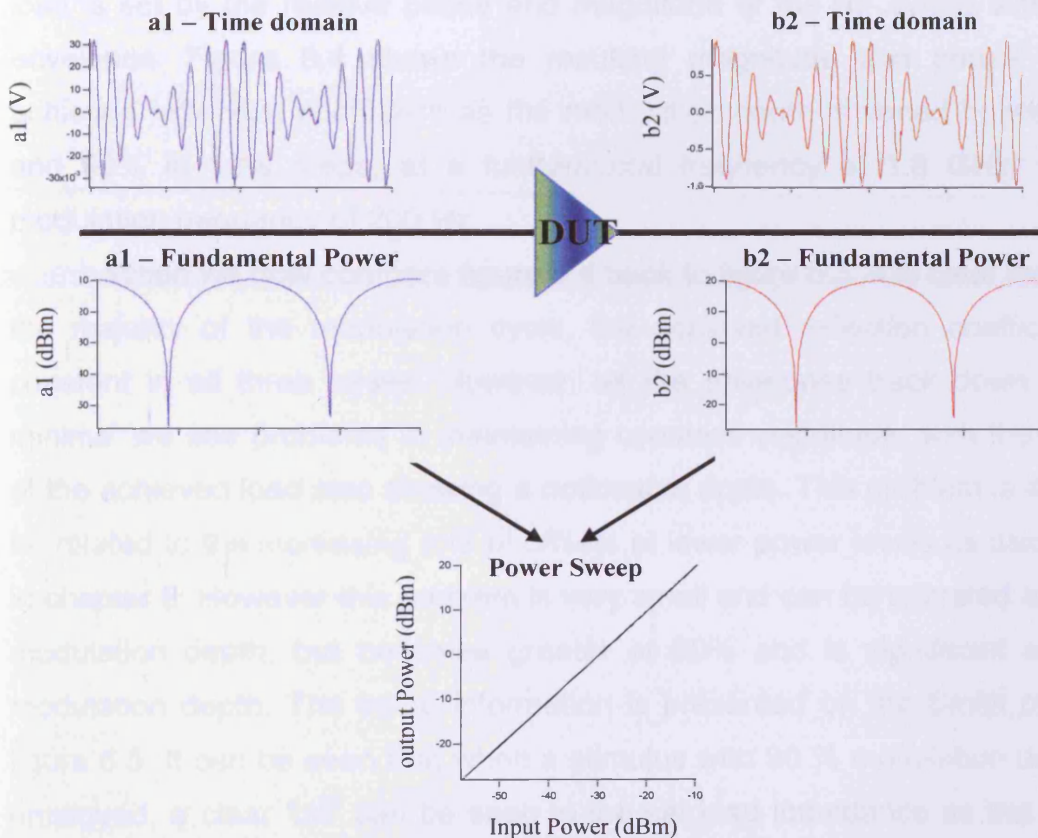


Figure 6.2 – Diagrammatic view of the Real time power sweep Concept

6.2.1.1 Engineering the Stimulus

Using a classical two-tone AM stimulus results in a power sweep ranging from zero to some maximum power, over an infinite dynamic range, which can cause complications and issues that are discussed later in this section. It is important to note that by using asymmetric tones or introducing an additional tone, the stimulus can be engineered to uncover the relevant portion of the P_{out} versus P_{in} curve. Using a three-tone signal, it is possible to vary the relative power in the tones to select the modulation depth and peak power of the signal, thus allowing the user to make the most efficient use of the

dynamic range of the measurement system and uncover the most relevant part of the power characteristic. To this end, an investigation is discussed below where the modulation depth is varied in order to determine the optimum operating range of the envelope load-pull. Figure 6.3 shows the interaction of a_2 and b_2 that defines the achieved load. It is clear that the envelope load-pull, as required ensures that the modulation envelopes are still aligned. The load is set by the relative phase and magnitude of the RF cycles within the envelopes. Figure 6.4 shows the resulting magnitude and phase of the achieved reflection coefficient as the modulation depth is varied between 70 and 90% in 10% steps, at a fundamental frequency of 1.8 GHz, with a modulation frequency of 200 Hz.

When we now compare figure 6.4 back to figure 6.3, it is clear that over the majority of the modulation cycle, the achieved reflection coefficient is constant in all three cases. However, as the envelopes track down to the minima, we see problems in maintaining constant magnitude, with the phase of the achieved load also showing a noticeable ripple. This problem is likely to be related to the increasing role of offsets at lower power levels as discussed in chapter 5. However this problem is very small and can be tolerated at 70 % modulation depth, but becomes greater at 80% and is significant at 90% modulation depth. The same information is presented on the Smith chart in figure 6.5. It can be seen that when a stimulus with 90 % modulation depth is employed, a clear 'tail' can be seen in the set load impedance as the power sweep is conducted.

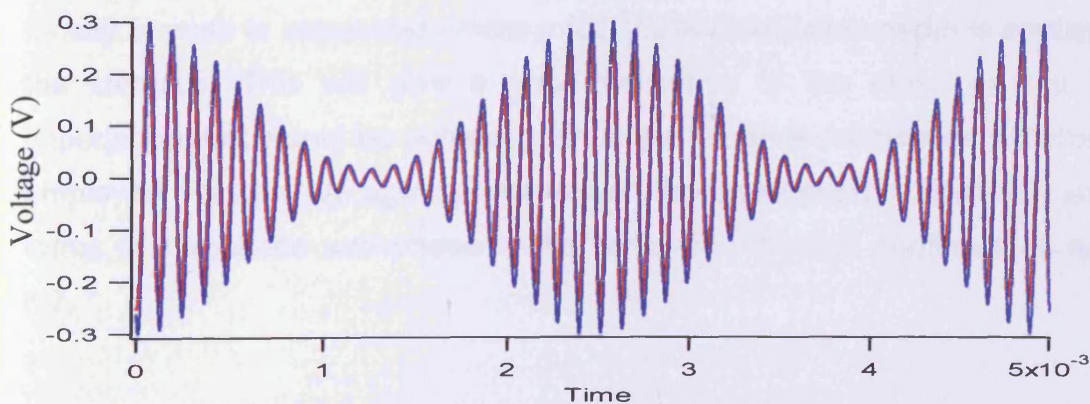


Figure 6.3 – Interaction of a_2 and b_2 waves when an AM stimuli used to conduct a modulated power sweep for rapid characterization (90 % Modulation depth)

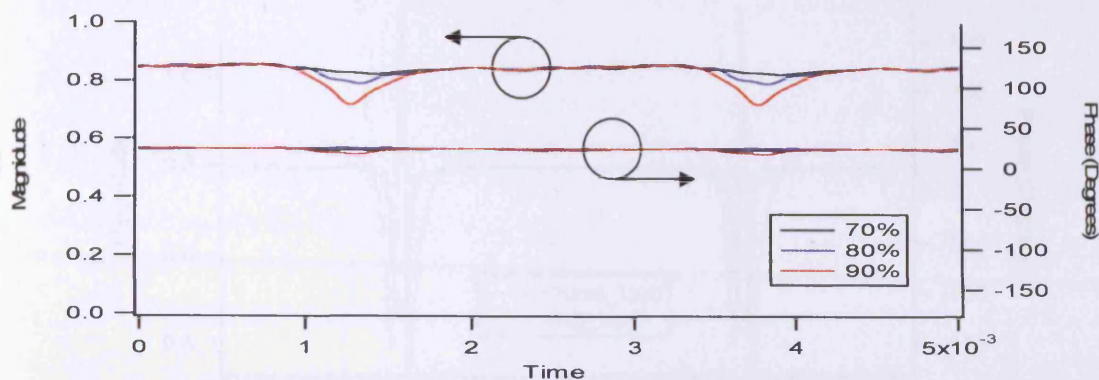


Figure 6.4 – Magnitude and phase of achieved load reflection coefficient as the modulation depth is varied

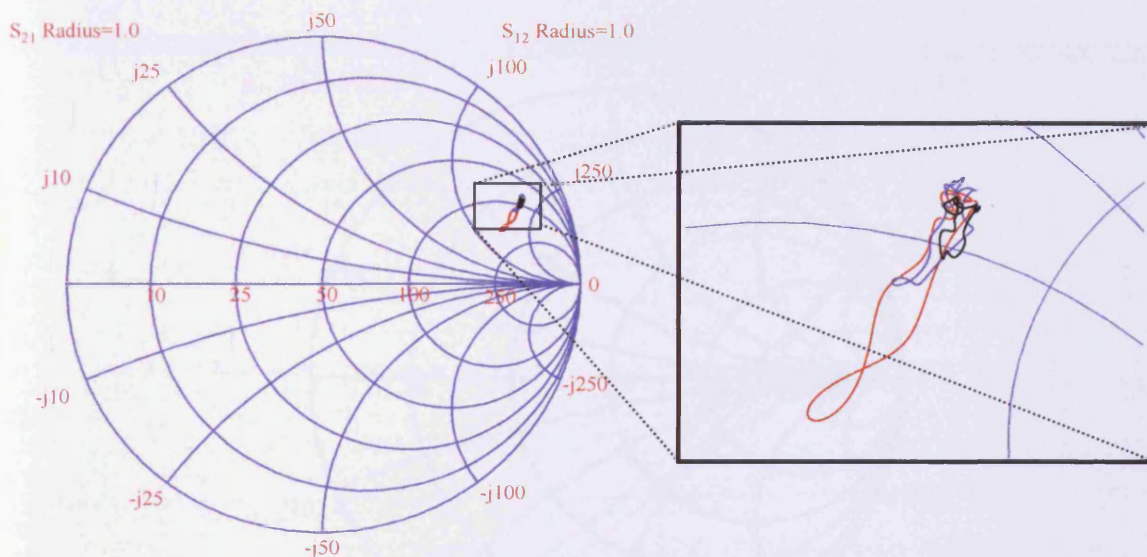


Figure 6.5 – Time Varying Load Reflection coefficient achieved for varying modulation depth shown on the Smith chart

Finally, a case is presented where a full 100% modulation depth is applied as the stimulus. This will give a good indication of the effect on the load impedance that would be achieved, should a two-tone modulation scheme be employed. Results are again presented on the Smith chart in figure 6.6 and in terms of magnitude and phase of the achieved reflection coefficient in figure 6.7.

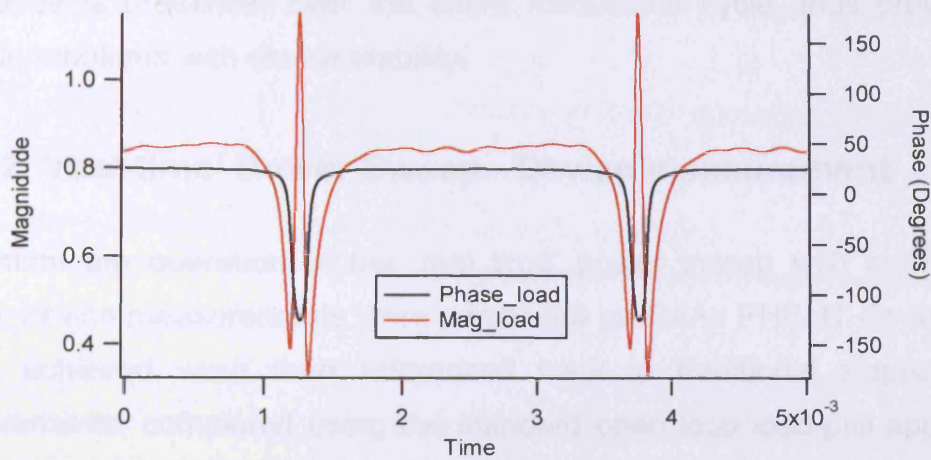


Figure 6.6 – Variation in measured magnitude and phase of load reflection coefficient for 100 % modulation depth case

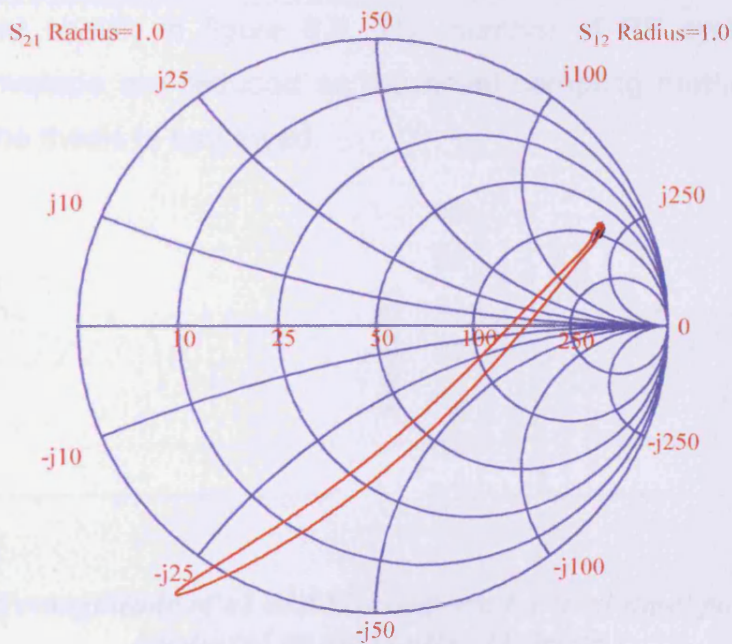


Figure 6.7 – Variation in measured load reflection coefficient for 100 % modulation depth case shown on Smith chart

Clearly, employing a stimulus with such a large dynamic range is problematic. Not only is the power sweep useless at the lower power levels as a rapidly varying impedance is loading the device, but more importantly setting such a load could in fact cause a device to oscillate if the ‘tail’ of the set load impedance intercepts the stability circles of the device at any time. Clearly such a load variation would increase the possibility of such issues. Therefore in summary, the use of three tone is not only useful to control the power range over which any sweep is conducted, but is also vital to ensure a constant

impedance is presented over the entire modulation cycle, thus preventing possible problems with device stability.

6.2.1.2 'real-time' Power Sweep - Device measurement

To confirm the operation of the 'real time' power sweep with active load control, device measurements were completed on GaAs PHEMT device. The results achieved were then referenced back to traditional stepped CW measurements, completed using the standard open loop load-pull approach. A three-tone signal with carrier frequency of 1.8 GHz and modulation rate of 1 kHz was used as the stimulus with 60% modulation depth. The load was set to 75Ω using the X and Y control signals. The measured a_1 and b_2 waveforms are shown in figure 6.8. The number of RF cycles within the modulated envelope are reduced as the novel sampling method outlined in chapter 2 of the thesis is employed.

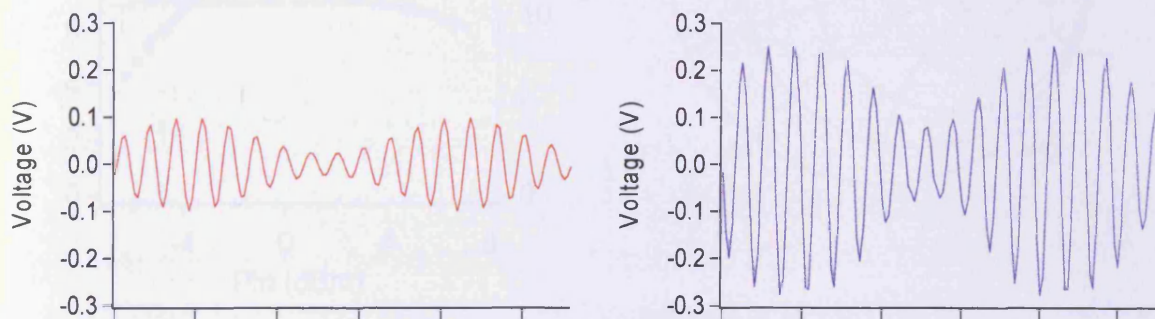


Figure 6.8 –magnitude of a_2 and b_2 waveform for 'real-time' power sweep conducted on GaAs pHEMT device

These multi-tone waveforms can now be analysed in the envelope domain, to uncover the time varying behaviour of fundamental and harmonic components of the waveforms. By plotting the magnitude of the time varying b_2 fundamental envelope component versus the magnitude of the time varying a_1 fundamental envelope component, we reveal all of the information contained within a multi-point power sweep. The result is shown in figure 6.9 (a) and is compared to a stepped CW sweep into the same load impedance (CW measurements are shown with markers, "real time" results shown with

straight lines). The time invariant load impedance at the fundamental as the real time power sweep is conducted is shown on the Smith chart in figure 6.9 (b). It can be seen from the plots that a very good agreement is achieved between CW and “real time” results over the entire 15 dB dynamic range. This demonstrates how the same measurement can now be performed in a fraction of the time. It is important to point out that since the measured waveform contains multiple-harmonic information, the envelope domain harmonic information as a function of P_{in} can be simply extracted in the same way as the fundamental carrier information.

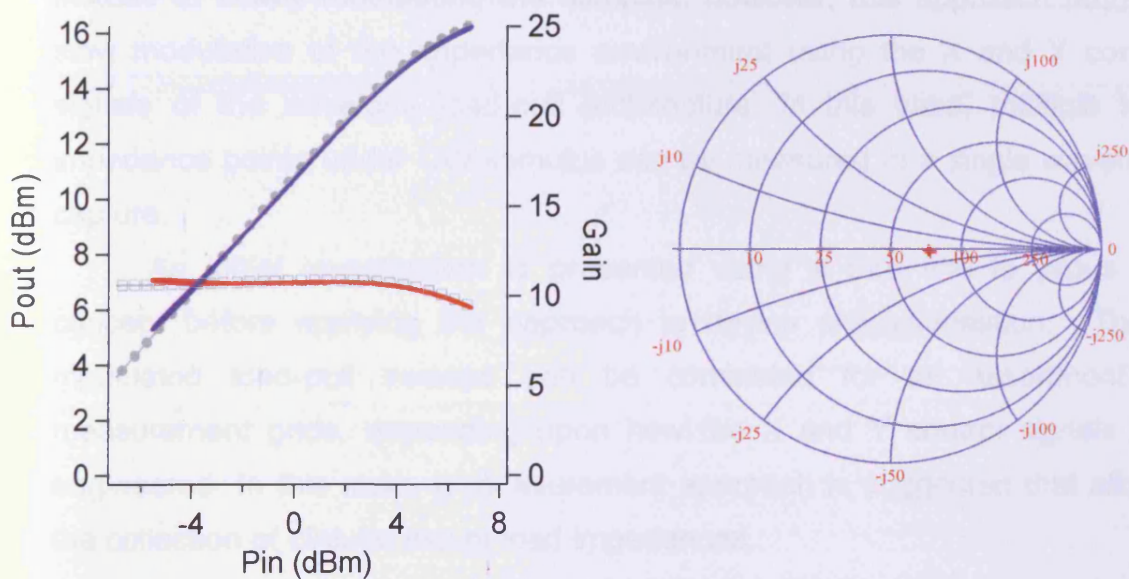


Figure 6.9 – a) measured power performance of pHEMT device measured using ‘real-time’ approach compared to power performance using traditional CW open loop load-pull b) Measured constant load reflection coefficient maintained displayed on the smith chart

Although this investigation has shown that the real-time approach is valid at the modulation rate of 1 kHz for this particular device, care should be taken when adopting real-time data extraction. It is clear that should we choose some modulation rate where device or system related memory is induced, results achieved using a stepped CW measurement and using the real-time approach would no longer overlay. Therefore care would be required if for example we wanted to further increase measurement speed by increasing the modulation frequency. This ‘issue’ however could also be used as a characterisation tool, for memory effects. Simply varying the modulation rate

and comparing back to a reference stepped CW case would allow any dispersion to be observed. This divergence in the measured power performance could then be directly attributed to memory. Furthermore, if we know the timescales upon which the memory is excited, this information could well be used to make some conjecture on the cause of the memory exhibited.

6.2.2 Real Time Load-Pull Sweeps

In a similar same vain as the real-time power sweeps presented above, applying a similar philosophy, real-time load sweeps can also be achieved. Instead of slowly modulating the stimulus, however, this approach requires slow modulation of the impedance environment using the X and Y control signals of the envelope load-pull architecture. In this case, multiple load impedance points under CW stimulus can be measured in a single waveform capture.

An initial investigation is presented using a thru line to prove the concept before applying the approach to device characterisation. These modulated load-pull sweeps can be completed for an assortment of measurement grids, depending upon how the X and Y control signals are engineered. In this case, a measurement approach is suggested that allows the collection of circular loci of load impedances.

If we apply quadrature sinusoidal signals to the X and Y control signals of the envelope load-pull loop, as shown in figure 6.10, this results in a time varying impedance environment that maps a circle of loads on the Smith chart at the modulation rate. The measurement system is then configured to collect one cycle of 'modulation' at the frequency rate of the applied quadrature sinusoids. Collecting a single waveform capture therefore results in the collection of an entire circle of load impedances, where the number of load points on any circle is limited only by the memory depth of the sampling oscilloscope. As the maximum memory depth of the Tektronix system is 4000 points, this results in collection of up to 2000 load points in a single measurement. Clearly this approach could be extremely useful, allowing for a much more detailed analysis of device performance with load-impedance. The diameter of the mapped impedance loci can be varied, by simply increasing

the peak-to-peak value of the applied sinusoids. This is demonstrated on a thru-line in figure 6.11 for 4 different magnitudes of applied sinusoids, with values of 100 mV (Red), 200 mV (Black), 300 mV (Green) and 400 mV (Yellow) respectively.

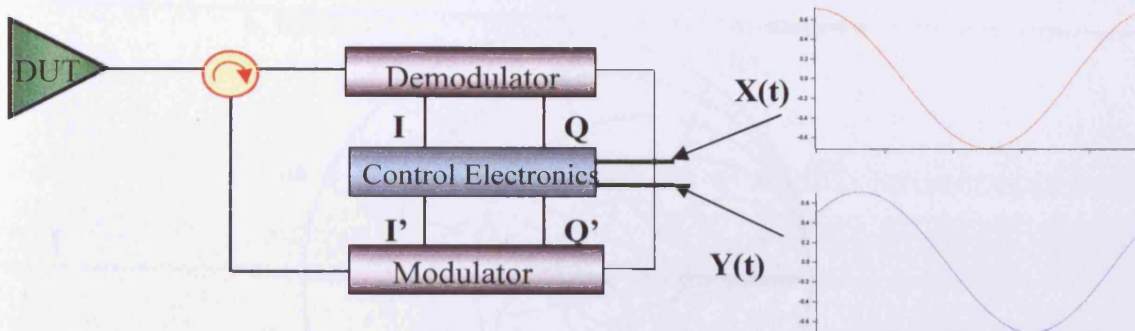


Figure 6.10 – Measurement Approach adopted for the ‘real time’ load pull sweeps

The results shown in figure 6.11 as expected show that the impedance presented to the ‘DUT’ takes the form of circles around the nominal ‘50 Ω’ system impedance. While this is useful in some cases, obviously as we attempt to measure different device technologies it would be useful to centre the captured load-pull loci around the optimum impedance of the DUT.

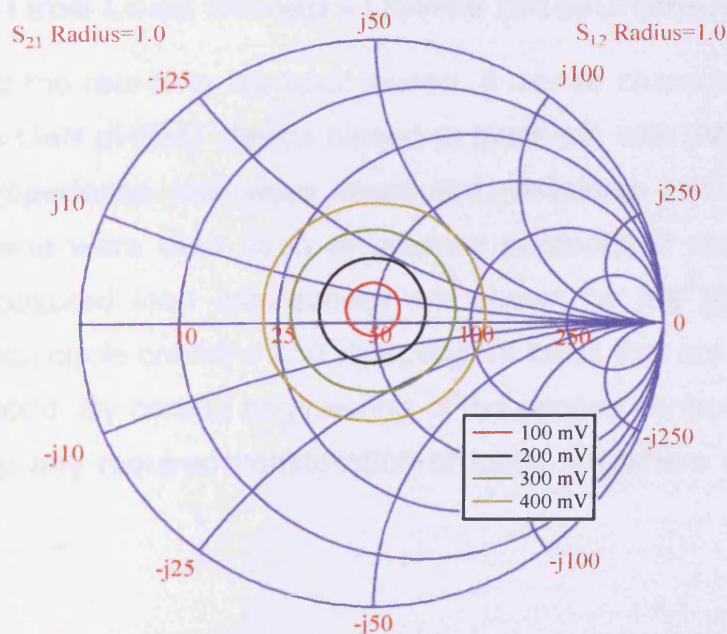


Figure 6.11 – Measured load reflection coefficient for varying magnitude of applied quadrature X and Y control signals

This can again be simply achieved by adding DC offsets to the sinusoids applied to X and Y. An example of this is shown in figure 6.12, where positive and negative offsets of 100 mV have been applied to the X and Y signals, thus producing load impedance loci that are no longer centred about the system impedance.

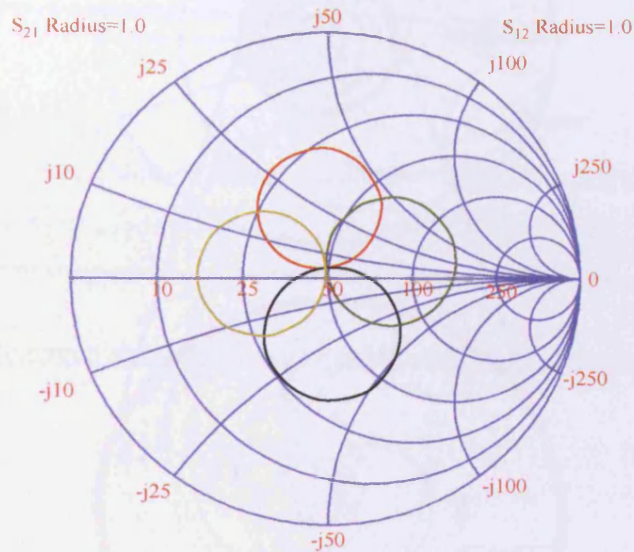


Figure 6.12 – Measured load reflection coefficient for varying offset of applied quadrature X and Y control signals

6.2.2.1 Real-Time Load Sweep - Device measurement

To fully validate the real-time load-pull sweep, a device characterisation was performed on a GaN pHEMT device biased at pinch-off, with 9V drain bias. 5 circular load impedance loci were measured, requiring just 5 measured waveforms. These were then used to produce contours of constant output power. The measured load impedances are shown on the Smith chart in figure 6.13. Each circle contains 250 independent loads that are measured in less than a second. By careful engineering of the applied control signals, it is possible to map any required constellation of loads, anywhere on the Smith chart.

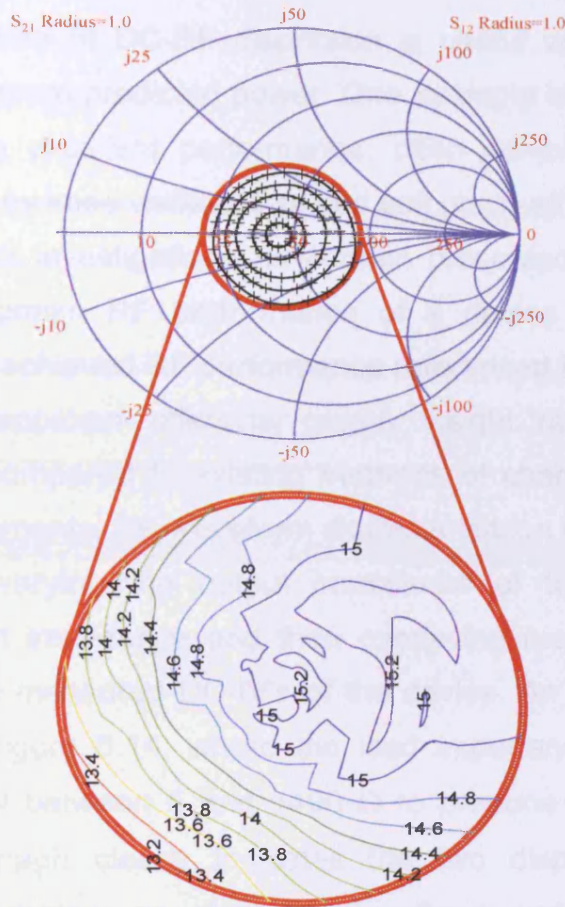


Figure 6.13 – Device Measurements showing load reflection coefficient for varying magnitude of applied quadrature X and Y control signals and resulting contours of constant output power

Unfortunately the existing base-band test-sets, are limited in their lower operational frequency to 200 kHz (low power) and 100 kHz (high power). Therefore, current capabilities of such measurements are limited as the base-band components or time varying DC is not measured. This means for example that the efficiency contours could not be found. This problem it is not however considered to be a fundamental issue. Possible solutions are presented in the future work section of the thesis.

6.2.2.2 Real Time Load-pull for analysis of DC-RF Dispersion

Detailed investigation of DC-RF dispersion is useful where devices fail to achieve their maximum predicted power. One example is GaN devices, while potentially offering excellent performance, often exhibit significant DC-RF dispersion caused by knee walkout [10] and soft pinch-off.

A number of investigations have been presented that show that the measured time domain RF performance of a device allows for a direct comparison of the achieved RF performance referenced to the measured DC-IVs [11-12]. This approach offers far greater insight into the causes of the dispersion when compared to existing methods of characterisation such as pulsed IV measurements. RF waveform characterisation of the dispersion can be achieved by varying the output impedance of the device from low impedance to high impedance and then overlaying measured dynamic RF load-lines onto the measured DC-IV's of the device. An example taken from [11] is shown in figure 6.14, where the load impedance of a AlGaIn/GaN HFET's was swept between 5 and 1400 Ω to produce a 'fan' of measured load-lines. This graph clearly indicates the two dispersion mechanisms exhibited by the device, as clear knee walkout and soft pinch off are observed.

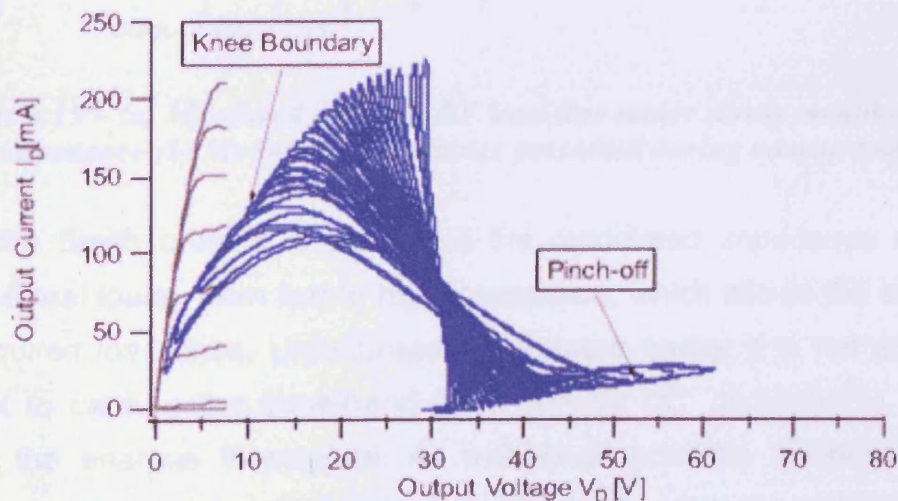


Figure 6.14 –Example Graph taken from [11], showing how the measured time domain RF performance can be used to analyse DC-RF Dispersion.

The main problem with such measurements is that they are very time consuming to perform, requiring many measurements, particularly to uncover the detail shown in figure 6.14. The presented 'real time' load-pull sweeps could therefore be employed to dramatically speed up such analysis by presenting a modulated impedance environment that allows for collection of all required impedance points in a single waveform capture.

An example is shown in figure 6.15 (a), where a GaAs pHEMT device has been characterised at a frequency of 1.8 GHz, demonstrating the captured dynamic load-line performance under slowly modulated load impedance. The dynamic impedance presented to the device is shown in figure 6.15 (b). This measurement was completed in a matter of seconds, whereas an analysis using a traditional active open-loop load-pull system could take hours.

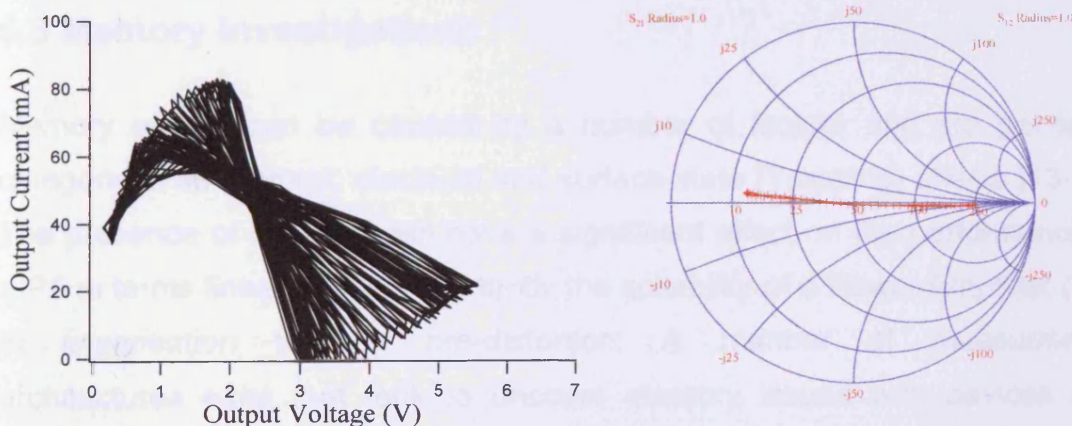


Figure 6.15 – (a) Measured dynamic RF load-line under slowly modulated load-impedance (b) Modulated impedance presented during measurement.

From the Smith chart it is clear that the modulated impedance maps the required real loads, from low to high impedance, which allows the analysis of the required load lines. Unfortunately, as stated earlier it is not possible at present to capture the base-band 'time varying DC' components, and this makes the analysis incomplete. As mentioned possible solutions allowing measurement of the low frequency base-band components are suggested in the future work.

To summarise, a number of "real-time" measurement concepts have been demonstrated that allow for the accurate and rapid characterisation of large-

signal device performance under quasi-CW modes of operation. This has been achieved by the integration of a multi-tone waveform measurement system with the active envelope load-pull architecture. Measurements are presented to demonstrate a number of applications. Further engineering of the multi-tone modulated stimulus and/or load-pull electronic control signals will enable this system to rapidly perform all the relevant non-linear device characterisation measurements necessary. For example a combination of modulated stimulus and modulated control signals could be used to simultaneously capture multiple power sweeps into multiple load impedances all in a single waveform capture. It would not be inconceivable that when these fast measurements become possible, that large signal measurements could become much more widely used, particularly in the area of wafer mapping.

6.3 Memory investigations

Memory effects can be caused by a number of factors and are generally categorised as thermal, electrical and surface-state (Trapping) effects [13-14]. The presence of memory can have a significant effect on the performance of a PA in terms linearity and importantly the suitability of a Power Amplifier (PA) to linearisation through pre-distortion. A number of measurement architectures exist that look to uncover memory issues with devices and provide feedback in the design process by generation of models that take account of memory. Generally however, these systems provide only scalar measurements, and hence do not allow the possibility to indicate the cause of the observed memory.

The ability of the presented system to measure all generated components under variable modulation states makes it an ideal tool to characterise a device for optimum linearity and to uncover the cause of memory issues. For example it is possible to remove the effects of electrical memory through the correct termination of all significant generated base-band components, thus allowing any memory observed to be clearly attributed to either thermal or trapping mechanisms. As thermal and trapping mechanisms are known to occur on different timescales, it should therefore be possible to

directly determine the causes of memory. This section will demonstrate how the realised multi-tone measurement system can be used in such investigations. The results shown in this section have been published along with more detailed analysis in [4-5].

The base-band active load-pull described in chapter 4 of this thesis is used to provide an effective way to engineer all the significant base-band components generated as a result of a multi-tone excitation, independent of modulation frequency. Specific base-band impedance environments are presented to a device with this approach in order to probe sensitivity to base-band impedance variations. The base-band load-pull employs two AWG's to actively vary the impedance of the two most significant base-band distortion components (IF1 and IF2).

Ideally, to eliminate the effect of the generated base-band signals, a short circuit termination should be used. This eliminates any voltage being developed as a result of the generated base-band current components. Fig 6.16 illustrates the almost invariant impedance achieved at IF1 and IF2 when using active base-band load-pull to maintain a frequency independent short circuit impedance with varying tone spacing from 1 to 10MHz, at a centre frequency of 2.1 GHz. It is important to note that during this experiment it was not possible to load-pull the second largest base-band component for modulation frequencies greater than 7MHz due to bandwidth limitations of the base-band PA used for the load-pull. This is highlighted in figure 6.16, which shows the significant variation in the impedance of IF2, from the desired short circuit for modulation frequencies from 8 MHz to 10 MHz.

Measurements were conducted into two different base-band impedance environments. In the first case, a nominal 50 Ω impedance was presented (state 1) and in the second case the two most significant base-band components were load-pulled to a short circuit (state 2).

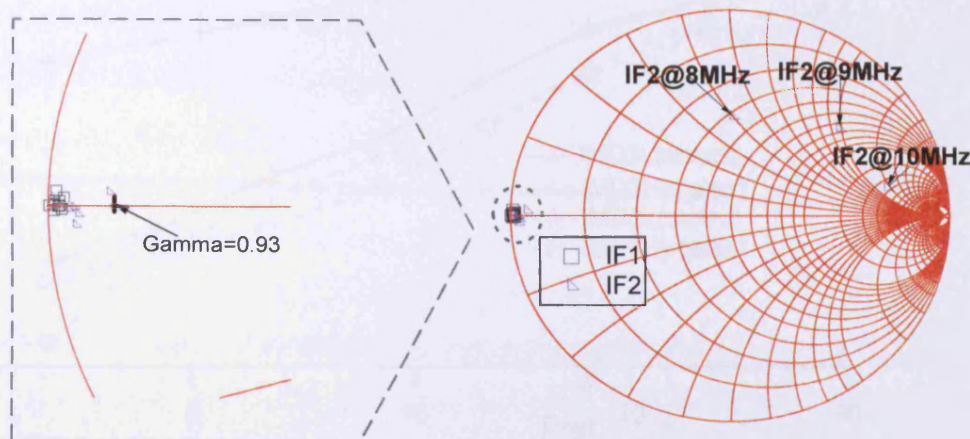


Figure 6.16 – Smith Chart plot highlighting the ability to accurately present constant impedance over bandwidth at IF1 and IF2 using active load control

As the envelope load-pull cannot currently be employed over such wide bandwidths, the RF impedance was controlled using broad-band 5:1 impedance transformers [15] to establish a wide bandwidth input and output RF system impedance of 10Ω . The measured RF two-tone spectral power performance for 5 MHz tone spacing is shown in figure 6.17, for the two cases of IF impedance. A typical behaviour, 1:1 slope for the two tones and 1:3 for the IM3 inter-modulation components, is observed over a power sweep covering a 30 dB dynamic range.

The variation of measured IM3 response as a function of IF impedance can be seen, with a clear improvement in linearity shown when the significant base-band components are driven into a short circuit. Fig 6.18 considers the IM3 behaviour again using the two different IF impedance states for different values of tone spacing ranging between 1 and 10 MHz, at a single drive level (P_{Ref}) highlighted by an arrow in figure 6.17. This reference point is 1 dB backed off from the 1 dB compression point.

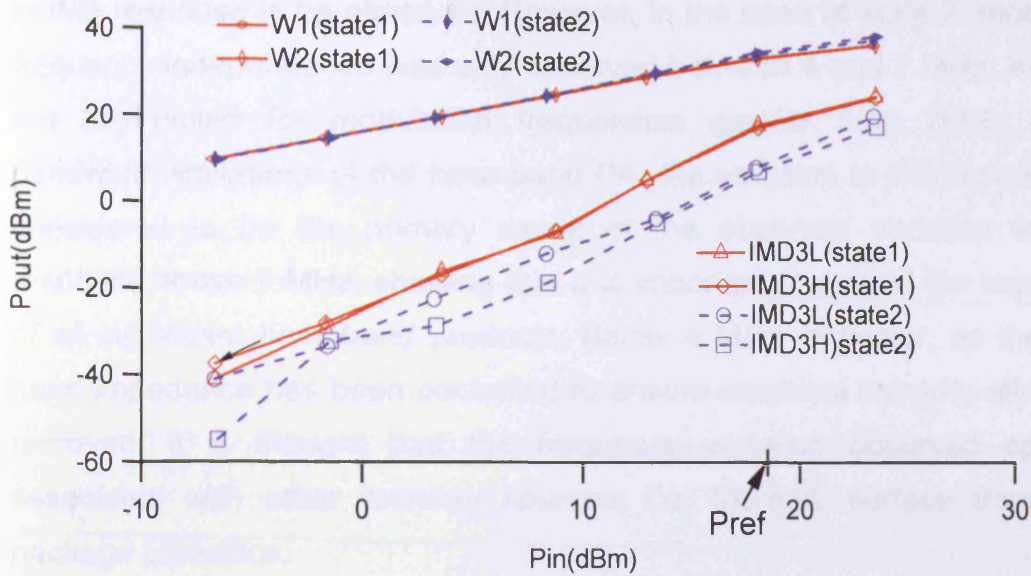


Figure 6.17 – Graph Highlighting Pout Vs Pin for main tones and IM3 Distortion products

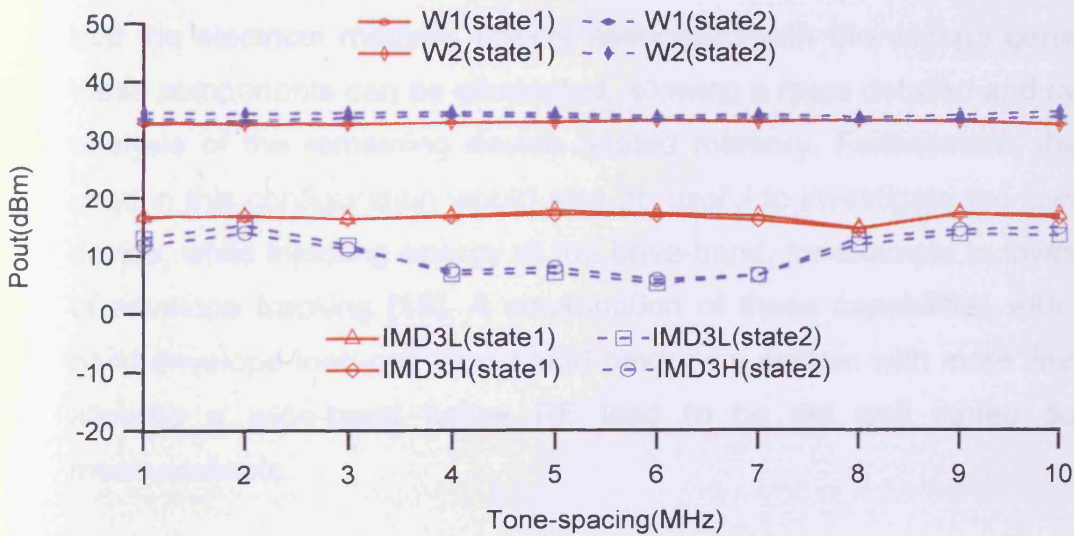


Figure 6.18 – Graph indicating output power levels of the two output tones along with IM3 distortion products as the tone-spacing is swept.

The behaviour of the two output tones (w1 and w2) is clearly almost independent of tone spacing frequency. In state 1 (base-band 50 Ω) the observed IMD3 response, while higher than the reference state 2 (base-band short), is found to be independent of tone-spacing. This result indicates that provided a frequency independent, constant base-band termination is utilized in the Power Amplifier drain bias network, no modulation frequency sensitivity

in IM3 response is be observed. However, in the case of state 2, modulation frequency independence was only observed between 4 and 7 MHz. As IF2 is not load-pulled for modulation frequencies greater then 7MHz due to bandwidth limitations of the base-band PA, the variation in IF2 impedance is considered to be the primary cause of the observed variation in IMD3 response above 7 MHz, showing that it is important to control the impedance of all significant base-band products. Below 4 MHz, however, as the base-band impedance has been controlled to ensure electrical memory effects are removed, it is thought that the frequency variation observed could be associated with other memory sources; i.e. thermal, surface trapping or package parasitics.

These measurements clearly show that the presented multi-tone, large-signal waveform measurement system is a valuable tool in the investigation of memory. As shown, the base-band impedance can be controlled to ensure that the electrical memory effects associated with the voltage generated by these components can be eliminated, allowing a more detailed and systematic analysis of the remaining device related memory. Furthermore, the system used in this configuration would also be useful to investigate the linearity of a device, while injecting energy at the base-band, for example in investigations of envelope tracking [16]. A combination of these capabilities with a wider-band envelope load-pull loop would produce a system with more flexibility, by allowing a wide-band active RF load to be set and varied during the measurements.

6.4 Multi-tone Time Domain Waveforms – Depth of Captured Information

As the captured time domain waveforms contain all the information about a device in a particular mode of operation, it is possible to extract the data in many different forms, some of which may already look familiar to a design engineer: spectral data, as presented in the previous memory investigation, Adjacent Channel Power Ratio (ACPR), Error Vector Magnitude (EVM) or Bit Error Rate (BER) and some that may be unfamiliar such as the time-domain waveforms themselves, dynamic load-lines or envelope domain information.

Perhaps the most useful way to view measured data is the envelope domain, which uses time domain and frequency domain techniques to allow analysis of the measured data. In this domain, a modulated signal is described as a complex time varying envelope containing magnitude and phase information for each Fourier coefficient. Analysis of these input and output time varying envelopes offers the ability to directly measure and engineer linearity and memory through active load-pull of all components in the device output. This section will present some example measurements presented in the envelope domain, showing how useful such measurements can be in characterisation and design. The importance of capturing and engineering all components in the device output will also become clear.

In the first measurement, a GaN PHEMT device biased in class B with a drain voltage of 8V is stimulated by a suppressed carrier, fifteen-tone signal with centre frequency of 1.8 GHz and 4MHz tone spacing. RF components are nominally terminated into 50 Ω , while the fundamental base-band component is actively load-pulled to a short circuit. Figure 6.19 shows the generated base-band, fundamental and second harmonic output current envelopes in magnitude and phase. In this domain, it becomes absolutely clear exactly what contribution each of the bands has on the final waveform.

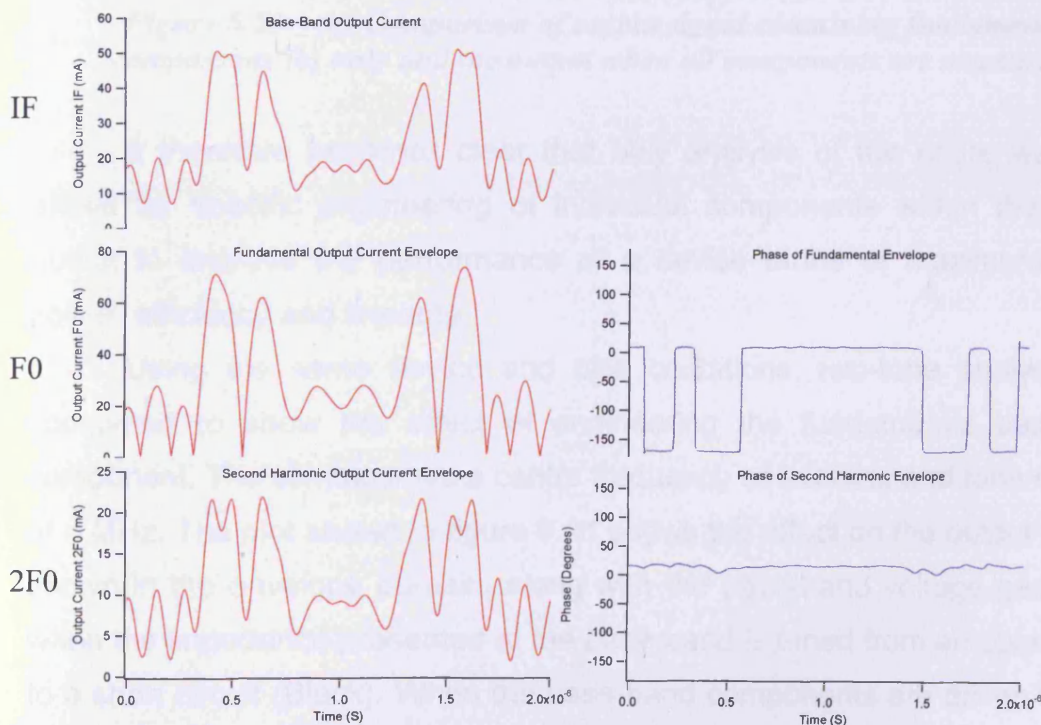


Figure 6.19 – Envelope domain Analysis of output Current

Figure 6.20(a) shows the waveform achieved if only the fundamental (in-band) components are measured, as is the case with many VSA based architectures. This is realised by filtering the other bands after measurement with the system. Figure 6.20(b) then shows the result of the addition of all three envelopes in the time domain, overlaid on top of the measured output current waveform. It is clear that it is only when all components are measured that the true waveforms can be seen. Interestingly, only when the base-band and harmonic information is added is it possible to determine the class of operation of the amplifier as only then can you see the current waveform clipping at the bottom as the transistor pinches off, indicating that the device is operating in class B.

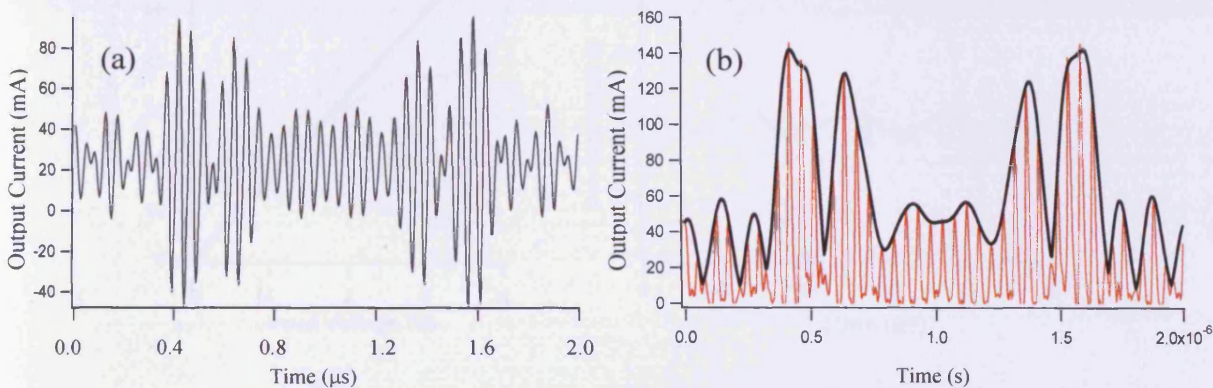


Figure 6.20 – (a) Comparison of output signal containing fundamental components (b) only and the output when all components are measured

It therefore becomes clear that only analysis of the entire waveform allows for specific engineering of individual components within the device output to improve the performance of a device terms of maximum output power, efficiency and linearity.

Using the same device and bias conditions, two-tone analysis was completed to show the effect of engineering the fundamental base-band component. The stimulus has a centre frequency of 1.8 GHz and tone spacing of 4 MHz. The plot shown in figure 6.21 shows the effect on the output current shown in the envelope domain, along with the base-band voltage generated when the impedance presented at the base-band is tuned from an open (Red) to a short circuit (Black). When the base-band components are driven into an open circuit, a large base-band voltage is generated which effectively

modulates the drain voltage. In this case, where the device is operated close to compression, this causes the output to 'slide' along the knee boundary, causing a looping current characteristic. When the fundamental IF component is tuned to a short circuit, the generated voltage is dramatically reduced with only a small ripple remaining. The remaining ripple is caused by the other base-band components, which are nominally terminated into the system impedance. The looping is removed from the current transfer characteristic (Red) indicating that the system induced "electrical memory" caused by the base-band impedance has been removed.

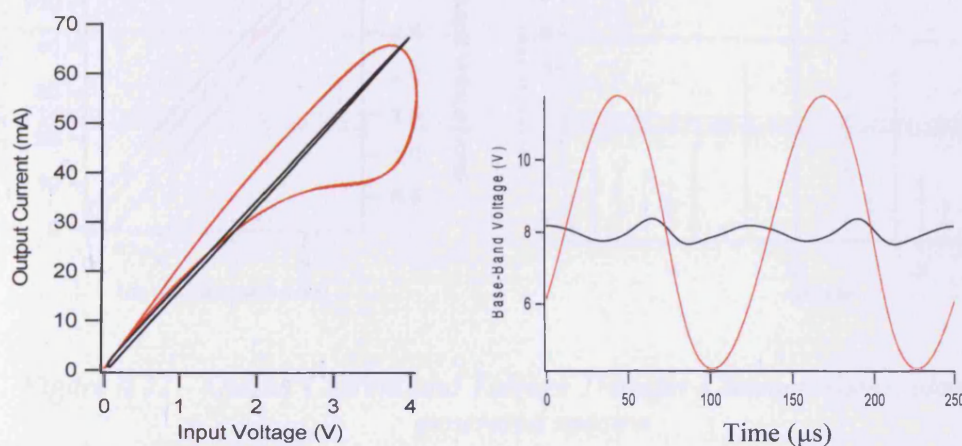


Figure 6.21 – Output Current and Voltage Transfer Characteristics along with generated base-band voltage

In this case, having the ability to measure the magnitude and phase of all components and conversion of the a and b travelling waves into individual voltage and current components provided vital information about the cause of the memory effect. This could easily be misconstrued if only magnitude information were available, as is the case with the spectrum analyser.

The next investigation considered the effects of in-band impedance. For this measurement, the impedance of the lower-tone was load-pulled slightly to create a non-constant impedance across the modulated bandwidth. The fundamental base-band component has been shorted to negate the effects of electrical memory. In this case, it can be seen from the resulting envelope domain plots shown in figure 6.22, that the current transfer characteristic exhibits no-looping, indicating that the device has no memory

(Red). The voltage transfer characteristic (black) however does have a looping nature. This can be directly attributed to the non-constant in-band impedance, highlighting the effect of variable in-band impedance on the measured non-linearity. A spectral plot is also included, showing the IM3 distortion observed. This investigation, along with the previous experiment, indicate that envelope domain plots therefore uncover vital information that can easily be misinterpreted if only frequency domain spectra were captured.

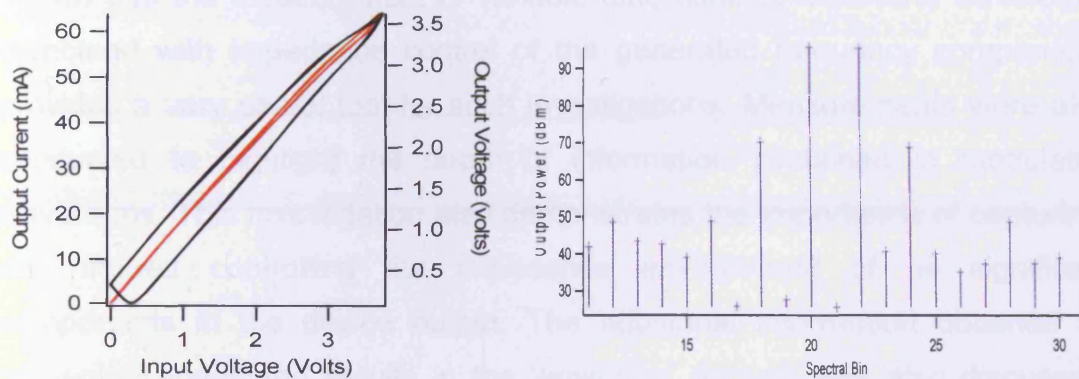


Figure 6.22 – Output Current and Voltage Transfer Characteristics along with generated spectra

The investigations presented above give some indication of depth of information contained in the measured modulated waveforms. Data has been presented in the time domain, the frequency domain and in the less familiar envelope domain. It has been shown that the envelope domain is a very useful format to display measured information. Examples were given where the envelope domain plots provide an indication of the cause of memory observed, where the spectral information alone would only have indicated the presence of memory. It is also apparent from these measurements that only the measurement and engineering of the entire multi-tone waveform, including all generated distortion products, will allow for the optimum design solution. The system's ability to capture complex multi-tone signals, including pulsed waveforms lends itself to the application of power amplifier design for communication and RADAR systems.

6.5 Chapter Summary

This chapter has presented a number of possible applications for the new multi-tone large-signal waveform measurement system. Numerous applications have been presented that take advantage of real-time measurement concepts, where slowly modulated stimuli or load impedance are used in the ultra-rapid collection of quasi-CW data sets. An investigation is also presented that considers memory effects in a 20 W LDMOS device. It is shown that the measurement of variable tone spacing multi-tone waveforms combined with impedance control of the generated frequency components provides a very useful tool for such investigations. Measurements were also conducted to highlight the depth of information contained in modulated waveforms. This investigation also demonstrates the importance of capturing, and indeed controlling the impedance environment of all significant components in the device output. The additional information obtained by presenting measured results in the 'envelope' domain was also discussed, with presented measurements highlighting how useful this information can be in device characterisation

Even with the identified limitations of the envelope load-pull architecture, specifically upper bandwidth and the inability to measure low-frequency IF components below 100 kHz, the presented system has already proved itself as a useful tool in device characterisation, both for ultra-rapid data collection, and in applications for engineering linearity and quantifying device memory.

6.6 References

1. Williams, T.; Benedikt, J.; Tasker, P.J. "**Fully Functional 'Real Time' Non-Linear Device Characterization System Incorporating Active Load Control**" 36th European Microwave Conference, September 2006, Page(s): 1610-1613 .
2. Williams, T.; Benedikt, J.; Tasker, P.J. "**Application of a novel active envelope load pull architecture in large signal device characterization**" 35th European Microwave Conference, Volume 1, October 2005.
3. Williams, T.; Benedikt, J.; Tasker, P.J. "**Experimental evaluation of an active envelope load pull architecture for high speed device characterization**" IEEE MTT-S International Microwave Symposium Digest, June 2005.
4. Alghanim A.; Lees J.; Williams T.; Benedikt J., Tasker P.J. "**Using active IF load-pull to investigate electrical base-band memory effects in high-power LDMOS transistors**" IEEE Asia-Pacific Microwave Conference 2007.
5. Alghanim A.; Lees J.; Williams T.; Benedikt J., Tasker P.J. "**Investigation of Electrical Base-Band Memory Effects in High Power 20W LDMOS Amplifiers**" IEEE Asia-Pacific Microwave Conference 2007.
6. S.A. Maas "**Nonlinear Microwave Circuits Second Edition**" Artech House Microwave Library 2003, ISBN 1-58053-484-8.
7. Lees, J.; Benedikt, J.; Hilton, K.P.; Powell, J.; Balmer, R.S.; Uren, M.J.; Martin, T.; Tasker, P.J. "**Characterisation of an experimental gallium nitride microwave Doherty amplifier**" 2005 European Microwave Conference, Volume 2, 4-6 Oct. 2005.
8. McGovern, P.; Benedikt, J.; Tasker, P.J.; Powell, J.; Hilton, K.P.; Glasper, J.L.; Balmer, R.S.; Martin, T.; Uren, M.J. "**Analysis of DC-RF dispersion in AlGaIn/GaN HFETs using pulsed I-V and time-domain waveform measurements**" IEEE/MTT-S International Microwave Symposium Digest 2005.
9. Curras-Francos, M.C.; Tasker, P.J.; Fernandez-Barciela, M.; O'Keefe, S.S.; Campos-Roca, Y.; Sanchez, E. "**Direct extraction of nonlinear FET I-V functions from time-domain large-signal measurements**" Electronics Letters, Volume 34, Issue 21, 15 Oct. 1998 Page(s):1993 – 1994
10. S.C. Binari, K. Ikossi, J.A. Roussos, W. Kruppa, Doewon Park, H.B. Dietrich, D.D. Koleske, A.E. Wickenden and R.L. Henry, "**Trapping effects and microwave power performance in AlGaIn/GaN HEMTs,**" IEEE Transactions on Electron Devices, volume 48, Issue 3, March 2001, pp. 465-4 71.
11. Roff, C.; McGovern, P.; Benedikt, J.; Tasker, P.J.; Balmer, R.S.; Wallis, D.J.; Hilton, K.P.; Maclean, J.O.; Hayes, D.G.; Uren, M.J.; Martin, T. "**Detailed Analysis of DC-RF Dispersion in AlGaIn/GaN HFETs using Waveform Measurements**" 36th European Microwave Conference, September 2006, Page(s): 43-45.

12. McGovern, P.; Benedikt, J.; Tasker, P.J.; Powell, J.; Hilton, K.P.; Glasper, J.L.; Balmer, R.S.; Martin, T.; Uren, M.J.. “***Analysis of DC-RF dispersion in AlGaN/GaN HFETs using pulsed I-V and time-domain waveform measurements***” IEEE MTT-S International Microwave Symposium Digest, June 2005.
13. Joel H. K. Vuolevi, Timo Rahkonen, Jani P. Manninen, “***Measurement technique for characterizing memory effects in RF power amplifiers***” IEEE Transactions on Microwave Theory and Techniques, volume 49, no.9, pp. 1383-1389, Aug. 2001.
14. A. E. Parker and J. G. Rathmell, “***Bias and frequency dependence of FET characteristics***” IEEE Transactions on Microwave Theory and Techniques, vol. 51, pp. 588–592, Feb. 2003.
15. Aboush, Z.; Benedikt, J.; Tasker, P. “***High power harmonic active load-pull using broadband impedance transformers [power transistor measurement]***” High Frequency Postgraduate Student Colloquium, 2004 6-7 Sept. 2004 Page(s):145 – 150.
16. Feipeng Wang; Yang, A.H.; Kimball, D.F.; Larson, L.E.; Asbeck, P.M. “***Design of wide-bandwidth envelope-tracking power amplifiers for OFDM applications***” IEEE Transactions on Microwave Theory and Techniques, Volume 53, Issue 4, Part 1, April 2005 Page(s):1244 – 1255

Chapter 7 – Conclusion and Future Work

7.1 Conclusion

A large-signal measurement system capable of measuring and engineering complex multi-tone waveforms has been conceived, realised, demonstrated and validated. The presented system, using multi-tone waveforms, allows for a more considered design approach, with an ultimate goal of 'right-first-time' design. By overcoming the need for the generally adopted iterative design approach, it is hoped that the presented system will provide the foundations of a system that will enable the microwave community to fully embrace the significant benefits of large-signal measurements in design.

An optimum hardware configuration has been realised that combines RF and base-band test-sets, and allows measurement of all significant generated distortion terms at the base-band, fundamental-band and relevant harmonic bands. The RF and base-band components are coupled separately and combined before measurement by a single sampling oscilloscope, thus ensuring phase coherence of all measured components. Both RF and baseband test-sets incorporate directional couplers to simultaneously measure all incident and reflected waveforms (a_1 , b_1 , a_2 and b_2) at the input

and output ports of a two port device. Calibration of the system allows extraction of the time domain waveforms at the device plane. The presented system has an RF bandwidth of 1-12 GHz, and a base-band bandwidth of 100 kHz-10 MHz. The measurement system bandwidth is only limited by the components used within the test-sets, although application at higher RF frequencies would also require new samplers.

The key ability to capture modulated, multi-tone, signals using this instrument was made possible through the development and implementation of a novel frequency-folded sampling approach, which is combined with time interleaved sampling, allowing multi-tone waveforms to be captured in a spectrally efficient way. This enables instruments with a limited memory depth (such as the sampling oscilloscope used in these investigations) to capture multi-tone waveforms with detailed IF, in-band (RF) and harmonic-band (RF) information, without sacrificing measurement quality. To improve the dynamic range of the system, a novel software waveform alignment algorithm was also developed to allow for averaging of the multi-tone signals.

The presented measurement system has been validated against a number of other large-signal measurement systems, including established CW waveform measurement systems and a spectrum analyser. Successful comparisons offer proof that the system is capable of capturing high quality vector-corrected multi-tone information, and confirms that all of the multi-tone concepts have been successfully realised. Measured results show that almost perfect agreement was achieved over a dynamic range of around 35 dB.

In addition to the multi-tone waveform measurement capabilities, active load-pull architectures were required to allow engineering of the multi-tone waveforms, allowing impedance control of all generated frequency components. Load-pull is not straightforward for multi-tone stimulus however as impedance must be controlled over bandwidth; at the base-band, in-band (RF) and at harmonic bands (RF). Two separate solutions were developed and demonstrated; one covers control of the generated base-band distortion terms and one covers the RF distortion products generated in the fundamental and harmonic bands.

The solution for the base-band load-pull led directly on from the standard open loop active load-pull approach using a signal generator to

inject a signal back into the device to set the impedance, this was possible as the number of significant tones generated at base-band is small. As this approach has been well documented in previous thesis [1] it was only covered briefly in this thesis.

The solution for the control of the RF band impedances was a little more difficult and required the development and optimisation of a novel active load-pull architecture. This architecture, also presented in [2-4] overcomes the major limitations of existing active load-pull architectures by offering drive independent impedance, control, while ensuring stable operation by avoiding a direct RF feedback loop in the load-pull architecture. This made the architecture ideal for impedance control in applications involving multi-tone signals, as well as offering a significant improvement in measurement time for CW measurements. This was achieved by removing the need for an iterative setting of the impedance, as is required in current active open-loop configurations. The architecture has a unique ability to present constant impedance to all frequency components within an output signal, including those around the carrier and its harmonics. Thus for the first time, an active broad-band load can be applied across a modulation bandwidth.

The envelope load-pull architecture has been fully validated and optimised. Measured results where the system has been employed in device characterisation show that the architecture can be used to successfully maintain a near invariant load under varying drive conditions. The main limitation of the system is the useable bandwidth over which the envelope load-pull can be employed; group delay around the load-pull loop causes the envelope of the reflected signal to become misaligned, causing impedance variation across the modulated bandwidth. The architecture has however been demonstrated and fully validated at lower frequencies, up to 10 kHz.

The combination of the large-signal multi-tone measurement system with the impedance engineering capabilities of the novel active load-pull architecture has resulted in a multi-tone measurement solution that has significantly expanded the capabilities and application of large signal measurements. Although the primary aim of this thesis was to design, realise and validate a new multi-tone, large-signal waveform measurement system, a number of measurements that have become possible through the realisation

of the new system were also presented. The presented results do not aim to offer detailed characterisation or observation, and they serve only to provide example measurements and investigations that others could make using the realised multi-tone measurement system.

Applications are presented that show how slow modulation of either the stimulus or the synthesised load allow ultra-rapid CW characterisation of a DUT. It is hoped that by enabling such ultra-rapid measurement concepts, the presented multi-tone waveform measurement and engineering solution will advance the take-up of large signal measurements in modern mobile communication system design. The realisation of the presented solution means that it is now possible for complex, large-signal measurements to be completed on a similar time scale to small-signal linear measurements.

Measurements aimed at engineering linearity and memory performance are also presented in chapter 6, showing that the system could be a very useful tool in such investigations. From these measurements, it becomes clear that analysis of the magnitude and phase of all significant generated distortion terms is the only way to fully understand device behaviour.

The presented investigations are only limited by two factors which have been discussed in detail, namely, the limited bandwidth of the envelope load-pull architecture and the inability to measure very low frequency base-band information using the current base-band test sets. Neither of these shortcomings are considered to be fundamental failings of the system however, and possible solutions to these problems, along with other possible improvements of the system are discussed in the future work section below.

7.2 Future work

While the aim of designing, realising and validating a new large signal measurement system capable of measuring and engineering multi-tone waveforms has been met, further work is still required to fully optimise the approach. This section looks to offer solutions to the two main limitations previously discussed and highlight some of the other areas that need further development, before the system can be employed to the peak of its abilities.

7.2.1 Increase Operational Bandwidth of Modulated Load-Pull

The measurement of virtually any repetitive modulated waveform is now possible using the realised measurement system. Envelope load-pull bandwidths are limited however to between 100 kHz and 10 MHz, and there is significant scope for improvement in the realisation of RF impedance control across modulation bandwidths relevant to modern communications systems. One key problem that has been identified is associated with the group delay in the envelop-loop, which results in misalignment of the incident (b_2) and injected (a_2) envelopes, as the modulation frequency is increased. This limited bandwidth has a large impact on the load-pull impedance generated when a device is driven under a more realistic communications type signals. Clearly to take full advantage of this new measurement approach, it is therefore necessary to increase the operational bandwidth of the envelope load-pull loop.

While the bandwidth of the electronics used in the envelope load-pull architecture will eventually limit performance, the first bandwidth 'bottleneck' that needs to be addressed originates directly from delay imparted on the signal as it propagates around the load-pull loop. Simply replacing the rather simplistic electronic components currently used with faster equivalents would not actually solve this problem. However this delay issue is not insurmountable as the measured signals are always repetitive, and so adding additional delay could be used to precisely align the load-pull with the next available modulated cycle. While it is not inconceivable that an analogue solution could be found, it is quite difficult to induce large variable delays in analogue electronics, so by far the easiest and most flexible solution would be to replace the analogue control circuit with some digital implementation using for example a Field-Programmable Gate Array (FPGA). The use of digital electronics would allow the delay issue to be dealt with quite simply and also opens a number of other interesting opportunities. For example, using such an approach it would be possible to Fourier transform the I and Q signals to engineer the impedance of each of the components in the spectrum completely independently, which would dramatically simplify the architecture

required to emulate 'real' matching circuits. Additionally, any unresolved issues with DC offsets in the architecture could also be more easily dealt with.

7.2.2 Extending the bandwidth of the base-band measurements

As discussed earlier in the thesis, the bandwidth of the base-band test-set is currently limited to frequencies as low as 100 kHz and as high as 10 MHz. The maximum frequency of operation does not cause any significant issues as it can be easily increased by integration of new components in the base-band test-set. Measurement of lower frequency base-band components is, however, a little more involved. Clearly, it is unrealistic to extend a test-set incorporating conventional couplers down to lower frequencies, thus an alternative solution is required. Two solutions could be considered; the first is to measure the voltage and current directly, using an oscilloscope, which becomes possible at low frequencies. Alternatively, a new class of instrument, the DC power analyser (produced by Agilent [5]) could be used. This instrument is capable of supplying and measuring 'time-varying DC', and has fully incorporated data logging and oscilloscope capabilities. In either case, some triggering solution would be required to ensure the captured low frequency base-band components are phase aligned to the base-band and RF components collected by the sampling oscilloscope.

7.2.3 Integration of a Spectrum Analyser into the Multi-tone Measurement system

Simply integrating a spectrum analyser into the measurement architecture could extend the capabilities of the multi-tone large signal measurement system. At present the dynamic range of the multi-tone measurements is 35 dB. This is perfectly acceptable for the intended use of the system in modulated device characterisation, where such small spectral components have a very limited effect on the waveforms. However, integration of a spectrum analyser into the measurement setup would allow the same measurement system to deal with linearity testing of realised circuits where in band distortion must meet very tight spectral masks. Spectrum analysers due

to their swept frequency nature can achieve dynamic range greater than 100 dB although it is important to note that phase information is no longer measured. This architecture would however offer all the information provided by the waveforms at higher power levels, where this vital characterization information would allow for example, an investigation into why a circuit has failed to meet its linearity specification. The spectrum analyser also becomes the ideal tool to perform in-situ validation of the new measurement system, particularly as the user approaches the lower end of the dynamic range. The spectrum analyser could be integrated as shown in figure 7.1, using one additional RF coupler and one additional base-band coupler at the output side of the device. Provided this configuration was fixed during the calibration process, it would allow the spectrum analyser to measure all of the information at all bands without influencing the waveform measurement or the load pull applied. Importantly, the spectrum analyser could also give direct feedback of any device oscillations during measurements, which are often very difficult to detect with the sampling oscilloscope, especially if the oscillation frequency does not lie somewhere on the measured frequency grid.

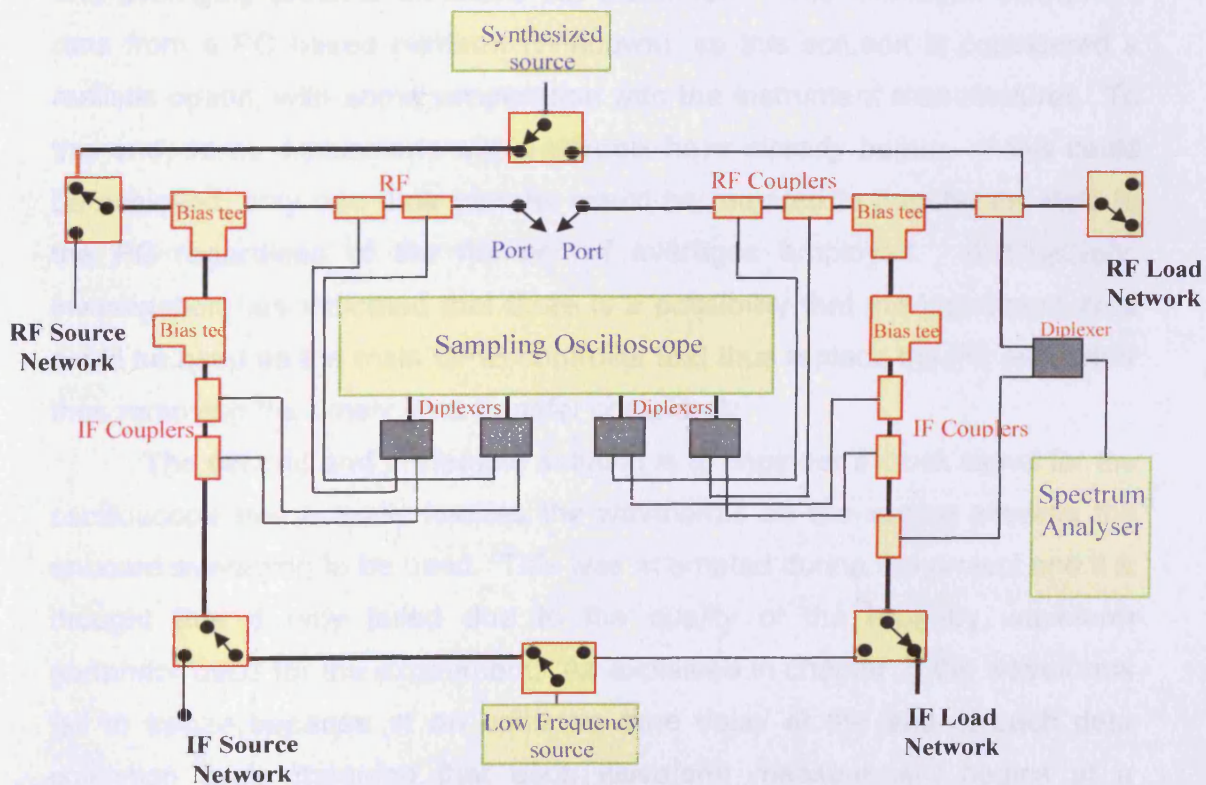


Figure 7.1 Modulated Large signal measurement system with fully integrated Spectrum Analyser

7.2.4 Optimisation of multi-tone alignment and averaging process

As discussed in chapter 2 of the thesis, when the necessary frequency-folded sampling approach is employed, it is no longer possible to freeze the waveforms on the screen of the sampling oscilloscope. Thus, it is not possible to use the on-board averaging of the instrument. In the thesis, a solution was developed and implemented that uses a software algorithm to re-align consecutive waveforms, hence enabling averaging of a set of measured waveforms. While this approach proved successful and has been used for a number of different multi-tone measurements, it does make the averaging process rather slow. The reason for this is the requirement for multiple slow data transfers between the instrument and a PC over a General Purpose Instrument Bus (GPIB). The number of data transfers required increases as a greater number averages are required. There are two possible solutions to this time consuming averaging process, which will be discussed below.

The first and perhaps most obvious solution is to perform the alignment and averaging process on-board the instrument. The CSA8000 instrument runs from a PC based platform (Windows), so this solution is considered a realistic option, with some cooperation with the instrument manufacturer. To this end, some discussions with Tektronix have already begun. If this could be achieved, only one data transfer would be required to transfer the data to the PC regardless of the number of averages employed. Alternatively, investigation has indicated that there is a possibility that the instrument itself could be used as the main GPIB controller and thus replace the PC altogether thus removing the timely data transfer completely.

The second and preferable solution is to engineer a clock signal for the oscilloscope that actually freezes the waveforms on the screen allowing the onboard averaging to be used. This was attempted during the project and it is thought that it only failed due to the quality of the arbitrary waveform generator used for the experiment. As explained in chapter 2, the waveforms fail to freeze because of an unknown time delay at the end of each data collection cycle meaning that each waveform measurement begins at a different relative point in time. The idea is to use a 'burst' clock signal to

freeze the multi-tone waveform on screen, hence allowing the user to employ the in built averaging routines of the scope. By calculating the total time taken to capture an entire set of points it is possible to have a master trigger to ensure that each waveform is captured at the same relative time reference point. The formulation presented below should therefore be effective in freezing the waveforms.

The total time taken to capture an entire set of points T_{Total} is given by equation 1, where N_{Clock} is the total number of trigger clock edges applied during the measurement, calculated by equation 2, T_{Clock} is the trigger period and T_{Window} is the measurement time window.

$$T_{Total} = (N_{Clock} \times T_{Clock}) + T_{Window} \quad (1)$$

Equation 2 gives the total number of trigger clock cycles in a given measurement cycle, where X is the number of missed triggers at each measurement point, given here by equation 3 and derived in chapter 2. P is the number of points.

$$N_{Clock} = (X \times (P - 1)) + P \quad (2)$$

Equation 3 gives the number of missed clock edges for every valid triggered measurement point, where T_{Hold} is the hold time or re-arm time of the trigger circuitry of the sampling oscilloscope and T_{Clock} is the clock period.

$$X = \frac{T_{Hold}}{T_{Clock}} \quad (3)$$

Once the total measurement time is known, the burst clock signal should consist of a burst of length N_{Clock} with each subsequent burst of clock starting at some multiple of the total measurement time T_{Total} ; this is shown pictorially in figure 7.2.

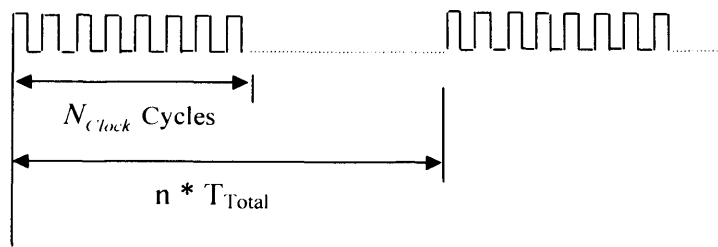


Figure 7.2 Burst clock Arrangement that should freeze waveforms on sampling oscilloscope

As stated, this investigation was conducted during the project, however the best result that was achieved was a very slowly moving modulated waveform. Unfortunately, even a slowly moving waveform cannot be averaged without degrading the measurement. It is likely that the measurement failed to work due to an insufficient time resolution on the AWG signal generator used in the investigation, so a high quality AWG instrument should be sourced for future investigations.

7.2.5 Increase the Bandwidth of the New Multi-tone Waveform Measurement System

The presented architecture has a bandwidth of 12 GHz, limited by the samplers of the sampling oscilloscope. This bandwidth is more than sufficient for the desired application to design PA's for the mobile communications industry. Current mobile communication signals typically operate at frequencies around 1.8 – 2.1 GHz, so a 12 GHz bandwidth allows the measurement of all significant generated harmonics. However by extending the bandwidth of the measurement system to higher frequencies, the useful information provided by the system could be adopted in the design of military communication and radar systems, typically operating above 6 GHz. It is thought that expanding the system to higher frequencies would be relatively simple if a little costly. A new sampling oscilloscope mainframe has become available (Tektronix 8200 series [6]) with samplers operating up to 60 GHz. This, in addition with a new test set, could be employed with the existing software to create a very wide band measurement system. The highest

frequency connector available on all of the required components is a 2.4 mm connector, which would expand the bandwidth up to 40 GHz. This would dramatically expand the market for the measurement system allowing deployment into a completely different market.

7.3 References

1. Williams, D.J. (2003) *Non-Linear Measurement System and Techniques for RF Power Amplifier Design*. PhD thesis. Cardiff University
2. Williams, T.; Benedikt, J.; Tasker, P.J.; “*Experimental evaluation of an active envelope load pull architecture for high speed device characterization*” IEEE/MTT-S International Microwave Symposium 2005.
3. Williams, T.; Benedikt, J.; Tasker, P.J.; “*Application of a novel active envelope load pull architecture in large signal device characterization*” 2005 European Microwave Conference, Volume 1, 4-6 Oct. 2005.
4. Williams, T.; Benedikt, J.; Tasker, P.J.; “*Fully Functional "Real Time" Non-Linear Device Characterization System Incorporating Active Load Control*” 2006 European Microwave Conference, Page(s):1610-1613.
5. Agilent Technologies, Product Overview. “*DC Power Analyser*” (<http://cp.literature.agilent.com/litweb/pdf/5989-6319EN.pdf>) accessed October 2007.
6. Tektronix, Data Sheet. “*8200 Series Digital Signal Analyser Sampling Oscilloscope*” (http://www.tek.com/site/ps/0,,85-17654-INTRO_EN,00.html) accessed March 2007.

Appendix 1

Appendix 1 – Selection of order and number of points when employing the compressed frequency sampling approach

As discussed in chapter 2 of the thesis, it is vital that care is taken, when employing the compressed frequency folded sampling approach. A user must be aware that spectral leakage and spectral folding will occur. Thus to ensure that only one significant component is measured in each spectral bin, two things must be verified; Firstly the user must allow enough order to allow for all significant distortion terms in each band, thus avoiding spectral leakage; the user also has to ensure enough data points are allowed to collect all significant harmonics, thus avoiding unwanted spectral folding. Worked examples are shown below. In the first case not enough points are used, this results in significant harmonic distortion terms folding back on top of other measured components, which would clearly distort the measurements. A second case is shown where sufficient order and points are used to ensure each spectral bin contains only one significant frequency component.

Worked Example

For the examples, we assume a two-tone signal is used as the input to a device, thus using mixing theory summarised in chapter 3 of the thesis it is possible to predict the mixing terms that would be generated at the output of the device. This includes in-band and harmonic components. For simplicity it is assumed that only components up to the 5th order are significant, which in reality is unlikely to be the case, but will be sufficient to outline the problem.

- In the first example shown in table 1, the user sets an order of 5 for the measured grid, which ensures the carrier is at location 11. 80 data points are used on the oscilloscope, resulting in 40 possible spectral bins.

Although the user has clearly employed sufficient order, it is clear that due to the limited number of points, significant higher harmonics (4th and 5th) fold back in the spectrum and distort the measurement; these 'unexpected' components are highlighted in red.

- The solution in this case, shown by table 2, is to leave the measured grid order as 5 and to increase the number of data points to 122, thus allowing 61 spectral bins for the measurement. It is clear from the table that all distortion products are now measured in individual spectral bins.

Summary

Worked examples have been used to demonstrate that care must be taken when employing the folded spectral approach. In the examples it was assumed that only distortion terms up to the 5th order are significant, however this is not generally the case. In reality, a sensible approach is to gradually increase the order used in setting the sampling grid until there are clearly a number of 'empty' spectral bins between each band. The number of points should then be increased until there are clearly no significant components remaining in the higher harmonics. As there are a maximum of 4000 points, it is clearly possible to ensure that enough order and points are used to avoid these issues.

	Base-Band	F0-Band	2F0-Band	3F0-Band	4F0-Band	5F0-Band
0	DC				$4\omega_1$	
1						
2	$\omega_2 - \omega_1$				$3\omega_1 + \omega_2$	
3						
4	$2\omega_1 - 2\omega_2$				$2\omega_1 + 2\omega_2$	
5						
6		$3\omega_1 - 2\omega_2$			$3\omega_2 + \omega_1$	
7						
8		$2\omega_1 - \omega_2$			$4\omega_2$	
9						
10		ω_1				$5\omega_1$
11		*				
12		ω_2				$4\omega_1 + \omega_2$
13						
14		$2\omega_2 - \omega_1$				$3\omega_1 + 2\omega_2$
15						
16		$3\omega_2 - 2\omega_1$				$3\omega_2 + 2\omega_1$
17						
18			$3\omega_1 - \omega_2$			$4\omega_2 + \omega_1$
19						
20			$2\omega_1$			$5\omega_2$
21						
22			$\omega_1 + \omega_2$			
23						
24			$2\omega_2$			
25						
26			$3\omega_2 - \omega_1$			
27						
28				$4\omega_1 - \omega_2$		
29						
30				$3\omega_1$		
31						
32				$2\omega_2 - \omega_1$		
33						
34				$2\omega_2 + \omega_1$		
35						
36				$3\omega_2$		
37						
38				$4\omega_2 - \omega_1$		
39						

Table 1 – Compressed Sampling with Unwanted Frequency Fold-back

	Base-Band	F0-Band	2F0-Band	3F0-Band	4F0-Band	5F0-Band
0	DC					
1						
2	$\omega_2 - \omega_1$					
3						
4	$2\omega_1 - 2\omega_2$					
5						
6		$3\omega_1 - 2\omega_2$				
7						
8		$2\omega_1 - \omega_2$				
9						
10		ω_1				
11		*				
12		ω_2				
13						
14		$2\omega_2 - \omega_1$				
15						
16		$3\omega_2 - 2\omega_1$				
17						
18			$3\omega_1 - \omega_2$			
19						
20			$2\omega_1$			
21						
22			$\omega_1 + \omega_2$			
23						
24			$2\omega_2$			
25						
26			$3\omega_2 - \omega_1$			
27						
28				$4\omega_1 - \omega_2$		
29						
30				$3\omega_1$		
31						
32				$2\omega_2 - \omega_1$		
33						
34				$2\omega_2 + \omega_1$		
35						
36				$3\omega_2$		
37						
38				$4\omega_2 - \omega_1$		
39						
40					$4\omega_1$	
41						

42					$3\omega_1+\omega_2$	
43						
44					$2\omega_1+2\omega_2$	
45						
46					$3\omega_2+\omega_1$	
47						
48					$4\omega_2$	
49						
50						$5\omega_1$
51						
52						$4\omega_1+\omega_2$
53						
54						$3\omega_1+2\omega_2$
55						
56						$3\omega_2+2\omega_1$
57						
58						$4\omega_2+\omega_1$
59						
						$5\omega_2$

Table 2 – Compressed Sampling with no unwanted frequency fold-back

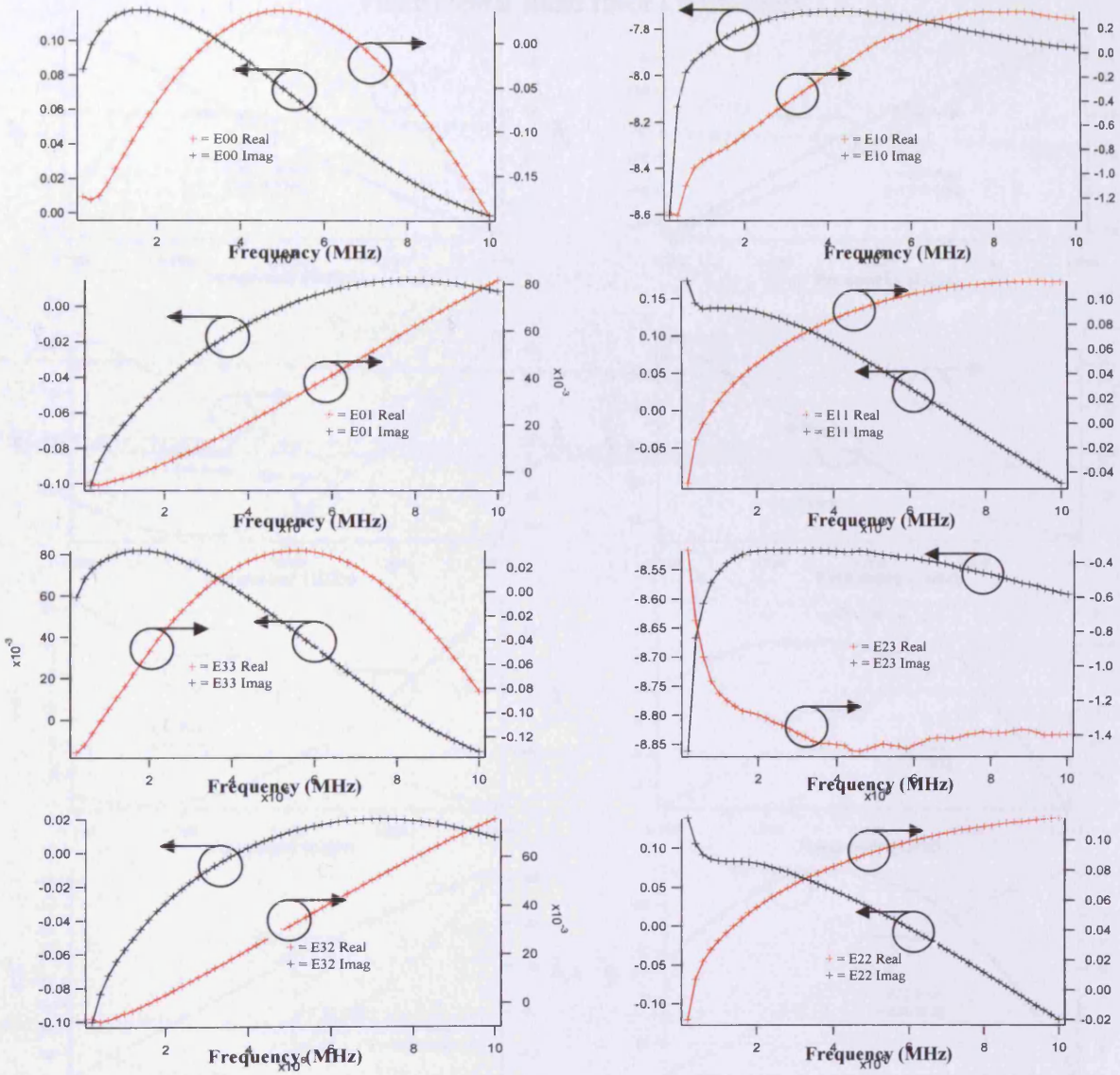
Appendix 2

Appendix 2

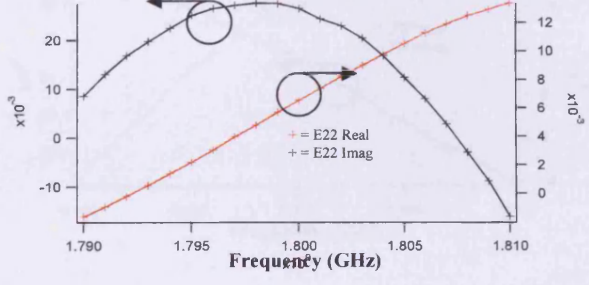
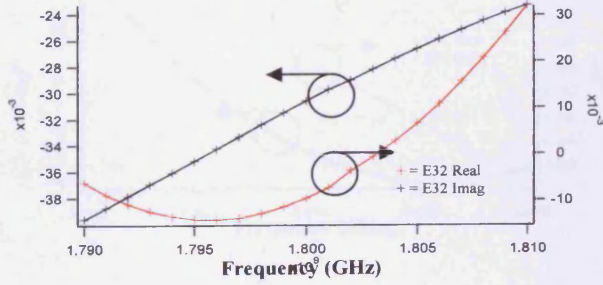
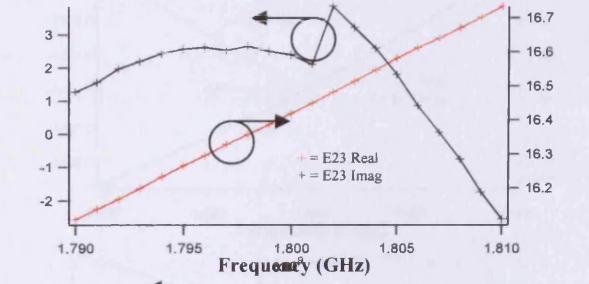
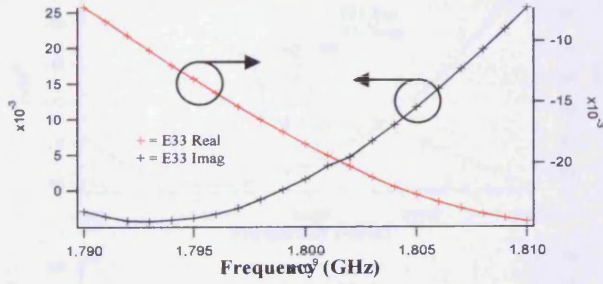
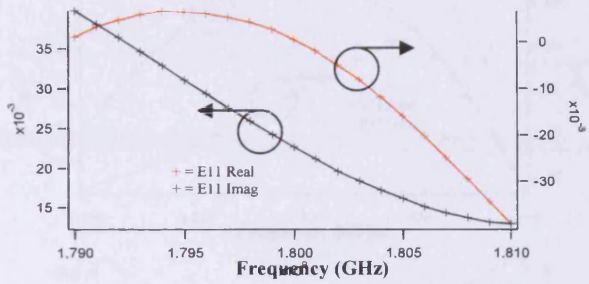
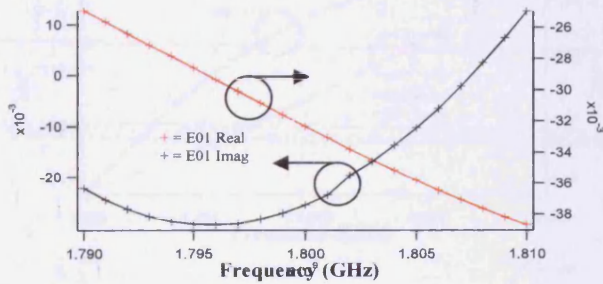
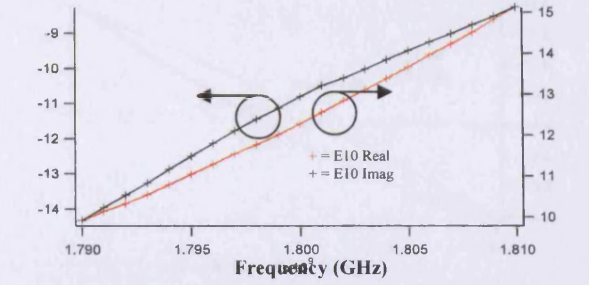
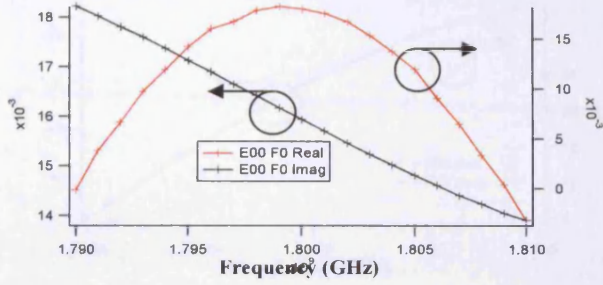
The following graphs show the calculated error coefficients of the measurement system, the system is calibrated at base-band, fundamental-band and harmonic-bands up to the 5th harmonic. The system has been calibrated over a 10 MHz bandwidth at the base-band, and over a 20 MHz band at RF.

The presented graphs of the error coefficients confirm that the system does not vary widely over the calibrated bandwidth, making it possible to easily interpolate the error coefficients.

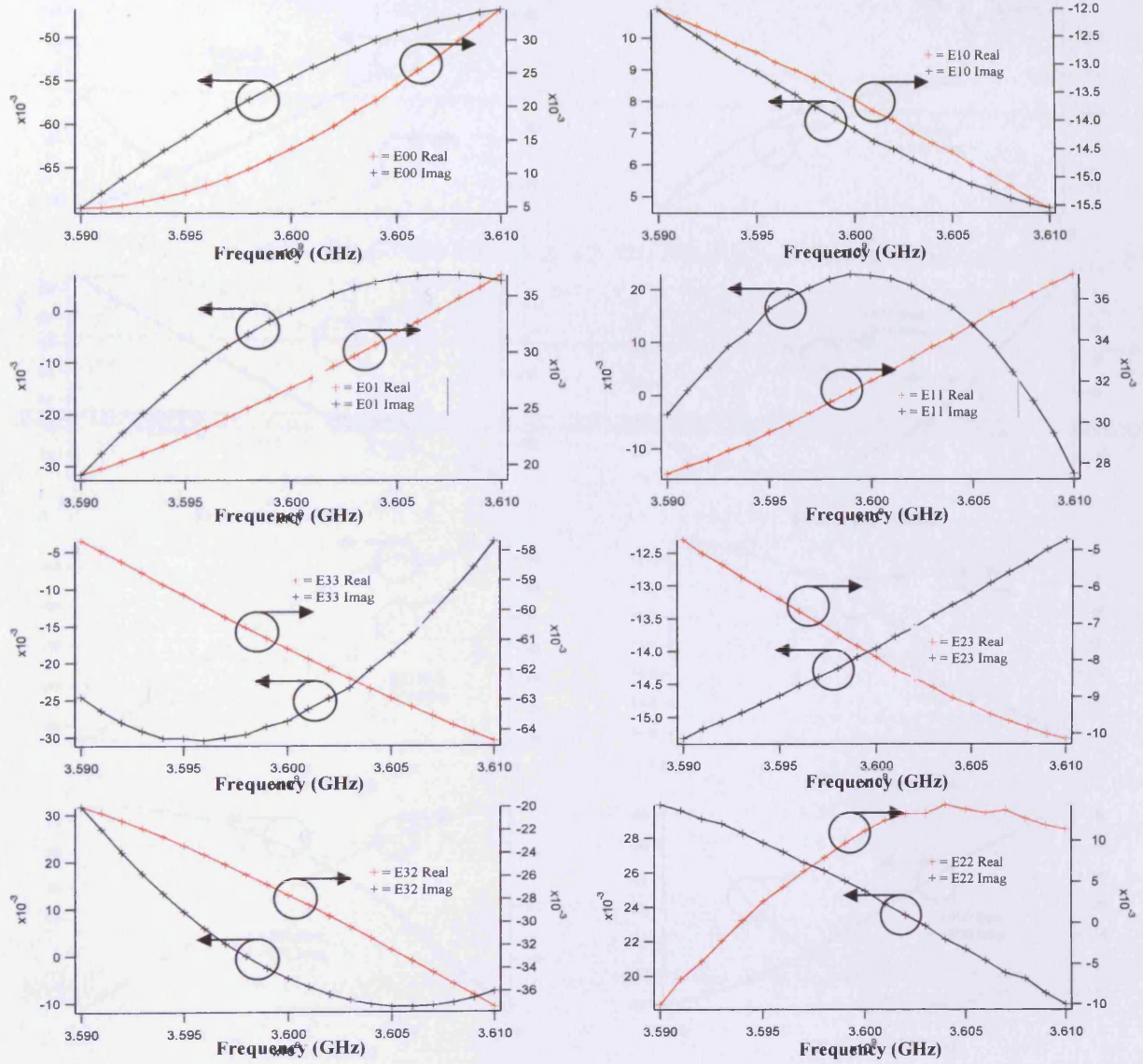
Base-Band Error Coefficients



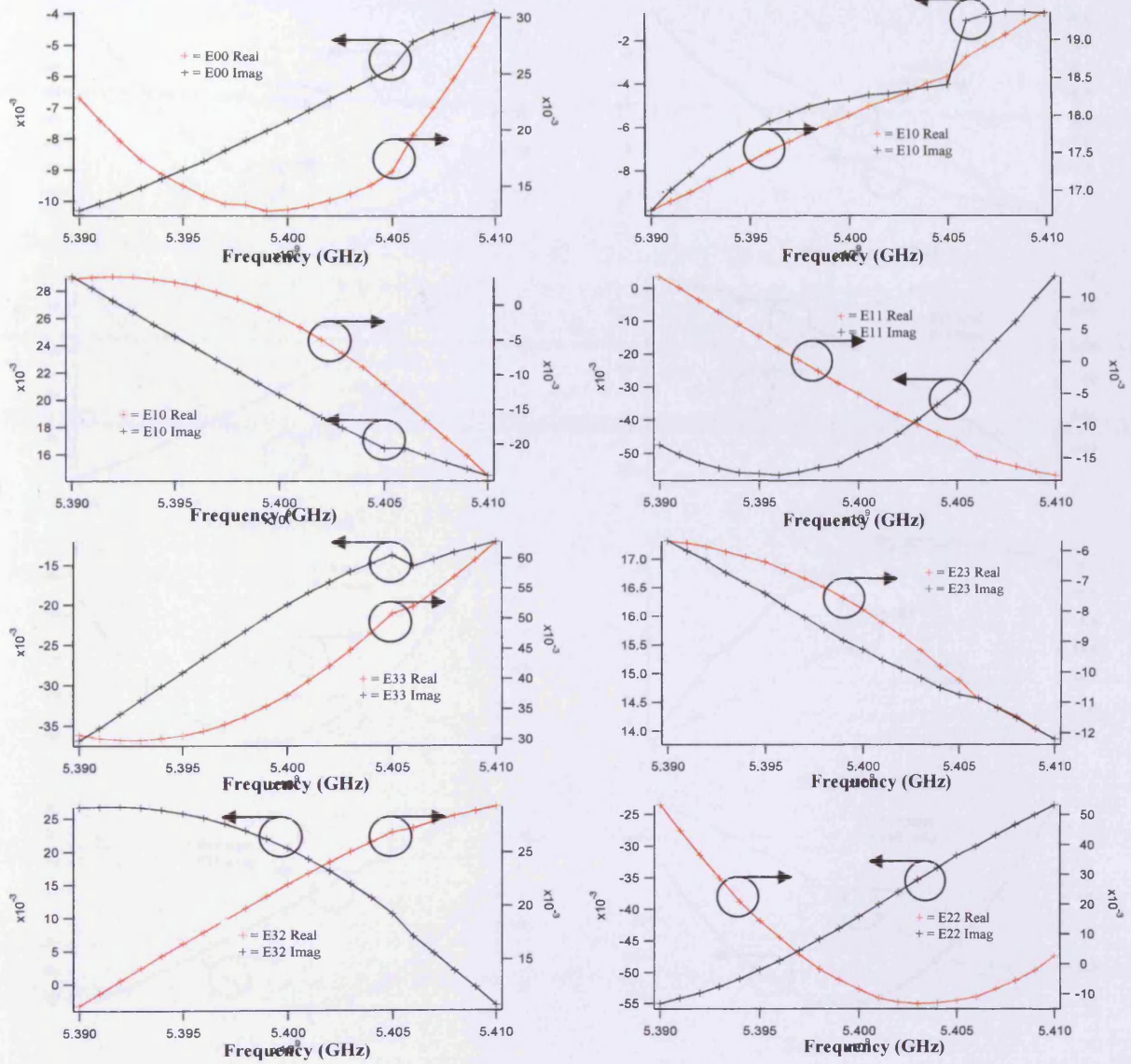
Fundamental Band Error Coefficients



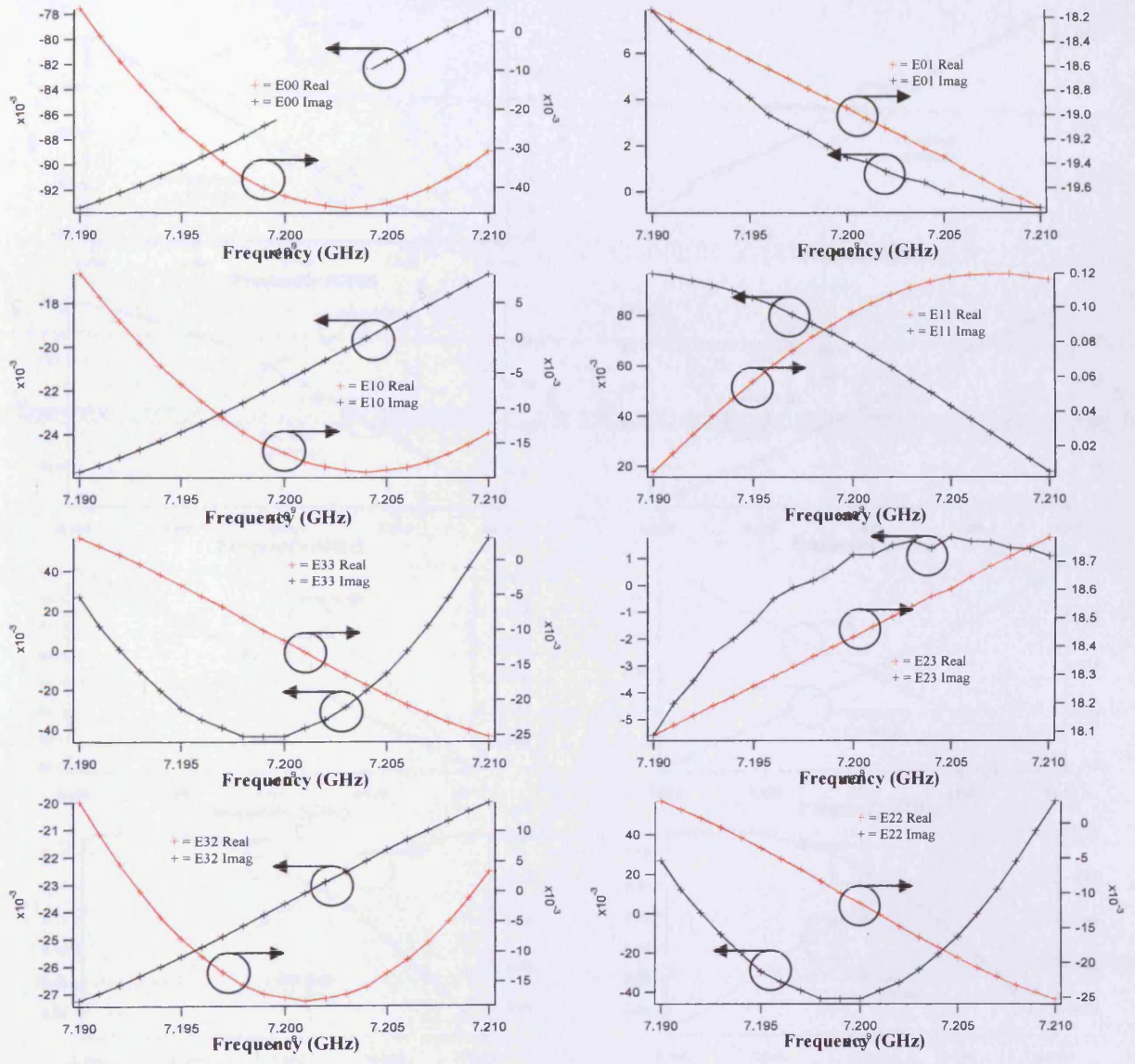
2nd Harmonic Band Error Coefficients



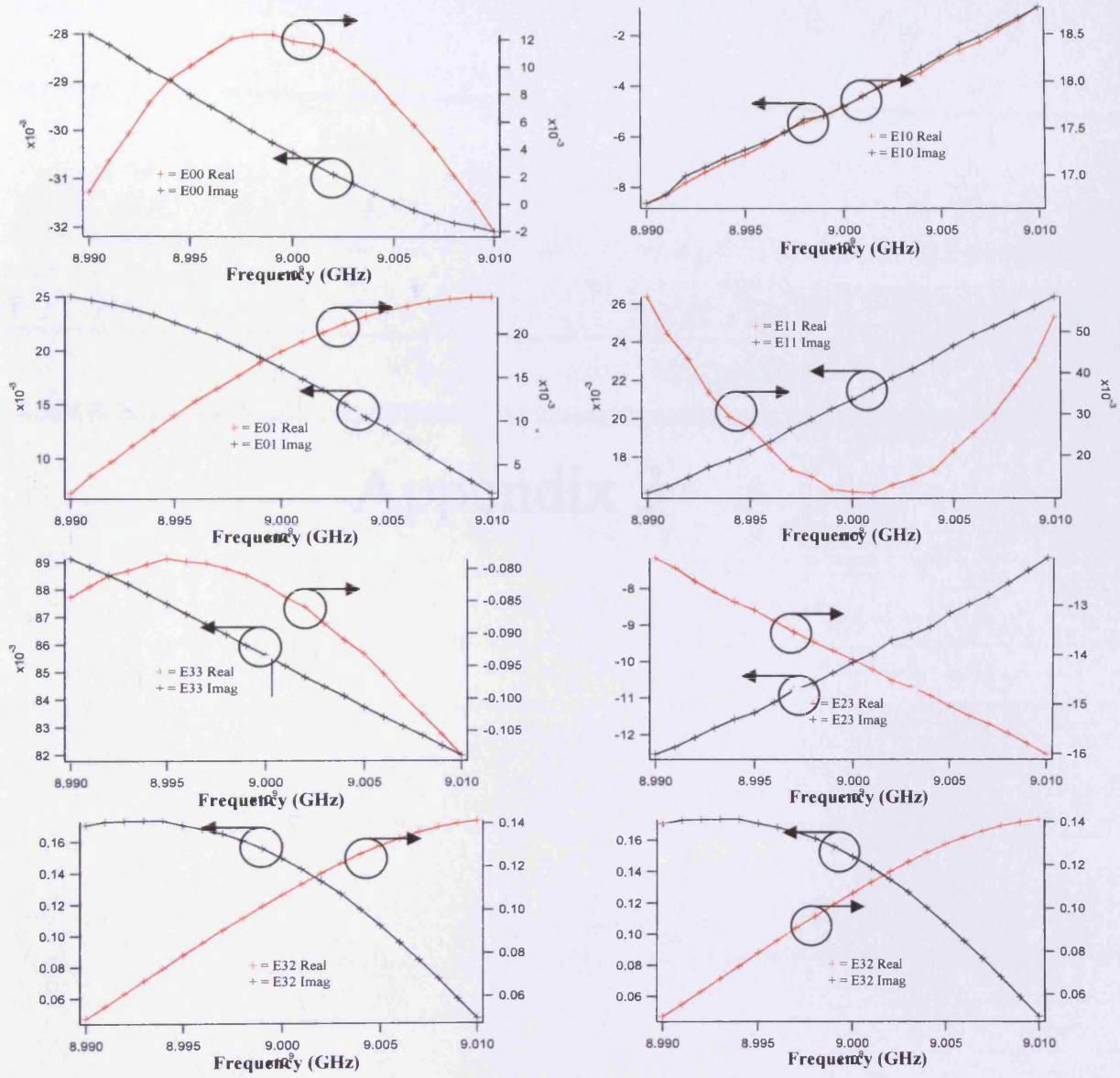
3rd Harmonic Band Error Coefficients



4th Harmonic Band Error Coefficients



5th Harmonic Band Error Coefficients



Appendix 3

***Fully Functional 'Real Time' Non-Linear Device Characterization System
Incorporating Active Load Control***

Williams, T.; Benedikt, J.; Tasker, P.J.

Presented at 36th European Microwave Conference, Manchester, September 2006

Page(s): 1610-1613 of the conference Proceedings

Fully Functional "Real Time" Non-Linear Device Characterization System Incorporating Active Load Control

Tudor Williams, Johannes Benedikt and Paul J. Tasker
School of Engineering, Cardiff University, Cardiff CF24 3TF
Tel: +44 2920 876347, e-mail: williamst5@cf.ac.uk

Abstract — This paper demonstrates, for the first time, a fully functional "real time" large signal characterization system; achieved by successful integration of a large signal multi-tone waveform measurement system with active load-pull based on the envelope load-pull principle. This approach allows for the utilization of slowly modulated signals to provide rapid and improved large signal device characterization capabilities. For example, the power amplifier is a key component in many systems; the successful design of which is reliant on the availability of comprehensive non-linear measurement data of the transistors utilized. Unfortunately, non-linear device measurements are both complex and generally very time consuming to perform, hence design is often based on a limited data set. Performing non-linear measurements under slowly modulated conditions could considerably speedup the measurement of non-linear device performance. However, to date these measurements approaches have only been possible in passive load-pull systems. The solution presented here overcomes this major limitation. A number of measurements are demonstrated showing both the present utilization and future potential of this approach to rapidly provide the comprehensive measurement data sets needed for accurate, cost and time efficient power amplifier design.

Index Terms — Power Amplifiers, Device Characterization, Load-Pull

I. INTRODUCTION

Large signal measurement systems are becoming an established part of the power amplifier design process; required to provide both improved device understanding and the data sets critical for successful power amplifier design [1-4]. The problem with such systems is that generally, irrespective of the use of passive or active load-pull, the measurements are time consuming; this usually results in the collection of only minimal data sets, restricting their use in the design process. The solution presented in this paper overcomes this problem, exploiting multi-tone waveform measurements performed utilizing active load-pull under slowly modulated conditions, to uncover the CW performance of a device within a single waveform capture.

The work presented in [5-6], demonstrated the feasibility of realizing an active load-pull architecture; allowing for both electronic control of the load impedance and oscillation free self tracking; a concept the authors termed "envelope load-pull". The active envelope load-pull architecture has now been optimized and connected to a fully calibrated waveform measurement system capable of measuring both CW and multi-tone signals (see figure 1). Since the active envelope load-pull loop is capable of holding a constant load under varying drive conditions, both

CW and modulated, it enables, for the first time, the utilization of active rather than passive load control during the application of a slowly modulated stimulus. This will result in a significant reduction in measurement time.

The system can, for example, use a slowly modulated AM stimulus to perform a power sweep characterization of a device in a single measurement, taking only a few seconds, into any impedance on the smith chart. Alternatively slow modulation of the active load-pull control signals allows the CW performance of the device into user defined multiple load impedances to be captured in a single measurement. The system thus provides a tool for both the rapid evaluation of transistor performance and the measurement of the necessary amplifier design data sets. Once optimized the system could even be used to verify performance in production environments.

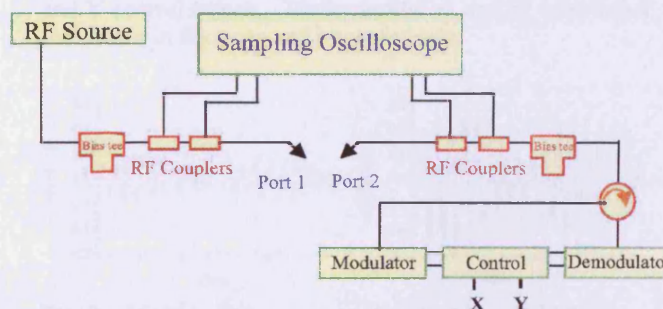


Figure 1. Full System Schematic

II. CW PERFORMANCE VERIFICATION

To demonstrate the tracking capability of the active envelope load-pull architecture; its ability to present a constant load, set electronically, over varying drive conditions has been evaluated. One verification test involved a power sweep over a 20 dB dynamic range; the minimal variation in load is shown on the smith chart in figure 2a. Alternatively the phase of the input signal was swept over a 360° range and the effect on the load is shown, in figure 2b.

These measurements demonstrate significant improvement on results presented in the previous papers [4-5]; this improvement can be attributed to the demodulator now used, which has, as demonstrated, a far superior dynamic range and improved phase performance. Hence, this envelope active load-pull architecture is a viable alternative to passive load-pull.

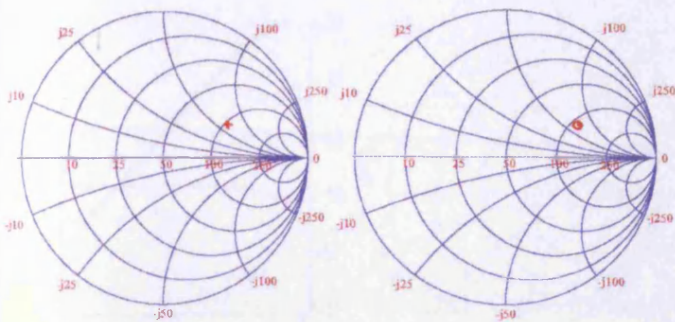


Fig. 2a. Load with power Sweep

Fig. 2b Load with phase sweep

The system is thus capable of providing rapid characterization of transistor performance during CW power sweeps into any load impedance on the smith chart. An example is shown in figure 3(a). In this case the CW power sweep was performed on a Gallium Nitride PHEMT device at 1.8GHz. The device was deliberately biased in class B, where the device is likely to exhibit AM to PM behavior, giving the opportunity to fully test the systems capability of holding the constant load under varying magnitude and phase conditions. The P_{out} vs P_{in} over a 20dB dynamic range is shown in figure 3(a). The magnitude and phase of the load reflection coefficient as the sweep is conducted is shown in figure 3(b).

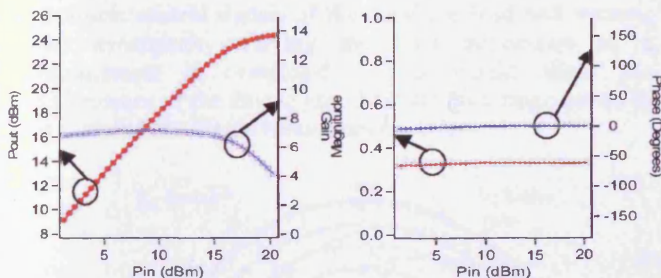


Fig. 3a. P_{out} Vs P_{in}

Fig. 3b. Magnitude and phase of maintained load

The system now exhibits excellent performance, almost invariant load impedance, for CW device power sweep characterization. This was achieved without the need to iteratively adjust the active load-pull signals, thus providing a significant time saving over the majority of open loop active load-pull concepts currently utilized.

III. "REAL TIME POWER SWEEPS"

An alternative to a CW power sweep would be to slowly AM modulate the stimulus signal. This can be achieved by exploiting the multi-tone capabilities of the measurement system. Since the magnitude and phase of the load reflection coefficient can be held constant during varying

drive conditions, it is now possible to utilize multi-tone stimulus. The envelope load-pull architecture by holding the active load constant over a limited modulation bandwidth enables a complete power sweep, into any set load impedance, to be performed in a single measurement. Thus measurement time is even more dramatically reduced.

For example, if we stimulate the device with a very slowly varying AM signal, we can see that the device is put into a quasi-CW state, where none of the device memory effects are excited; effectively a slow CW power sweep has been performed. By measuring one cycle of modulation, a single waveform capture, gives all the information contained in a multi-point power sweep into a constant active load-impedance effectively in "real time". For such measurements it is useful to use a three-tone stimulus as this gives the user the flexibility to engineer the stimulus signal to uncover the relevant part of the P_{out} vs P_{in} curve, by selecting modulation depth and peak power.

To confirm the operation of the "real time" power sweeps with active load control, device measurements were completed on GaAs PHEMT device and the results achieved were then compared to CW measurements. A three-tone signal with carrier frequency of 1.8 GHz and modulation rate of 1KHz was used as the stimulus with 50% modulation depth. The load was set to 75 Ω using the X and Y control signals. The measured a1 and b2 waveforms are shown in figure 4a and b respectively.

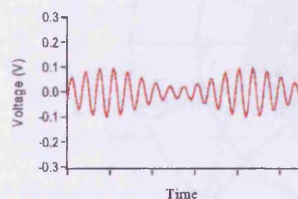


Fig. 4a. Measured a1 waveform

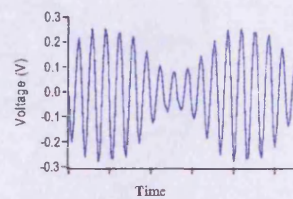


Fig. 4b. Measured b2 waveform

The number of RF cycles in the envelope are reduced as a novel sampling method is used to collect the multi-tone waveforms, the sampling technique ensures the waveforms are captured in the most efficient manner, by only measuring desired frequency components, allowing us to capture multi-tone waveforms in detail at both the fundamental and harmonic frequencies. These modulated waveforms can be analyzed in the envelope domain to provide the time varying behavior of fundamental and harmonic components of the waveforms.

For example, plotting the magnitude of the time varying b2 fundamental component Vs the magnitude of the time varying a1 fundamental component gives all the information contained within a multi-point power sweep. The result is shown in figure 5a and is compared to a CW sweep into the same impedance (CW measurements are shown with markers, "real time" results shown with straight lines).

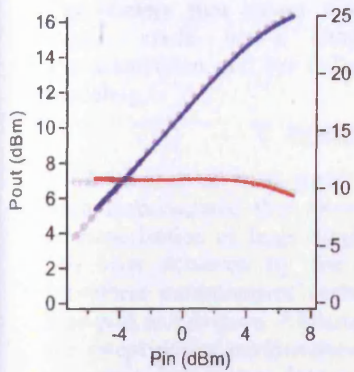


Fig. 5a P_{out} Vs P_{in}

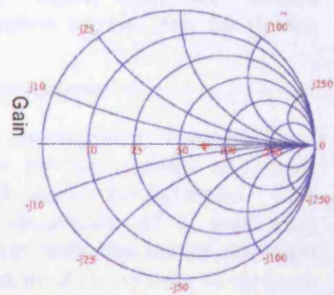


Fig. 5b reflection coefficient

As can be seen from the plots a very good agreement is achieved between CW and “real time” results, thus the same measurement can now be performed in a fraction of the time. The plot shown in figure 5b, confirms the time invariant load impedance at the fundamental, again extracted from the envelope information. It is important to note that, since the measured waveform contains multiple harmonic information, the harmonic information as a function of P_{in} can be simply extracted in the same way as the fundamental carrier information.

IV. “REAL TIME” LOAD SWEEPS

An alternative would be to slowly modulate the electronic control signals of the envelope load-pull system, thus dynamically varying the load impedance as a measurement is completed. This would allow the performance of the device into different load impedances to be captured in a single measurement.

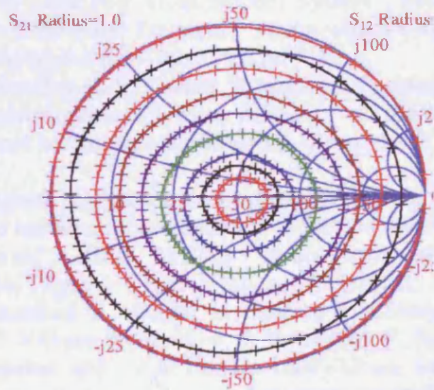


Figure 6. “Real Time” swept load.

For example, sinusoidal 1kHz waveforms are applied to both X and Y. If the signals are 90° out of phase, a circle of loads is generated on the smith chart; the amplitude of the sinusoids can control the diameter of the circle.

Furthermore the circle of generated loads can be moved to any part of the smith chart by simply applying DC voltage offsets to the sinusoids. This is a very useful feature for finding the ideal operating conditions of a device or for extracting contours of constant power and gain.

To confirm the operation of the “real time” load sweeps, measurements were completed on a thru line. Sinusoidal waveforms of equal amplitude were applied to the X and Y control signals, the magnitude of these signals were increased between each measurement. The measured load impedances are shown on the smith chart in figure 6. Each circle contains 250 independent loads that are measured in less than a second. By careful engineering the control signals applied, it would be possible to map any constellation of loads on the smith chart.

Further device measurements were completed on the Gallium Nitride PHEMT device used earlier, the load impedance of the device was swept in circles around the centre of the smith chart and contours of constant output power were plotted, figure 7 shows the impedance sweeps and the resulting contour plot.

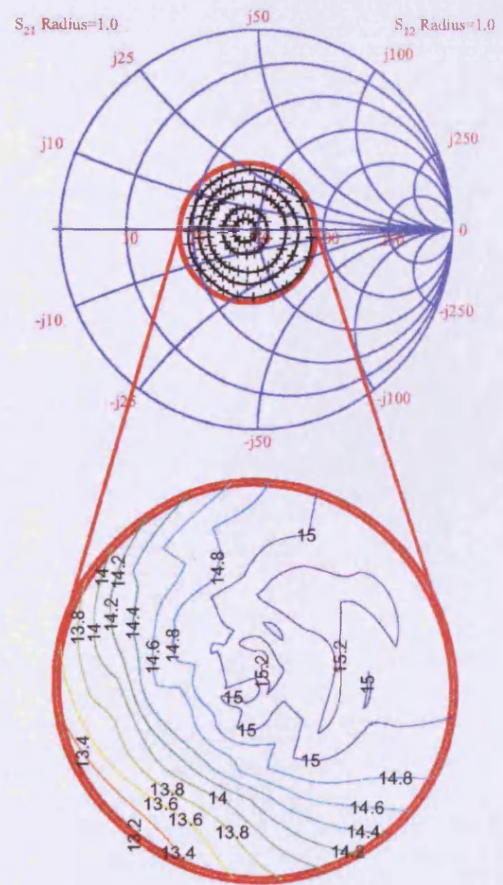


Figure 7. “Real Time” device contour plot.

The contour plot shows how modulation of the control signals could be a very useful tool for device characterization and for collection of data sets for device modeling.

V. CONCLUSION

A number of "real time" measurement concepts have been demonstrated that allow for the accurate and rapid characterization of large single device performance. This has been achieved by the integration of a multi-tone waveform measurement system with the active envelope load-pull architecture. Utilization of the system to measure the swept power performance of a device during a single waveform capture was demonstrated and the results verified against those obtained during a more conventional CW power sweep. An alternative application is presented which shows how the load impedance can be varied dynamically and captured in a single waveform measurement, device measurements were used to demonstrate how contour plots could be plotted using the systems within minutes of probing a device. The key to both applications is the envelope load-pull architectures ability to hold a constant load with varying drive conditions, across a modulation bandwidth. Combined with the systems ability to accurately measure multi-tone waveforms. Further engineering of the multi-tone modulated stimulus and/or load-pull electronic control signals will enable this system to rapidly perform all the relevant non-linear device characterization measurements necessary. This capability would be of interest to many sectors of the microwave community from design right through to production control.

REFERENCES

- [1]. D.J. Williams, P.J. Tasker, "An Automated Active Source and Load Pull Measurement System", Proceedings of the 6th IEEE High Frequency Postgraduate Colloquium, Cardiff, September 9th-10th 2001, pp 7-12.
- [2] P.D. Bradley, R.S. Tucker "Computer-Corrected Load-pull characterization of Power MESFET's" IEEE MTT-S international Microwave Symposium Digest 1983, pp 224-226.
- [3] B. Hughes, A. Ferrero, A. Cognata, "Accurate on-wafer power and harmonic measurements of MM-wave amplifiers and devices", IEEE MTT-S international Microwave Symposium Digest 1-5 June 1992, pp 1019-1022.
- [4]. D. Barataud, F. Blache, A. Mallet, P.P Bouysse, J.M Nebus, J.P Villotte, J. Obregon, J. Verspecht, P. Auxemery, " Measurement and control of Current/Voltage waveforms of microwave transistors using a harmonic load-pull system for the optimum design of high efficiency power amplifiers", IEEE Transactions on Instrumentation and measurement, Volume 48, Issue 4, August 1999, PP 835-842.
- [5]. T. Williams, J. Benedikt and P.J Tasker, "Experimental Evaluation of an Active Envelope Load Pull Architecture for High Speed Device Characterization", IEEE MTT-S

international Microwave Symposium Digest 12-17 June 2005, pp 1509-1512.

[6]. T. Williams, J. Benedikt and P.J Tasker, "Application of a Novel Envelope Load-Pull Architecture in Large Signal Device Characterization", EuMC Symposium Digest 2005.

“Application of a novel active envelope load pull architecture in large signal device characterization”

Williams, T.; Benedikt, J.; Tasker, P.J.

Presented at the 35th European Microwave Conference, October 2005, Paris

Volume 1 of the conference proceedings

Application of a Novel Active Envelope Load Pull Architecture in Large Signal Device Characterization

Tudor Williams, Johannes Benedikt and Paul J. Tasker

School of Engineering, Cardiff University, Cardiff CF24 3TF

Tel: +44 2920 876347, e-mail: williamst5@cf.ac.uk

Abstract — This paper presents the large signal characterization of an on-wafer PHEMT device using a novel closed loop active envelope load pull architecture. The architecture addresses active load-pull measurement system stability issues associated with previously realized closed loop architectures by utilizing a feedback loop at envelope frequencies. It solves, for the first time, many of the problems associated with existing active load pull architectures. Stability of the system is demonstrated and evaluated using device measurements. Example, load pull contour plots and P_{out} Vs P_{in} achieved by the systems are shown and analyzed. The results suggest that the new approach, by overcoming the problems of existing active load pull architectures, opens up the possibility of their utilization in high speed production test.

Index Terms — Load Pull, Power Amplifiers, Device Characterization, Waveform measurements.

I. INTRODUCTION

Active load-pull systems can be separated into two groups, being either “closed loop”, or “open loop” architectures. A typical closed loop architecture is shown in figure 1.

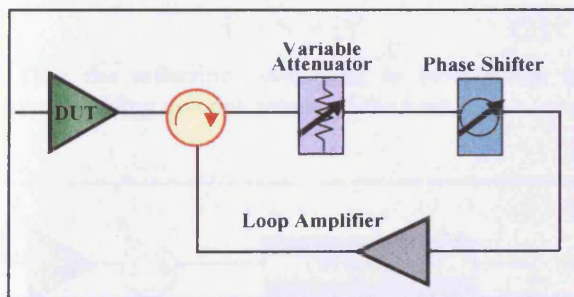


Fig.1. – Typical Closed Loop System

In a “closed loop” system, first presented by Bava [1], the injected signal is a modified version of the device under test (DUT) output signal. This ensures the emulated load impedance (matching circuit) is independent of drive level, however the major problem with such architectures is that they are prone to oscillations. For this reason people have tended to move towards “open loop” solutions as shown in figure 2, open loop architectures were first introduced by Takayama [2], in such systems the injected signal is generated independently. This avoids the oscillation problem but now, to maintain constant emulated load impedance (reflection coefficient) under changing drive conditions requires a slow iterative feedback

process; a number of magnitude and phase adjustments of the injected signal are required to maintain the target reflection coefficient.

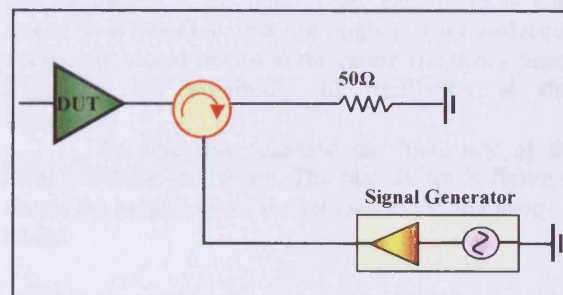


Fig.2. – Typical Open Loop System

The measurements in this paper utilize a novel active load-pull architecture first presented in [3], which overcomes these limitations. It incorporates a “closed loop” architecture not at RF but at the envelope frequency to ensure that the injected signal is a modified version (direct function) of the DUT output signal, hence maintaining the required constant emulated load impedance as drive level changes. Results have shown that this solution appears to address the measurement system instability problems associated with traditional closed loop systems. The immediate advantage of the system is the increased speed of device characterization, achieved by removing the iterative nature of setting the load. This system is drive level independent which means the load no longer needs to be set for each change of the input stimulus, thus making measurements such as power sweeps many times faster than the open loop systems that are currently used.

Some initial measurements investigating system stability are shown. To further test the stability of the architecture device measurements are completed at the outer limits of the smith chart, giving the sternest possible test of system stability, throughout the measurement process no oscillations occurred. In order to test the systems capabilities, a load pull sweep was conducted in order to find the optimum impedance for the device. This has been followed by a P_{out} Vs P_{in} characterization of a device shown in the results section, the duration of this sweep was considerably shorter compared to an on-site open-loop system outlining its speed advantage, thus proving that the

new architecture is a viable solution to the outlined problems. In effect the system now feels like a passive system, allowing the user to make changes to bias and the input signal whilst maintaining the set load reflection coefficient. The system has the added advantage of being able to emulate impedances anywhere within and even outside the smith chart; this is not possible in passive systems as the losses between the DUT and tuner significantly reduce the maximum reflection coefficient obtainable.

Overall, the proposed architecture has shown that it would make significant time savings while maintaining its performance, making it a highly attractive solution for production and test environments.

II. SYSTEM ARCHITECTURE

The system architecture is shown in figure 3, a circulator is used at the output of the device, this signal is then down converted to the base band using an I-Q demodulator, after which the I and Q signals are manipulated using analogue circuitry with transfer function $F(X,Y)$, shown below –

$$F(X,Y) = I' + jQ' = (XI - YQ) + j(XQ + YI) \quad (1)$$

Conversion to RF, providing the injected output signal is achieved using the internal modulator of the load signal generator (ESG), as shown in Fig. 1. Since the ratio of input and output now remains constant it can be seen that the set reflection coefficient is no longer a function of b_2 , instead it has the following equation –

$$\Gamma = X + jY \quad (2)$$

Thus the reflection coefficient is independent of drive, avoiding iterative setting of the load.

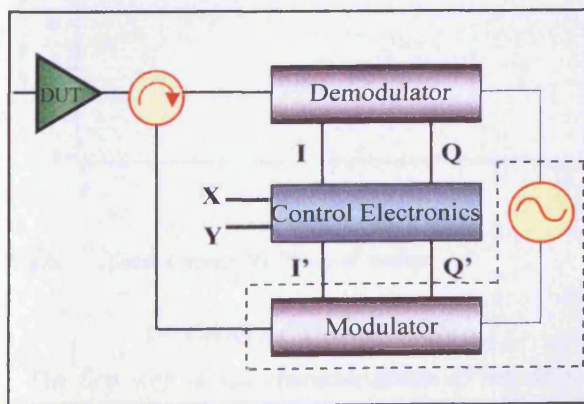


Fig. 3. Envelope Load Pull Architecture.

The developed load-pull system, termed “envelope load pull”, is then attached to a waveform measurement system previously developed at Cardiff University [4,5].

The electronics incorporates error correction and allows for modulation of the load presented to the DUT by variation of the x and y signals, allowing emulation of any load, reaching all parts of the smith chart.

III. STABILITY MEASUREMENTS

The stability of the circuit is enhanced by the fact that the electronic circuitry is narrow band with a pass band of only 200 KHz, thus avoiding oscillations outside this band. However it is important to consider the frequency response of the active load-pull across this bandwidth. If the gain of the electronics is non-linear it is possible that the highest load reflection coefficient would not be at the centre frequency hence triggering the possibility of oscillation at that frequency.

To find this response the frequency of the local oscillator was swept. The plot shown in figure 4, shows the magnitude of the set load as the frequency is swept.

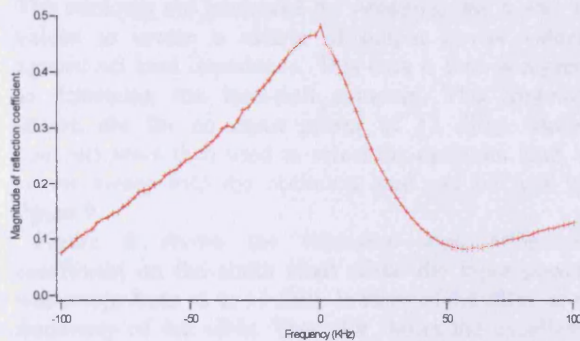


Fig.4. Measured magnitude of load reflection as carrier frequency is swept.

The plot shows that the frequency response is very well behaved in the pass band, the magnitude never goes above that at the centre frequency. This analysis suggests that the system would be stable across the bandwidth.

Further to the above analysis, device measurements have been completed to demonstrate the stability of the system. To fully test the stability a sweep around the smith chart was completed at a magnitude of 1, achieved by varying the control variables X and Y, the device (GaAs PHEMT), has an input signal of 10 dBm, with a frequency of 1.8 GHz. Figure 5 shows the set load reflection coefficient and resultant measured S_{11} as the sweep is conducted (S_{11} is shown by circles and the load reflection coefficient by squares). As can be seen from the plot S_{11} is actually outside the smith chart during some of the sweep, the input impedance circle is shown on the plot in black dots and the relating stability circle calculated from the S-parameters is shown on the plot in blue, it can be seen that the set load clearly enters the stability circle of the

device giving the sternest possible test of system stability.

Despite these extreme operating conditions, no oscillations are observed; this can be shown by analysis of the Drain current shown in figure 6 which remains relatively constant throughout the sweep. Showing at least for this device architecture the system is stable.

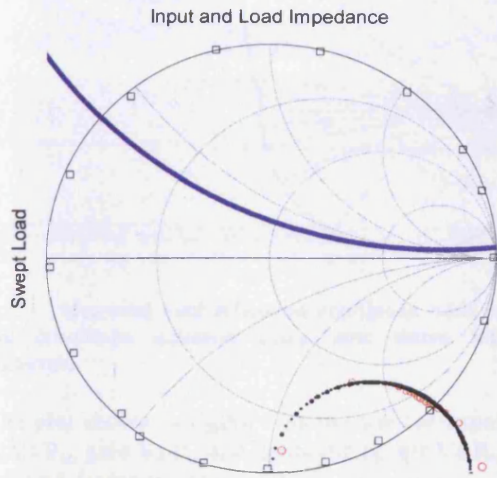


Fig.5. Measured load reflection coefficient and S_{11} as sweep with magnitude 1 is conducted.

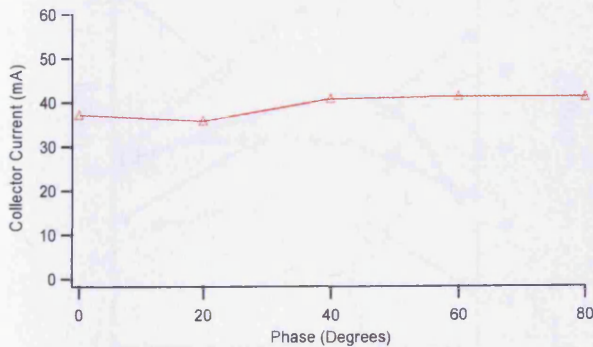


Fig.6. Drain Current Vs Phase of sweep.

IV. CHARACTERIZATION

The first step in the characterization of the device was to use the active system to determine load-pull contours. Figure 7 shows the measured load pull contours for the device which is a 200 micron (2x100micron) GaAs PHEMT when it is biased at pinch off with a drain voltage of 10 V.

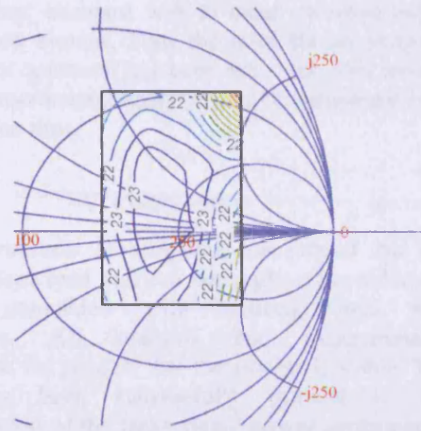


Fig.7. Measured Load pull contours around the optimum load.

The contours are measured by sweeping the X and Y values to create a matrix of output power values against set load impedance. This data is then analyzed to determine the load-pull contours. The contours shown are for an input power of 13 dBm. These contours were then used to select the optimum load, a power sweep into the optimum load can be seen in figure 9

Figure 8 shows the measured load reflection coefficient on the smith chart while the input power was swept from -2 to 13 dBm in steps of 0.5 dBm, at a frequency of 1.8 GHz. This plot shows the excellent tracking performance of the active load pull loop; an almost constant reflection coefficient is maintained for the varying drive conditions, with only a small variation in both magnitude (less than 3%) and phase (less than 0.5%). The target reflection coefficient had a magnitude of 0.72 and a phase of 5° .

In this case the error was small however; measurements suggest that errors could be significantly reduced by the introduction of a superior demodulator. The demodulator currently used in the system is a rather cheap simplistic solution, which works well for varying drive level, but has problem with changes in phase due to a phase imbalance, thus any AM-PM in the device will make the load harder to maintain, thus a simple substitution could be made to further improve results. As an interim solution if a very steady load is required (not the case in most situations) the software utilized in the open loop system could be used to reset the load as stimulus changes. Although this would slow the system a little it would still be significantly faster than the open loop system, where a small change in drive could introduce a dramatic change in load.

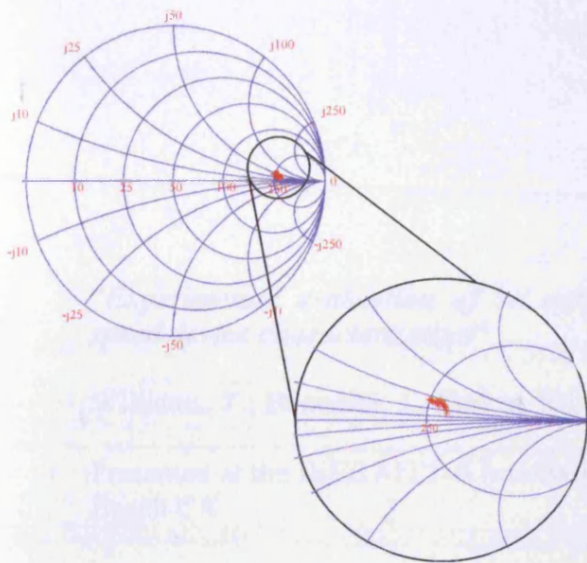


Fig.8. Measured load reflection coefficient with varying drive conditions achieved using new active load-pull architecture.

The plot shown in figure 9 shows the corresponding P_{out} Vs P_{in} , gain Vs P_{in} and harmonic power Vs P_{in} plots measured during the power sweep.

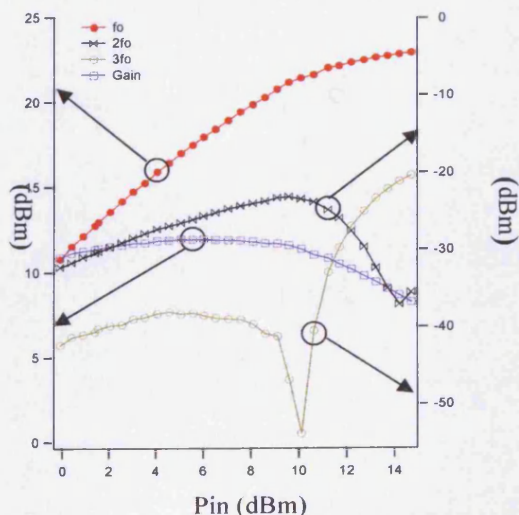


Fig. 9. Measured P_{out} Vs P_{in} , Gain Vs P_{in} and harmonic power plots achieved using new active load-pull architecture.

As can be seen from the plots all the behavior of the device is typical showing that the system is well

behaved. They compare well to those captured using the open loop system. Thus the need for an iterative measurement approach has been removed. This means the same experimental analysis can be completed in a fraction of the time.

V. CONCLUSION

The experimental investigation has proved that the active envelope pull can be employed to solve the problems associated with existing load pull architectures. All analysis and measurements performed so far suggest that the system is stable. The system has been successfully utilized in the characterization of the large signal power performance of a PHEMT device. This improved active load-pull architecture has significantly advanced the performance and usability of non-linear microwave device characterization systems. The closed loop nature of the system means that traditional swept measurements become many times faster and allows for a more intuitive measurement process allowing the user to vary bias and input signal with the load remaining constant, in a similar way to a passive load.

REFERENCES

- [1]. G.P. Bava, U. Pisani, V. Pozzolo, "Active Load Technique for Load-Pull Characterisation at Microwave Frequencies" *Electronic Letters* 18th February 1982, Vol. 18, No. 4, pp. 178-180.
- [2]. Yoichiro Takayama "A New load-Pull Characterisation Method for Microwave Power Transistors" *IEEE MTT-S international Microwave Symposium Digest* 1976, pp. 218-220.
- [3]. T. Williams, J. Benedikt and P.J Tasker, "Experimental Evaluation of an Active Envelope Load Pull Architecture for High Speed Device Characterization", *IEEE MTT-S international Microwave Symposium Digest* 2005.
- [4]. D.J. Williams, P.J. Tasker, "An Automated Active Source and Load Pull Measurement System", *Proceedings of the 6th IEEE High Frequency Postgraduate Colloquium*, Cardiff, September 9th-10th 2001, pp 7-12.
- [5]. J. Benedikt, R. Gaddi, P.J Tasker, M.Goss, "High-power Time-domain Measurement System with Active Harmonic Load-pull for High-efficiency Base station Amplifier Design", *IEEE trans, Microwave Theory Tech.*, Vol. 48, pp. 2617-2624, December 2000.
- [6]. T. Williams, J. Benedikt and P.J Tasker, "Novel Base-Band Envelope Load pull Architecture", *proceedings of 9th IEEE High Frequency Postgraduate Colloquium Manchester* September 2004.

“Experimental evaluation of an active envelope load pull architecture for high speed device characterization”

Williams, T.; Benedikt, J.; Tasker, P.J.

Presented at the IEEE MTT-S International Microwave Symposium 2005, Long Beach CA

Conference Digest

Experimental Evaluation of an Active Envelope Load Pull Architecture for High Speed Device Characterization

Tudor Williams, Johannes Benedikt and Paul J. Tasker

School of Engineering, Cardiff University, Cardiff CF24 3TF

Tel: +44 2920 876347, e-mail: williamst5@cf.ac.uk

Abstract — This paper presents a solution to the iterative nature of load pull characterization of transistor power performance. This has been achieved using a novel load pull architecture with a feedback loop at envelope frequencies within an active load pull system, which has been demonstrated and evaluated for single tone excitation. Furthermore employing the new architecture a novel application is demonstrated which could be potentially useful in production environments, this is achieved using an amplitude modulated stimulus that reduces measurement time from hours to seconds.

Index Terms — Load Pull, Power Amplifiers, Device Characterization, Waveform measurements.

I. INTRODUCTION

Traditionally load-pull, emulation of load impedance, has been achieved using passive techniques [1,2], however, limitations are introduced due to losses in the network between the device under test (DUT) and the tuner, which reduce the maximum reflection coefficient obtainable. The solution to this problem is active load-pull where emulation of load impedance is achieved by injecting an amplified signal of specific magnitude and phase into the DUT output. Such active systems can have either an “open loop” or “closed loop” architecture. In a “closed loop” system, first presented by Bava [3], the injected signal is a modified version (direct function) of the DUT output signal. This ensures that the emulated load impedance (matching circuit) is independent of drive level, however this architecture is prone to oscillations. In the alternative “open loop” system, first introduced by Takayama [4], the injected signal is generated independently. This avoids the oscillation problem but now, to maintain a constant emulated load impedance (reflection coefficient) under changing drive conditions, results in a slow iterative process; a number of magnitude and phase adjustments, manual or automated, of the injected signal are needed to maintain the target reflection coefficient.

This paper presents a novel active load-pull architecture, which overcomes these limitations. It incorporates a “closed loop” architecture not at RF but at the envelope frequency to ensure that the injected signal is a modified version (direct function) of the DUT output signal, hence maintaining the required constant emulated load impedance as drive level changes. All measurements conducted thus far suggest this solution overcomes the instability problems associated with traditional closed loop systems. The

immediate advantage of the system is the increased speed of device characterization, achieved by removing the iterative nature of setting the load. As this system is drive level independent, the load does not have to be set for each change of the input stimulus making measurements such as power sweeps many, many times faster than the open loop systems that are currently used.

Excitingly the system also opens up the opportunity to bring active load-pull into the modulated domain. This allows us to increase the speed of device characterization even further by introducing a novel application where an Amplitude Modulated (AM) signal is used to perform a multi-point power sweep in a single measurement.

Experimental results confirm the operation of the envelope load pull architecture; single tone analysis shows full control of the system and proves that the presented load is independent of drive level, providing a significant time saving over existing load pull architectures. The results using a modulated stimulus show very positive results, demonstrating that the load can be held constant with time and hence amplitude, this means that a power sweep measurement over a 20 dB drive level range can be completed in a matter of seconds.

II. REALIZATION

In the proposed architecture, see figure 1, a circulator is used at the output of the device, this signal is then down converted to the base band using an I-Q demodulator, after which the I and Q signals are manipulated using analogue circuitry with transfer function $F(x,y)$, derived below, shown in (3) –

As the relationship between input and output must be a constant it can be seen that the following is required;

$$(I' + jQ')/(I + jQ) = Z = x + jy \quad (1)$$

Re-arranging gives;

$$I' + jQ' = (x + jy)*(I + jQ) \quad (2)$$

Therefore giving the transfer function;

$$F(x,y) = I' + jQ' = (xI - yQ) + j(xQ + yI) \quad (3)$$

Hence, this formulation will ensure a drive level independent emulated load, quantified by the user defined values of x and y , is presented to the DUT. Conversion to RF, providing the injected output signal is achieved using

the internal modulator of the load signal generator (ESG), as shown in Fig. 1. The developed load-pull system, termed "envelope load pull", is then attached to a waveform measurement system previously developed at Cardiff University [5,6].

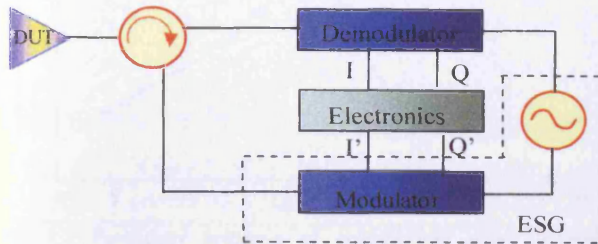


Fig. 1. Envelope Load Pull Configuration.

As well as the circuitry to generate the transfer function $F(x,y)$, the electronics component of Fig. 1 also incorporates error correction. Consisting of "off the shelf" analogue multipliers and op-amps.

The circuit allows for modulation of the load presented to the DUT by variation of the x and y signals, Set by transforming the required magnitude and phase into rectangular format, thus allowing emulation of any load, reaching all parts of the smith chart.

III. ERROR FLOW MODEL

To aid in the understanding, and correction of any errors of the system a simple error model was developed, along with simulations, this meant that errors in the system could be accounted for and hence corrected within the electronics. Fig. 2 shows the simplified error flow model for the system, which ignores the losses associated with the cables, circulators and couplers. In the Model T_d is the transmission coefficient for the demodulator, D is the offset associated with the demodulator, Γ is the set reflection coefficient associated with the control electronics, M is the offset associated with the modulator and the electronics module, T_m is the transition coefficient of the modulator, and Γ_o is the reflection coefficient of the system.

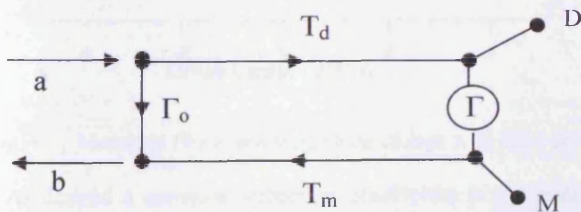


Fig. 2. Error Flow Model for Envelope Load Pull System.

From the error model it can be shown that the b signal will be given by (4).

$$b = (T_m \Gamma T_d + \Gamma_o) a + (M + \Gamma D) T_m \quad (4)$$

As the modulator used is internal to the ESG we can assume this has no imperfections, the offset from the electronics along with the offset caused by D are corrected by the conditioning electronics, hence the expression simplifies to (5).

$$b = (T_m \Gamma T_d + \Gamma_o) a \quad (5)$$

The conditioning electronics can also be used to remove the constant offset caused by Γ_o the reflection coefficient of the system, Therefore giving (6)

$$b = (\Gamma T_m T_d) a \quad (6)$$

Hence giving the final presented reflection coefficient Γ_{set} shown in (7) –

$$\Gamma_{set} = b/a = (\Gamma T_m T_d) \quad (7)$$

Therefore provided errors are accounted for the reflection coefficient presented to the DUT (Γ_{set}) is a direct function of the user entered reflection coefficient (Γ).

IV. STABILITY OF THE SYSTEM

This analysis considers the basic constraint that to have instability the condition shown in (8) must be satisfied –

$$\Gamma_{device} * \Gamma_{set} \geq 1 \quad (8)$$

To consider the stability of the system it is important to look at the frequency response of the electronic circuitry. Obviously oscillations due to the active load pull can only occur in band, as it can be seen if the gain of the electronics is non-linear it is possible that the gain could go above that at the carrier hence possibly breaching the condition outlined above.

To find this response the frequency of the local oscillator was swept with the magnitude of the reflection coefficient measured each time. The frequency of the local oscillator was swept 200 KHz either side of the centre frequency in steps of 2 KHz. Fig. 3 shows the magnitude of the load reflection coefficient as the frequency sweep is conducted.

As the response shows, the envelope architecture has the benefit that the electronic circuitry is narrow band effectively creating a narrow band pass filter with a pass band of only 200 KHz, this in fact is smaller in bandwidth than any realistic matching network.

Now since the reflection coefficient of the device will always be less than 1 it is clear from the plot that the circuit is very well behaved within the pass band, this means the likelihood of oscillation is very small, even if an oscillation did occur it would be caused by an impedance inside the smith chart. Thus we can see that the same oscillation would be caused by any matching or tuning circuit, which typically

cover a much larger bandwidth. It can therefore be concluded that the system is at least as good as any passive matching or tuning circuit.

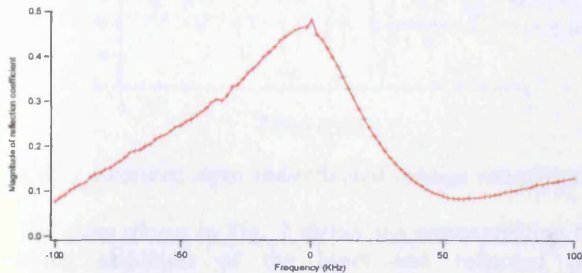


Fig. 3. Frequency response of control and error correction electronics

It is important to note that even if an oscillation did occur the effect would be limited by the fixed maximum output power of the source driving the modulator, which means that any oscillations that occur would be nondestructive, thus the cause of the oscillation could be dealt with, without damaging measurement equipment.

V. SINGLE TONE STEPPED ANALYSIS

The first experiment conducted was to ensure the reflection coefficient set was independent of drive level. To demonstrate this, the input drive level is swept from -5 to 5 dBm for a constant value of the control variables X and Y. The plot shown in Fig. 4 shows the variation in magnitude and phase as the sweep is conducted. The measurement is conducted with a 1.8 GHz single tone stimulus.

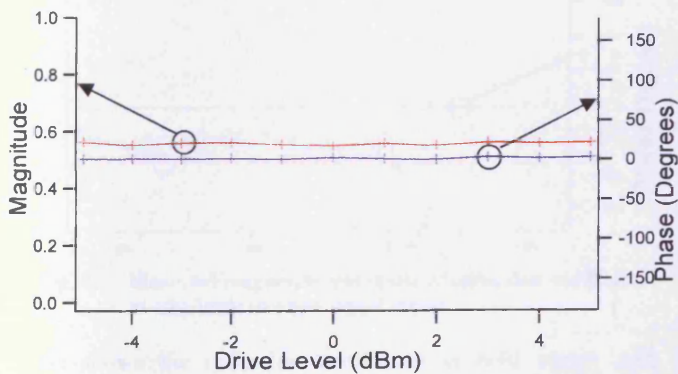


Fig. 4. Measured Phase and Magnitude change with drive level.

As desired a constant reflection coefficient is maintained for the varying drive conditions, with only a small variation in both magnitude and phase of less than 1%. This experiment was repeated for a constant drive level while sweeping the phase of the input signal, this was made difficult by the phase imbalance of the demodulator,

however the results showed a linear region of 80 degrees where the phase deviation was less than 2° and the magnitude variation was less than 0.08. Over the entire sweep (-180 to 180°) there was phase deviation of less than 5% and magnitude variation of 15%, this could be easily improved by the introduction of a superior demodulator.

The next experiment considered the control of the architecture to test this the X and Y values were used to sweep the set reflection coefficient in steps of 20 degrees around the smith chart while keeping the input signal constant at 0dBm, this was repeated for magnitudes of 0.25, 0.5, 0.75 and 1. The plot shown in Fig. 5 shows full control of the reflection coefficient by varying the X and Y control variables.

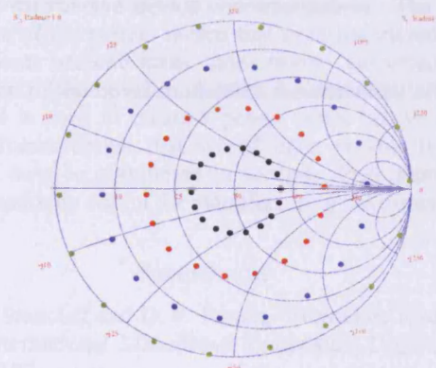


Fig. 5. Experimentally achieved load control.

VI. MODULATED INPUT POWER SWEEP

As the measurement system used has the ability to measure modulated signals, an interesting opportunity arises. The discussed envelope load pull architecture holds the load constant over the modulation bandwidth, thus a novel approach can be used to further increase the speed of device characterization.

If an amplitude modulated signal is used as the input and the envelope frequency is set to be a low frequency, then it can be seen that effectively a power sweep has been set up, now if the measurement system is set up to measure one cycle of modulation then each waveform measurement contains all the information of a power sweep with multiple points. This is demonstrated using an three tone AM signal with 80 % modulation depth, a carrier frequency of 1.8 GHz and envelope frequency of 200 Hz. The first plot shown in Fig. 6 shows the measured input and reflected voltage waveforms, necessary to emulate a constant load. It is important to note that there is a reduction in the number of RF cycles seen in the envelope due to the sub sampling approach utilized when collecting the waveforms.

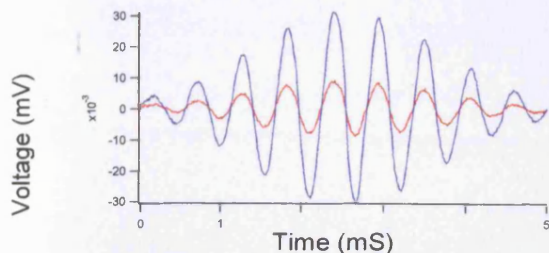


Fig. 6. measured input and reflected voltage waveforms.

The plots shown in Fig. 7 shows the corresponding time varying amplitude of the input and reflected input waveforms –

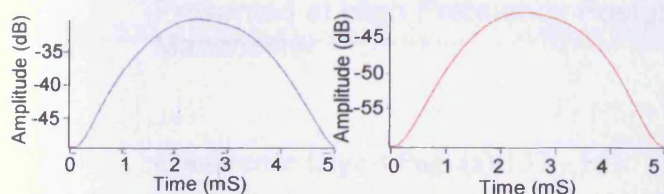


Fig. 7. Variation in amplitude with time of input and feedback signals.

Thus we have in effect a CW input with a slow time varying amplitude or by any other name a power sweep, in effect creating a power swept “Curve Tracer”. Finally Fig. 8 shows the magnitude and phase variation of the reflection coefficient as the power sweep takes place, proving that the load is independent of amplitude variation.

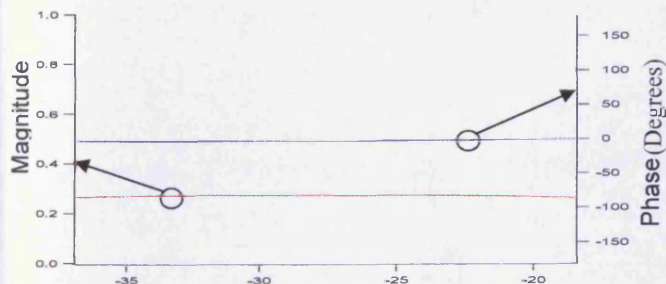


Fig. 8. Measured magnitude and phase of reflection coefficient as amplitude of input signal varies.

As shown the reflection coefficient is held steady with amplitude variation, a result of the time invariant load. This allows analysis over the dynamic range of the input signal which in this case is 20 dBm. Now in a single waveform measurement we have captured all the information contained in a stepped CW power sweep, this means a P_{out}

versus P_{in} measurement could now be completed in only 5 ms.

VII. CONCLUSION

The experimental investigation has proved that envelope load pull solves many of the problems associated with existing load pull architectures. This novel concept has been achieved by introducing a feedback loop that occurs only at envelope frequencies, hence, separating the feedback frequency from the RF frequency of the active loop, this along with analysis presented suggests that the system will be stable. Experimental results have shown good agreement with theory showing the architecture could be very useful in non linear microwave device characterization. The closed loop nature of the system means that even traditional swept measurements become many times faster. Importantly the introduction of the novel modulated measurement where an AM signal is used to create a power swept “curve tracer” means a measurement that would have previously taken hours can now be completed in seconds, thus making the system potentially useful for manufacturing environments.

REFERENCES

- [1]. R. B. Stancliff and D. P. Poulin, “Harmonic load-pull,” MTT-S International Microwave Symposium Digest, 1979, pp. 185 – 187.
- [2]. Maury Passive load pull system, www.maurymw.com.
- [3]. G.P. Bava, U. Pisani, V. Pozzolo, “Active Load Technique for Load-Pull Characterisation at Microwave Frequencies” Electronic Letters 18th February 1982, Vol. 18, No. 4, pp. 178-180.
- [4]. Yoichiro Takayama “A New load-Pull Characterisation Method for Microwave Power Transistors” IEEE MTT-S international Microwave Symposium Digest 1976, pp. 218-220.
- [5]. D.J. Williams, P.J. Tasker, “An Automated Active Source and Load Pull Measurement System”, Proceedings of the 6th IEEE High Frequency Postgraduate Colloquium, Cardiff, September 9th-10th 2001, pp 7-12.
- [6]. J. Benedikt, R. Gaddi, P.J Tasker, M.Goss, “High-power Time-domain Measurement System with Active Harmonic Load-pull for High-efficiency Base station Amplifier Design”, IEEE trans, Microwave Theory Tech., Vol. 48, pp. 2617-2624, December 2000.
- [7]. T. Williams, J. Benedikt and P.J Tasker, “Novel Base-Band Envelope Load pull Architecture”, proceedings of 9th IEEE High Frequency Postgraduate Colloquium Manchester September 2004.

“Novel base-band envelope load pull architecture”

Williams, T.; Benedikt, J.; Tasker, P.J.

Presented at High Frequency Postgraduate Student Colloquium, 2004,
Manchester

Conference Digest Page(s):157 - 161

Novel Base-Band Envelope Load Pull Architecture

Tudor Williams, Johannes Benedikt and Paul J. Tasker

School of Engineering , Cardiff University, Cardiff CF24 3TF

Tel: +44 2920 876347, e-mail: williamst5@cf.ac.uk

Abstract: The paper presents a novel active load-pull architecture capable of providing a constant broadband load with varying drive conditions that is unconditionally stable thus overcoming for the first time many of the problems associated with existing active load pull architectures.

1. INTRODUCTION

Traditionally load-pull, emulation of load impedance, has been achieved using passive techniques [1,2], however, limitations are introduced due to losses in the network between the device under test (DUT) and the tuner which reduce the maximum reflection coefficient obtainable. The solution to this problem is active load-pull where emulation of load impedance is achieved by injecting an amplified signal of specific magnitude and phase into the DUT output. Such active systems can have either an "open loop" or "closed loop" architecture. In a "closed loop" system, first presented by Bava [3], the injected signal is a modified version (direct function) of the DUT output signal. This ensures that the emulated load impedance (matching circuit) is independent of drive level, however this architecture is prone to oscillations. In the alternative "open loop" system, first introduced by Takayama [4], the injected signal is generated independently. This avoids the oscillation problem but now, to maintain a constant emulated load impedance (reflection coefficient) under changing drive conditions, requires in a slow iterative process; a number of magnitude and phase adjustments, manual or automated, of the injected signal are needed to maintain the target reflection coefficient.

This paper presents a novel active load-pull architecture, which overcomes these limitations. It incorporates a "closed loop" architecture not at RF but at the envelope frequency to ensure that the injected signal is a modified version (direct function) of the DUT output signal, hence maintaining the required constant emulated load impedance as drive level changes. Since the loop is closed only at the envelope frequencies no oscillations can occur at RF, conversely the active loop generates signals only at RF frequencies thus preventing the loop introducing oscillations at the envelope frequencies, making the system unconditionally stable. Applications for the system are numerous, the system is particularly useful as any load impedance presented is broadband making it possible to emulate matching circuits over the modulation bandwidth, furthermore emulated impedances can reach the entire impedance plane, making the system ideal for characterising devices used in the communications industry. A particularly valuable application can be found in high-speed test and measurement. The system will allow multiple power sweep and load condition measurements to be captured in a single waveform, thus dramatically decreasing measurement time.

2. REALISATION

In the proposed architecture, see figure 1, a fraction of the signal is coupled from the output of the device, this is then down converted to the base band using an I-Q demodulator, after which the I and Q signals are manipulated using analogue circuitry ($F(x,y)$) providing the transfer function derived below, shown in equation 1 –

As the relationship between input and output must be a constant it can be seen that the following is required;

$$(I' + jQ')/(I + jQ) = Z = x + jy$$

Re-arranging gives;

$$I' + jQ' = (x + jy) * (I + jQ)$$

Therefore giving the transfer function;

$$F(x,y) = I' + jQ' = (xI - yQ) + j(xQ + yI) \quad (1)$$

Hence, this formulation will ensure a drive level independent emulated load, quantified by the user defined values of x and y , is presented to the device under test (DUT). Conversion to RF, providing the injected output signal is achieved using the internal modulator of the load signal generator (ESG), as shown in figure 1. The developed load-pull system, termed “envelope load pull”, is then attached to a waveform measurement system previously developed at Cardiff University [5,6].

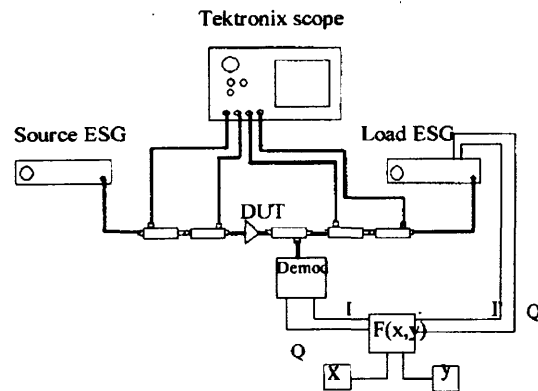


Figure 1 – Envelope Load pull configuration

During initial investigations a through line is utilized as the DUT. To simplify the problem further the internal demodulator of the source ESG is used rather than an external demodulator at the output of the DUT. This set up allows full testing of the envelope load pull concept without unnecessary increased complexity; see figure 2.

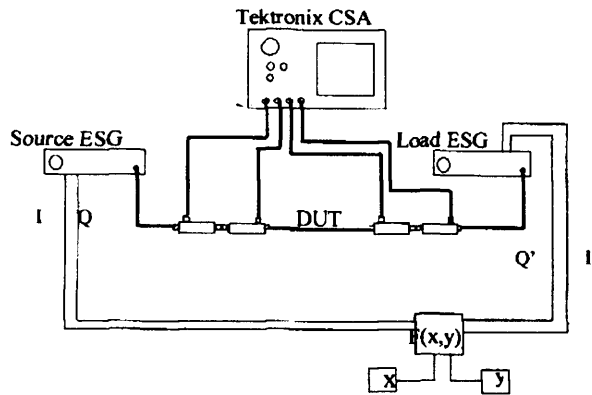


Figure 2 – Demonstration Envelope Load pull configuration

The circuit to generate the transfer function $F(x,y)$ is made up of “off the shelf” analogue multipliers and op-amps, the circuit is realised using the configuration shown in figure. 3.

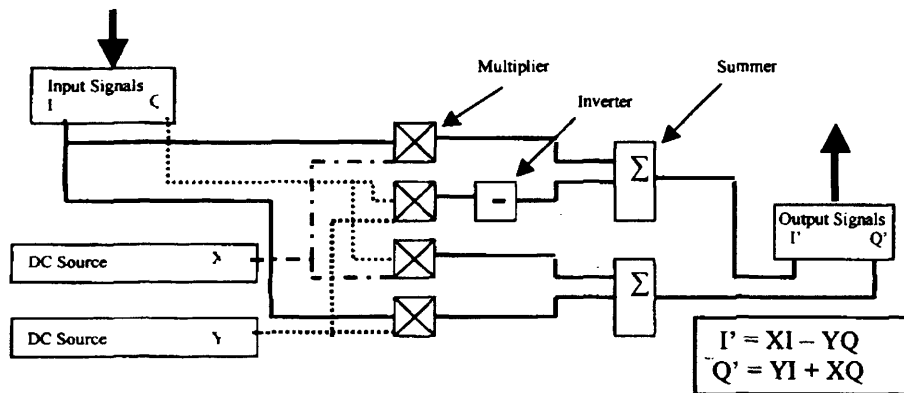


Figure 3 – Configuration of Analogue Circuit $F(x,y)$

The circuit allows for modulation of the load presented to the DUT by variation of the x and y signals, allowing emulation of any load. It was mentioned earlier that multiple measurements could be collected in a single waveform, for instance, in the case of a two-tone signal the device input power could be varied from zero to maximum with the modulation frequency, dramatically reducing time required to complete measurements such as P_{out} vs. P_{in} characterisation, making this system highly advantageous in a production environment.

To achieve this the DC sources providing x and y should be replaced by arbitrary waveform generators (AWG's), the Tektronix CSA has 500 data points available, this is equivalent to 250 frequency “slots” after taking an FFT. For example, if the tone spacing is set to a low frequency say 1kHz and the CSA set up to measure a data point every millisecond, 250 separate measurements can occur for every waveform captured. In order to ensure the power and load change for each measurement the two AWG's are used to produce step waveforms changing on the same 1 KHz grid, hence

each collected waveform contains the same information as completing 250 separate measurements.

3. EXPERIMENTAL RESULTS

To demonstrate the functionality of the envelope load-pull, the source ESG was set up to provide a 100 % AM modulation; a three tone signal around 1.8 GHz with tone separation of 20 KHz. For the purpose of these experiments two DC power supplies provide the x and y control signals. To automate the measurements, software has been written to control the CSA, ESG's and DC power supplies via a GPIB cable. Two experimental results are shown (figures 5 and 7) and compared to the respective ADS simulations (figures 4 and 6) of the system. In the first case the magnitude of the load signal is set to be half that of the input signal, and the phase angle is varied in 90 degree steps. In the second case the impedance is swept in a circle around the smith chart with a measurement taken every degree, this is achieved by sweeping values of X and Y. In all plots the emulated reflection coefficient relating to the carrier appear in red, points for the upper sideband in blue and for the lower sideband in black. Ideally the system is designed to emulate a frequency, hence drive level, independent load impedance.

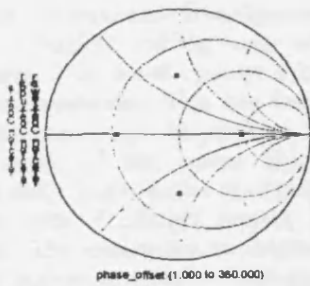


Figure 4 – Simulation every 90 degrees

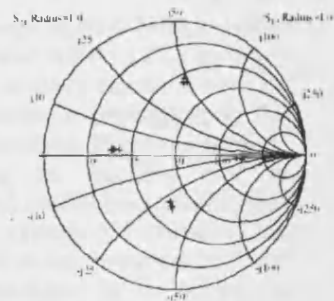


Figure 5 – Measurements every 90 degrees

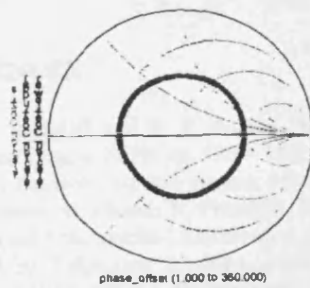


Figure 6 – Simulation every Degree

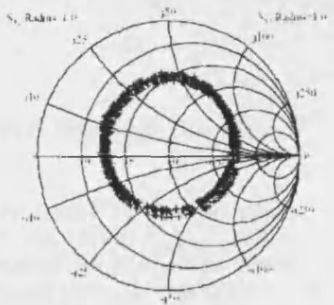


Figure 7 – Measurements every Degree

As can be seen from the results, this is the case, and there is a good agreement between simulated and experimental results. Importantly the impedance variation between the carrier, upper and lower sidebands is small. This experiment can be repeated for any value of magnitude hence allowing any impedance to be emulated. The misalignment from the centre of the smith chart seen most clearly in figure 7 is caused by the un-calibrated state of the system.

4. FURTHER WORK

The next step is to assemble the full system shown in figure 1. This full system will allow the loop to react to all output frequency components generated by the DUT rather than just those in the original input signal. Finally the bandwidth of the analogue circuitry should be improved to allow higher frequency tone separations to be measured, enabling the system to emulate existing communication standards.

5. CONCLUSION

The experimental investigation has proved the concept of base band envelope load pull is feasible, solving many of the problems associated with existing load pull architectures. This novel concept allows impedance to be actively emulated over the modulation bandwidth. This has been achieved by introducing a feedback loop that occurs only at envelope frequencies, hence, separating the feedback frequency from the RF frequency of the active loop, therefore providing for the first time an unconditionally stable active load pull system. Experimental results have shown good agreement with simulation results, although as yet the system has remained un-calibrated. The system can be improved using some simple developments, which will allow the system to react to inter-modulation products introduced by the device and incorporate current and future communication modulation standards. Simulations of the improved system have shown very promising results although to date the practical implementation remains incomplete.

REFERENCES

- [1]. R. B. Stancliff and D. P. Poulin, "Harmonic load-pull," MTT-S International Microwave Symposium Digest, 1979, pp. 185 – 187.
- [2]. Maury Passive load pull system, www.maurymw.com.
- [3]. G.P. Bava, U. Pisani, V. Pozzolo, "Active Load Technique for Load-Pull Characterisation at Microwave Frequencies" Electronic Letters 18th February 1982, Vol. 18, No. 4, pp. 178-180.
- [4]. Yoichiro Takayama "A New load-Pull Characterisation Method for Microwave Power Transistors" IEEE MTT-S international Microwave Symposium Digest 1976, pp. 218-220.
- [5]. D.J. Williams, P.J. Tasker, "An Automated Active Source and Load Pull Measurement System", Proceedings of the 6th IEEE High Frequency Postgraduate Colloquium, Cardiff, September 9th-10th 2001, pp 7-12.
- [6]. J. Benedikt, R. Gaddi, P.J Tasker, M.Goss, "High-power Time-domain Measurement System with Active Harmonic Load-pull for High-efficiency Basestation Amplifier Design", IEEE trans, Microwave Theory Tech., Vol. 48, pp. 2617-2624, December 2000.

“Large-Signal Vectorial Load–Pull Characterization of MEMS RF-Actuation”

Gaddi, R.; Williams, T.; Benedikt, J.; Tasker, P. J.; Giacomozzi, F.; Margesin, B.; Gnudi, A.;

Presented in IEEE Microwave and Wireless Components Letters, Volume 17, issue 12, Dec. 2007

Large-Signal Vectorial Load–Pull Characterization of MEMS RF-Actuation

Roberto Gaddi, T. Williams, J. Benedikt, P. J. Tasker, F. Giacomozzi, B. Margesin, and A. Gnudi

Abstract—Electrostatic actuated radio frequency microelectromechanical systems (RF-MEMS) switches and variable capacitors are susceptible to issues related to RF actuation or even RF pull-in under large-signal regime. This phenomenon is strictly related to the average RF voltage more than power, and the impedance environment of the device should be fully accounted for. We perform for the first time large-signal time-domain measurements to characterize the RF actuation effect on the real-time capacitance value of a suspended membrane-based RF-MEMS varactor, while controlling the load impedance presented to the device with an active load-pull. The dependence of RF-actuation on both real impedance and inductive admittance is directly extracted, giving strong insights on how power handling should be carefully scrutinized against each specific circuit design.

Index Terms—Load-pull, microelectromechanical devices, microwave measurements, nonlinearities.

I. INTRODUCTION

THE ubiquitous applicability of microelectromechanical systems (MEMS) to radio frequency (RF) circuit design has witnessed a multitude of device design approaches as well as reconfigurable circuit realizations [1], [2]. Particularly appealing are all potential implementations of impedance matching networks for multiband and multimode RF power applications. Besides, RF power handling and linearity under large-signal conditions are still open issues for this class of MEMS-enabled circuit designs [3]. In this respect, large-signal characterization under real device operating conditions remains the ultimate approach to both verification of available models and full qualification of a MEMS technology.

In the following, a large-signal time-domain measurement technique widely applied to the characterization of solid-state RF power devices is exploited for the inspection of RF power handling of a MEMS capacitive switch/varactor. Diverse impedance environment conditions are synthesized using an active load-pull system, and their influence on the device RF-actuation is directly extracted.

Manuscript received April 24, 2007; revised May 22, 2007. This work was supported in part by the Italian Ministry of Research under Grant PRIN 2005-091729.

R. Gaddi and A. Gnudi are with the Advanced Research Centre on Electronic Systems (ARCES), University of Bologna, Bologna I-40136, Italy (e-mail: rgaddi@arces.unibo.it).

T. Williams, J. Benedikt, and P. J. Tasker are with the School of Engineering, Cardiff University, Cardiff CF24 3TF, U.K.

F. Giacomozzi and B. Margesin are with Fondazione Bruno Kessler, Povo I-38050, Italy.

Color versions of one or more of the figures in this letter are available online at <http://ieeexplore.ieee.org>.

Digital Object Identifier 10.1109/LMWC.2007.908049

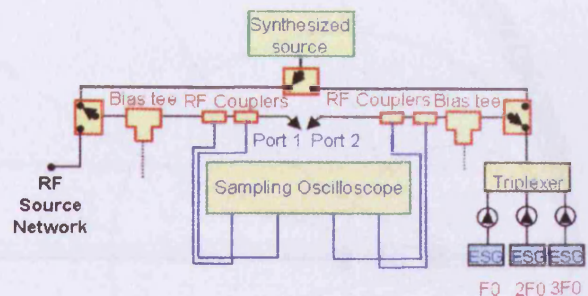


Fig. 1. Schematic of the time domain waveform measurement system.

II. MEASUREMENT SYSTEM DESCRIPTION

A fully automated time-domain waveform measurement system is utilized, capable of measuring waveforms with frequencies up to 12 GHz, implemented as a modified version of that presented in [4]. The system is built around a Tektronix CSA 8000 sampling oscilloscope. The RF test set consists of broad-band directional couplers, used to simultaneously measure the incident, a , and reflected, b waveforms at both ports. DC biasing and read-out of the device is achieved by a computer-controlled dc source through broad-band bias tees. The sampler data and the dc voltage and current information are composed into complete waveforms after error correction. Vector calibration and error correction are applied to the measured data to fully calibrate the system to the device reference plane, ensuring the removal of all losses and dispersions in the connecting hardware. Error corrected voltages and currents are made available both as time-domain waveforms and as harmonics magnitude and phase, allowing the user to work in real-time on both input and output time-domain curves and frequency-domain extracted parameters. Additional active harmonic load-pull hardware and software are added to the system, allowing the impedance of the fundamental, second and third harmonic frequencies to be fully controlled. Unlike passive load-pull architectures, the active approach adopted allows the synthesis of any impedance on the Smith chart, through active compensation of system losses.

III. DEVICE DESCRIPTION AND MEASUREMENT RESULTS

The MEMS technology process is based on surface micro-machining, with a dual thickness suspended gold membrane layer, electroplated on a Chromium seed layer (see Fig. 1). A TiN–Ti–Al–TiN–Ti multilayer is used for the RF-signal underpass. A detailed process description can be found in [5], while key dimensions of the device are shown in the layout and cross section of Fig. 2. The RF-MEMS shunt capacitive switch/varactor device is designed to work with a bias voltage coupled to

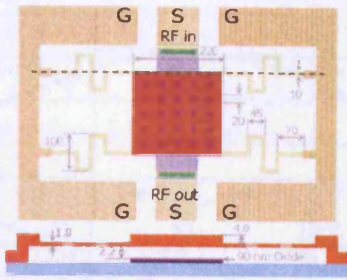


Fig. 2. Layout (top) and schematic cross section along the dotted line (bottom) of the MEMS switch/varactor used for characterization (dimensions are in microns).

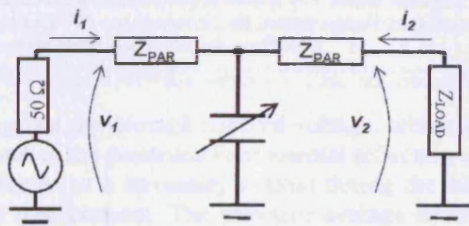


Fig. 3. Schematic of the RF-MEMS shunt switch/varactor measurement configuration; RF frequency is 1 GHz.

the RF signal path, hence without a separate actuation electrode, with a pull-in voltage of 5 V.

During large signal load-pull testing, the device is measured on-wafer at the GSG probe tips reference plane. The load impedance conditions are synthesized aiming at exhibiting RF actuation [3], while the RF power level is chosen so as to bring the device close to but not above the RF pull-in, since a hot switching event under high RF driving conditions would lead to device failure. The electrostatic force expression, in the case of a parallel plate capacitor transducer of effective area A and gap g , takes the following simplified form: $F_{ES} = \epsilon_0 A V^2 / 2g^2$. The electromechanical system will not respond at RF frequencies that are much higher than its mechanical cut-off frequency of 3 kHz. Nonetheless, an average electrostatic force resulting from the average ("DC") component of the squared RF voltage waveform will act on the mechanical system counteracted by the mechanical spring restoring force. The different equilibrium condition for each RF voltage amplitude level involves changing air-gap height below the suspended plate and intrinsic MEMS parallel plate capacitance. Besides, increasing load impedance leads to increasing effective voltages for a given level of source available power. Therefore, the value of the shunt MEMS capacitance is expected to change also with the load impedance even at constant source available power.

The schematic of the measurement conditions, large-signal currents and voltages definitions and input/output parasitic series impedances are shown in Fig. 3. The effects of changing either the real or the reactive components of the load impedance are observed separately, by first sweeping a real load impedance, and subsequently sweeping the load susceptance at constant load admittance value, at an RF frequency of 1 GHz.

In the first case, the device is presented with a real load impedance of increasing magnitude at constant source available

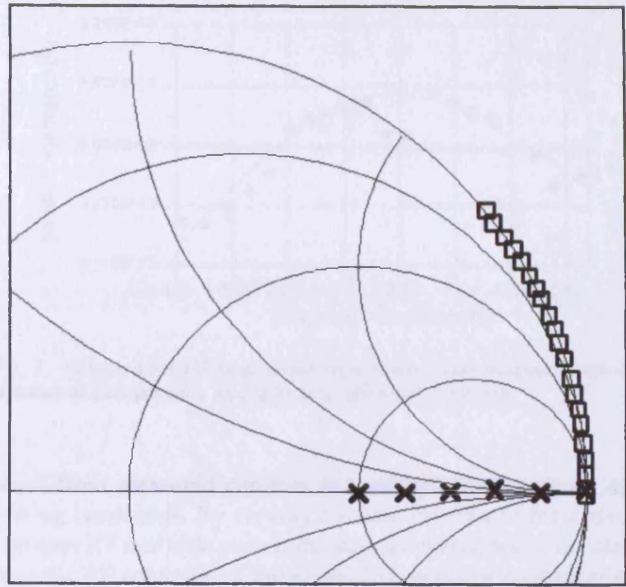


Fig. 4. Collection of the synthesized load reflection coefficients during measurements: increasing magnitude real load (crosses); purely reactive susceptance sweep (squares).

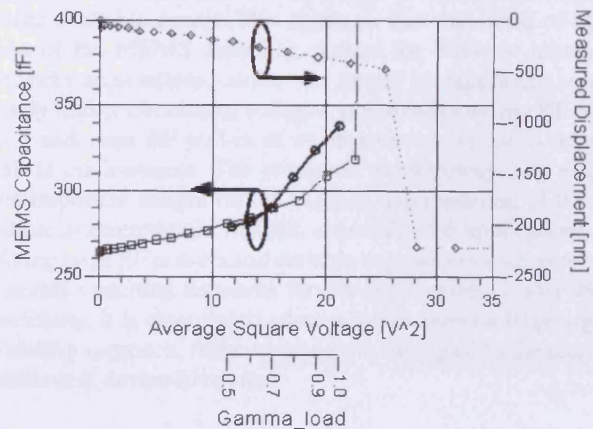


Fig. 5. Extracted large signal MEMS capacitance (thick circles), plotted against both the presented load reflection coefficient (bottom x -axis) and the corresponding average square voltage; the measured small signal capacitance and switch plate displacement are also plotted on the same squared voltage scale, showing device actuation.

power ($P_{av} = 21$ dBm). The real Γ is increased from 0.5 up to 1.0 at 0.1 steps, as shown in Fig. 4 (crosses). The large signal capacitance can be directly extracted from the measured fundamental frequency components of the large signal current flowing into the MEMS device $I_{MEMS} = I_1 + I_2$, and of the output voltage time derivative

$$C_{MEMS} = \text{imag} \left(\frac{I_{MEMS}}{\omega V_2} \right). \quad (1)$$

Fig. 5 compares the extracted large-signal capacitance to the same quantity as measured under small signal s -parameters regime with superimposed dc bias. The device plate displacement is also plotted, as measured with a Veeco Wyko NT1100 optical profiler system under the same dc bias. All quantities are

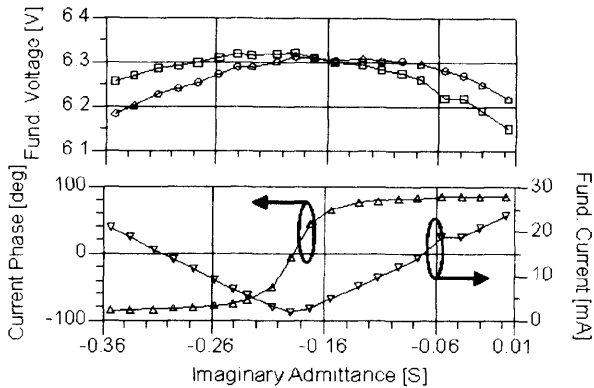


Fig. 6. Measured fundamental input voltage (\circ), output voltage (\square) and input current magnitude (∇) and phase (\triangle), all plotted against imaginary load admittance, at constant unity load reflection coefficient.

plotted against the average squared voltage, which is directly proportional to the presented fundamental reflection coefficient (also indicated as a secondary x -axis) during the large signal load-pull measurement. The effective average square voltage is clearly responsible for both small-signal dc and large-signal RF actuation. The less than 10% difference between the two capacitance curves approaching pull-in can be attributed to large-signal extraction accuracy.

The further effect of parallel resonating the MEMS capacitance with an inductive load on the effective RF voltage was investigated by sweeping the load susceptance presented to the device. This was performed at different values of real load admittance, but only the zero admittance case of Fig. 4 resulted in a measurable change in extracted MEMS capacitance. In this case, the RF available power was slightly backed-off ($P_{av} = 20.5$ dBm) again to avoid RF pull-in. Fig. 6 (top) shows the input and output fundamental voltage components for all synthesized susceptance values. The effect of series parasitics creates a voltage drop proportional to the current flowing into the respective terminal. For open circuit conditions, the current at port 2 is zero and v_2 will coincide with the voltage across the intrinsic MEMS capacitor. As the parallel load susceptance resonates with the intrinsic MEMS capacitance, the input current at port 1 goes through zero and phase inversion (Fig. 6, bottom).

At resonance, v_1 will equal the intrinsic MEMS voltage since no voltage drops will appear at port 1. For first-order analysis of the measured data, the average of the input and output voltages is used for the extraction of the MEMS capacitance. Further deembedding should be performed for more accurate capacitance extraction. Fig. 7 shows the extracted capacitance values versus load susceptance, confirming an increased RF actuation leading to a further 50 fF capacitance rise from the open circuit. All values are lower than the previous extraction in Fig. 5 due to the 0.5 dBm reduction of the available power level.

IV. CONCLUSION

The RF actuation behavior of a MEMS switch/varactor has been observed by directly extracting the large-signal capaci-

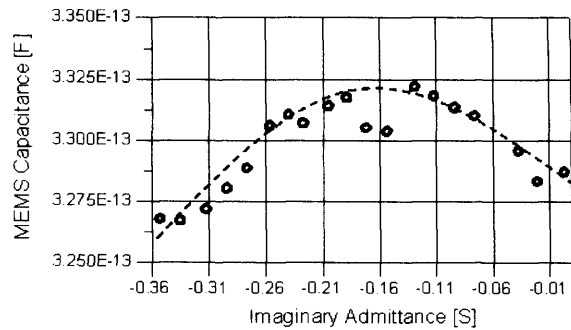


Fig. 7. Extracted MEMS large signal capacitance versus imaginary load admittance at constant unity load reflection coefficient magnitude.

tance from measured currents and voltages under various operating conditions. By varying the load impedance for a given constant RF available power, the strong dependence of the electrostatic RF actuation of the suspended capacitor membrane on the real load has been directly shown. A further increase of the RF actuation has been verified when operating the MEMS under parallel resonance with an inductive load, which leads to the maximum average squared RF voltage component for a given source available power. This confirms that this mode of operation of the MEMS capacitor, typical for filters or matching networks applications, causes the device to experience significantly higher circulating voltages, potentially causing RF actuation and even RF pull-in at much lower drive levels than in a 50 Ω environment. The presented methodology and results give important insight on the analysis and modeling of RF actuation in electrostatic MEMS, especially for applications involving large RF powers and variable impedances such as reconfigurable matching networks for PA applications. Under those conditions, it is essential to adopt a mixed-domain large-signal modeling approach, fully coupling the RF signal to the electro-mechanical device behavior.

REFERENCES

- [1] Q. Shen and N. S. Barker, "A reconfigurable RF MEMS based double slug impedance tuner," in *Proc. 35th Eur. Microw. Conf.*, Paris, France, 2005, pp. 537–540.
- [2] C. D. Nordquist, C. L. Goldsmith, C. W. Dyck, G. M. Kraus, P. S. Finnegan, F. Austin, IV, and C. T. Sullivan, "X-band RF MEMS tuned combline filter," *Electron. Lett.*, vol. 41, no. 2, pp. 76–77, Jan. 2005.
- [3] C. Palego, A. Pothier, A. Crunteanu, and P. Blondy, "High power reliability aspects on RF MEMS varactor design," *Microelectron. Rel.*, vol. 46, pp. 1705–1710, 2006.
- [4] D. J. Williams and P. J. Tasker, "An automated active source and load pull measurement system," in *Proc. 6th IEEE High Freq. Postgrad. Stud. Colloq.*, Sep. 2001, pp. 7–12.
- [5] F. Giacomozzi, M. Bellei, P. Farinelli, G. Mannocchi, R. Marcelli, B. Margesin, and V. Mulloni, "Electromechanical aspects in the optimization of the transmission characteristics of series ohmic RF-switches," in *Proc. 5th MEMSWAVE Workshop*, Uppsala, Sweden, Jun./Jul. 30-2, 2004, pp. C25–C28.

“Investigation of Electrical Base-Band Memory Effects in High Power 20W LDMOS Amplifiers”

Alghanim A.; Lees J.; Williams T.; Benedikt J., Tasker P.J.

Presented at 37th European Microwave Conference, 2007, Page(s):48-51

Investigation of Electrical Base-Band Memory Effects in High-Power 20W LDMOS Power Amplifiers

Abdulrahman Alghanim, Jonathan Lees, Tudor Williams, Johannes Benedikt, and Paul Tasker

*Dept of Electrical and Electronic Engineering, Cardiff School of Engineering, Cardiff University
The Parade, Cardiff, CF24 3TF, Wales, UK*

alghanima@Cardiff.ac.uk

Abstract— Memory effects are complex phenomena that present major problems in modern high-power linear microwave PA design. Specifically, these effects have a large influence on spectral symmetry and modulation frequency sensitivity which in turn impacts overall linearity and importantly the suitability of a Power Amplifier (PA) to linearisation through pre-distortion. This paper presents detailed two-tone modulated measurements that clearly show how electrical memory introduced by non-ideal low-frequency base-band impedances represent the most significant contributor to overall observed memory effects in high-power LDMOS PA design. The analysis is achieved through the characterisation of a 20W LDMOS device at 2.1 GHz using two-tone excitation and a purpose built high-power measurement system that allows the collection of both RF and IF voltage and current waveforms along with all associated impedances.

I. INTRODUCTION

Memory effects in microwave PAs are generally attributable to a number of physical processes that involve thermal [1], electrical [2] and surface effects [3]. Although electrical memory is generally considered as the major contributor, the relative significance of the different effects is however still not clearly understood. One obvious way to develop a more complete understanding is to attempt to remove the most likely contributing factor, and to measure and analyse any residual effects due to the others.

In this work, and for the first time at high power levels, simple two-tone modulation and inter-modulation product symmetry as a function of varying excitation tone-spacing is used as reliable indicator of the presence of memory effects [4, 5]. Using this approach, it can be shown that by controlling the sources of base-band electrical memory and specifically by using passive IF load-pull to maintain a constant IF impedance environment for a wide range of two-tone stimulus frequency separations, the measured IM3 terms remain largely symmetrical and tone spacing invariant.

II. MEASUREMENT SYSTEM

This investigation has been made possible by the development of a novel high-power modulated waveform measurement system that allows the observation and control of all relevant frequency components (RF, IF and DC) [4, 6]. The developed measurement system is capable of handling IF and RF power levels in excess of 100W which makes it

particularly relevant to the characterisation of devices used in mobile communications system base-station applications.

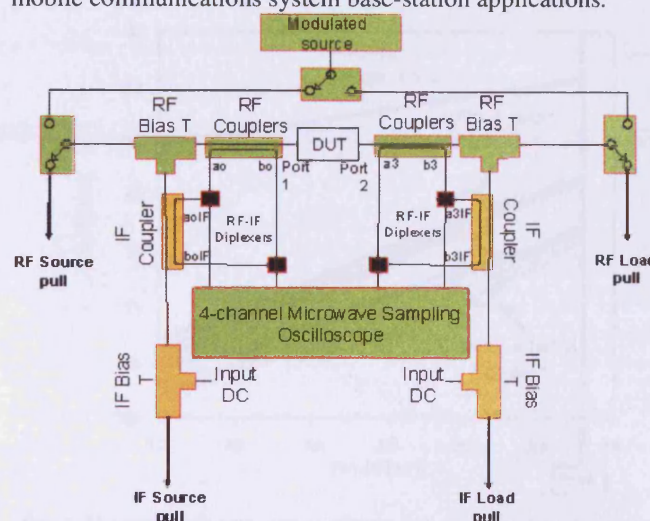


Fig 1 Schematic of the high power measurement system

The measurement system itself is shown in Figure 1 and consists of two main entities: the RF test-set (upper level) and the IF test-set (lower level) which are identical in terms of both component architecture and principle of operation.

The architecture incorporates combined IF and RF capabilities allowing the collection of all four travelling waves at both IF and RF frequencies. Diplexing the coupled RF and IF components of the signal prior to measurement is a key feature, and ensures phase coherence between measured IF and RF components. The system is fully vector-error corrected, and can therefore account for any errors introduced due to losses, mismatches and imperfect directivities in the system, thus allowing for the measurement of the complete modulated voltage and current waveforms and impedances that exist at the DUT plane.

Whereas the RF test-set is made up of off-the-shelf components, it was not possible to source an IF bias-tee possessing the combined DC current, RF power and bandwidth capabilities required. It was necessary therefore to design and manufacture suitable bias networks in-house to meet the required criteria and to allow the measurements discussed in this paper. This completed the measurement

architecture and provides the ability to present specific impedances to the significant IF frequency components, allowing for instance a near constant IF impedance environment to be maintained across a wide IF bandwidth during two-tone excitation.

III. MEASUREMENT RESULTS

Active harmonic load-pull is a relatively simple concept and is effective in allowing the presentation of specific loads to specific frequency components generated by a device [7]. Presenting constant IF and RF loads actively across wide modulation bandwidths is however extremely difficult in comparison, and fraught with complexity. For the measurements presented in this paper, input and output RF impedances were established at 10 Ohms using broad-band 5:1 impedance transformers [8].

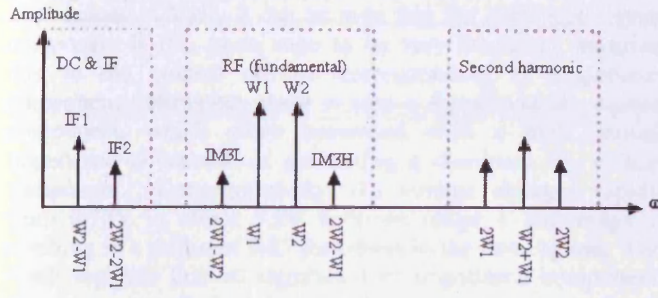


Fig 2 simplified two-tone spectrum

In terms of IF, and with reference to fig-2, passive load-pull was employed as a means of presenting a near short to IF_1 - the most significant IF component, for tone-spacing ranging between 1MHz and 9MHz. In order to minimise the physical length of the passive delay elements required at IF_1 , an offset-short termination was used for values of tone-spacing between 1MHz and 3MHz (range-1), whereas an offset-open termination was used for values of tone-spacing between 4MHz and 9MHz (range-2). It is important and interesting to note however that this approach, although very effective in presenting near constant impedances to IF_1 is ineffective in stabilising the impedance presented to IF_2 and other, higher IF components that are generally ignored during memory investigations and discussions. For example, figure 3 shows how the impedance presented to IF_2 varies significantly, moving around the Smith chart for the two termination cases and values of tone spacing.

It is important to note however that when the offset-short termination is used (range-1), the IF_2 load presented to the device is low impedance, whereas when the offset-open termination is used (range-2), the IF_2 load presented to the device is relatively high impedance.

Fig. 4 shows the measured RF two-tone power performance as a function of input drive level for all tone spacing. The behaviour of the two output tones (w_1 and w_2) is clearly almost independent of the tone spacing frequency.

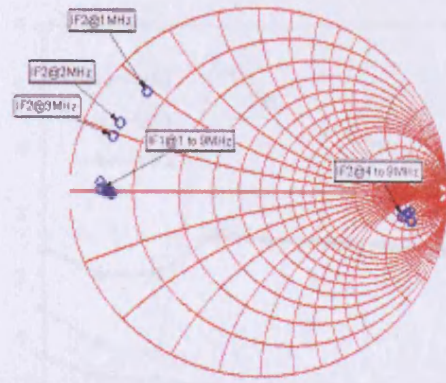


Fig 3 Measured IF_1 and IF_2 impedance vs. tone spacing

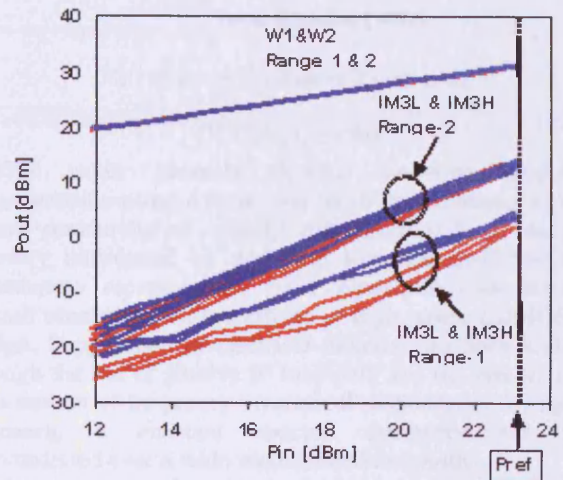


Fig 4 Measured two-tone power sweeps (w_1 and w_2) for all two-tone frequency separations

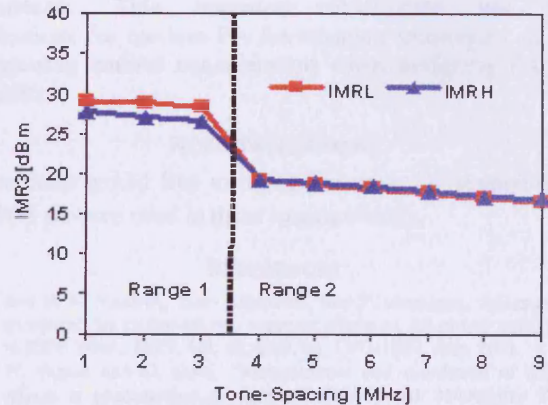


Fig 5 Measured IMR_{3L} and IMR_{3H} vs. Tone-Spacing

With regards to the inter-modulation products, IM_{3L} and IM_{3H} , two distinct responses are observed. This is clearly summarized in fig. 5 which plots the measured value of inter-modulation distortion ratio IMR_3 as a function of tone-spacing, at a fixed input power level of about 23.2 dBm which

is 5dB below the 1 dB compression point and identified as Pref (see fig4). As can be seen from this graph, two distinct regions are observed correlating directly to the two different passive load-pull regions. IMR3 is approximately 26 dB over range-1 and approximately 17 dB over range-2. This symmetry and a lack of any variation with tone separation frequency is a clear indication of the absence of memory effect in an environment where IF impedances are frequency invariant. The results show clearly that the variation of the impedance of the higher orders IF terms, which in this passive load-pull case are not deliberately controlled, contribute significantly to the observed variation over frequency.

To help understand this, figures 6 and 7 show the corresponding measured IF current components generated by the non-linear behavior of the transistor along with the resulting IF voltage components developed by the IF load impedances. Clearly it can be seen that the dominant current component is IF_1 , again seen to be very frequency invariant due to the control of the corresponding IF impedance component. However, there is also a significant IF_2 current component, which when presented with a high enough impedance is capable of generating a dominant IF_2 voltage component. Consequentially, IF_2 voltage changes rapidly from 0.73V to about 5.5V between range 1 and range 2, resulting in a different IM3 distortion in the two regions. This result suggests that all significant IF impedance components must be controlled and correctly terminated in order to remove the electrical memory.

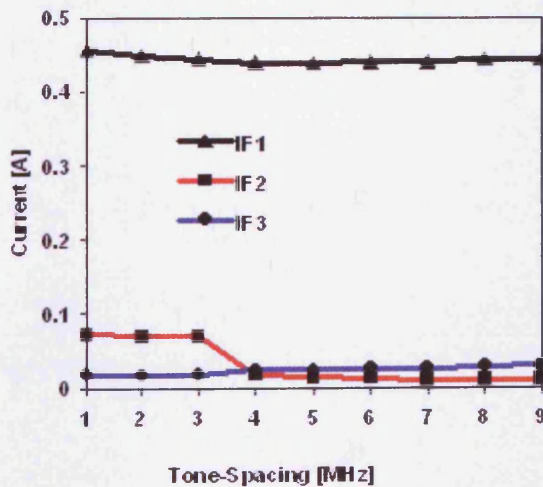


Fig 6 Measured IF current vs. Tone-Spacing

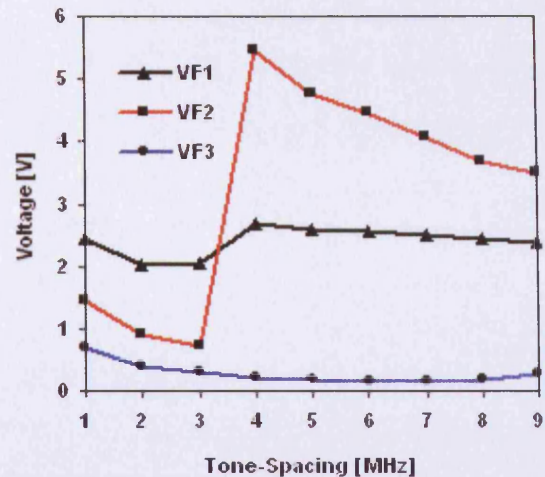


Fig 7 Measured IF voltage vs. Tone-Spacing.

IV. CONCLUSIONS

This paper presents detailed two-tone modulated measurements using a combined RF-IF measurement system. These measurements clearly demonstrate how electrical memory introduced by non-ideal low-frequency base-band impedances represent the most significant contributor to overall observed memory effects in high-power LDMOS PA design. Suppression of electrical memory has been achieved through the use of passive IF load-pull, and the synthesis and presentation of frequency invariant IF impedances. Using this approach, a constant spectral symmetry has been demonstrated over a wide modulation bandwidth.

Measurements show that third order inter-modulation behaviour is not only dependent on the most significant IF component (IF_1), but is also very sensitive to higher order IF components. This important observation has large implications for modern PA linearisation techniques, as well as requiring careful consideration when designing PA bias networks.

ACKNOWLEDGMENT

The authors would like to thank Freescale for supplying the LDMOS devices used in these measurements.

REFERENCES

- [1] Joel H. K. Vuolevi, Timo Rahkonen, Jani P. Manninen, "Measurement technique for characterizing memory effects in RF power amplifiers," in *IEEE Trans. MTT*, vol. 49, no.9, pp. 1383-1389, Aug. 2001.
- [2] W. Bosch and G. Gatti, "Measurement and simulation of memory effects in predistortion linearizers," *IEEE Trans. Microwave Theory Tech.*, vol. 37, pp. 1885-1890, Dec. 1989
- [3] A. E. Parker and J. G. Rathmell, "Bias and frequency dependence of FET characteristics," in *IEEE Trans. Microwave Theory Tech.*, vol. 51, pp. 588-592, Feb. 2003
- [4] D.J. Williams, I. Lakey, P.J. Tasker "A Study of the Effect of Envelope Impedance on intermodulation asymmetry using a two-tone Time Domain Measurement System" *IEEE MTT-S Int. Microwave S p p . Dig.*, Vol. 3, 2002 pp. 1841-1844,

- [5] N.B. Carvalho, J.C. Pedro, "Two-Tone IMD Asymmetry in Microwave Power Amplifiers" IEEE MTT-S Int. Microwave Symp. Dig., Vol. 1, 2000 pp. 445-448
- [6] Alghanim, A.; Benedikt, J.; Tasker, P., "A measurement test-set for characterisation of high power LDMOS transistors including memory effects." High Frequency Postgraduate Student Colloquium, 2005, vol., no.pp. 29- 32, 5-6 Sept. 2005.
- [7] Benedikt, J.; Gaddi,R.; Tasker, P.J.; Goss, M.; "High-power time-domain measurement system with active harmonic load-pull for high-efficiency base-station amplifier design", IEEE Transactions on Microwave Theory and Techniques, Vol. 48, Issue 12, Dec. 2000, pp. 2617-2624.
- [8] Z. Aboush, C. Jones, G. Knight, A. Sheikh, H. Lee, J. Lees, J. Benedikt, and P. J. Tasker, "High Power Active Harmonic Load-Pull System for Characterization of High Power 100Watt Transistors," IEEE MTT-S Int. Microwave Symposium, 2005 .

“Using active IF load-pull to investigate electrical base-band memory effects in high-power LDMOS transistors”

Alghanim A.; Lees J.; Williams T.; Benedikt J., Tasker P.J.

Presented at IEEE Asia-Pacific Microwave Conference 2007

Using active IF load-pull to investigate electrical baseband induced memory effects in high-power LDMOS transistors

Abdulahman Alghanim, Jonathan Lees, Tudor Williams, Johannes Benedikt, and Paul Tasker

Dept of Electrical and Electronic Engineering, Cardiff School of Engineering, Cardiff University, The Parade, Cardiff, CF24 3TF, Wales, UK

E-mail: alghanima@Cardiff.ac.uk Tel: +44 2920 876349,

Abstract— Memory effects are generally attributable to thermal, electrical, packaging and/ or surface effects. This behaviour in turn impacts overall linearity and importantly the suitability of a Power Amplifier (PA) to linearisation through pre-distortion. It is assumed that electrical memory introduced by the low-frequency baseband impedance environments associated with the power amplifier bias insertion networks being frequency dependent represents a significant contributor to overall observed memory effects in high-power LDMOS PA design. In this work, baseband or IF active load-pull is used to provide an effective way to engineer all the significant IF components generated as a result of multi-tone excitation, independent of modulation frequency. Specific IF impedance environments are presented to a device with this approach in order to probe the sensitivity to IF impedance variations. These investigations are performed on a 12W LDMOS device characterised at 2.1 GHz within a purpose built, high-power measurement system, that allows the collection of both RF and IF voltage and current waveforms along with all associated impedances.

I. INTRODUCTION

One approach in developing understanding of memory effects in microwave PAs is to analyze and control the most likely contributing factors, frequency varying IF impedance. Previous work[1] employed passive IF load-pull in order to control the low-frequency impedances presented to the most significant IF components generated by a device. This approach however is restricted by a number of factors: firstly the realisable reflection coefficients are limited by the presence of significant losses associated with both the IF test-set and the physically long delay-lines necessary to realize the required necessary offset short terminations. As a consequence, the minimum IF impedance realizable using this system was approximately 7Ω , which is some way from a short circuit. This is especially true considering the relatively low optimum output impedance of the high-power LDMOS device employed. Secondly, only one IF frequency component could be controlled at any one time. As a consequence, while controlling of the most significant IF frequency component, the other IF components are terminated in arbitrary impedances, making results difficult to interpret.

In this work, and for the first time at power levels relevant to base-station PA design, active IF load-pull has been used to offer fully independent control of the

impedance presented to all the significant IF components generated by a 12W LDMOS device, overcoming all of the problems associated with the previously described passive approach. Using two-tone modulation, the IM3 inter-modulation products are measured as a function of varying excitation tone-spacing and IF impedance. By using active IF load-pull to control IF drain impedance, it can be shown that the measured IM3 terms are a strong function of the IF impedance over bandwidths that are at least four times that of the modulation frequency.

II. MEASUREMENT SYSTEM

This investigation has been made possible by the development of a novel high-power modulated waveform measurement system that allows the observation and control of all relevant frequency components (RF, IF and DC) [2, 3]. The developed measurement system is capable of handling IF and RF power levels in excess of 100W which makes it particularly relevant to the characterization of devices used in mobile communications system base-station applications.

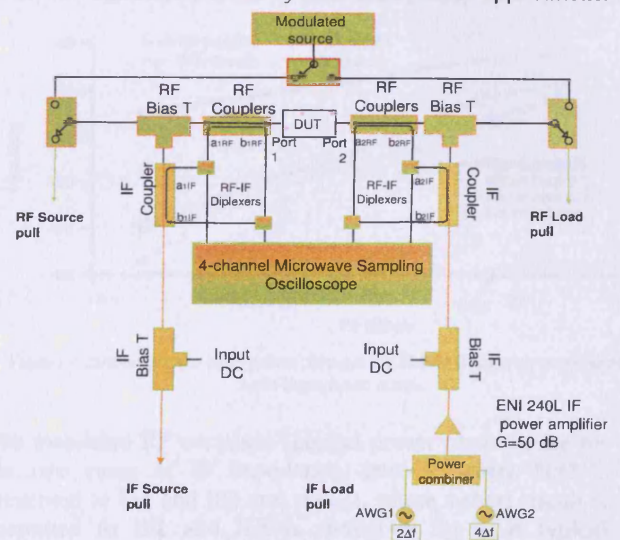


Figure 1 Schematic of the high power measurement system

The measurement system itself is shown in fig 1 and consists of two main entities: the RF test-set (upper level) and the IF test-set (upper level) and (lower level) which are identical both in terms of component architecture and principle of operation.

The architecture incorporates combined IF and RF capabilities allowing the collection of all four traveling waves at both IF and RF frequencies. Diplexing the coupled RF and IF components of the signal prior to measurement is a key feature, and ensures phase coherence between measured IF and RF components. The system is fully vector-error corrected, and can therefore account for any errors introduced due to losses, mismatches and imperfect directivities in the system, thus allowing for the measurement of the complete modulated voltage and current waveforms and impedances that exist at the DUT plane.

Whereas the RF test-set is made up of off-the-shelf components, it was not possible to source an IF bias-tee possessing the combined DC current, RF power and bandwidth capabilities required. It was necessary therefore to design and manufacture suitable bias networks in-house to meet the required criteria and to allow the measurements discussed in this paper. In addition, for a high power device, such as the 12W LDMOS used in this measurement, the IF components generated are large. This is especially true of IF1 (twice the modulation frequency) and IF2 (four times the modulation frequency), the most significant base-band components. In order to actively load-pull these components; an ENI 240L 20 KHz to 10 MHz, 40W linear power amplifier was used to amplify the signal from the arbitrary wave generators (AWG) as seen in fig 1. This integrated measurement architecture provides the ability to present, independently, specific impedances to the two significant IF frequency components, allowing for instance a constant IF impedance environment to be maintained across a wide IF bandwidth during two-tone excitation.

III. MEASUREMENT RESULTS

Active harmonic load-pull is a relatively simple concept and is effective in allowing the presentation of specific loads to specific frequency components generated by a device [4]. Presenting constant RF loads actively across wide modulation bandwidths is however extremely difficult in comparison, and fraught with complexity. For the measurements presented in this paper, input and output RF system impedances were established at 10 Ohms using broad-band 5:1 impedance transformers [5], while IF system impedances remained at 50 Ohms. To achieve IF impedances other than 50 Ohms active IF load-pull was employed to independently engineer different, frequency independent, impedance environments at the two significant IF components; IF1 and IF2, defined in fig 2. Termination of these frequency components into a short circuit would be desirable, particularly for tone-spacing ranging between 1MHz and 10MHz. Fig 3 illustrates just how effective the IF load-pull is in maintaining a frequency independent IF1 short circuit impedance. The observed variation is very

small and can be seen to be less than 0.07 magnitude and 1.5 degrees in phase over the entire IF bandwidth. It is important to note that IF2 is not successfully load-pulled for modulation frequencies greater than 7MHz due to bandwidth limitations of the IF PA. This is highlighted in fig 3, which shows the significant variation in IF2 impedance from the desired short circuit for frequencies from 8 MHz to 10 MHz.

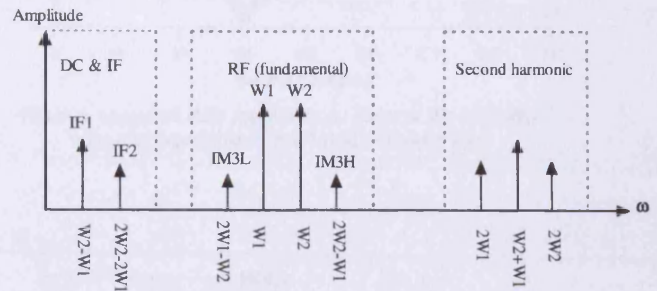


Figure 2 simplified two-tone spectrum

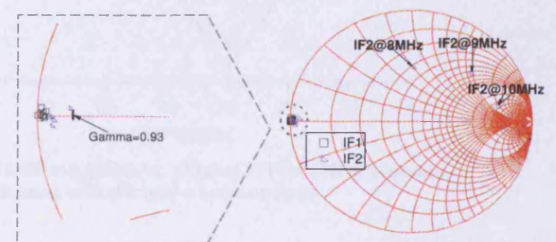


Figure 3 Measured IF1 vs. tone spacing at $Z_0=50\Omega$

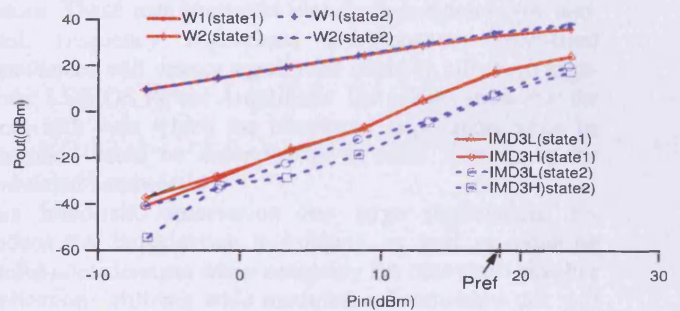


Figure 4 measured two-tone power sweeps for 5MHz frequency separation for both impedance states.

The measured RF two-tone spectral power performance for the two cases of IF impedance, state 1, where 50Ω is presented to IF1 and IF2 and state 2, where a short circuit is presented to IF1 and IF2 is shown in fig 4. A typical IM3 inter-modulation components, is observed over a power sweep of some 30 dB. In this case the tone-spacing is 5

MHz. The variation of measured IM3 response as a function of IF impedance is clearly seen.

Fig 5 summarizes the IM3 behavior at these two different IF impedance states for different values of tone spacing ranging between 1 and 10 MHz, at a single drive level (Pref), this power level corresponds to a point 1dB below the 1dB compression point.

The behavior of the two output tones (w_1 and w_2) is clearly observed to be almost independent of both the tone spacing frequency and IF termination. In the IF impedance state 1 the observed IMD_3 response, while higher than the reference state 2, is found to be independent of tone-spacing. This result indicates that if a frequency independent constant base-band termination is utilized in the Power Amplifier drain bias network no modulation frequency sensitivity in $IM3$ response would be observed. However, in the case of state 2, short circuit base-band terminations, modulation frequency independence was only observed between 4 and 7 MHz.

It is important to note that IF2 is not load-pulled for modulation frequencies greater than 7MHz due to bandwidth limitations of the IF PA. This variation in IF2 impedance is considered to be the primary cause of the observed variation in IMD_3 response above 7 MHz. This conclusion is consistent with observations made in previous work [1]. To confirm this interpretation the value of the IF2 impedance was varied while fixing the IF1 at a short circuit. The variation of IMD_3 response versus IF2 impedance at 5MHz tone spacing is shown in fig 6. This result clearly shows that variations in IF2 impedance, which is four times the modulation frequency, modify the levels of $IM3$ inter-modulation components. Thus to achieve modulation frequency independent response the base-band impedance must be engineered to be frequency independent over a bandwidth that must be at least four times that of the modulation frequency. The results also indicated that there is an optimum IF2 impedance that minimizes the $IM3$ terms. A similar response is obtained if the IF1 impedance is varied while the IF2 impedance is held constant see fig 7. The frequency variation observed below 4 MHz is not related to variation in base-band impedance and thus must be associated with other memory sources; i.e. thermal, surface trapping, package parasitics.

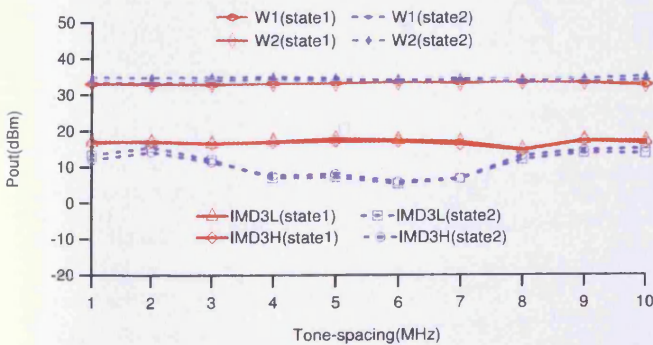


Figure 5 Measured fundamental and IMD power for two impedance states at different two-tone frequency separations at a constant drive level.

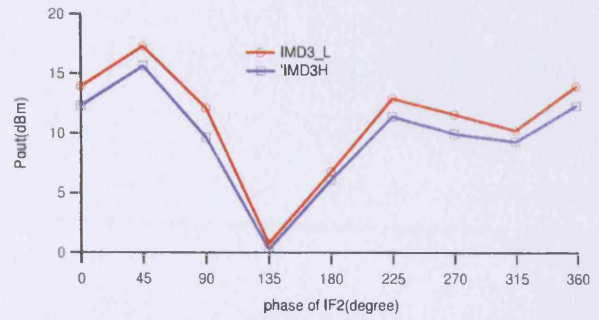


Figure 6 Measured IMD magnitude vs. phase of IF2 for 5MHz frequency separation with IF1 held a constant short

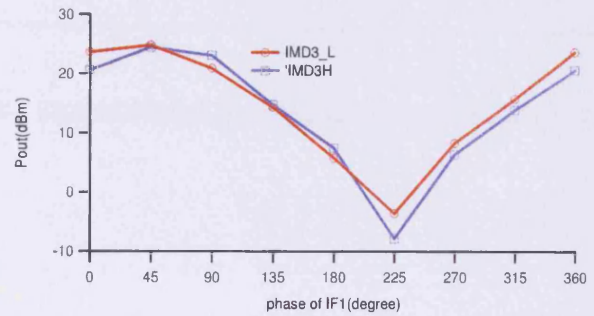


Figure 7 Measured IMD magnitude vs. phase of IF1 for 5MHz frequency separation with IF2 held a constant short.

IV. CONCLUSIONS

This paper presents detailed two-tone modulated measurements using a combined RF-IF measurement system. These measurements clearly demonstrate how non-ideal, frequency dependent, low-frequency base-band impedances will induce significant memory effects in high-power LDMOS Power Amplifiers. The results show that the bandwidth over which the base-band impedances must be controlled must be extended to at least four times the modulated bandwidth.

This important observation has large implications for modern PA linearisation techniques, as well as requiring careful consideration when designing PA bias networks. For applications utilizing wide modulation bandwidths this will become a serious design constraint.

ACKNOWLEDGMENT

The authors would like to thank Freescale for supplying the LDMOS devices used in these measurements.

REFERENCES

- [1] Alghanim, A.L., J.; Williams, T.; Benedikt, J.; Tasker, P. Investigation of electrical base-band memory effects in high-power 20W LDMOS Power Amplifiers. in EUMC. 2007. Munich., in press.
- [2] D.J. Williams, I. Leckey, P.J. Tasker "A Study of the Effect of Envelope Impedance on intermodulation asymmetry using a two-tone Time Domain Measurement System" IEEE MTT-S Int. Microwave S p p . Dig., Vol. 3, 2002 pp. 1841-1844,
- [3] Alghanim, A.; Benedikt, J.; Tasker, P., "A measurement test-set for characterisation of high power LDMOS transistors including memory effects," *High Frequency Postgraduate Student Colloquium, 2005* , vol., no.pp. 29- 32, 5-6 Sept. 2005.
- [4] Benedikt, J; Gaddi, R; Tasker,P.J.; Goss,M; "High-Power time domain measurement systems with active harmonic load-pull for high-efficiency base-station amplifier design". IEEE Transactions on Microwave Theory and Techniques, Vol.48, Issue 12, Dec 2000, pp.2617-2624.
- [5] Z. Aboush, C. Jones, G. Knight, A. Sheikh, H. Lee, J. Lees, J. Benedikt, and P. J. Tasker, "High Power Active Harmonic Load-Pull System for Characterization of High Power 100Watt Transistors," IEEE MTT-S Int. Microwave Symposium, 2005.

